



جامعة خليفة
Khalifa University

Numerical Modeling and Simulation of Viscoelastic Polymer Flow in Porous Media

Mursal Zeynalli

M.Sc. Thesis

July 2021

A thesis submitted to Khalifa University of Science and Technology in accordance with the requirements of the degree of Master of Science in Petroleum Engineering in the Department of Petroleum Engineering



Numerical Modeling and Simulation of Viscoelastic Polymer Flow in Porous Media

by

Mursal Zeynalli

A thesis submitted in partial fulfillment of the
requirements for the degree of

M.Sc. in Petroleum Engineering

at

Khalifa University

Thesis Committee

Dr. Emad W. Al Shalabi (Supervisor)
Khalifa University

Dr. Waleed AlAmeri (Co-Supervisor)
Khalifa University

Dr. MD Motiur Rahman (Internal Examiner)
Khalifa University

Dr. Saeed Al Hassan (Internal Examiner)
Khalifa University

July 2021

Abstract

Mursal Zeynalli, “Numerical Modeling and Simulation of Viscoelastic Polymer Flow in Porous Media”, M.Sc. Thesis, Petroleum Engineering, Department of Petroleum Engineering, Khalifa University of Science and Technology, United Arab Emirates, July 2021.

With the continuously accelerated energy demand, the petroleum industry needs to apply more advanced techniques to enhance production from existing fields or make new field discoveries in order to satisfy future energetic requirements. Enhanced Oil Recovery (EOR) is a crucial stage in oil production that may increase ultimate oil recovery to more than half of the reservoir's original oil in place (OOIP). Polymer flooding is one of the most commonly used chemical EOR methods. Conventionally, this technique was believed to improve macroscopic sweep efficiency by sweeping only bypassed oil. Nevertheless, recently it has been found that polymers exhibiting viscoelastic behavior in the porous medium can also improve microscopic displacement efficiency resulting in higher additional oil recovery. Therefore, an accurate prediction of the complex rheological response of polymers is crucial to obtain a proper estimation of incremental oil to polymer flooding.

In this research, we proposed a novel viscoelastic model to comprehensively analyze the polymer rheological behavior in porous media. This model is considered an extension of the unified apparent viscosity model provided in the literature and is termed as extended unified viscosity model (E-UVM). The main advantage of our model is its ability to capture the polymer mechanical degradation at ultimate shear rates primarily observed near wellbores. Furthermore, the fitting parameters used in the model were correlated to the rock and polymer properties, significantly reducing the need for time-consuming coreflooding tests for future polymer screening works.

Moreover, the model was implemented and verified in a reservoir simulator. The comparison between various viscosity models existing in the literature and E-UVM in the reservoir simulator revealed that using the latter model can predict oil recovery with more accuracy since it accommodates the mechanical degradation of polymers. The core-scale predictions of polymer flooding also showed a positive effect of polymer concentration and injection rate on oil mobilization. Finally, field-scale predictions of the polymer flooding technique were performed in a quarter 5-spot well pattern, using rock and fluid properties representing the Middle East carbonate reservoirs. The effect of various parameters on the polymer flooding efficiency was investigated during sensitivity analysis.

Indexing Terms: Polymer Flooding, Extended Viscoelastic Model, Shear-Thinning, Shear-Thickening, Mechanical degradation, Core-Scale and Field-Scale Simulation Studies.

Acknowledgement

Firstly, I would like to express my appreciation and frankly thank my advisor Dr. Emad W. Al Shalabi and co-advisor Dr. Waleed AlAmeri, for their constant guidance and assistance during my master's degree. They have played a significant role in my development as a graduate student. Dr. Emad W. Al Shalabi and Dr. Waleed AlAmeri both invested much time and persistent effort, shared their knowledge, and taught the proper means of conducting research. This study would not have been feasible without their constant comments and guidance during regular weekly meetings for the last two years.

Secondly, I would like to express gratitude to the committee members, Dr. MD Motiur Rahman and Dr. Saeed Al Hassan, for their assistance and helpful feedback. I would also like to thank my colleagues: Mr. Omar Chaabi, Mr. Umar Alfazazi, the research group team members, and the Petroleum Engineering Department of Khalifa University for their constant support.

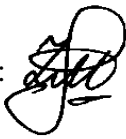
Finally, I thank my precious parents and sisters for their motivation and big love to obtain my M.Sc. degree.

Declaration and Copyright

Declaration

I declare that this work was carried out under the Khalifa University of Science and Technology regulations. The work is completely conducted by me except where specified by particular reference in the text. Any views stated in the thesis belong to the author and do not represent those of Khalifa University of Science and Technology. The thesis has not been fully or partially presented to any other university for any degree.

Author Name: Mursal Zeynalli

Author Signature: 

Date: 01/07/2021

Copyright ©

No part of this work may be stored in a retrieval system, reproduced, or transmitted, by any means or in any form, photocopying, recording, mechanical, scanning, or otherwise, without the author's prior written approval. The thesis may be available for consultation in Khalifa University of Science and Technology Library and inter-library lending for use in another library. It may be copied in whole or in part for any bonafide library or researcher, understanding that users are made familiarized of their obligations under copyright, i.e., that no quotation and no information derived from it may be published without the author's prior consent.

Contents

Abstract	i
Acknowledgements.....	ii
Declaration and Copyright.....	iii
Contents	iv
List of Figures	vii
List of Tables	xii
List of Abbreviations	xiv
List of Symbols.....	xvi
CHAPTER 1: INTRODUCTION	1
1.1 Problem Statement	1
1.2 Motivation.....	3
1.3 Research Objectives.....	3
1.4 Thesis Organization	3
CHAPTER 2: LITERATURE REVIEW	5
2.1 Enhanced Oil Recovery	5
2.2 Polymer Flooding as an EOR technique	13
2.3 Mechanisms of Polymer Flooding	15
2.3.1 Recovery Efficiency	15
2.3.2 Mobility Ratio.....	18
2.3.3 Other Flow Parameters	18
2.4 EOR Polymers Used Under Harsh Reservoir Conditions.....	20
2.4.1 Classification of Polymers	20
2.4.2 Hydrolysis of Polyacrylamides	21
2.4.3 Screening Studies for Harsh Conditions	22

2.5	Polymer Viscoelastic Properties	24
2.5.1	Deborah Number.....	24
2.5.2	Relaxation Time.....	25
2.5.3	Residence Time.....	30
2.5.4	Flow of Viscoelastic Polymers in the Porous Medium.....	31
2.6	Apparent Viscosity Models.....	33
2.6.1	Shear Viscosity	33
2.6.2	Elastic Viscosity.....	34
2.6.3	Models for Apparent Viscosity Estimation.....	36
2.7	Impact of Polymer Viscoelasticity on Residual Oil Recovery	37
2.7.1	Trapping Number.....	40
2.7.2	Capillary Desaturation Curve	42
2.7.3	Residual Saturations as a Function of Trapping Number and Deborah Number.....	45
2.7.4	Relative Permeability Models.....	48
2.8	Mechanical Degradation of Viscoelastic Polymers	49
2.9	Injectivity of Viscoelastic Polymers	51
2.10	Polymer Flooding Field Applications.....	52

CHAPTER 3: COMPREHENSIVE CORRELATION FOR PREDICTING POLYMER APPARENT VISCOSITY IN POROUS MEDIA		57
3.1	Development of Extended Unified Apparent Viscosity Model.....	57
3.2	Validation of Extended Unified Apparent Viscosity Model.....	58
3.2.1	List of Experimental Coreflooding Data.....	58
3.2.2	Validation of the Model Against Coreflooding Data.....	59
3.3	Empirical Correlations for Estimating the Model Parameters	70
3.3.1	Model Parameters Obtained from Fitting the E-UVM to Coreflooding Data	70
3.3.2	Development of Empirical Correlations to Predict Model Parameters	72

CHAPTER 4: POLYMER FLOODING SIMULATION WITH MATLAB RESERVOIR SIMULATION TOOLBOX.....		77
4.1	Introduction to MATLAB Reservoir Simulation Toolbox (MRST).....	77
4.2	Core-Scale Simulation Model.....	78

4.2.1	Experimental Data	78
4.2.2	Core-Scale Simulation Model Data	81
4.3	The Polymer Model Used in MRST	83
4.3.1	Polymer Mixing Effect	83
4.3.2	Permeability Reduction Effect	84
4.3.3	Polymer Non-Newtonian Behavior	84
4.4	Implementation of E-UVM in MRST	86
4.4.1	Modifying Shear Multipliers by E-UVM Viscosities	86
4.4.2	Verification of the E-UVM Technique Against Original Implementation	88
4.5	Modeling the Effect of Polymer Viscoelasticity on Displacement Efficiency	91
4.5.1	Trapping Numbers Implementation	91
4.5.2	Modeling N_T Effect on Residual Saturation and Relative Permeabilities	93
4.5.3	Verification Against the UTCHEM Simulator	98
CHAPTER 5: SIMULATION STUDIES AT CORE- AND FIELD-SCALES		103
5.1	Core-Scale Simulation Studies	103
5.1.1	Simulation and History Matching of Waterflooding Cycle	103
5.1.2	Polymer Rheological Studies	105
5.1.3	Polymer Concentration and Injection Rate Effects on Polymer Flooding	110
5.1.4	Polymer Flooding Simulation at Secondary and Tertiary Injection Modes	116
5.2	Field-Scale Simulation Studies	119
5.2.1	Field-Scale Simulation Model	119
5.2.2	Base Case Simulation Results	124
5.2.3	Sensitivity Analysis	132
CHAPTER 6: CONCLUSIONS AND RECOMMENDATIONS		140
6.1	Summary and Conclusions	140
6.2	Recommendations	142
REFERENCES		143
APPENDICES		155

List of Figures

Figure 2.1: Classification of oil recovery techniques (Oil and Gas Journal, 1990).....	6
Figure 2.2: Schematic of IOR from a typical EOR response (modified after Lake <i>et al.</i> , 2014)	7
Figure 2.3: Evolution of EOR projects in the USA (modified after Alvarado and Manrique, 2010)	9
Figure 2.4: The classification of EOR techniques (modified after Lake <i>et al.</i> , 2014).....	12
Figure 2.5: Production profiles for waterflooding and polymer flooding with the corresponding economic limits (modified after Sorbie, 1991)	14
Figure 2.6: Schematics of the different scales involved in oil recovery processes (Zitha <i>et al.</i> , 2011)	15
Figure 2.7: Schematic of volumetric sweep improvement resulted by polymer flooding: (a) waterflooding, (b) polymer flooding (modified after Sorbie, 1991)	17
Figure 2.8: Hydrolysis of PAM to HPAM (modified after Ma <i>et al.</i> , 2015).....	22
Figure 2.9: The Cross-Over Point Model to determine relaxation time (Sheng, 2011).....	26
Figure 2.10: Schematic illustration of viscoelastic fluid flow behavior (modified after Sheng, 2011)	32
Figure 2.11: Capillary desaturation curve schematic (modified after Lake <i>et al.</i> , 2014).	43
Figure 2.12: Pore-size distribution effect on CDC (Lake <i>et al.</i> , 2014).....	44
Figure 3.1: Fitting the models to Experiment № 1 data (1.5 g/L-20 MDa-HPAM at 20 g/L TDS, Berea Sandstone Core)	60
Figure 3.2: Fitting the models to Experiment № 2 data (1.5 g/L-20 MDa-HPAM at 35 g/L TDS, 0.361 D Berea sandstone core).....	61
Figure 3.3: Fitting the models to Experiment № 3 data (1 g/L-20 MDa-HPAM at 38.81 g/L TDS, 2.17 D Bentheimer sandstone core)	61
Figure 3.4: Fitting the models to Experiment № 4 data (1 g/L-20 MDa-AMPS at 103.3 g/L TDS, 1.26 D Bentheimer sandstone core)	62
Figure 3.5: Fitting the models to Experiment № 5 data (0.5 g/L-20 MDa-HPAM at 20 g/L TDS, 0.048 D Glass Bead Pack).....	62
Figure 3.6: Fitting the models to Experiment № 6 data (0.5 g/L-20 MDa-HPAM at 20 g/L	

TDS, 0.022 D Glass Bead Pack).....	63
Figure 3.7: Fitting the models to Experiment № 7 data (1 g/L-8 MDa-SAV10 at 180 g/L TDS, 1.616 D reservoir carbonate core).....	63
Figure 3.8: Fitting the models to Experiment № 8 data (1 g/L-8 MDa-SAV10 at 180 g/L TDS, 0.121 D reservoir carbonate core).....	64
Figure 3.9: Fitting the models to Experiment № 9 data (1 g/L-20 MDa- Flopaam 3830S at 3 g/L TDS, 0.573 D Berea sandstone core).....	64
Figure 3.10: Fitting the models to Experiment № 10 data (1 g/L-20 MDa- Flopaam 3830S at 41.95 g/L TDS, 0.573 D Berea sandstone core).....	65
Figure 3.11: Fitting the models to Experiment № 11 data (1 g/L-2 MDa- Xanthan K9D236 at 41.95 g/L TDS, 0.551 D Berea sandstone core).....	65
Figure 3.12: Fitting the models to Experiment № 12 data (1.5 g/L-15 MDa- HPAM 3530S at 38.88 g/L TDS, 0.16113 D Berea sandstone core).....	66
Figure 3.13: Fitting the models to Experiment № 13 data (1.5 g/L-15 MDa- HPAM 3530S at 38.88 g/L TDS, 2.0188 D Berea sandstone core).....	66
Figure 3.14: Fitting the models to Experiment № 14 data (1 g/L-18 MDa- Flopaam 3630S at 0.5 g/L TDS, 4 D Reservoir Sandstone Core).....	67
Figure 3.15: Fitting the models to Experiment № 15 data (1.35 g/L-18 MDa- Flopaam 3630S at 0.5 g/L TDS, 4 D Reservoir Sandstone Core).....	67
Figure 3.16: Fitting the models to Experiment № 16 data (1.5 g/L-20 MDa- Flopaam 3630S at 20.04 g/L TDS, 0.647 D Berea Sandstone Core).....	68
Figure 3.17: Fitting the models to Experiment № 17 data (1.5 g/L-8 MDa- AN-125 at 20.04 g/L TDS, 0.578 D Berea Sandstone Core).....	68
Figure 3.18: E-UVM Schematic for Experiment № 3 using original fitting parameters (Case A) and modified fitting parameters (Case B).....	74
Figure 3.19: E-UVM Schematic for Experiment № 9 using original fitting parameters (Case A) and modified fitting parameters (Case B).....	74
Figure 3.20: E-UVM Schematic for Experiment № 13 using original fitting parameters (Case A) and modified fitting parameters (Case B).....	75
Figure 3.21: E-UVM Schematic for Experiment № 14 using original fitting parameters (Case A) and modified fitting parameters (Case B).....	75

Figure 4.1: E-UVM results for different polymer concentrations	81
Figure 4.2: Core-scale simulation model with heterogeneous permeability.....	82
Figure 4.3: Comparison of pressure drops for PLYSHEAR and E-UVM models.....	90
Figure 4.4: Comparison of oil recoveries for PLYSHEAR and E-UVM models.....	90
Figure 4.5: Capillary Desaturation Curve for the given input parameters.....	94
Figure 4.6: The typical plot illustrating residual oil saturation as a function of trapping number	95
Figure 4.7: Relative permeability curves used in simulations	96
Figure 4.8: The effect of injection rates on residual oil saturation (left) and relative permeabilities (right) at $C_p=1500$ ppm	97
Figure 4.9: Oil recoveries estimated using UTCHEM and MRST simulators	101
Figure 4.10: Pressure drop estimated using UTCHEM and MRST simulators.....	102
Figure 5.1: Pressure drop match for waterflooding cycle.....	104
Figure 5.2: Oil recovery match for waterflooding cycle.....	104
Figure 5.3: Average inlet apparent viscosities for different rheological models at 0.045 ml/min and $C_p=2000$ ppm.....	106
Figure 5.4: Average trapping numbers for different rheological models at 0.045 ml/min and $C_p=2000$ ppm	106
Figure 5.5: Oil recoveries for different rheological models at 0.045 ml/min and $C_p=2000$ ppm	107
Figure 5.6: Average inlet apparent viscosities for different rheological models at 4.5 ml/min and $C_p=2000$ ppm	108
Figure 5.7: Average trapping numbers for different rheological models at 4.5 ml/min and $C_p=2000$ ppm	108
Figure 5.8: Oil recoveries for different rheological models at 4.5 ml/min and $C_p=2000$ ppm...	109
Figure 5.9: Pressure Drops as a function of polymer concentrations at 0.045 ml/min.....	111
Figure 5.10: Average trapping numbers as a function of polymer concentrations at 0.045 ml/min	111
Figure 5.11: Oil recoveries as a function of polymer concentrations at 0.045 ml/min.....	112
Figure 5.12: Pressure Drops as a function of polymer concentrations at 4.5 ml/min.....	113
Figure 5.13: Average trapping numbers as a function of polymer concentrations at 4.5	

ml/min.....	113
Figure 5.14: Oil recoveries as a function of polymer concentrations at 4.5 ml/min.....	114
Figure 5.15: Pressure drops as a function of injection rate at $C_p=2000$ ppm.....	115
Figure 5.16: Average trapping numbers as a function of injection rate at $C_p=2000$ ppm	115
Figure 5.17: Residual oil saturations as a function of injection rate at $C_p=2000$ ppm	116
Figure 5.18: Simulation results for tertiary polymer flooding.....	117
Figure 5.19: Simulation results for secondary polymer flooding	118
Figure 5.20: Field-scale simulation model with heterogeneous permeability	120
Figure 5.21: BHP (left) and injection rate (right) for injection well during secondary waterflooding and tertiary polymer flooding.....	122
Figure 5.22: Effect of grid resolution on oil recovery during both waterflooding and polymer flooding processes.....	123
Figure 5.23: 2D map of remaining oil saturation at 2 injected PVs (after secondary waterflooding)	124
Figure 5.24: 3D map of remaining oil saturation at 2 injected PVs (after secondary waterflooding).....	125
Figure 5.25: 2D map of water saturation at 2 injected PVs (after secondary waterflooding)	125
Figure 5.26: 3D map of water saturation at 2 injected PVs (after secondary waterflooding)	126
Figure 5.27: 2D map of remaining oil saturation at 4 injected PVs (after tertiary polymer flooding).....	127
Figure 5.28: 3D map of remaining oil saturation at 4 injected PVs (after tertiary polymer flooding).....	127
Figure 5.29: 2D map of water saturation at 4 injected PVs (after tertiary polymer flooding)....	128
Figure 5.30: 3D map of water saturation at 4 injected PVs (after tertiary polymer flooding)....	128
Figure 5.31: Polymer concentration in the reservoir model at 4 PVs.....	129
Figure 5.32: Normalized effluent polymer concentration vs. injected pore volumes.....	130
Figure 5.33: Trapping numbers in the reservoir model at 4 PVs.....	130
Figure 5.34: Residual oil saturations to polymer flooding at 4 PVs.....	131
Figure 5.35: Base case predictions of oil recovery for secondary waterflooding and tertiary polymer flooding.....	131
Figure 5.36: Base case predictions of water and oil cuts for secondary waterflooding and	

tertiary polymer flooding	132
Figure 5.37: Effect of average reservoir permeability on oil recovery	134
Figure 5.38: Effect of reservoir heterogeneity on oil recovery	135
Figure 5.39: Effect of polymer concentration on oil recovery	137
Figure 5.40: Effect of polymer injection pressure effect on oil recovery	138

List of Tables

Table 2.1: Summary of viscoelastic polymer flooding field applications	54
Table 3.1: Conditions relevant to the obtained experimental data from the literature	58
Table 3.2: Fitting parameters of E-UVM used to match the model to experimental data.....	71
Table 4.1: Core petrophysical properties (Chandrasekhar and Mohanty, 2013)	78
Table 4.2: Oil properties (Chandrasekhar and Mohanty, 2013)	78
Table 4.3: Water properties (Chandrasekhar and Mohanty, 2013).....	79
Table 4.4: Polymer properties used in polymer flooding simulations	79
Table 4.5: Rock and polymer solution properties used for core-scale simulation studies.....	80
Table 4.6: Predicted E-UVM fitting parameters based on known properties.....	80
Table 4.7: Core-scale simulation model data.....	81
Table 4.8: Input parameters used to verify E-UVM implementation	89
Table 4.9: Input parameters for Capillary Desaturation Curve.....	93
Table 4.10: Corey’s relative permeability model parameters for initial conditions (Adegbite <i>et al.</i> , 2017)	96
Table 4.11: Relative permeability parameters before and after exceeding critical N_T at 4.5 ml/min	98
Table 4.12: Input parameters for the simulation model used to verify trapping numbers.....	99
Table 4.13: Input parameters used for calculation residual saturations and relative permeabilities at initial conditions	100
Table 4.14: Average trapping numbers and corresponding residual saturations estimated in MRST and UTCHEM at initial conditions and after 5 PVs	101
Table 5.1: Field-scale simulation model dimensions.....	119
Table 5.2: Input parameters for the field-scale simulation model (base case).....	121
Table 5.3: Applied pressure gradient and trapping number calculations (base case).....	122
Table 5.4: Grid refinement analysis for the quarter 5-spot field model.....	123
Table 5.5: Parameters used for sensitivity analysis	133
Table 5.6: Effect of average reservoir permeability on oil recovery	133
Table 5.7: Effect of reservoir heterogeneity on oil recovery	135
Table 5.8: Effect of polymer concentration on oil recovery	136

Table 5.9: Effect of polymer injection pressure on oil recovery 138

List of Abbreviations

AMPS	=	Acrylamido-2-Methylpropane-Sulfonate
AP	=	Alkali-Polymer
AS	=	Alkali-Surfactant
ASP	=	Alkaline-Surfactant-Polymer
ATBS	=	Sodium Acrylamido Tertiobutyl Sulfonate
AT-VEM	=	Azad-Trivedi Viscoelastic Model
BHP	=	Bottom-Hole Pressure
CaBER	=	Capillary Breakup Extensional Rheometer
CDC	=	Capillary Desaturation Curve
DM	=	Degradation Multiplier
DP	=	Dykstra Parson's coefficient
EDC	=	Elastic Desaturation Curve
EL	=	Economic Limit
EOR	=	Enhanced Oil Recovery
ESP	=	Electrical Submersible Pump
E-UVM	=	Extended Unified Apparent Viscosity Model
EWI	=	Engineered Water Injection
HPAM	=	Partially Hydrolyzed Polyacrylamide
IFT	=	Interfacial Tension
IOR	=	Improved Oil Recovery
IOR	=	Incremental Oil Recovery
LSWI	=	Low Salinity Water Injection
MMP	=	Minimum Miscibility Pressure
MRST	=	MATLAB Reservoir Simulation Toolbox
MWD	=	Molecular Weight Distribution
NVP	=	N-vinylpyrrolidone
OOIP	=	Original Oil in Place
PAM	=	Polyacrylamide
PF	=	Polymer Flooding

PV	=	Pore Volume
RF	=	Resistance Factor
RRF	=	Residual Resistance Factor
SGS	=	Sequential Gaussian Simulation
SP	=	Surfactant-Polymer
TDS	=	Total Dissolved Solid
UTCHEM	=	University of Texas Chemical Simulator
UVM	=	Unified Apparent Viscosity Model
WAG	=	Water Alternating Gas
WF	=	Waterflooding

List of Symbols

C	=	shear correction factor
De	=	Deborah number
G', G''	=	storage and loss moduli, respectively (Pa)
k_w, k_o	=	permeabilities of aqueous and oleic phases, respectively (D)
M	=	mobility ratio
n_1	=	shear-thinning index
n_2	=	shear-thickening index
n_3	=	mechanical degradation index
t	=	residence time (sec)
u_w	=	Darcy's velocity (m/s)
λ_1	=	shear-thinning constant
λ_2	=	shear-thickening constant (0.01)
λ_3	=	mechanical degradation constant
λ_w, λ_o	=	mobilities of aqueous and oleic phases, respectively (D/cP)
$\mu_{elastic}$	=	elastic viscosity (cP)
μ_{max}	=	maximum elongational viscosity (cP)
μ_{shear}	=	shear viscosity (cP)
μ_w, μ_o	=	viscosities of aqueous and oleic phases, respectively (cP)
μ_∞, μ_0	=	zero-shear rate and infinity-shear rate viscosities, respectively (cP)
τ_r	=	relaxation time (sec)
$\dot{\gamma}$	=	shear rate (s^{-1})

CHAPTER 1: INTRODUCTION

1.1 Problem Statement

Fossil fuel remains the primary source to satisfy the continuously accelerating energy demand despite the recent development in the renewable energy sector (Abas *et al.*, 2015). Total oil consumption reached around 100 million barrels per day in 2020 (IEA, 2020). Moreover, population growth and global economic expansion in 2015-2035 are forecasted to increase the total energy needs by around 38%, where oil is expected to contribute the highest fraction of 27.4% and retain its first place in energy supply (BP, 2014). Therefore, the petroleum industry needs to apply more advanced techniques to enhance production from existing fields or make new field discoveries in order to satisfy future energetic requirements.

Enhanced Oil Recovery (EOR) is an essential stage in oil production that may increase ultimate oil recovery to more than half of the reservoir's original oil in place (OOIP) (Aladasani and Bai, 2010). It is implemented by injecting chemicals, solvents, or high-temperature steam into the reservoir. Polymer flooding is a mature chemical EOR technique that has been extensively used to reduce the mobility of the injectant fluid. Conventionally, polymer flooding technology was believed to improve macroscopic sweep efficiency by producing bypassed oil. This fraction of movable oil remained unflooded after water injection due to higher water mobility and/or reservoir heterogeneities (Sheng, 2011). Nevertheless, recently it has been found that polymers exhibiting viscoelastic behavior in the porous medium can also improve microscopic displacement efficiency resulting in higher additional oil recovery. Residual oil mobilization by viscoelastic polymers was related to extensional flow resistance in high shear rate regions. The stretchability of elastic polymers during converging flow results in considerable extensional viscosity and improves pore-scale production (Azad and Trivedi, 2020).

It is worth mentioning that although polymer flooding is an extensively applied chemical enhanced oil recovery (CEOR) technique in sandstones, its applicability in carbonates is still limited. Carbonate reservoirs account for about 60% of the worldwide oil reservoirs. However, EOR applications in carbonates represent only 18% based on the international EOR project database comprising 1,507 projects (Manrique *et al.*, 2010). Most of these carbonate EOR field

cases are either continuous miscible gas or water alternating gas (WAG) injection. Additionally, Masalmeh *et al.* (2019) reported that no successful polymer flooding project was performed in a carbonate reservoir at high temperature and high salinity conditions heretofore. Generally, carbonate rocks are characterized by complex features due to the mixed-to-oil wettability nature and high heterogeneity with low permeability. Harsh conditions also prevail in carbonates such as high temperatures (above 85°C), high salinity (above 100,000 ppm), and high hardness (above 1,000 ppm). These conditions are challenging for the application of polymer flooding in carbonates (Diab and Al-Shalabi, 2019). Additionally, high permeable natural fracture network in heterogeneous carbonate reservoirs may cause injection fluid channeling, leaving a considerable amount of oil behind in unswept parts of the reservoir (Azad and Sultan, 2014). Recently, new types of polymers have been developed for overcoming the harsh conditions in carbonates. These novel polymers incorporate several monomers, such as N-vinylpyrrolidone (NVP), 2-Acrylamido-2-Methylpropane-Sulfonate (AMPS), and Sodium Acrylamido Tertiobutyl Sulfonate (ATBS) that protect the polymer from thermal and chemical degradations.

Generally, most polymers exhibit a complex rheological behavior in porous media. At low shear rates, the entropic forces exceed the hydrodynamic drag forces generated from the fluid flow, and polymer behaves like a Newtonian fluid with constant viscosity. As the shear rate increases and passes a first critical rate, the polymer molecules face larger drag forces that untangle polymer coils and align them along the flow direction reducing their resistance to flow (Skauge *et al.*, 2018). This regime, dominated by shear forces, is associated with shear-thinning where polymer solutions lose their viscosities with the shear rate. Furthermore, as the shear rate increases further and passes the next critical rate, the polymer exhibits shear-thickening behavior. The latter behavior is associated only with flexible viscoelastic polymers. The onset rate for this dilatant regime is a function of both polymer molecular parameters and fluid flow conditions in porous media. Heemskerk *et al.* (1984) reported that the critical rate increases with increasing permeability, temperature, and salinity of the solution and with decreasing molecular weight and concentration of the polymer. Finally, once viscoelastic polymers undergo full stretching during the dilatant flow, they accumulate excessive stresses that eventually lead to chain scission of the polymer. After this third critical rate, the apparent viscosity reaching the maximum value drops due to mechanical degradation.

1.2 Motivation

There are various viscoelastic models predicting polymer rheology in porous media. However, most of the proposed models either require extensive coreflooding data to estimate the model parameters or cannot comprehensively characterize polymer rheological behavior. Generating an extended viscoelastic model capturing all four regimes observed during polymer flooding (Newtonian, shear-thinning, shear-thickening, and mechanical degradation) may significantly improve the prediction of polymer apparent viscosity at various shear rates. Moreover, relating the model fitting parameters to known data might considerably reduce the number of model parameters as well as the need for performing a time-consuming coreflooding measurement, which result in accelerating polymer screening. Finally, conducting core- and field-scale simulation studies using the generated model may substantially improve the oil recovery predictions.

1.3 Research Objectives

This research will focus on investigating the polymer rheological behavior under various flow conditions. Moreover, the simulation studies will be conducted based on representative fluid and rock properties from the Middle East carbonate reservoirs. The main objectives of this research are:

- Develop a comprehensive model for viscoelastic polymer flow in porous media that captures all regimes, including Newtonian, shear-thinning, shear-thickening flows, and mechanical degradation of polymers;
- Correlate the empirical fitting parameters of the model to rock and polymer properties;
- Conduct core-scale and field-scale simulation studies using the generated viscoelastic model.

1.4 Thesis Organization

The next chapter provides an extensive literature review on viscoelastic polymer flooding and its effect on recovery efficiency. Moreover, Chapter 3 presents the development and validation of the new viscoelastic model. Additionally, the correlations relating the fitting parameters to rock and polymer properties are also included in the latter chapter. Furthermore, Chapter 4 characterizes the

core-scale simulation model as well as it describes the implementation and verification of the proposed viscoelastic model in the reservoir simulator. Additionally, calculations of trapping number and the corresponding residual oil saturation and relative permeabilities are included in the latter chapter. Next, Chapter 5 extensively defines the core- and field-scale predictions. Lastly, Chapter 6 includes conclusions of this study and recommendations for future work.

CHAPTER 2: LITERATURE REVIEW

2.1 Enhanced Oil Recovery

Recovery from an oilfield typically comprises three stages, including primary, secondary, and tertiary (**Figure 2.1**). Primary recovery is controlled by natural reservoir drive energy, such as water influx, solution gas drive, gravity drainage, rock and fluid expansion, gas cap drive, or a combination of these. Additionally, artificial lift techniques may be implemented later during primary recovery if the bottomhole pressure is not adequate to bring hydrocarbons up to the surface (Zitha *et al.*, 2011). Typical artificial lift forms include gas-lift installations, electrical submersible pumps (ESP), sucker-rod pumps, and other systems aiming to boost oil production. On the other hand, the secondary recovery of hydrocarbons is implemented by injecting external fluids targeting to improve volumetric sweep efficiency and support reservoir pressure (Sheng, 2011). The second stage starts when the formation pressure falls so low that primary production drops and reaches the economic limit (EL). Conventionally, this phase includes waterflooding, water and gas injection. Water injection is performed in the aquifer to increase a reservoir pressure to its initial level while waterflooding usually refers to the processes that improve macroscopic sweep efficiency by introducing water to porous media, although these two terms are interchangeably used. On the other hand, gas injection during a secondary production phase is performed into the gas cap for pressure maintenance. Additionally, some authors also include the injection of immiscible gases into the oil column to sweep oil toward producers if the recovery mechanism strongly depends on the immiscible frontal displacement (Green and Willhite, 1998). However, immiscible displacement by gas as a secondary recovery technique is not that actively used today as waterflooding due to the latter's better performance and relative simplicity. Finally, tertiary oil recovery or Enhanced Oil Recovery (EOR) starts usually when waterflooding (or other secondary recovery method used) becomes uneconomical. This stage includes injecting chemicals, solvents, or high-temperature steam into the reservoir. EOR is considered an essential stage in hydrocarbon production since it may increase ultimate oil recovery to over half of the reservoir's original oil in place (Aladasani and Bai, 2010).

Although this chronological order is traditionally accepted, various production operations may be implemented in an unspecified sequence. For instance, Enhanced Oil Recovery, which is

usually considered a tertiary recovery method, may be used as a second or even first stage in production depending on the reservoir type and economics. In particular, the crude in most heavy oil reservoirs often is so viscous that both primary and secondary production may become insignificant. In these cases, thermal EOR is the only choice to obtain economic production and is used at the first stage (Green and Willhite, 1998).

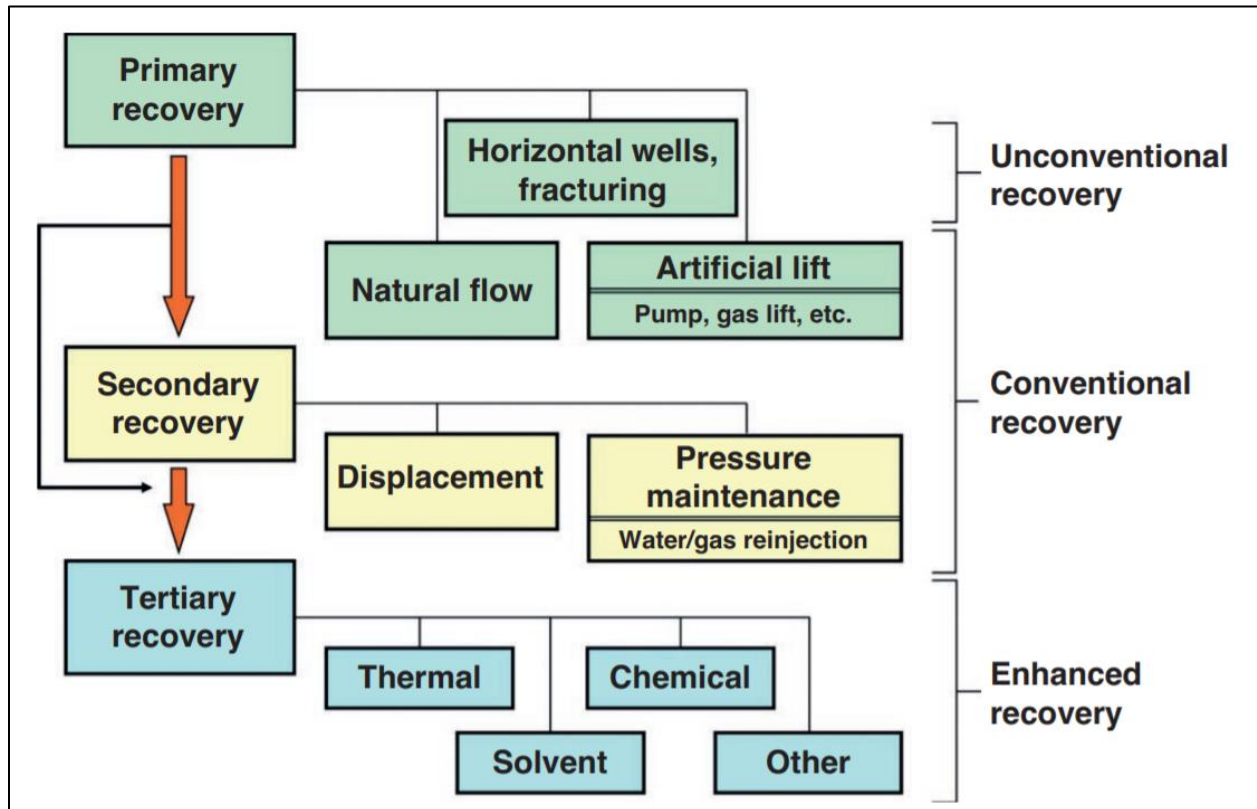
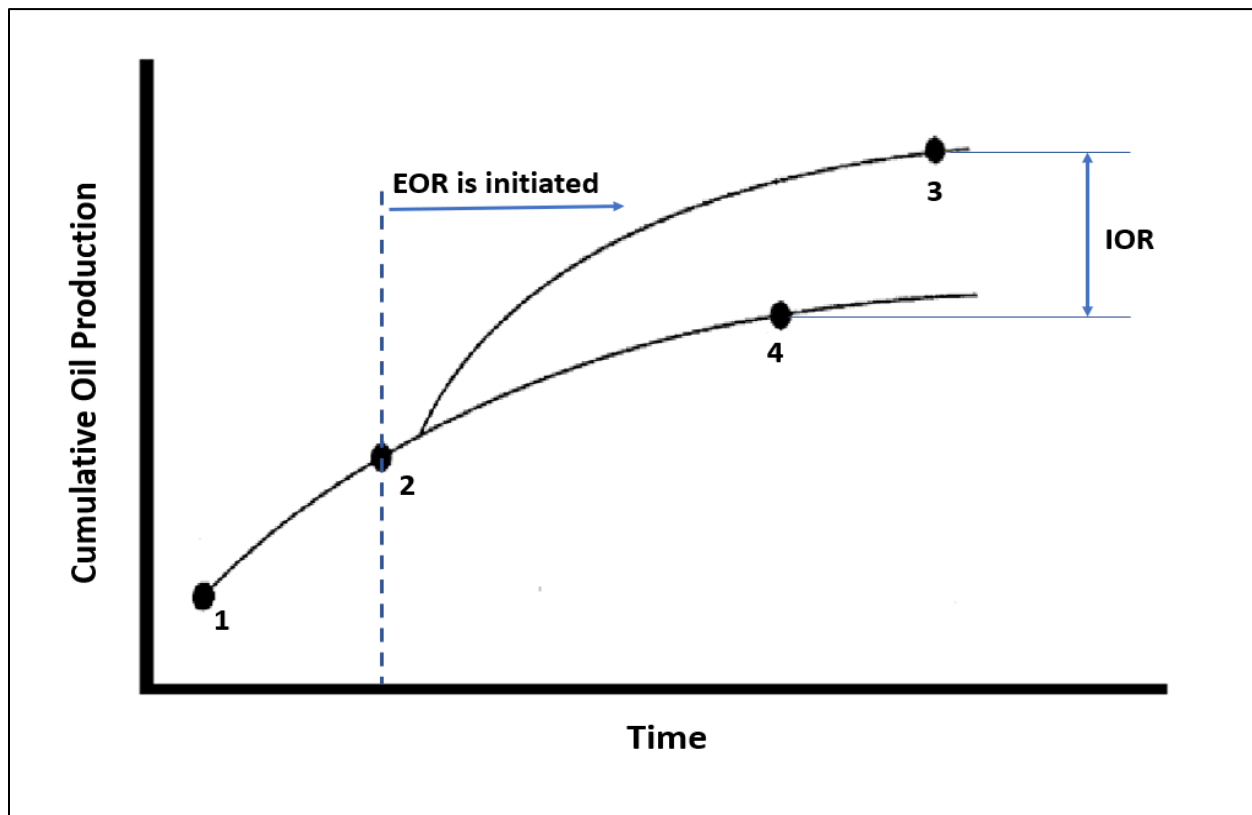


Figure 2.1: The classification of oil recovery techniques (Oil and Gas Journal, 1990).

Enhanced Oil Recovery operations are firmly dependent on oil price and economics (Mogollon and Lokhandwala, 2013). Conventional primary and secondary oil recovery phases produce the cheapest oil while implementing the EOR technique that involves the use of additional materials increases the project expenses. Therefore, the number of EOR projects is considerably reduced during the oil price collapse, as EOR processes become unprofitable, and the opposite effect is observed as the prices rise (Druetta *et al.*, 2019). Another important factor controlling the

interest in EOR is the size of a reservoir and the remaining oil saturation. It is widely accepted that the ultimate oil recovery after primary and secondary production is 35-45% (Zitha *et al.*, 2011; Lake *et al.*, 2014). The studies show that after conventional recovery ceases, a large volume of oil still remains in the subsurface as a target for EOR. The success of an EOR project can be estimated by a term called Incremental Oil Recovery (IOR). **Figure 2.2** illustrates the IOR concept with the help of cumulative oil production. According to the figure, the EOR operations start at Point 2, boosting oil recovery. Incremental oil recovery is defined as the difference between the actual oil recovery (2-3) and the recovery if the EOR project was not initiated (2-4).



**Figure 2.2: Schematic of IOR from a typical EOR response
(modified after Lake *et al.*, 2014).**

Furthermore, it is necessary not to confuse the Incremental Oil Recovery term with Improved Oil Recovery since both are identically abbreviated as IOR. The latter term refers to the numerous processes and activities targeting to increase production rates and improve oil recovery

(Green and Willhite, 1998). In addition to EOR techniques, improved oil recovery includes drilling multilateral or horizontal wells, hydraulic fracturing, infill drilling, well acidizing, advanced reservoir monitoring techniques, and near-wellbore conformance control procedures (Sheng, 2011; Druetta *et al.*, 2019).

The primary goal of EOR techniques is to reduce the remaining oil saturation of a preceding secondary recovery process by injecting materials that are not indigenous to the reservoir. The injected fluids develop auspicious oil recovery conditions by interacting with the reservoir rock and oil. Based on the injectant type and the mechanisms that it initiates in porous media, EOR can be subdivided into four major groups:

- *Thermal Enhanced Oil Recovery.* The thermal injection is a mature and commercially successful EOR technique. It is performed by injecting steam or hot water into a reservoir. Alternatively, the thermal EOR may also include in-situ generation of thermal energy by starting a fire in a reservoir and burning some crude oil. The basic recovery mechanisms are oil viscosity reduction, oil expansion, steam distillation, hot water drive, and steam drive. Thermal EOR has proven successful in recovering hydrocarbons from shallow and thick heavy oil reservoirs. However, its efficiency diminishes in thin or deep formations due to significant heat losses (Lake, 1989). Another drawback of thermal EOR is that approximately one-third of produced oil is used to generate the steam for injection purposes. It increases the cost per incremental oil barrel and calls into question the EOR project (Green and Willhite, 1998).
- *Solvent Enhanced Oil Recovery.* Solvent EOR, also called gas flooding, involves injecting various gases (e.g., natural gas, nitrogen, carbon dioxide, air, hydrogen sulfide, or flue gas) to interact with the oil and further improve the microscopic recovery. An increase in oil recovery may be achieved through both miscible and immiscible gas flooding. Several factors control the miscibility of the gases used for EOR, such as temperature, reservoir pressure, and oil and gas composition. Solvent EOR is usually implemented for light and medium oil reservoirs, and it is one of the best candidates for heterogeneous and low permeable formations. Typical mechanisms increasing oil recovery during gas flooding are IFT reduction, oil viscosity decrease, solution gas drive, oil and water density alteration, immiscible gas displacement (e.g., enhanced gravity drainage), and oil swelling. However,

there are several challenges associated with solvent floodings, such as gravity override and viscous fingering, resulting in large oil volumes bypassed in the reservoir. Poor sweep efficiency of gas flooding may be mitigated by injecting alternating slugs of water and gas (WAG). Additionally, reservoir pressure plays an essential role during gas flooding operations as it may dictate gas miscibility and affect the efficiency of a project. Therefore, it is desired to apply solvent EOR in a deep reservoir with a pressure higher than the minimum miscibility pressure (MMP) of a gas to maintain a more stable miscible flow.

Nevertheless, the number of gas flooding projects has been dramatically increased during the last two decades, and a considerable amount of incremental oil has been economically produced by this method, especially if the source for the solvent is available (Lake *et al.*, 2014). For instance, as illustrated in **Figure 2.3**, thermal injection methods held the largest share of EOR projects in the USA till 2002, when the gas injection started to gain popularity among investors due to vast and cheap CO₂ sources (Alvarado and Manrique, 2010).

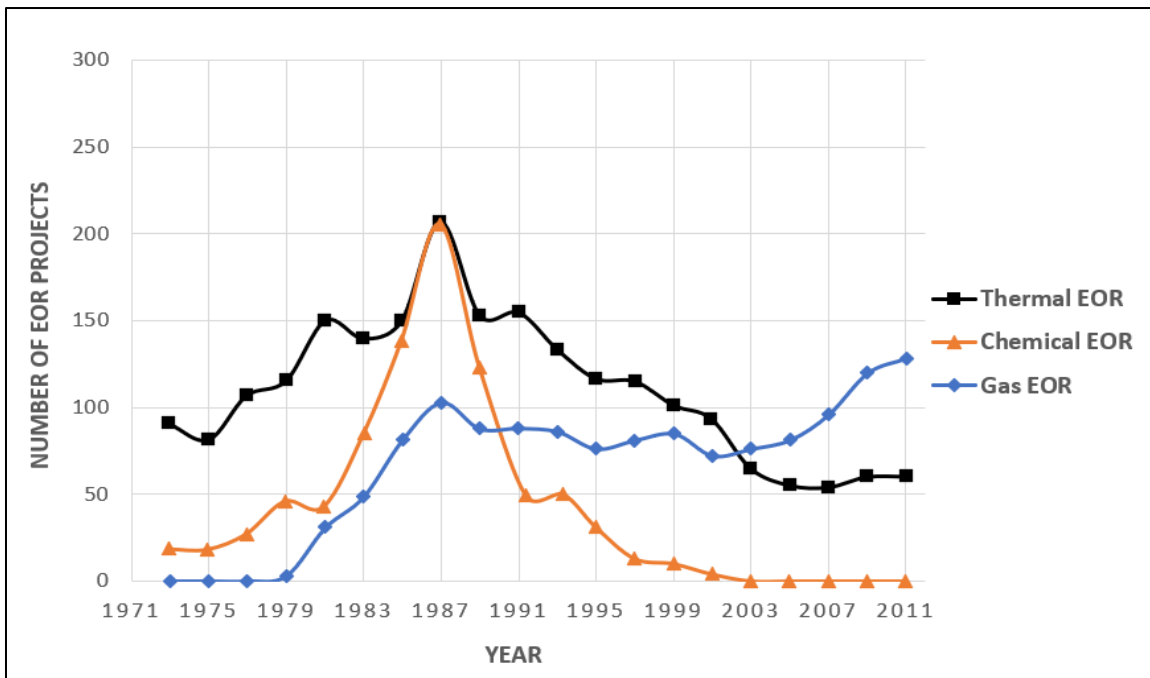


Figure 2.3: Evolution of EOR projects in the USA
(modified after Alvarado and Manrique, 2010).

- *Chemical Enhanced Oil Recovery*. Chemical EOR is another promising oil recovery method with economic and technical potential. Traditionally, this EOR branch is subdivided into surfactant, alkaline, polymer flooding, and their combination. The main target for surfactant flooding is the immobile oil trapped in a reservoir by capillary forces. Surfactants may either change the interactions between two fluids decreasing the interfacial tension between them or the one between fluid and rock, leading to wettability alteration (Druetta *et al.*, 2019). Surface active agents or surfactants are amphiphilic by nature and contain a water-soluble hydrophilic head and the nonpolar hydrophobic tail that is usually dissoluble in organic solutions. Several types of surfactants exist based on the ionic nature of a hydrophilic group: cationic, anionic, nonionic, and zwitterionic (Gbadamosi *et al.*, 2019). Anionic surfactants are actively used in sandstones, while cationic surfactants are more suitable for carbonate rocks. It is related to the surface charge of a rock, and utilizing the right surfactant may significantly reduce the adsorption of the chemical. Moreover, nonionic surfactants are mostly used as cosurfactants to improve the tolerance to elevated salinities. Similarly, zwitterionic or amphoteric surfactants containing two active groups also serve as "stability boosters" at high temperatures and salinities. However, the latter surfactants are comparatively costly (Sheng, 2011).

Furthermore, alkaline flooding involves injecting the inexpensive alkali (e.g., sodium hydroxide or sodium carbonate) into a reservoir that leads to a saponification reaction. This reaction between caustic alkali and active crude oil generates in-situ surfactants or soap. In-situ surfactants being cheaper alternatives to hydrophilic synthetic surfactants, increase oil recovery by generating favorable wettability conditions, reducing IFT between oleic and aqueous phases, and emulsifying crude oil.

The next type of chemical EOR, polymer flooding, is an extensively applied method, especially in slightly heterogeneous formations with low or medium viscosity crudes (Sorbie, 1991). Here, water-soluble polymers with high molecular weight are injected to ameliorate mobility and conformance in a reservoir. As polymer flooding is the main topic of interest of the thesis, it will be discussed in more detail in the subsequent chapters.

Conventional chemical EOR techniques mentioned before have several limitations. For instance, the elevated temperatures or brines with high salinity and hardness cause the

polymer solution to degrade and lose its viscosifying power. On the other hand, the severe problem associated with surfactant and alkaline flooding is adsorption resulting in a considerable volume of chemicals retained in porous media (Gbadamosi *et al.*, 2019). Therefore, various combinations of chemicals were designed and applied in the field to increase oil recovery further. It includes alkaline-surfactant-polymer (ASP) flooding and binary mixtures, such as alkali-polymer (AP), surfactant-polymer (SP), and alkali-surfactant (AS). Interactions between the individual components, or eventually the synergy among those chemicals, may considerably improve the total efficiency. In particular, the integrated synergy of each component in ASP flooding may bring the following advantages (Druetta *et al.*, 2019; Gbadamosi *et al.*, 2019):

- The polymers in ASP flooding mostly control mobility and improve volumetric sweep efficiency, while surfactants and alkali mobilize trapped oil, increasing microscopic recovery.
- The utilization of alkali in chemical flooding may result in a significant economic benefit due to its lower cost than one of polymers or surfactants.
- The degree of surfactant adsorption is substantially reduced due to competition between chemicals for rock surfaces where to be retained.
- The soap generated by the interaction between alkali and crude oil has comparatively lower optimum salinity. However, the synergy with synthetic surfactants extends the range of salinities where low interfacial tension can be achieved.

Consequently, ASP flooding is extensively treated as the most promising chemical EOR operation. Nevertheless, there are also several limitations for ASP flooding. The challenges are related to cation exchange and other reactions or conditions leading to the precipitation of components. Moreover, it is complex to design a robust mixture for ASP flooding where chemicals do not have any detrimental effect on one another, and it is expensive to implement this process in a field.

- *Other Enhanced Oil Recovery Techniques.* Other EOR methods include low salinity waterflooding, microbial plugging, and surface mining. Low salinity water injection (LSWI) involves the injection of diluted water into a reservoir to increase oil recovery with

low operational and capital expenses. Similarly, engineered water injection (EWI) is performed by utilizing the water with modified hardness. The main reason behind incremental oil obtained by these methods is believed to be a wettability adjustment, but the fine migration processes and dissolution are other mechanisms impacting oil recovery (Al-Shalabi *et al.*, 2014b; Alameri *et al.*, 2015).

In summary, various types of EOR are designed to reduce remaining oil saturation after previous production stages. The main EOR techniques are shown in **Figure 2.4**. Each method has its advantages and drawbacks, indicating the importance of EOR screening for a particular formation where it will be applied (Taber *et al.*, 1997).

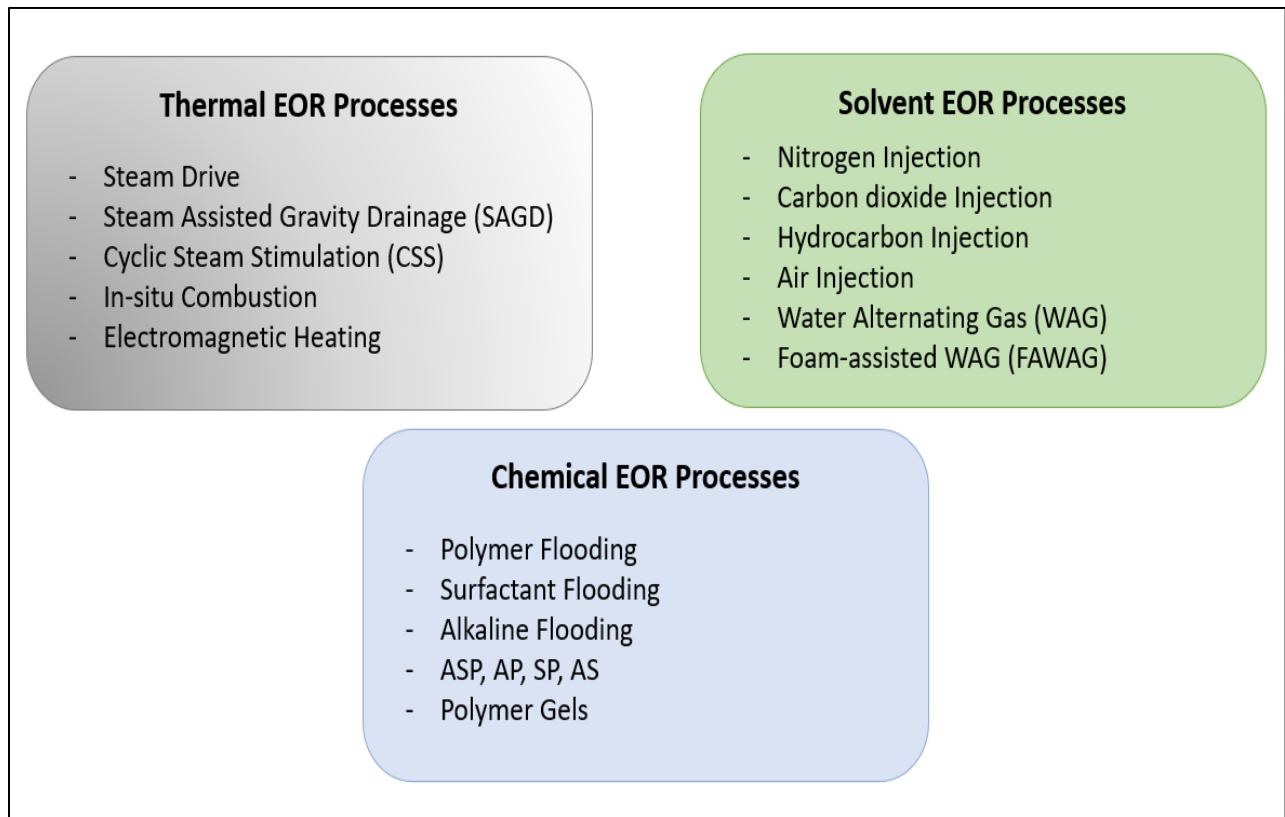


Figure 2.4: The classification of EOR techniques (modified after Lake *et al.*, 2014).

2.2 Polymer Flooding as an EOR technique

As discussed in the previous chapter, polymer flooding is a mature chemical EOR method that successfully reduces the remaining oil saturation after waterflooding and improves oil recovery. The method has more than 40 years of commercial application. Therefore, solid theoretical and practical knowledge has been acquired, considering the vast amount of gathered field data and the large number of studies conducted in this area (Mogollon and Lokhandwala, 2013). Polymer injection projects outnumber other chemical EOR types for a broader range of reservoir conditions. Despite the lower incremental oil recovery, polymer flooding seems more attractive for EOR investments due to lower operational risks. In particular, polymer flooding is the most frequently used chemical EOR technique in sandstones. Besides, it is the only commercially proven chemical method in carbonate reservoirs (Alvarado and Manrique, 2010).

Conventionally, polymer flooding technology is believed to improve macroscopic sweep efficiency by producing bypassed oil. This fraction of movable oil remained unflooded after water injection due to higher water mobility and/or reservoir heterogeneities (Sheng, 2011). Theoretically, both secondary waterflooding and tertiary polymer flooding may produce all mobile oil. However, the recovery process through waterflooding may last for a very long time, usually exceeding the practical reservoir development timescale. Therefore, it is recommended to replace waterflooding with a polymer injection technique to accelerate the production rate and shift forward the recovery profile in time (Sorbie, 1991; Standnes and Skjevrak, 2014). **Figure 2.5** depicts production profiles for waterflooding and polymer injection, which indicates that the ultimate oil recovery is eventually identical for both techniques. Nevertheless, it is more practical to compare recovery factors at the economic limit of processes, which can be reached at the maximum water cut to be handled. In **Figure 2.5**, RF_{PF-EL} and RF_{WF-EL} denote the moveable oil recovery at the corresponding economic limit for polymer flooding and waterflooding, respectively. Hence, according to the figure, it is possible to achieve an additional oil recovery by polymer flooding if we consider a limited injection timescale (Sorbie, 1991).

Furthermore, unlike solvent flooding, alkaline, or surfactant injection, waterflooding sweeps only mobile oil, and residual oil remains entrapped in porous media due to the lower capillary number of water injection processes. Traditionally, a similar behavior was also associated with polymer flooding, as the impact of polymers on microscopic sweep efficiency was highly

questionable. Nevertheless, recently several studies revealed that viscoelastic polymers might mobilize capillary trapped oil and improve microscopic displacement efficiency, in addition to macroscopic sweep efficiency (Wang *et al.*, 2000a; Urbissinova *et al.*, 2010; Clarke *et al.*, 2016; Hincapie *et al.*, 2017; Qi *et al.*, 2017). Azad and Trivedi (2020) related the additional oil recovery by viscoelastic polymers to the substantial extensional flow resistance in high shear rate regions; the stretchability of elastic polymers during converging flow results in considerable extensional viscosity and improves pore-scale production.

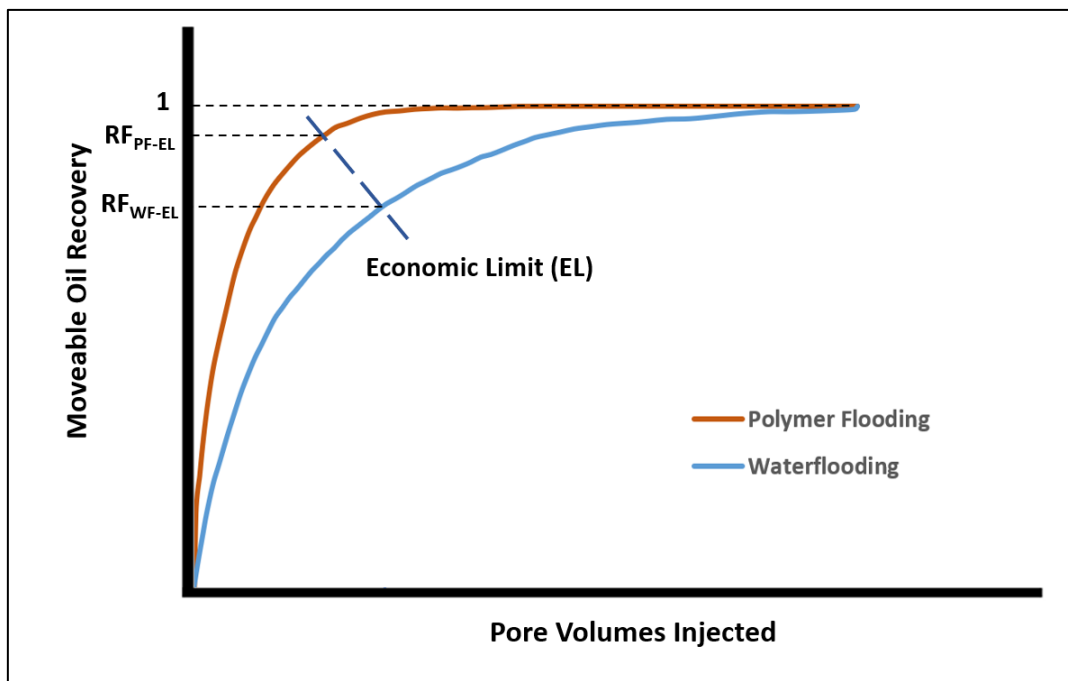


Figure 2.5: Production profiles for waterflooding and polymer flooding with the corresponding economic limits (modified after Sorbie, 1991).

In order to provide more insights into polymer flooding, the following chapters extensively describe the underlying mechanisms and types of EOR polymers used under harsh conditions, introduce the viscoelasticity of polymers, discuss the mobilization of residual oil by viscoelastic polymers, and characterize other factors affecting the efficiency of this EOR technology. Additionally, the analytical models estimating polymer apparent viscosity and a list of successful field applications are provided in the subsequent chapters.

2.3 Mechanisms of Polymer Flooding

2.3.1 Recovery Efficiency

Polymer flooding may be considered a potential remedy after waterflooding, associated with early water production and low oil recovery. Usually, there are two scenarios where polymer applications may result in a higher yield from oil fields; unfavorable mobility ratio and excessive reservoir heterogeneity (Sorbie, 1991). Practically, to have a clear understanding of polymer flooding, it is essential to characterize the process on different scales, starting from the pore-scale to the field-scale (**Figure 2.6**).

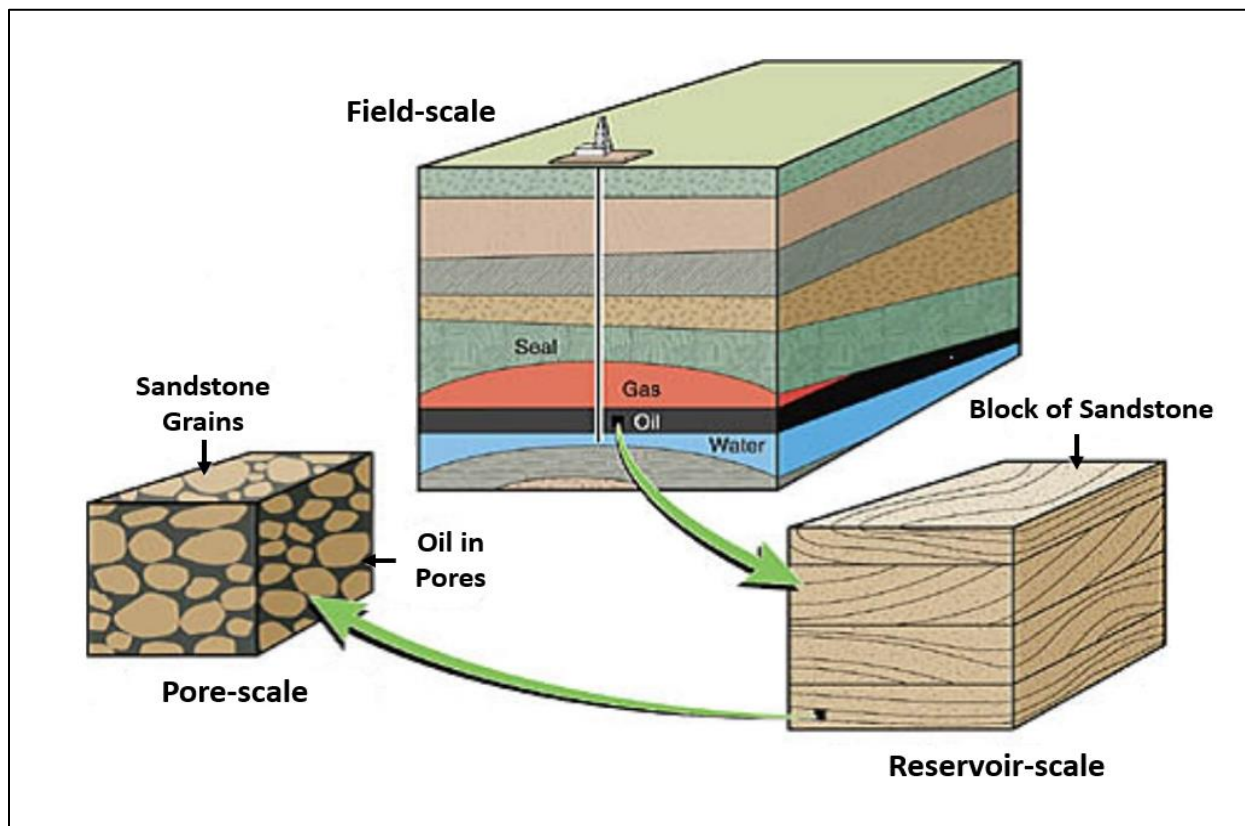


Figure 2.6: Schematics of the different scales involved in oil recovery processes (Zitha *et al.*, 2011).

During polymer flooding, the overall recovery factor (R_e) comprises field-scale volumetric sweep efficiency (E_v) and pore-scale displacement efficiency (E_d), as in **Equation 2.1** (Lake, 1989).

$$R_e = E_v \cdot E_d = E_I \cdot E_A \cdot E_d , \quad (2.1)$$

where E_I is the vertical sweep efficiency and E_A is the areal sweep efficiency.

Volumetric sweep efficiency evaluates the performance of displacing fluids in contacting the oil-bearing zone volumetrically relative to the total oil volume in place. As mentioned before, a large volume of hydrocarbons remains bypassed in a reservoir after waterflooding. By injecting the polymer solution, it is possible to viscosify the drive (or displacing) fluid and increase volumetric sweep efficiency. E_v is improved by controlling the mobility and conformance of the injected solution. By maintaining conformance control, the channeling through heterogeneous reservoirs may be impeded, and the vertical sweep efficiency may be ameliorated. Generally, the heterogeneous formations possess an uneven vertical distribution of permeabilities. During secondary oil recovery, water injection into these reservoirs causes excessive water production from high-permeable layers and leaves a significant amount of mobile oil in tight zones. Using polymers during the tertiary recovery regime reduces the relative permeability to water while ensuring negligible change in the oil relative permeability. This mechanism, called disproportionate permeability reduction (DPR), diverts the injection fluid from high permeable "thief zones" to low permeable regions of the reservoir and improves vertical sweep efficiency (Gbadamosi *et al.*, 2019).

Moreover, it is reported that the elasticity of viscoelastic polymers results in a drastic decrease in an aqueous phase's relative permeability and contributes to the conformance control (Azad *et al.*, 2018). On the other hand, mobility control is required to avoid viscous fingering that usually occurs when the viscosity of the oil is higher than the one of the drive fluid. Viscous fingering characterized by the uneven flow profile may eventually lead to early water breakthrough into production wells. As a solution, polymers are utilized to reduce the viscosity contrast between the fluids and to increment the areal sweep efficiency. **Figure 2.7** illustrates the improvement in volumetric sweep efficiency in a heterogeneous reservoir ($K_3 > K_1 > K_2 > K_4$) by maintaining conformance and mobility control through polymer flooding.

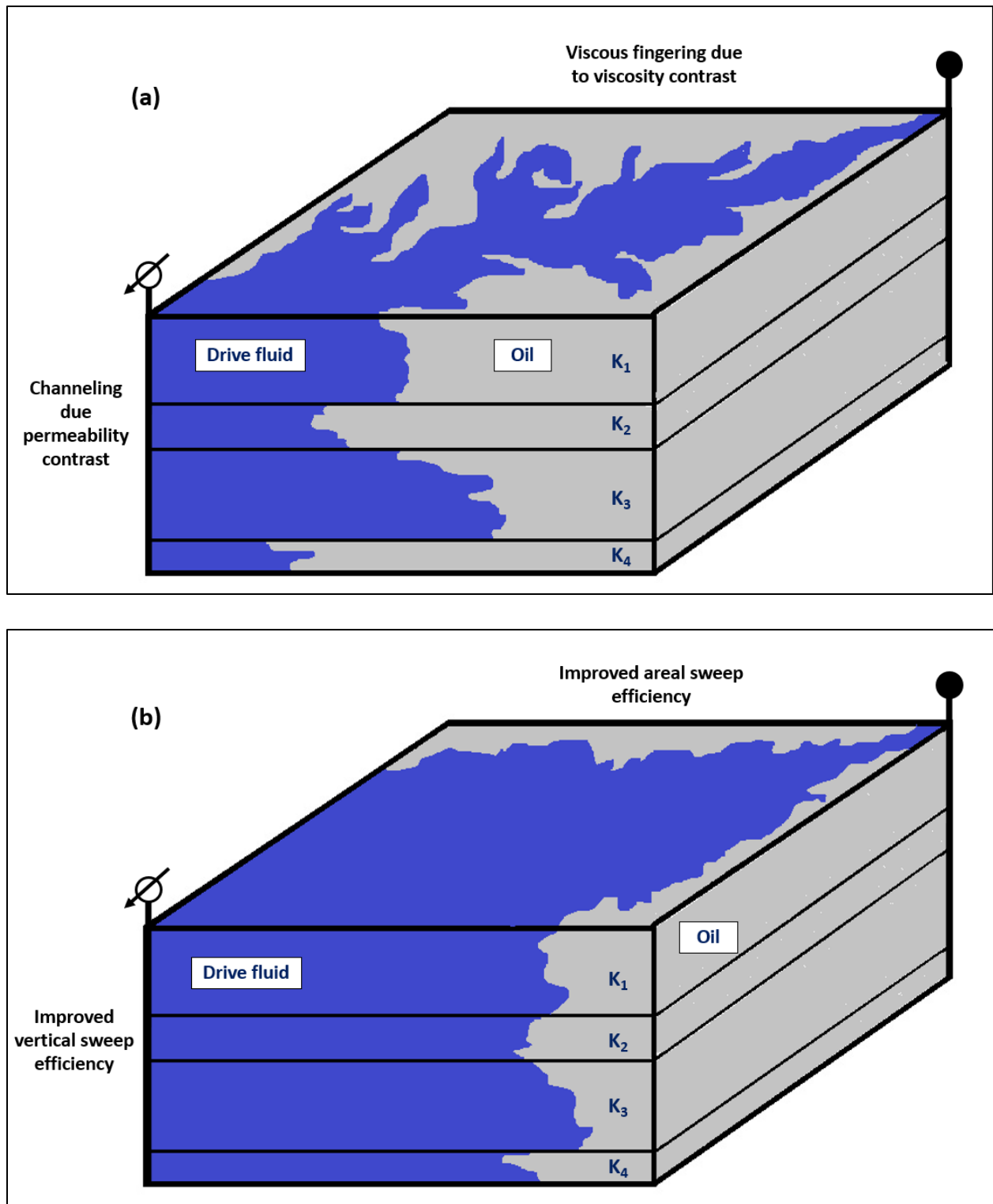


Figure 2.7: Schematic of volumetric sweep improvement resulted by polymer flooding: (a) waterflooding, (b) polymer flooding (modified after Sorbie, 1991).

Furthermore, microscopic displacement efficiency (E_d) is a pore-scale parameter related to the residual oil entrapped in a porous medium (Clarke *et al.*, 2016). It is reported by Wang *et al.* (2000a) that the viscoelastic polymers may pull residual oil trapped in a reservoir due to several factors, including rock attraction, capillary forces, and rock configuration. By reducing residual oil saturation, it is possible to improve E_d .

2.3.2 Mobility Ratio

In order to evaluate the ability of a polymer to improve waterflooding performance, it is essential to present the idea of mobility ratio (M), which is defined in **Equation 2.2** (Sheng, 2011):

$$M = \frac{\lambda_w}{\lambda_o} = \frac{k_w/\mu_w}{k_o/\mu_o}, \quad (2.2)$$

where λ , μ , and k indicate the mobility, viscosity, and effective permeability, respectively. The subscripts “o” and “w” denote oil and aqueous phases, respectively. Polymers improve volumetric sweep efficiency by providing a favorable mobility ratio ($M < 1$) between the displacing phase (aqueous) and the displaced phase (oleic). Polymer improves mobility ratio by increasing aqueous phase viscosity and reducing the aqueous phase effective permeability.

2.3.3 Other Flow Parameters

While having a positive effect on both sweep and displacement efficiencies, viscoelastic polymers may impair the injectivity. Poor injectivity occurs due to excessive shear-thickening and mechanical degradation of polymers at high shear rates and leads to voidage problems as well as flood front delay (Stavland *et al.*, 2010; Azad *et al.*, 2018; Al-Shakry *et al.*, 2018). Therefore, being one of the crucial aspects of polymer flooding application, injectivity should be carefully analyzed before implementing a project. It can be better controlled by understanding parameters such as resistance factor (RF), residual resistance factor (RRF), permeability reduction factor (R_k), and apparent viscosity (Alfazazi *et al.*, 2019). Resistance factor (RF), also known as the mobility reduction factor, is the ratio of the mobility of brine to the mobility of a single-phase polymer solution (Lake, 1989). This parameter shows the improvement in the mobility ratio (Alfazazi *et*

al., 2018). For constant flow rate experiments, RF is also defined as the inverse ratio of pressure drops (**Equation 2.3**). On the other hand, the residual resistance factor (*RRF*) is the ratio of the mobility of brine solutions before and after polymer injection, and it indicates the level of polymer retention (**Equation 2.4**). Additionally, the permeability reduction factor (R_k) is defined in **Equation 2.5**.

$$RF = \frac{\left(k_w/\mu_w\right)_{preflush}}{\left(k_p/\mu_p\right)_{PF}} = \frac{\Delta P_{PF}}{\Delta P_{preflush}}, \quad (2.3)$$

$$RRF = \frac{\left(k_w/\mu_w\right)_{preflush}}{\left(k_w/\mu_w\right)_{postflush}} = \frac{\Delta P_{postflush}}{\Delta P_{preflush}}, \quad (2.4)$$

$$R_k = \frac{k_w}{k_p}, \quad (2.5)$$

where $\left(k_w/\mu_w\right)_{preflush}$ and $\Delta P_{preflush}$ are brine mobility and pressure drop measured during preflush experiments, respectively. $\left(k_p/\mu_p\right)_{PF}$ and ΔP_{PF} are polymer mobility and pressure drop measured during polymer flooding, respectively. $\left(k_w/\mu_w\right)_{postflush}$ and $\Delta P_{postflush}$ are brine mobility and pressure drop measured during post flush experiments, respectively.

Furthermore, the apparent viscosity during injection test may be calculated by using *RF* and *RRF* (**Equation 2.6**) (Han *et al.*, 2012):

$$\mu_p = \mu_w \cdot \frac{RF}{RRF}, \quad (2.6)$$

where μ_p is the apparent polymer viscosity and μ_w is the brine viscosity.

2.4 EOR Polymers Used Under Harsh Reservoir Conditions

2.4.1 Classification of Polymers

In general, the EOR polymers are classified into two major groups; biopolymers and synthetic polymers. The former typically include xanthan gum, guar gum, welan gum, lignin, schizophyllan, sceluroglucan, and cellulose. Contrarily, synthetic polymers are usually comprised of partially hydrolyzed polyacrylamide (HPAM) and its derivatives (Gbadamosi *et al.*, 2019). Many researchers agree that biopolymers possess superior temperature and salinity tolerance capabilities than polyacrylamides (Akstinat, 1980; Davison and Mentzer, 1982; Jensen *et al.*, 2018). However, these polymers are susceptible to biological degradation and have poor injectivity (Hashmet *et al.*, 2017; Gbadamosi *et al.*, 2019). Biological degradation may occur during polymer storage before injection or in the reservoir under low-temperature conditions. During this process, bacteria attacking the macromolecule result in polymer breakdown. As a solution, effective biocides such as formaldehyde are added to the solution to protect the polymers from biological degradation in the cooler parts of the reservoir (Sorbie, 1991).

On the other hand, comparatively lower cost, better control on molecular weight distribution, and ease of manufacturing on-site are the factors favoring HPAM for polymer flooding (Kim *et al.*, 2010; Diab and Al-Shalabi, 2019). As a result, HPAM has been used in more polymer flooding field projects than biological polymers, as reported in several studies (Standnes and Skjevraak, 2014; Sheng *et al.*, 2015). Moreover, unlike biopolymers, synthetic polymers possessing a flexible, random-coil conformation may obtain dilatant behavior in porous media where their apparent viscosities increase several folds with shear rate (Wang *et al.*, 2008). Because of these viscoelastic properties, synthetic HPAM polymers may result in additional oil recovery (Hincapie *et al.*, 2017).

HPAM is generated by copolymerizing acrylamide with acrylic acid. At temperatures above 70 °C, acrylamide moieties within HPAM hydrolyze to acrylate groups, and the polymer may eventually lose its viscosifying power and precipitate (Moradi-Araghi and Doe, 1987; Dupuis *et al.*, 2017). Currently, the main priority in the application of HPAM is to develop new HPAM-based polymers that are resistant to harsh conditions. It is possible to expand the application envelope of these polymers by incorporating specific monomers such as N-vinylpyrrolidone (NVP), 2-Acrylamido-2-Methylpropane-Sulfonate (AMPS), and Sodium Acrylamido Tertiobutyl

Sulfonate (ATBS). AMPS anionic monomers are more resistant to cation shielding and precipitation; thus, they may ameliorate copolymer's calcium tolerance (Levitt and Pope, 2008). The NVP nonionic monomers protect the acrylamide groups from thermal hydrolysis and improve terpolymer's thermal stability up to 120 °C (Vermolen *et al.*, 2011). Moreover, in the presence of divalent ions, the concentration of NVP in the polymer chain should be 35-50 mol% to provide adequate stability at high temperatures (Gaillard *et al.*, 2014).

Nevertheless, it is necessary to mention that NVP increases the polymer's cost and deteriorates injectivity in low permeability carbonates (Masalmeh *et al.*, 2019). To a certain degree, it is possible to bring robustness to the polymer by incorporating ATBS with the lower cost and lower effect on molecular weight, if compared with NVP (Dupuis *et al.*, 2017). However, the polymers' performance containing ATBS worsens at high-temperature conditions, as they are more sensitive to hydrolysis at elevated temperatures, while NVP can confine acrylamide hydrolysis by the neighbouring effect (Moradi-Araghi and Doe, 1987; Gaillard *et al.*, 2010).

2.4.2 Hydrolysis of Polyacrylamides

Polyacrylamides are known for their tendency to adsorb on mineral surfaces. HPAM polymers are their partially hydrolyzed forms with a reduced degree of adsorption. During hydrolysis, some of the amide groups (CONH₂) are converted to carboxyl groups (COO⁻), as depicted in **Figure 2.8**. These negatively charged carboxyl groups introduced on the backbones of polymer chains have a significant effect on the rheological properties of the polymer solution (Lake, 1989; Sheng, 2011). In addition to lowering the adsorption level (especially in sandstone rock with a negative surface charge), the anionic charges of the carboxyl groups cause intramolecular repulsions. These interactions enlarge the hydrodynamic radius of the HPAM polymers and enhance the viscosifying effect. Furthermore, the degree of hydrolysis should be selected carefully, as the polymer is not dissolved in water at smaller hydrolysis, and it becomes too sensitive to hardness and salinity if hydrolysis is quite large (Lake, 1989; Magbagbeola, 2008). The degree of hydrolysis is estimated as follows (Ma *et al.*, 2015):

$$DOH = \frac{y}{y + x}, \quad (2.7)$$

where DOH is the degree of hydrolysis, y is the number of carboxyl groups, and x is the number of amide groups.

The degree of hydrolysis varies between 0.15 and 0.35 in commercial products (Gbadamosi *et al.*, 2019). However, throughout their residence in the porous media at high temperatures or pH, it rises further. Generally, the level of hydrolysis increases under acidic and basic conditions. Nevertheless, at high temperatures, rapid hydrolysis may occur even under neutral conditions (Sheng, 2011). With increasing hydrolysis level above critical, the cations present in the solution screen the negative charges of carboxyl groups and result in viscosity loss and precipitation. Divalent cations have a more adverse impact on viscosity than monovalent (Levitt and Pope, 2008). They do not only exacerbate precipitation, but also accelerate the hydrolysis of amide groups (Ma *et al.*, 2015). The critical concentration of calcium required for precipitation of HPAM decreases with temperature (Moradi-Araghi and Doe, 1987).

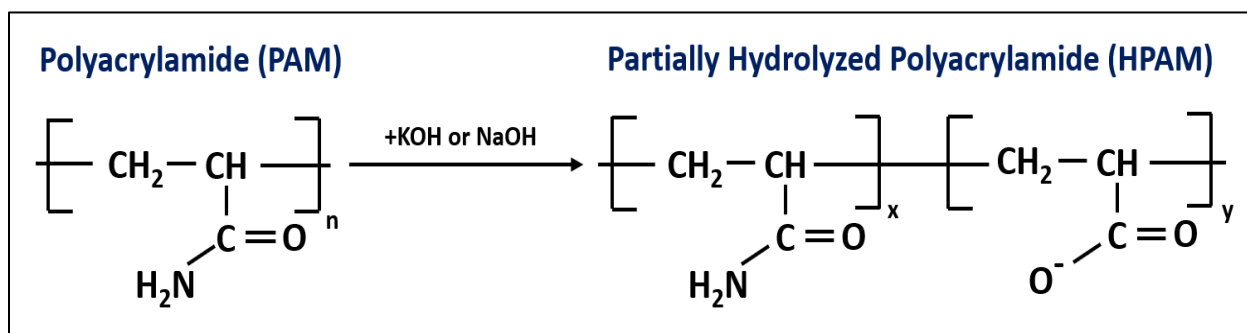


Figure 2.8: Hydrolysis of PAM to HPAM (modified after Ma *et al.*, 2015).

2.4.3 Screening Studies for Harsh Conditions

There is vast literature analyzing different polymers and their behavior in a porous medium under harsh conditions (Akstinat, 1980; Lake, 1989; Sorbie, 1991; Sheng, 2011). Akstinat (1980) compared various polymers under extreme conditions, including high oil viscosities, high salinities, and elevated reservoir temperatures. According to his study, only selected xanthan gums and glucans are suitable for EOR-processes under extreme reservoir conditions, while synthetic polymers mostly lose their efficiencies at higher salinities. Davison and Mentzer (1982) evaluated

the performance of 140 polymers in a porous medium under high temperature-salinity-pressure conditions. The authors found scleroglucan showing the best performance while polyacrylamides (PAAm's) are particularly inappropriate for mobility control. The advantages of scleroglucan over other polymers have also been confirmed by Jensen *et al.* (2018), where they reported the superior rheological properties and thermal stability achieved by these polymers with minimal shear degradation.

Polymer screening studies have also been conducted to evaluate various novel HPAM based polymers at harsh conditions. Levitt and Pope (2008) tested some commercially available polymers estimating their chemical and thermal stability as well as compatibility with surfactants. They reported that the polyacrylamide solutions are feasible at high temperatures only if the hardness is less than 200 ppm. AN-125, 20-30% AMPS copolymer, is found to be a desirable alternative in the presence of a higher concentration of divalent ions and extensive hydrolysis. Gaillard *et al.* (2014) aimed to optimize the chemistry of the NVP copolymers. In their research, the ageing tests were conducted at 105, 120, and 140 °C for one year. The experiments were performed under total anaerobic conditions as well as in the presence of 200 ppb of oxygen. It was reported that the stability of the NVP terpolymers could be rapidly improved if ATBS replaced the acrylic acid in the polymer chain. Moreover, SAV 225 (20-30 mol% NVP) and SAV 333 (30-45 mol% NVP) were characterized as the most efficient polymers for the temperatures of 105 °C and 120 °C, respectively. Dupuis *et al.* (2017) used polymers with different ATBS contents. One polymer contained NVP along with ATBS monomers. During the rheological measurements at the temperature of 25 °C and salinity of 100,000 ppm, the authors realized that the required dosage for the polymer with NVP was significantly higher than that for other polymers. Thus, they found it less attractive due to the higher cost of NVP-based polymers. Also, for NVP-free polymers, the minimum concentration to achieve the desired viscosity increased with the polymer's ATBS content. It was thought to be due to the ATBS tendency to decrease the polymer's molecular weight and ultimately reduce the viscosity of the solution. Alfazazi *et al.* (2018) conducted a polymer screening study where they tested three NVP-based HPAM polymers (SAV10, SAV28, and SAV37) to estimate the best candidate for the harsh conditions in the Middle East reservoirs. It was reported that SAV10 with a molecular weight of 2-4 million Daltons retained 90% of its viscosity at 167,000 ppm salinity and temperature of 120 °C after 100 days of ageing. SAV10 polymer was found more stable at elevated temperatures and retained higher viscosities than the

two other polymers. This was related to the larger NVP concentration in the backbone chain of SAV10. Moreover, shear-thickening was detected at high flow rates during the injectivity test, while the polymer showed shear-thinning at small flow rates, confirming the complex behavior of SAV10 in porous media.

As mentioned earlier, the monomers NVP, AMPS, and ATBS can provide the acrylamide with required stability and robustness at harsh conditions. However, the manufacturing of these novel polymers might be 3-10 times more expensive than the conventional HPAM polymers (Gaillard *et al.*, 2014). Nonetheless, in case a project is generating a profit, then there is no harm of using these stable polymers as soon the economics can be justified.

2.5 Polymer Viscoelastic Properties

In general, polymer flow in porous media can be subdivided into two separate flow regimes; shear dominant and extensional dominant. Most of the polymer solutions demonstrate pseudoplastic flow behavior in the shear dominant region. On the other hand, the shear-thickening or dilatant behavior of some polymer solutions occurs in the extensional dominant flow regime. In the latter regime, the elongational (or extensional) viscosity of the polymers rises rapidly to a high value and causes the apparent viscosity to increase correspondingly (Chauveteau, 1981).

It is important to note that polymer solutions show only shear-thinning behavior in a rheometer, while some polymers with viscoelastic properties may exhibit shear-thickening behavior above a critical shear rate in a porous medium. The reason for such flow behavior is the repeated variations of the capillary diameters that result in converging and diverging extensional flows, and consequently, stretching and contraction of the polymer chains occurs (Heemskerk *et al.*, 1984; Sheng *et al.*, 2015). At high shear rates, the frequency of the deformation of a polymer molecule grows so high that the polymer does not have time to relax to its original conformation. The resultant change in the shape is called an elastic strain, and it is thought to be responsible for the additional pressure drop and thickening of the flow (Delshad *et al.*, 2008; Clarke *et al.*, 2016; Tahir *et al.*, 2017).

2.5.1 Deborah Number

One significant parameter for representing the viscoelastic flow in porous media is the Deborah number (De), which is defined as the ratio of the materials characteristic time (relaxation time) to the characteristic flow time (residence time) (Macosko, 1994). It may also be explained as the ratio between elastic and viscous forces (Skauge *et al.*, 2018).

$$De = \frac{\tau_r}{t}, \quad (2.8)$$

where τ_r is the relaxation time and t is the residence time.

Large Deborah numbers lead to solid-like behavior, while fluid-like behavior occurs if the Deborah number is small (Sorbie, 1991). Therefore, a material can behave solid-like either because of its significant elasticity (high relaxation time) or/and the swift deformation process (short resident time). Thus, even mobile liquids with low characteristic times can behave like elastic solids in a speedy deformation process (Barnes *et al.*, 1989).

Marshall and Metzner (1967) stated that the viscoelastic effect for limited Deborah numbers is negligible due to the fluid's instant response to its local state of deformation when it does not "remember" its previous configurations. Furthermore, as De is increased to a critical value, the solid-like characteristics of viscoelastic materials start to appear. They also mentioned that the substantial effect of the fluid elasticity on the pressure drop is first felt at critical Deborah numbers around 0.05. Haas and Durst (1982) also denoted a negligible increment in elongational viscosity at low Deborah numbers. However, they observed a dramatic elongational increase at De of 0.5. According to Chauveteau (1981), the onset of dilatant behavior occurred when the critical Deborah number was 10. Heemskerk *et al.* (1984) reported that a polymer coil started to elongate and exhibit viscoelasticity at critical Deborah number around 1. Azad *et al.* (2018) conducted an extensional rheological characterization of HPAM and associative polymer and defined the onset of viscoelastic behavior to a Deborah Number of 0.132 and 0.156, respectively. Consequently, one can note that there is no consensus among the authors on a specific critical Deborah number, and the proposed values considerably differ in magnitude. The reason behind this wide range of proposed critical Deborah numbers is due to the inconsistency in the calculations of residence time.

The different ways of calculating residence time will be discussed later.

2.5.2 Relaxation Time

The polymer characteristic relaxation time is the time taken by the polymers to return to their original conformation after being disturbed. Elastic effects become more pronounced when the fluid suffers a significant deformation in a time comparable to the relaxation time of the fluid. For a Hookean elastic solid, the relaxation time is infinite, while for a Newtonian fluid, it is zero.

Several models might help to measure the relaxation time of a polymer molecule, such as "Rouse model" (Rouse, 1953) and "The G' and G'' Cross-Over Point Model" (Castelletto *et al.*, 2004). Magbagbeola (2008) provided a list of some other models as well. The Cross-Over Point Model suggests that the inverse of the frequency at which G' and G'' intersect is the characteristic relaxation time of the polymer solution (**Figure 2.9**). The data for this model include storage (or elastic) modulus (G') and loss (or viscous) modulus (G''), which can be acquired from dynamic oscillatory tests (Sheng, 2011). Despite the simplicity, the Cross-Over Point Model may estimate the relaxation time with adequate accuracy (Qi *et al.*, 2017).

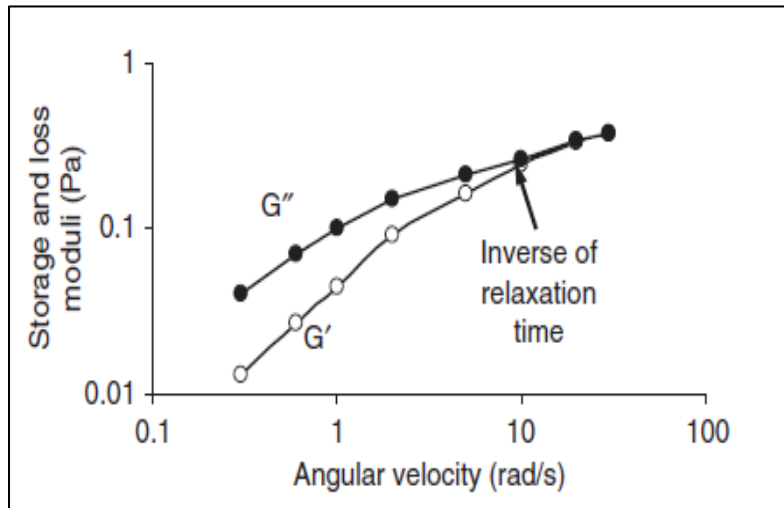


Figure 2.9: The Cross-Over Point Model to determine relaxation time (Sheng, 2011).

Another model mentioned above, the Rouse model, can be used by fitting with the experimental data. In this model, the polymer molecule is introduced as a flexible chain of N beads

connected by $N-1$ elastic springs. Moreover, a molecule has $N-1$ relaxation times related to the model's viscous and elastic moduli when immersed in a solvent fluid (Heemskerk *et al.*, 1984). Since critical Deborah numbers are first obtained for the longest relaxation time, the most extended spectrum of the obtained relaxation times is used for the calculations and injectivity tests.

In addition to the models listed above, several empirical correlations have also been provided to predict the polymer relaxation time. One of these correlations is developed by Kim *et al.* (2010) that is based on the generalized Maxwell model and can obtain relaxation time in terms of temperature, polymer concentration, brine salinity, and hardness. The relaxation time can also be estimated by a capillary breakup extensional rheometer (CaBER). In this correlation, the upper-convected Maxwell model is fitted with the filament diameter versus time plot, and the extensional relaxation time is obtained through regression (Azad and Trivedi, 2018).

The polymer viscoelastic properties may strengthen or weaken depending on polymer molecular parameters and fluid flow conditions in porous media. Several works were devoted to studying the factors that affect polymer characteristic relaxation time and their viscoelastic behavior in porous media. Some of these factors with their corresponding effect on characteristic relaxation time are discussed below.

Polymer Molecular Weight (M_w) Effect. Many researchers reported that polymer molecular weight positively affects its relaxation time, namely that polymer elasticity is pronounced more with higher M_w (Hester *et al.*, 1994; Jiang *et al.*, 2003; Delshad *et al.*, 2008; Magbagbeola, 2008; Clarke *et al.*, 2016). With the increase in molecular weight, the average length of the polymer chain increases, and it becomes harder for the molecule to relax (Jiang *et al.*, 2003). Delshad *et al.* (2008) compared the effect of molecular weight and concentration of polymers. They reported that the relaxation time of the higher M_w polymer at 500 ppm was larger than that of lower M_w polymer at 1500 ppm in the same solvent. The latter indicates the more substantial impact of the molecular weight on polymer relaxation time. On the other hand, polymers with high molecular weight are more susceptible to mechanical degradation, leading to breakage of the polymer backbone and deteriorating its viscosifying power (Taylor and Nasr-El-Din, 1995). Therefore, this factor requires careful design and optimization before implementing polymer flooding.

Polymer Concentration Effect. The effect of polymer concentration is also believed to be positive on polymer elasticity (Chauveteau, 1981; Heemskerk *et al.*, 1984; Wang *et al.*, 2000a; Delshad *et al.*, 2008; Clarke *et al.*, 2016; Khamees and Flori, 2019). Such an effect can be explained by intensifying the intermolecular interactions with the increase in polymer concentration in the solution. Therefore, it becomes more difficult for the polymer to return to its original conformation and eventually, resulting in a relaxation time increase. However, Jiang *et al.* (2003) analyzed the polymer concentration effect on relaxation time for Polystyrene/decalin of five various molecular weights. They reported a positive effect of polymer concentration that vanishes after a critical concentration (2500 ppm). This trend was related to supermolecular structuring of the different polymers used.

Temperature Effect. High-temperature conditions in the reservoir are proven to have a negative effect on the viscoelastic properties of a polymer (Edwards *et al.*, 2002; Jiang *et al.*, 2003; Skauge *et al.*, 2018; Alfazazi *et al.*, 2019). Jiang *et al.* (2003) reported that the kinetic motion of the individual atoms increases with a rise in temperature, which results in faster conformational rearrangements of a polymer chain. Therefore, the relaxation time at high temperatures decreases. Alfazazi *et al.* (2019) analyzed the sensitivity of the HPAM-based SAV10 polymer to the harsh conditions in carbonates. They reported that this polymer shows good thickening behavior at low temperatures. However, with temperature increase, the viscoelastic properties weaken and shear-thickening behavior disappears.

Water Salinity Effect. Generally, HPAM polymers have negative charges at their backbone chains. The repulsion between those charges causes the stretching of the polymer molecules and increases their hydrodynamic radius, resulting in a pronounced viscosity enhancement (Levitt and Pope, 2008). In high salinity solutions, the cations present in the brine screen the negative charges on the polymer backbone and hinder the stretching of the molecule, leading to viscosity loss (Alfazazi *et al.*, 2018). The high salinity solution is believed to degrade polymers and impair their viscoelastic properties. Garrouch (1999) observed the same oscillatory relaxation times for the rigid xanthan and flexible HPAM polymer in a high salinity solution although the latter one exhibits far more elasticity under normal conditions. He reported that synthetic elastic polymers

are more sensitive to solution salinity, which causes the collapse of their molecular chain and leads to a much smaller random coil structure. A degraded polymer with a shorter molecular chain is usually associated with lower oscillatory relaxation time and a smaller Deborah number. This explains the impaired viscoelastic properties of polymers in a highly saline solution.

Nevertheless, several studies show the positive effect of salinity on extensional rheological properties and oil recovery. Erincik *et al.* (2017) performed a series of polymer flooding experiments in sandstone rock at different brine salinities. They reported that higher salinity HPAM solution displaced more oil despite its smaller Deborah number. Azad and Trivedi (2020) related this to the inability of oscillatory relaxation time used for Deborah number calculations to reflect the effect of salinity change on oil recovery. They recommended estimating the extensional relaxation time. Being directly proportional to brine salinity, extensional relaxation time may be used to predict oil recoveries at different salinities more accurately than oscillatory relaxation time.

Water Hardness Effect. Brines with high concentrations of divalent cations are generally believed to degrade the polymer and deteriorate its viscoelastic properties (Tahir *et al.*, 2017). Nevertheless, Walter *et al.* (2019) reported that at a higher solution hardness, the divalent cations might coordinate the negative charges along the polyelectrolyte chain to each other, forming ionic bridges. These bridges represent the transient crosslinks between the charges within the same chain or on two different polyelectrolyte chains. The authors reported that an increase in calcium chloride concentration leads to a rise in polymer extensional viscosity and the related relaxation time.

Permeability Effect. Another factor influencing the viscoelastic properties is the permeability of the reservoir. Polymers flowing in porous media with low permeability demonstrate more pronounced viscoelasticity (Hirasaki and Pope, 1974; Heemskerk *et al.*, 1984; Ranjbar *et al.*, 1992; Zamani *et al.*, 2015). This could be related to the reduced median pore space where higher differential pressure increases the deformation of the polymer molecules and induces the viscoelastic flow even at comparatively lower flow rates. Nevertheless, it is also important to mention that permeability affects mechanical degradation, namely the earlier degradation of the polymers occurs if the permeability is low, as in the case with high M_w . Therefore, Wang *et al.* (2008) suggested using high molecular weight polymers only in high permeable rocks while

limiting M_w for those with lower permeability.

Hydrolysis Effect. Furthermore, the degree of polymer hydrolysis may affect the viscoelastic properties (Ranjbar *et al.*, 1992; Lewandowska, 2006; Magbagbeola, 2008). Ranjbar *et al.* (1992) showed that the storage modulus and corresponding relaxation time increase with increasing the degree of hydrolysis until a critical degree. In this study, the maximum elasticity of the HPAM polymers was observed for the critical degree of around 27% hydrolysis. Furthermore, Magbagbeola (2008) reported that at a higher degree of hydrolysis, the polymers become more sensitive to the cations present in brine and lose their elasticity. He also showed through corefloods that a polymer having a molecular weight of 20×10^6 Dalton and degree of hydrolysis of 28-30% is less elastic than 8×10^6 Dalton polymer with hydrolysis degree of 20-30%, which highlights the effect of hydrolysis level.

2.5.3 Residence Time

Residence time is the characteristic time for the flow in the porous media and is also called residential time or transient time. It is the time required for the polymers to flow from one constriction to another (Wilton and Torabi, 2013). In the Deborah number calculations, the residence time is usually considered as the inverse of the velocity gradient, either shear rate or strain rate (Azad and Trivedi, 2019). Shear rate is used to estimate the resident time by several authors (Masuda *et al.*, 1992; Delshad *et al.*, 2008). The shear rate is generally represented by the following equation (Canella *et al.*, 1988):

$$\frac{1}{t} = \dot{\gamma} = C \left[\left(\frac{3n + 1}{4n} \right)^{n/(n-1)} \left(\frac{4u_w}{\sqrt{8S_w \phi k_w}} \right) \right], \quad (2.9)$$

where t is the residence time, $\dot{\gamma}$ is the shear rate, n is the shear-thinning index, u_w is the Darcy's velocity, S_w is the aqueous phase saturation, ϕ is the porosity, k_w is the effective aqueous phase permeability, and C is the shear correction factor accounting for the difference between the actual porous medium and the equivalent capillary tube. Canella *et al.* (1988) have taken C as 6 for a

number of coreflooding experiments. Generally, Wreath *et al.* (1990) reported that C is a function of transport and petrophysical properties and presented various expressions for estimating the effective shear rate.

On the other hand, some researchers used the stretch rate (strain or elongational rate) to calculate the residence time (Hirasaki and Pope, 1974; Haas and Durst, 1982; Heemskerk *et al.*, 1984; Azad *et al.*, 2018). The most used equation for the stretch rate has been proposed by Hirasaki and Pope (1974) as follows:

$$\frac{1}{t} = \dot{\epsilon} = \left[\frac{u_w}{(1 - \phi S_w) \sqrt{150 k_w / S_w \phi}} \right], \quad (2.10)$$

where $\dot{\epsilon}$ is the stretch rate in s^{-1} .

Therefore, the residence times calculated by different methods show inconsistency in the reported Deborah numbers. The Deborah number estimated using the stretch rate will be lower than that calculated by the shear rate due to the higher coefficient in the denominator of the stretch rate calculation (Azad and Trivedi, 2019). Generally, both types of velocity gradients strongly depend on the flow rate and reservoir properties, such as porosity and permeability. For example, with increasing the flow rate applied during polymer flooding, the shear or stretch rate increases, and the time needed for the polymers to flow from one constriction to another (residence time) is reduced.

2.5.4 Flow of Viscoelastic Polymers in the Porous Medium

Figure 2.10 illustrates different flow regimes exhibited by viscoelastic polymers during the flow in porous media. At low shear rates, the entropic forces exceed the hydrodynamic drag forces generated from the fluid flow. Thus, polymer configuration remains in a coil shape, and the polymer behaves like a Newtonian fluid with constant viscosity during Regime 1. As the shear rate increases and passes the first critical rate ($\dot{\gamma}_{cr1}$), the polymer molecules face the larger drag forces that untangle polymer coils and align them along the flow direction reducing their resistance to

flow (Skauge *et al.*, 2018). Regime 2, dominated by shear forces, is called the shear-thinning region where polymer solutions lose their viscosities with the shear rate.

Furthermore, as the shear rate increases further and passes the second critical rate ($\dot{\gamma}_{cr2}$), the polymer exhibits shear-thickening behavior. It is associated only with flexible viscoelastic polymers. The dilatancy in Regime 3, dominated by elongational forces, is observed only at high shear rates (near injection wells) when polymers undergo deformation called elastic strain as they flow through a series of pore bodies and pore throats (Sheng, 2011). In some works, the term strain hardening (when the viscosity increases with strain) is preferable than shear-thickening, as the increment in viscosity during the extensional flow is not achieved by the shear but elastic forces (Azad and Trivedi, 2019). The onset rate for Regime 3 is the function of both polymer molecular parameters and fluid flow conditions in porous media, which were previously discussed. Heemskerk *et al.* (1984) reported that the critical flow rate increases with increasing permeability, temperature, and salinity of the solution and with decreasing molecular weight and concentration of the polymer.

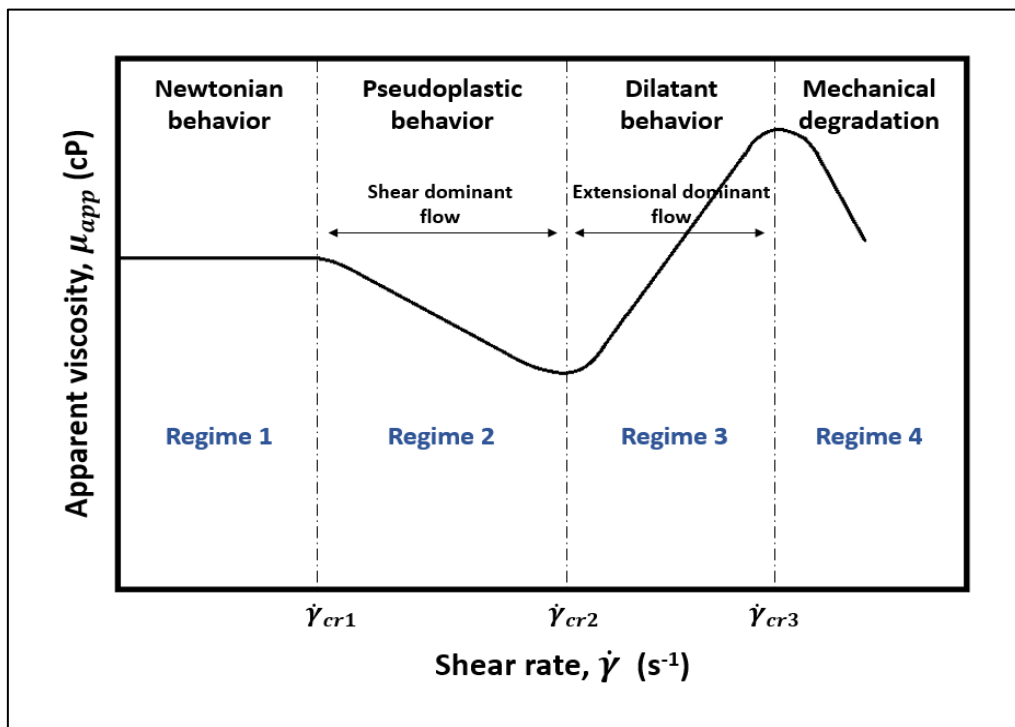


Figure 2.10: Schematic illustration of viscoelastic fluid flow behavior (modified after Sheng, 2011).

Once viscoelastic polymers undergo full stretching during the dilatant flow, they accumulate excessive stresses that eventually lead to chain scission of the polymer. After that third critical point ($\dot{\gamma}_{cr3}$), the apparent viscosity reaching the maximum value drops due to mechanical degradation (Regime 4). As mentioned earlier, the high molecular weight of the polymer and low permeability of the rock both accelerate this mechanical degradation.

2.6 Apparent Viscosity Models

This section includes various analytical models that characterize polymer rheology in porous media. The models aim to predict the apparent viscosity of polymer solution for ranges of shear rate. As was previously discussed, the polymer flow in porous media is shear dominated at low shear rates, as the amplitude of the elastic component is negligible. However, the flow at shear rates above a critical value is governed by elastic forces. Thus, in order to account for both shear-thinning in shear dominated and shear-thickening in elongation dominated regions, it is recommended to divide the total stress into shear and elastic components (Skauge *et al.*, 2018):

$$\Delta P = \Delta P_{shear} + \Delta P_{elastic} , \quad (2.11)$$

and therefore, total apparent viscosity can be represented by the sum of shear and elastic parts as follows:

$$\mu_{app} = \mu_{sh} + \mu_{el} , \quad (2.12)$$

where μ_{sh} and μ_{el} are the shear and elastic viscosities, respectively.

2.6.1 Shear Viscosity

Several viscosity models are designed to estimate the shear viscosity of polymer solution through

bulk shear rheological measurements. The Power-law model proposed by Bird *et al.* (1960) is one of the most frequently encountered analytical forms of the viscosity-shear rate relationship for shear-dominant flow (Sorbie, 1991):

$$\mu_{sh} = K\dot{\gamma}^{n-1}, \quad (2.13)$$

where K is consistency factor and n is the Power-law exponent, which is less than 1, equal to 1, and greater than 1 for pseudoplastic, Newtonian, and dilatant flows, respectively.

Another model for the shear dominated regime was introduced by Carreau (1972):

$$\mu_{sh} = \mu_{\infty} + (\mu_0 - \mu_{\infty})[1 + (\lambda\dot{\gamma})^2]^{(n_1-1)/2}, \quad (2.14)$$

where μ_0 and μ_{∞} are the zero-shear rate and infinite-shear rate viscosities, respectively. n_1 is the shear-thinning index, and λ is the time constant that represents a transition between zero-shear Newtonian and pseudoplastic regions. The parameters n and λ can be estimated by fitting the Carreau model to the polymer bulk viscosity data, and they vary with salinity, polymer structure, and molecular weight (Magbagbeola, 2008). The Carreau model offers a proper fit to bulk rheological data over a wide range of shear rates, including upper and lower Newtonian plateaus. However, it requires four fitting parameters instead of two Power-law parameters (Sorbie, 1991).

Generally, the Carreau model provides a reasonable prediction of purely viscous polymer behavior in porous media. This model that relied on bulk rheology tests successfully matches the shear-thinning region. Nevertheless, for viscoelastic polymers that exhibit dilatancy beyond a critical shear rate, the Carreau model underpredicts the viscosity with a considerable margin.

2.6.2 Elastic Viscosity

As stated before, estimating only shear viscosity is not enough for viscoelastic polymers, and elastic viscosity is essential to account for the additional pressure drop resulted from the dilatant behavior at high shear rates. Several expressions that determine the elastic component of viscosity

are listed below:

- The model proposed by Hirasaki and Pope (1974) uses shear viscosity and the Deborah Number (De) to calculate elastic viscosity. Nonetheless, this model is inapplicable for the cases where the Deborah Number becomes greater than unity:

$$\mu_{el} = \frac{\mu_{sh}}{[1 - De]}, \quad (2.15)$$

- Masuda *et al.* (1992) presented another model for elastic viscosity measurements where in addition to the Deborah Number and shear viscosity, they used the empirical constants. Although the model's accuracy was improved compared to the previous one, it still has some drawbacks. Particularly, μ_{el} values from this model can increase indefinitely as De increases, which should not be the case:

$$\mu_{el} = \mu_{sh} C_C (De)^{m_C}, \quad (2.16)$$

where C_C and m_C are empirical constants that are dependent on the degree of complexity of the pore geometry in the porous medium.

- A significant distinction of the model provided by Delshad *et al.* (2008) is the presence of the plateau value of μ_{max} . The model limits the elongational viscosity to the maximum value where mechanical degradation starts:

$$\mu_{el} = \mu_{max} [1 - \exp(-(\lambda_2 De)^{n_2-1})], \quad (2.17)$$

where μ_{max} is the maximum elongational viscosity, λ_2 is the universal constant that is usually taken as 0.01, and n_2 is the shear-thickening (or strain hardening) index.

2.6.3 Models for Apparent Viscosity Estimation

The apparent viscosity models are designed to predict polymer rheological behavior in porous media, which was previously depicted in **Figure 2.10**. Examples of the models are given below:

- The apparent viscosity model proposed by Delshad *et al.* (2008) is frequently called as Unified Apparent Viscosity Model (UVM). The model defines the apparent viscosity for both shear-thinning and shear-thickening regions. The shear viscosity is modeled by Carreau expression, while elastic viscosity is estimated by relating it to the Deborah Number and correspondingly to the polymer relaxation time:

$$\mu_{app} = \mu_{\infty} + (\mu_0 - \mu_{\infty})[1 + (\lambda\dot{\gamma})^2]^{(n_1-1)/2} + \mu_{max}[1 - \exp(-(\lambda_2\tau_r\dot{\gamma})^{n_2-1})]. \quad (2.18)$$

According to their model, the relaxation time (τ_r) and strain hardening index (n_2) identify the level of polymer shear-thickening behavior. Moreover, UVM also considers the maximum elongational viscosity (μ_{max}) before the mechanical degradation effect appears. The model extensional parameters (n_2, μ_{max}) may be estimated by coreflooding tests, while shear parameters ($\mu_{\infty}, \mu_0, \lambda, n_1$) are determined through bulk rheology measurements. The UVM has been successfully implemented in injectivity models to match the injection pressure data from coreflooding and field tests (Lotfollahi *et al.*, 2016a). Even though UVM overcomes the drawbacks of an unlimited increase in viscosity with respect to the Deborah Number, it still needs coreflooding data to predict the model parameters. Moreover, the drop in apparent viscosity due to mechanical degradation at ultimate shear rates cannot be characterized by UVM although the model provides the plateau value of μ_{max} .

- Azad and Trivedi (2018) developed another viscosity prediction model, called Azad-Trivedi Viscoelastic Model (AT-VEM):

$$\mu_{app} = \mu_{\infty} + (\mu_0 - \mu_{\infty})[1 + (\lambda\dot{\gamma})^2]^{(n_1-1)/2} + \mu_{max}^{0.35}[1 - \exp(-(\lambda_2\tau_r\dot{\gamma})^{n_2-1.2-1})]. \quad (2.19)$$

It is based on the Unified Viscosity Model (UVM); however, AT-VEM does not require coreflooding data to predict the empirical parameters. The extensional parameters may be determined by a capillary breakup extensional rheometer (CaBER). Based on CaBER measurements, the authors found that the maximum elongational viscosity occurs at the Deborah Number of 0.66. Additionally, the downscaling factor 0.35 was applied to μ_{max} , and subtrahend 1.2 was used with n_2 in order to scale down the pure elongation in the extensional bulk field to the combination of elongation and shear encountered in the porous media.

- The Extended Viscoelastic Model provided by Stavland *et al.* (2010) determines apparent viscosity in both shear- and elongation-dominated regions and accounts for polymer mechanical degradation at high shear rates. However, the model needs extensive coreflooding measurements to properly model the polymer rheology in shear-thickening and mechanical degradation regimes (Azad and Trivedi, 2019):

$$\mu_{app} = \mu_{\infty} + [(\mu_0 - \mu_{\infty})(1 + \lambda_1\dot{\gamma})^n + (\lambda_2\dot{\gamma})^m] \cdot [1 + (\lambda_3\dot{\gamma})^x]^{j/x}, \quad (2.20)$$

where μ_0 and μ_{∞} are the zero-shear rate and infinite-shear rate viscosities, λ_1 is the characteristic time constant, $\dot{\gamma}$ is the shear rate, n is the shear-thinning index, λ_2 is the relaxation time, m is the elongational exponent, λ_3 is the characteristic time constant for degradation, x is the mechanical degradation index, and j is the tuning parameter for degradation. Similarly, shear parameters (μ_0 , μ_{∞} , λ_1 , n) may be found through shear rheology measurements. On the other hand, the parameters accounting for elongation and mechanical degradation are estimated by coreflood data and effluent sample.

2.7 Impact of Polymer Viscoelasticity on Residual Oil Recovery

Residual oil is usually referred to as the oil entrapped in thoroughly water-flooded regions of a reservoir (Lake, 1989). Several factors induce the residual oil saturation. Capillary pressure is the

main reason behind oil ganglia snapped off from the flow stream and immobilized, especially in water-wet reservoirs. Additionally, for the oil-wet or mixed wet reservoirs, the adsorption of oil molecules on rock surfaces is another factor causing a considerable amount of oil trapped in porous media. The rock configuration can also affect the residual oil saturation considering that oil molecules can be immobilized in dead ends and other stagnant flow pockets (Wang *et al.*, 2000a; Afsharpoor *et al.*, 2012; Ehrenfried, 2013).

Generally, residual oil mobilization can be evaluated by comparing drive and capillary forces acting on oil globules. As mentioned before, capillary forces may result in disconnected and immobilized oil ganglia in porous media during immiscible fluid displacement (Sorbie, 1991). On the contrary, viscous forces applied through injection fluids and possibly gravity forces may mobilize the entrapped oil if they locally balance and exceed the capillary forces. Here, the contribution of gravity forces to oil mobilization strongly depends on the direction of displacement and density difference between displacing and displaced fluids (Sheng, 2011). Moreover, viscous forces are determined by the applied pressure drop, the permeability of the porous medium, and the viscosity of displacing fluid. On the other hand, capillary forces are controlled by the pore geometry, the interfacial tension between two fluids, and the wettability of the rock (Delshad *et al.*, 1986).

The average pressure gradients applied during waterflooding at a Darcy velocity of 1 ft/D in a strongly water-wet reservoir (with a contact angle of zero) and effective aqueous permeability of 100 mD is around 4-5 orders of magnitude lower than the critical pressure gradient required to mobilize residual oil (Afsharpoor *et al.*, 2012). Therefore, it is believed that water injection is not capable of reducing the nonflowing oil saturation. However, adding surfactants to the water may reduce the capillary forces in porous media and eventually bring down the critical pressure gradient for oil mobilization. Accordingly, surfactant or alkaline flooding are considered a potential remedy to produce much immobile oil in a reservoir, in addition to other EOR techniques. On the other hand, the higher pressure gradients or greater viscous forces may be obtained using polymers which increase injectant viscosity from 1 cP to 10-100 cP. However, even the additional pressure gradients provided by purely viscous polymer flooding cannot achieve oil mobilization, explained by the viscous forces being still lower than the critical capillary forces. Therefore, traditionally, polymer flooding was only associated with the production of bypassed oil and improvement in

volumetric sweep efficiency, while its effect on residual oil displacement at a micro-scale was highly questionable (Lake, 1989; Sorbie, 1991).

Nevertheless, recent studies and field observations indicate that the polymers with viscoelastic properties may impact recovery efficiency at both macro and micro-scales despite the conventional belief. Wang *et al.* (2000a) reported that micro-scale displacement efficiency might be considerably improved using elastic polymers with large molecular weight and high polymer concentrations prepared in low-salinity makeup water. Moreover, various mechanisms to mobilize different types of residual oil were thoroughly discussed in this study. Urbissinova *et al.* (2010) also investigated the impact of viscoelastic polymers on residual oil recovery. They used two polymers with similar molecular weights but different molecular weight distributions (MWD) to separate the effect of elasticity on oil mobilization. It was reported that residual oil recovery by two polymers exhibiting the same shear viscosity was higher for the one with wider MWD and, thus, with more pronounced elastic properties. The positive effect of viscoelastic polymers on trapped oil mobilization was also confirmed by Qi *et al.* (2017). They conducted a series of polymer corefloods in Bentheimer sandstones saturated with heavy oil (120 cP) and observed a significant incremental oil recovery obtained by the elastic HPAM polymers. Furthermore, they reported that flow rate is a crucial factor affecting the polymer elasticity and residual oil recovery. Notably, an additional 10% OOIP was produced using polymers with enhanced elasticity at higher flow rates ($De > 25$). However, it is not very easy to detect and quantify polymer elasticity with the experimental approaches devised so far (Ehrenfried, 2013). Azad and Trivedi (2020) reported that estimation of polymer apparent viscosity using an extensional rheometer might be more representative of porous media and better explain the residual oil recovered by viscoelastic polymers.

The additional oil recovery using viscoelastic polymers is thought to be obtained by pulling, stripping off, and dragging the oil molecules entrapped in porous media (Wang *et al.*, 2000a). Additionally, viscoelastic polymers face significant extensional deformation in high-shear rate regions, especially in the vicinity of injection wells. The resultant elastic strain causes the extensional viscosity and normal forces to rise. The normal forces are strongly related to the polymer elasticity and increase rapidly with the Deborah number (De). Moreover, these micro forces may even dominate over viscous forces at a higher De , resulting in oil mobilization by

impinging upon a trapped oil interface (Afsharpoor *et al.*, 2012; Ehrenfried, 2013).

2.7.1 Trapping Number

It is essential to model the combined effect of both gravity and viscous forces on residual oil recovery; that is possible by using the trapping number (N_T). It is a dimensionless parameter that relates viscous and gravity forces to the capillary forces. There are several expressions available in the literature to compute the trapping number. The most acceptable definition proposed by Jin (1995) is shown below:

$$N_T = \frac{|\bar{k} \cdot \vec{\nabla} \Phi_p + \bar{k} \cdot [(\rho_p - \rho_{p'})g\vec{\nabla} D]|}{\sigma_{p'p}}, \quad (2.21)$$

$$\Phi_p = P_p - g\rho_p \Delta D, \quad (2.22)$$

where \bar{k} is the permeability tensor, $\vec{\nabla} \Phi_p$ is the flow potential gradient of displacing phase, $\sigma_{p'p}$ is the interfacial tension between the phases, $\vec{\nabla} D$ is the depth gradient, g is the gravitational constant, and ρ_p and $\rho_{p'}$ are the densities of displacing and displaced phases, respectively. Moreover, ΔD in Equation 2.22 is the positive vertical distance between the datum level and a point below it (Ahmed, 2000).

Moreover, the trapping number can be also calculated using the Bond and capillary numbers, as in **Equation 2.23** (Pennell *et al.*, 1996). In the latter equation, Bond number (N_B) refers to the ratio of gravity forces to capillary forces, while the capillary number (N_C) is defined as the ratio of viscous forces to capillary forces.

$$N_T = \sqrt{N_B^2 + 2N_B N_C \sin \alpha + N_C^2}, \quad (2.23)$$

$$N_B = \left| \frac{k_w g (\rho_p - \rho_{p'})}{\sigma_{p'p} \cos \theta} \right|, \quad (2.24)$$

$$N_C = \left| \frac{k_w \cdot \nabla \Phi_p}{\sigma_{p'p} \cos \theta} \right|, \quad (2.25)$$

where k_w is the effective aqueous phase permeability, α is the angle of flow with respect to positive x axis, and θ is the contact angle.

In the case of horizontal flow, α becomes equal to zero, and **Equation 2.23** is simplified to the following form:

$$N_T = \sqrt{N_B^2 + N_C^2}. \quad (2.26)$$

Furthermore, for a vertical flow, **Equation 2.23** becomes as follows:

$$N_T = |N_C \pm N_B|. \quad (2.27)$$

In the latter equation, "+" and "-" are used for vertical upward flow and vertical downward flow, respectively. The Bond number provides the quantitative means to estimate the effect of gravity forces on trapped oil recovery. The traditional capillary number method may not accurately predict the oil mobilization if gravity forces are significant. According to Pennell *et al.* (1996), the vertical displacement in 20-30 mesh Ottawa sand conducted at Darcy velocities below 2.8 ft/d had Bond numbers one order of magnitude higher than capillary numbers. Therefore, using only a capillary number was not adequate to predict the observed oil recovery. Generally, the Bond number's effect on the trapping number may vary depending on the direction of flow and density difference between displacing and displaced phases. In particular, higher aqueous phase density than the one of the oleic phase yields a positive density difference, and consequently, a positive Bond number during polymer flooding applications. Eventually, to get a higher trapping number, it is required to maintain the vertical upward flow ($\alpha = 90^\circ$) of the heavier fluid. On the contrary, it is

recommended to have a vertical downward flow ($\alpha = -90^\circ$) for a lighter displacing fluid having a negative Bond number (Sheng, 2011).

2.7.2 Capillary Desaturation Curve

As discussed before, the capillary number relates the viscous forces to capillary forces. Initially, Moore and Slobod (1956) introduced the concept of capillary number to explain the mobilization of oil ganglia entrapped in porous media. Subsequently, several modifications have been made to N_c to improve its correlation with residual oil saturation. Some of those advancements were briefly discussed by Azad and Trivedi (2020). Generally, **Equation 2.25** is frequently used to compute a capillary number during coreflooding tests. Moreover, it is also possible to compute N_c by using interstitial velocity and viscosity of displacing phase, and neglecting $\cos\theta$ as follows (Green and Willhite, 1998):

$$N_c = \frac{\mu V}{\sigma}, \quad (2.28)$$

where μ is the apparent viscosity of displacing fluid, V is the interstitial velocity, and σ is the interfacial tension between displaced and displacing phases.

The capillary number is considered a useful tool to estimate residual saturation in porous media. Residual wetting and nonwetting phase saturations can be represented as a function of a capillary number by the capillary desaturation curve (CDC). **Figure 2.11** shows that at low capillary numbers, residual-phase saturations remain nearly constant at a plateau value till the "knee" in CDC. Then, phase mobilization starts as the critical capillary number $(N_c)_C$ of the corresponding phase is reached (Qi *et al.*, 2017). As expected, the higher capillary numbers are required to reduce the wetting phase residual saturation since the rock surface has an affinity for that phase (Sheng, 2011). Furthermore, complete desaturation, where all residual-phase saturation is displaced, corresponds to the total desaturation capillary number $(N_c)_T$.

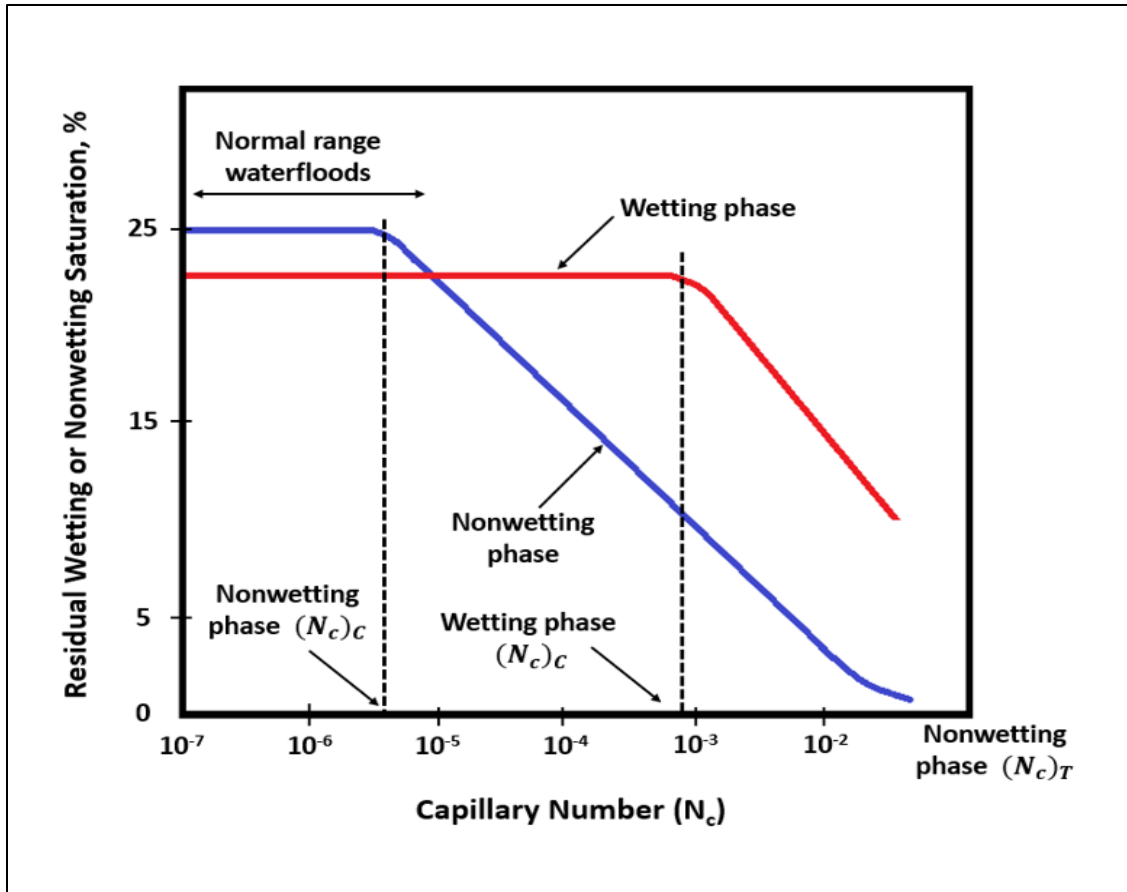


Figure 2.11: Capillary desaturation curve schematic
 (modified after Lake *et al.*, 2014).

Usually, most sandstones have $(N_c)_c$ for the non-wetting phase between 10^{-5} and 10^{-4} and $(N_c)_T$ above 10^{-3} . On the other hand, the typical N_c for waterflooding conditions ranges from 10^{-7} to 10^{-6} and stays at the left plateau of CDC (Green and Willhite, 1998). Therefore, it is impracticable for water to displace immobile oil in sandstones during secondary recovery. However, several factors change the shape of the capillary desaturation curve and may affect the residual-phase production. Namely, it becomes less challenging to displace residual saturation for media with larger average pore size and smaller ratios of pore body-to-throat size. Moreover, the pore-size distribution is also very critical for CDC (Lake *et al.*, 2014). Typically, the rock with wider pore-size distribution has increased critical-to-total capillary number range, as illustrated in **Figure 2.12**. Therefore, carbonate rocks with wide pore-size distribution are associated with low critical capillary numbers and usually do not have left plateau on CDC. The critical capillary

numbers for carbonates, being in the range of 10^{-8} - 10^{-6} , are at least two orders of magnitude lower than those for sandstones. However, heterogeneous carbonates have comparatively shallower CDC with $(N_c)_T$ higher than in sandstones. As a result, it is easier to initiate oil mobilization in carbonates and extract some oil entrapped in porous media. However, it is a challenging task to mobilize and produce the rest residual oil (Al-Shalabi, 2020).

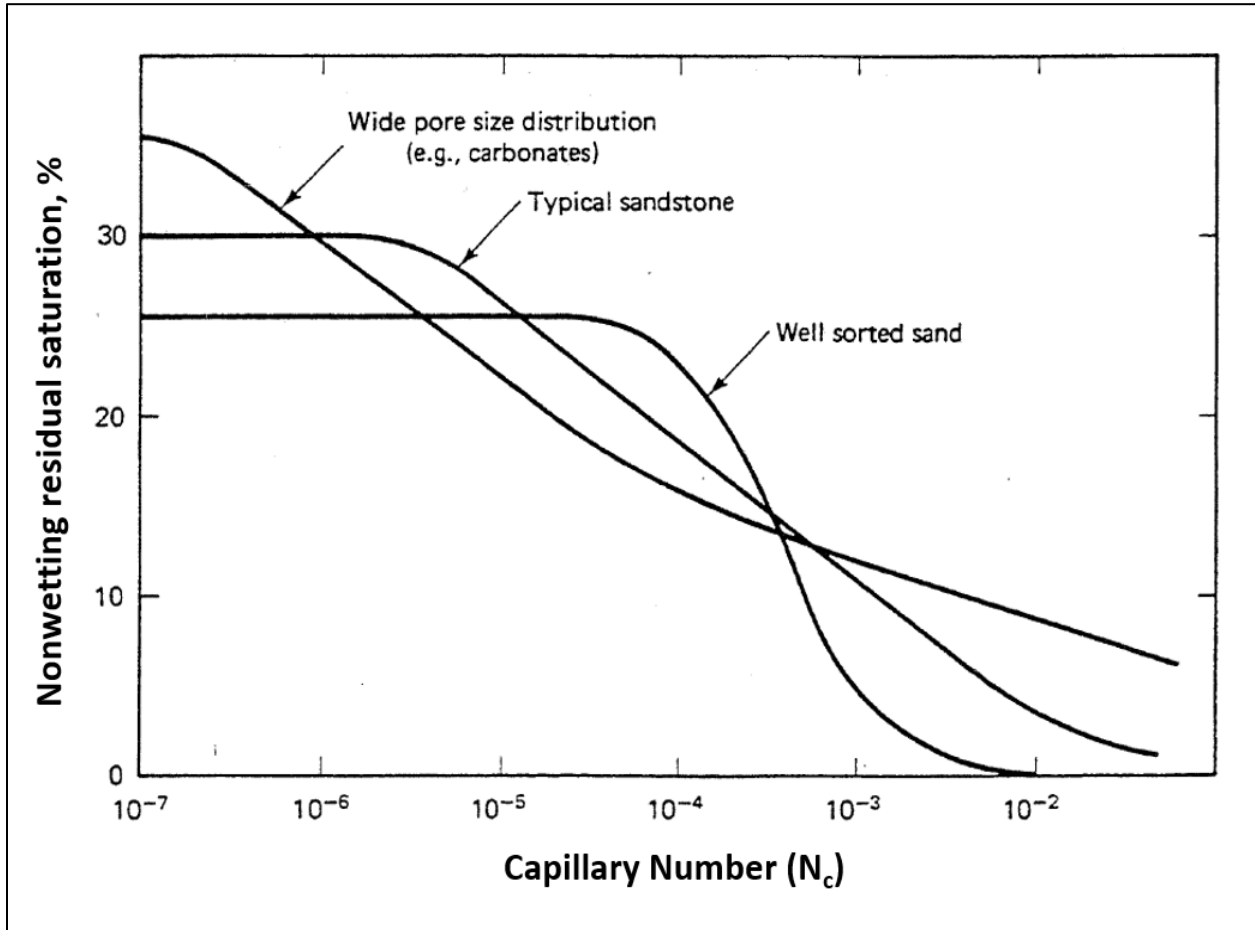


Figure 2.12: Pore-size distribution effect on CDC (Lake *et al.*, 2014).

Generally, it is possible to increase the capillary number by the following methods (Green and Willhite, 1998; Azad and Sultan, 2014; Gbadamosi *et al.*, 2019; Azad and Trivedi, 2019):

- An increment in the viscosity of displacing fluid that may be achieved by polymers;
- A decrease in interfacial tension (IFT) between displaced and displacing fluids which is

attainable with surfactant or alkaline flooding;

- An increase in the displacing fluid velocity, and correspondingly in the injection pressure. It is essential to consider a formation fracture pressure while incrementing the injection rate;
- A reduction in IFT and increment in viscosity simultaneously by viscoelastic surfactants;
- A wettability alteration toward less water-wet. Particularly, the capillary number term may markedly increase if the fluids are close to neutral wettability ($\theta \rightarrow 90^\circ$).

Surfactants decrease the interfacial tension between oil and injectant from about 30 to 10^{-3} - 10^{-4} mN·m⁻¹, and it is the main reason for the dramatic increase in capillary number and improvement in displacement efficiency. On the other hand, polymers result in a rise of a capillary number several dozen times due to their viscosifying effect although it is believed not to exceed the critical capillary number and mobilize residual oil, especially in sandstones. Therefore, polymers are commonly thought to affect volumetric sweep efficiency only. However, recent studies are consistent with the idea that viscoelastic polymers can reduce residual oil saturation beyond that of waterflooding during secondary recovery through their elastic properties. Substantial extensional viscosities and normal forces attributed to the high Deborah numbers explain the mobilization of residual oil by viscoelastic polymers. Accordingly, synthetic polymers with viscoelastic properties increase both displacement efficiency and volumetric sweep efficiency. In addition to synthetic polymers, inelastic biopolymers are also reported to reduce residual oil saturation in carbonates (Al-Shalabi, 2020). It was explained by the heterogeneous nature of that rock and comparatively lower critical capillary numbers.

Finally, it is crucial to replace the capillary number term with the trapping number while conducting field-scale or core-scale studies where the gravity forces are significant.

2.7.3 Residual Saturations as a Function of Trapping Number and Deborah Number

As indicated before, the capillary desaturation curve is frequently used to analyze oil mobilization as a function of trapping numbers. Typically, a series of laboratory measurements are conducted to generate the experimental data, which can be later fitted into theoretical models to obtain the

CDC (Sheng, 2011). A number of models to estimate the residual-phase saturations as a function of the trapping/capillary numbers are provided in the literature. The well-known model proposed by Delshad (1990) is shown below:

$$S_{pr} = S_{pr}^{high} + \frac{S_{pr}^{low} - S_{pr}^{high}}{1 + T_p N_T^\tau}, \quad (2.29)$$

where S_{pr} is the phase residual saturation, T_p is the phase trapping parameter used to fit the laboratory measurements, N_T is the trapping number, τ is the model parameter dependent on the pore size distribution of the rock, and S_{pr}^{high} and S_{pr}^{low} are the phase residual saturations at $(N_c)_T$ and $(N_c)_C$, respectively. Here, the subscript “p” stands for the displaced phase that can be water, oil, or microemulsion.

Additionally, Lotfollahi *et al.* (2016b) developed a similar model correlating the residual oil saturation with either trapping or Deborah numbers. They reported that considerable oil recovery might be obtained even at trapping numbers below the critical trapping number. It was attributed to viscoelastic polymers and was modeled using Deborah number:

$$S_{or1} = S_{or1}^{high} + \frac{S_{or1}^{low} - S_{or1}^{high}}{1 + T_1 N_T}, \quad (2.30)$$

$$S_{or2} = S_{or2}^{high} + \frac{S_{or2}^{low} - S_{or2}^{high}}{1 + T_2 De}, \quad (2.31)$$

$$S_{or} = \min(S_{or1}, S_{or2}), \quad (2.32)$$

where S_{or1} and S_{or2} are the residual oil saturations estimated by trapping and Deborah numbers, respectively; S_{or2}^{low} and S_{or2}^{high} are the residual oil saturations at low Deborah number (determined from waterflooding) and high Deborah number (determined from polymer flooding), respectively; T_2 is the viscoelastic fitting parameter (taken as 0.3-0.5 in their study). The authors used **Equation**

2.30 to estimate residual oil saturation at high trapping numbers, while at low trapping numbers, the residual oil saturation was controlled by Deborah number, and it was computed using **Equation 2.31**. The model was successfully used to match the particular experimental data for oil recovery and pressure drop for secondary and tertiary polymer flooding. However, the model may be improved further to simulate the oil recovery by viscoelastic polymers under a broader range of rock and fluid conditions (Qi, 2018).

Similarly, Qi *et al.* (2018) developed another model relating the reduction in residual saturation to the Deborah number. Their model called Elastic Desaturation Curve (EDC) was applied to simulate polymer flooding at the core and field scales. The experimental oil recovery and pressure drop data were well matched by the model. The reduction in residual oil saturation by viscoelastic polymers was modeled using Deborah number, as shown below:

$$S_{or}^* = \begin{cases} 1 & \text{if } De < 1 \\ 1 - 0.133 \log De & \text{if } De \geq 1 \end{cases}, \quad (2.33)$$

where S_{or}^* is the normalized oil saturation that is the ratio of residual oil saturation after polymer flooding to the one before polymer injection. Apparently, no oil mobilization occurred at low Deborah numbers, while the residual oil saturation was considerably reduced at higher Deborah numbers starting from unity. It was reported that incremental oil recovery strongly depends on the polymer relaxation time and shear rates in porous media. Several factors were found to affect the elasticity of polymers and oil recovery. Polymer concentration, reservoir permeability and heterogeneity, oil viscosity, injection rate, brine salinity, and well pattern size were the main variables affecting the Deborah number and oil recovery.

Nevertheless, Azad and Trivedi (2020) reported that the previous model has limitations in predicting the residual oil saturation for low- and high-salinity polymer flooding. It was related to the oscillatory Deborah number that overestimates the elastic effects for low-salinity and underestimates that for high-salinity solutions. As a solution, they proposed a new model based on the extensional properties of viscoelastic polymers. As extensional resistance increases with solution salinity, the residual saturations predicted by the Azad and Trivedi (2020) model were

closer to actual values for the solutions with various salinities. The authors correlated an extensional capillary number with residual oil saturation, as follows:

$$S_{or} = \begin{cases} -0.009 * \ln(N_{ce}) + 0.3348 & \text{if } N_{ce} < N_{crt} \\ 0.287 * \exp(-3.42 * N_{ce}) & \text{if } N_{ce} > N_{crt} \end{cases}, \quad (2.34)$$

$$N_{ce} = \frac{V * \mu_{pore}}{\sigma}, \quad (2.35)$$

where N_{ce} is the extensional capillary number, N_{crt} is the critical capillary number, V is the interstitial velocity, σ is the interfacial tension between displaced and displacing slugs, and μ_{pore} is the pore-apparent viscosity that is calculated using extensional parameters. The authors stated that their model provides more reliable predictions of residual oil saturation and captures the increase in oil recovery at higher salinities. Nevertheless, the extensional parameters (μ_{max} , τ_r , n_2), measured using an extensional rheometer, result in significantly large pore-apparent viscosities. In particular, the viscosities reported in the study vary between 1,000-500,000 cP in the cases where viscoelastic polymers were used, which looks pretty unrealistic for the field applications.

2.7.4 Relative Permeability Models

Relative permeabilities strongly depend on phase saturations and frequently curve fitted using the Brooks-Corey model, defined below (Brooks and Corey, 1964):

$$k_{rw}(S_w) = k_{rw}^* \left(\frac{S_w - S_{wir}}{1 - S_{wir} - S_{or}} \right)^{n_w}, \quad (2.36)$$

$$k_{ro}(S_w) = k_{ro}^* \left(\frac{1 - S_w - S_{or}}{1 - S_{wir} - S_{or}} \right)^{n_o}, \quad (2.37)$$

where k_{rw} and k_{ro} are the aqueous and oleic phase relative permeabilities, respectively; S_{wir} is

the irreducible water saturation, S_{or} is the residual oil saturation, k_{rw}^* is the Corey's endpoint aqueous phase relative permeability, k_{ro}^* is the Corey's endpoint oleic phase relative permeability, and n_w and n_o are the Corey's exponents for water and oil, respectively.

The phase (p) endpoint relative permeabilities strongly depend on the rock wettability and residual saturation of another phase (p') if the two-phase flow is considered. Generally, endpoint relative permeabilities increase with the trapping number and may be estimated using the following expression (Delshad *et al.*, 1986):

$$k_{rp}^* = (k_{rp}^*)^{low} + \frac{S_{prr}^{low} - S_{prr}}{S_{prr}^{low} - S_{prr}^{high}} \left[(k_{rp}^*)^{high} - (k_{rp}^*)^{low} \right], \quad (2.38)$$

where $(k_{rp}^*)^{low}$ and $(k_{rp}^*)^{high}$ are the phase endpoint relative permeabilities at low and high trapping numbers, respectively. Similarly, Corey's exponents can be calculated:

$$n_p = (n_p)^{low} + \frac{S_{prr}^{low} - S_{prr}}{S_{prr}^{low} - S_{prr}^{high}} \left[(n_p)^{high} - (n_p)^{low} \right], \quad (2.39)$$

where $(n_p)^{low}$ and $(n_p)^{high}$ are the phase Corey's exponents at low and high trapping numbers, respectively.

2.8 Mechanical Degradation of Viscoelastic Polymers

As stated in previous chapters, viscoelastic polymers can substantially improve both macroscopic and microscopic recovery efficiencies by sweeping bypassed oil and mobilizing residual oil, respectively. However, mechanical degradation may significantly reduce viscoelastic polymer efficiency. Mechanical degradation leads to the breakage of the polymer backbone in the high flow rate regions due to significant stresses exerted on a solution and results in considerable viscosity

loss. This process usually takes place in polymer handling equipment, pumps, chokes, and perforations. However, the polymers may also be irreversibly degraded in the porous medium, particularly in the wellbore vicinity associated with high shear rates (Sorbie, 1991). During mechanical degradation, chain scission causes higher molecular weight polymer components to break into smaller ones altering MWD and reducing the viscosifying power of polymer solution (Sorbie, 1991; Azad and Trivedi, 2019). There are different methods to evaluate mechanical degradation. Comparing the solution viscosities may provide a rough estimation of degradation. However, considering only viscosity loss may not be accurate since mechanical degradation usually lowers the resistance factor significantly than reduces viscosity (Seright, 1983). Other methods frequently used to quantify mechanical degradation are Millipore filter ratio and screen factor methods (Sheng, 2011). Screen factor refers to the ratio of times for fixed volume of polymer solution and brine to flow through a stack of five 100-mesh screens. However, it is essential to note that the degree of mechanical degradation observed in the field may be less than the one predicted experimentally using core plugs (Martin, 1986). Experiments in the lab assume the polymer flows directly into the rock matrix. On the other hand, the actual wellbore may be stimulated, so the permeability in the near-wellbore region may be much greater than the matrix permeability leading to reduced mechanical degradation observed in the field.

Furthermore, most of the biopolymers having rigid rod structures are shear-stable resisting shear degradation. At the same time, synthetic viscoelastic polymers are pretty susceptible to shearing, and their viscosities may be considerably reduced if mechanical degradation occurs (Diab and Al-Shalabi, 2019). It is related to the flexible coil structure of synthetic polymers that leads to dilatant behavior at high flow rates. As a result, ultimate elongational stresses are exerted on a polymer molecule, stretching it apart. Beyond the critical flow rate, the elongational stresses prevail macromolecular covalent bonding forces and result in polymer breakdown (Odell and Keller, 1986).

The degree of mechanical degradation in porous media primarily depends on several factors, including formation permeability, injection rate, polymer molecular weight, brine salinity, and hardness. The degradation effect becomes more pronounced in tight formations with lower permeabilities; larger stresses are exerted on the polymer solution flowing through narrower pore throats, leading to severe degradation and pore plugging. Similarly, polymer molecular weight

exacerbates mechanical degradation. In other words, polymers with higher M_w are more likely to be degraded than smaller molecular weight polymers due to higher flow resistance and larger mechanical stresses (Taylor and Nasr-El-Din, 1995). Furthermore, Maerker (1975) and Martin (1986) reported that brine salinity and hardness also negatively affect the process. They mentioned that it is possible to mitigate the polymer degradation by diluting or softening the injection brine.

Mechanical degradation poses severe economic constraints on the polymer flooding application and may lead to project failure, especially in low-permeable and heterogeneous carbonates (Manrique *et al.*, 2017). Proper designing and equipping an injection well with special flowmeters, tubings, and pumps may reduce the degradation before polymers flow into the porous media (Sheng *et al.*, 2015). Moreover, increasing polymer concentration may compensate for the viscosity loss if little mechanical degradation is observed in the wellbore interface. However, supplementary techniques must be applied to tackle more severe mechanical degradation cases (Martin, 1986). Namely, injecting polymer solution using horizontal wells (to expand sand-face area), increasing the number of perforations in cased hole completions, fracturing near-wellbore region by injecting above the formation parting pressure, and pre-shearing the polymer solution before the injection is initiated are the main methods to mitigate mechanical degradation (Maerker, 1975; Manrique *et al.*, 2017). Polymer pre-shearing before injection refers to stirring a polymer solution to eliminate longer chain polymer components while keeping similar mean MWD. It is reported that the pre-sheared higher molecular weight polymer solution may maintain its original viscosity better than the lower molecular weight commercial polymer solution (Jouenne *et al.*, 2018). Being more tolerant to mechanical degradation, the pre-sheared polymers may exhibit enhanced injectivity and obtain optimum mobility reduction (Diab and Al-Shalabi, 2019).

2.9 Injectivity of Viscoelastic Polymers

As was discussed before, the main objective of polymers used during tertiary oil recovery is to maintain mobility and conformance control by increasing the aqueous phase viscosity and decreasing its effective permeability. Viscoelastic polymers exhibit shear-thickening behavior in high shear rate regions near the injection well. The dilatancy observed during a viscoelastic flow dramatically increases the polymer solution viscosity, enhancing the sweep and possibly displacement efficiencies. Nevertheless, the drastic pressure build-up in the near-wellbore region

associated with the viscoelastic flow and mechanical degradation significantly limits polymer injectivity. Well injectivity defines the ease of fluid injection into the reservoir and is calculated using the following equation (Seright, 1983):

$$I_p = \frac{q}{\Delta P}, \quad (2.40)$$

where q is the injection flow rate and ΔP is the injection pressure drop.

Injectivity is one of the main concerns for successful polymer flooding applications, so ideally, the polymer solution needs to have improved injectivity and preserve the desired solution viscosity at the same time (Kumar *et al.*, 2012). Poor injectivity during viscoelastic polymer flooding may have undesirable effects, such as slow flood-front, voidage problems, and delayed oil production from flooded patterns (Seright *et al.*, 2009; Azad and Trivedi, 2019). Therefore, it is desirable to avoid excessive shear-thickening near wellbore to achieve adequate injectivity and save polymers from mechanical degradation. As a solution, pre-shearing the polymers before injection reduces their elastic properties and shifts the onset for dilatant behavior to comparatively higher flow rates (Al-Shakry *et al.*, 2018).

Furthermore, injecting the viscoelastic polymers at high rates causes the injection pressures to rise and surpass formation parting pressures resulting in induced fractures around the wellbore. Creating the fractures during polymer injection may have a double effect on polymer flooding. Firstly, it may result in fluid channeling and negatively impact the polymer sweep and displacement efficiencies if the fracture growth is not controlled (Azad and Trivedi, 2019). However, the fracturing may also positively affect the process since inducing short fractures extending only 5-15 m from the wellbore may improve injectivity and prevent polymer mechanical degradation (Martin, 1986; Manichand *et al.*, 2013; Al-Shakry *et al.*, 2018).

2.10 Polymer Flooding Field Applications

Polymer flooding is the most frequently used chemical EOR technique in terms of the number of field projects (Alvarado and Manrique, 2010). The technique may lead to satisfactory incremental

oil recovery at a low cost and for wider reservoir conditions. The incremental oil recovery from the polymer flooding project strongly depends on the mobility contrast of aqueous and oleic phases, detailed slug size, permeability distribution, and other factors. Frequently, a higher amount of injected polymers yields larger incremental oil recovery for a specific project. The amount of injected polymers refers to injected polymer slug size (in PV) multiplied by the polymer concentration (in ppm). However, it was found that the incremental oil recovery becomes less sensitive to the amount of injected polymer after exceeding the threshold value of around 400 ppm·PV (Sheng *et al.*, 2015).

On the other hand, polymer molecular weight is another factor that substantially affects a polymer flooding project. Using polymers of higher M_w generally results in better viscosifying power, higher permeability reduction, and eventually higher oil recovery. However, polymer molecular weight should be carefully selected for the formation of interest, having particular rock permeability and pore-throat size. It is accepted that pore plugging would not occur if the gyration radius of the polymer molecule is five times smaller than the median size of pore space (Wang *et al.*, 1998). Generally, the radius of gyration is used to estimate the polymer chain dimensions, and it is defined as follows (Fixman, 1961):

$$R = \sqrt{\left(\frac{1}{N}\right) \sum_{i=1}^N r_i^2}, \quad (2.41)$$

where R is the gyration radius of polymer with N beads, and r_i is the distance from the i^{th} bead to the mass center.

Generally, polymer flooding is more applicable in slightly heterogeneous formations with low or medium viscosity crudes. Additionally, polymer injection may also be applied in the thin heavy-oil reservoir, where thermal recovery will be uneconomical due to heat losses. However, it is worth mentioning that there are few limitations of polymer flooding application in such reservoirs. Namely, it is impractical to obtain the mobility ratio of unity by injecting highly viscous polymer solutions in the field since it causes critical injectivity issues and increases the project

cost. For this purpose, horizontal injectors may be used to improve injectivity. However, it is preferred to keep the polymer solution viscosity below 100 cP regardless of the oil viscosity (Sheng *et al.*, 2015).

Many commercial polymer flooding projects have been carried out in China, yielding an average incremental oil recovery of about 8.9% (Sheng, 2013). The first extensive commercial polymer flooding application was implemented in Daqing Oil Field, and it remains the largest polymer application in the world heretofore. In this chapter, we collected and reported several field applications of synthetic polymer flooding and summarized them in **Table 2.1**. A more comprehensive review on polymer flooding field applications may be found elsewhere (Sheng, 2013, Guo *et al.*, 2020).

Table 2.1: Summary of synthetic polymer flooding field applications.

Field	Rock and Fluid Properties					Polymer Properties			IOR (%)	References
	Rock Type	\bar{k} (mD)	\bar{T} (°C)	Oil Viscosity In-situ (cP)	Connate Salinity (ppm)	C_p (ppm)	Solution Viscosity In-situ (cP)	Solution Salinity (ppm)		
West Coyote (USA)	Sandstone	450	57	8	12,000	2,000	10-35	12,000	17	Shuler <i>et al.</i> (1987)
Eliasville Caddo (USA)	Limestone	11	46	3	165,000	630-1,500	5-35	1,200	4.2	Weiss (1992)
Daqing (China)	Sandstone	454	45	10	8,217.5	1,750-2,250	47.4	5,328	20	Wang <i>et al.</i> (2000b), Guo <i>et al.</i> (2020)
Marmul (Oman)	Sandstone	8,000-25,000	46	90	7,404	1,000	15	600	59 (total)	Sheng (2013)
Xiaermen (China)	Fault-Block Sandstone	4,780	50	70	2,127	600-1,200	12-16.5	2,127	10	Sheng (2013)

East Bodo (Canada)	Sandstone	1,000	50	1300	25,000- 29,000	1,500	60	3,700	N. A.	Sheng (2013)
Dalia (Angola)	Sandstone	>1,000	50	1-10	120,000	900	3-6	52,000	7	Morel <i>et al.</i> (2015)
Tambaredjo (Suriname)	Sandstone	4,000	38	400	2,500- 5,000	1,000	50	400-500	11	Delamaide <i>et al.</i> (2016)
Mangala (India)	Sandstone	200- 20,000	65	15	N. A.	500- 2,000	2.5-30	5,267	7	Mehta <i>et al.</i> (2016)
Shengli (China)	Sandstone	1,800	71	46.3	5,923	1,500	20.5	5,727	20.6	Guo <i>et al.</i> (2020)
Xinjiang (China)	Conglomerate	189	34.3	5.13	28,868	1,000- 1,200	>60	7,031	12.1	Guo <i>et al.</i> (2020)

According to **Table 2.1**, most polymer flooding field applications have been implemented in sandstone reservoirs under mild temperature conditions where polymer injection yielded around 10% average incremental oil recovery. One of the very few examples of field-scale polymer flooding implementation in carbonates is the polymer injection project in Eliasville Caddo Unit, where commercial polymer flooding started at the end of 1980. Laboratory and field testing were conducted to specify the polymer that would not plug this tight limestone rock. Biopolymers were eliminated due to biological degradation concerns. It was established that 1500 ppm of the HPAM polymer dissolved in the makeup water with TDS of 2000 ppm would produce 20 cP non-plugging fluid. This viscosity was also conceivable using higher molecular weight polymers at a lower concentration. However, it was preferred to inject lower M_w polymers to avoid severe plugging in this low permeable rock (11 mD). Moreover, an emulsion polymer was selected for the field-scale application based on handling simplicity, availability, and performance. The polymer was injected in 4 stages over three years. First, 0.038 PVs slug with the surface viscosity of 40 cP was injected, followed by 0.048 PVs slug at 20 cP. At the next stage, the viscosity was reduced to 15 cP and injected for an additional 0.028 PVs. Finally, 5 cP polymer solution was used at the last stage for

0.015 PVs, followed by freshwater injection. On the other hand, in-situ polymer solution viscosity was 70-90% lower than the surface viscosity (Weiss and Baldwin, 1985). Mild temperature conditions in this carbonate reservoir as well as proper polymer solution design resulted in 4.2% OOIP or 0.46 barrels of incremental oil per pound of polymer (Weiss, 1992).

Moreover, in all reported cases, the polymer viscosity was not exceeding 100 cP due to injectivity considerations. In particular, the injected polymer solution viscosity was around 60 cP even in heavy-oil East Bodo and Tambaredjo oil fields with in-situ oil viscosity of 1300 and 600 cP, respectively.

Limitations in polymer flooding applications in carbonates are related to the complex features and harsh conditions of high temperature and high salinity existing in this reservoir type. The highly heterogeneous reservoirs with harsh conditions may result in relatively poor efficiency of polymer flooding projects. The latter is related to injection fluid channeling through natural fractures and polymer degradation under harsh conditions. Therefore, there are almost no successful polymer field applications reported in carbonates with harsh carbonates (Rachapudi *et al.*, 2020). However, recently, new polymers have been developed to overcome the harsh conditions in these reservoirs. As was previously discussed, the novel polymers incorporate several monomers, such as N-vinylpyrrolidone (NVP), 2-Acrylamido-2-Methylpropane-Sulfonate (AMPS), and Sodium Acrylamido Tertiobutyl Sulfonate (ATBS) that protect the polymer from thermal and chemical degradations.

Recently, ATBS-rich polymers were utilized for a polymer flooding project in a carbonate reservoir located in Abu Dhabi. Rachapudi *et al.* (2020) reported that a novel polymer injectivity test was started in 2018 and continued for five months. As a result of single-well injectivity test, 150,000 barrels of the polymer solution were injected into the reservoir with success. As reported, the next stage in carbonate field application is a multi-well pilot test for five consecutive years by simultaneously injecting water and polymer. Finally, the field derisking strategy will be finalized by a full-field implementation. Furthermore, the authors mentioned that the single-well injectivity test showed good performance of novel polymers in terms of injectivity and viscosity at a target concentration and rate. Additionally, the study described candidate well selection for the injectivity test, included detailed information regarding the injection skid and design, investigated polymer solution quality management, and the operational difficulties encountered during the pilot.

CHAPTER 3: COMPREHENSIVE CORRELATION FOR PREDICTING POLYMER APPARENT VISCOSITY IN POROUS MEDIA

As discussed in Section 2.6, there are several analytical models used to predict aqueous phase apparent viscosity during polymer flooding. However, most of the proposed models either require extensive coreflooding data to predict the model parameters or cannot comprehensively characterize polymer behavior in porous media. Therefore, a new model is proposed, called Extended Unified Apparent Viscosity Model (E-UVM), which captures all four regimes observed during viscoelastic polymer flooding, including Newtonian, shear-thinning, shear-thickening, and mechanical degradation regimes. Additionally, the model fitting parameters are correlated with the rock and polymer properties. These correlations reduce the number of model parameters as well as the need for extensive coreflooding tests and hence, accelerate polymer screening for future studies and field applications.

3.1 Development of Extended Unified Apparent Viscosity Model

As the name indicates, the Extended Unified Apparent Viscosity Model (E-UVM) is based on the UVM published earlier (Delshad *et al.*, 2008). E-UVM is comprised of different sections attributed to the specific rheological regimes. Particularly, the Newtonian and shear-thinning regimes observed at low shear rates are captured using the Carreau model (**Equation 2.14**), while the shear-thickening behavior of viscoelastic polymers usually observed near the wellbores is modeled by relating elastic viscosity to the Deborah number (**Equation 2.17**). Although the original UVM provides the plateau value of μ_{max} , it cannot characterize the drop in apparent viscosity due to mechanical degradation at ultimate shear rates. Nevertheless, it is essential to consider the mechanical degradation regime in the viscoelastic models since it may significantly impact polymer injectivity and oil recovery. Therefore, a degradation multiplier (DM) is added in E-UVM to capture the reduction in polymer apparent viscosity beyond critical shear rates. It was found that the multiplier strongly depends on permeability and polymer properties. The Extended Unified Apparent Viscosity Model (E-UVM) is shown below (**Equation 3.1**):

$$\mu_{app} = (\mu_{shear} + \mu_{elastic}) * DM , \quad (3.1)$$

$$\mu_{shear} = \mu_{\infty} + (\mu_0 - \mu_{\infty}) \cdot (1 + (\lambda_1 \dot{\gamma})^2)^{\frac{n_1-1}{2}}, \quad (3.2)$$

$$\mu_{elastic} = \mu_{max} [1 - \exp(-(0.01 * \tau_r \dot{\gamma})^{n_2-1})], \quad (3.3)$$

$$DM = (1 + (\lambda_3 \dot{\gamma})^2)^{\frac{-n_3}{2}}, \quad (3.4)$$

where μ_{app} is the polymer solution apparent viscosity, μ_0 and μ_{∞} are the zero-shear rate and infinite-shear rate viscosities, respectively. n_1 is the shear-thinning index, λ_1 is the time constant that represents a transition between zero-shear Newtonian and pseudoplastic regions, μ_{max} is the maximum elongational viscosity, λ_2 is the universal constant that is usually taken as 0.01, τ_r is the relaxation time, n_2 is the shear-thickening (or strain hardening) index, λ_3 is the mechanical degradation constant that is usually in the range 10^{-5} - 10^{-3} , and n_3 is the mechanical degradation index. The effective shear rate, $\dot{\gamma}$, is calculated using **Equation 2.9**.

3.2 Validation of Extended Unified Apparent Viscosity Model

3.2.1 List of Experimental Coreflooding Data

Several experimental coreflooding test results reported in the literature were extracted and used to validate our model. The experimental conditions for each study are listed in **Table 3.1**. The latter table summarizes the experimental data including polymer molecular weight (M_w) and concentration (C_p), aqueous solution salinity (S) as well as core permeability (k) and porosity used during coreflooding tests. Moreover, polymer and rock types are also indicated in this table. One should note that N.A. is used for the cases where data is not applicable or not available.

Table 3.1: Summary of experimental data from the literature used to validate E-UVM

Nº	References	Polymer Type	M_w (MDa)	C_p (g/L)	S (g/L)	Core Type	k (Darcy)	Porosity
1	Delshad <i>et al.</i> (2008)	Flopaam 3630S	20	1.5	20	Berea	N.A.	N.A.

2	Stavland (2010)		HPAM	20	1.5	35	Berea	0.361	0.22
3	Asen <i>et al.</i> (2019)		HPAM	20	1	38.81	Bentheimer	2.17	0.21
4	Brakstad and Rosenkilde (2016)		AMPS	20	1	103.3	Bentheimer	1.26	0.23
5	Southwick and Manke (1988)	Exp1	HPAM	20	0.5	20	Glass Bead Pack	0.048	0.25
6		Exp2						0.022	
7	Masalmeh <i>et al.</i> (2019)	C-2	SAV10	8	1	180	Reservoir Carbonate Core	1.616	0.26
8		C-6						0.121	
9	Seright <i>et al.</i> (2009)	Exp1	Flopaam 3830S	20	1	3	Berea	0.573	0.21
10		Exp2	Flopaam 3830S	20		41.95		0.573	
11		Exp3	Xanthan K9D236	2		41.95		0.551	
12	Lohne <i>et al.</i> (2017)	Exp1	HPAM 3530S	15	1.5	38.88	Berea	0.1613	0.177
13		Exp2						2.0188	0.235
14	Manichand <i>et al.</i> (2013)	Exp 1	Flopaam 3630S	18	1	0.5	Reservoir Sandstone Core	4	0.3
15		Exp 2			1.35				
16	Magbagbeola (2008)	BV1	Flopaam 3630S	20	1.5	20.04	Berea	0.647	0.23
17		BV2	AN-125	8				0.578	

3.2.2 Validation of the Model Against Coreflooding Data

The proposed E-UVM was validated by matching the coreflooding test results. Original Unified Apparent Viscosity Model (UVM) was also fitted to the experimental data to highlight the

improvement in polymer rheological behavior prediction using the E-UVM. **Figures 3.1-3.17** show the mechanical degradation occurring at ultimate shear rates and corresponding viscosity reduction are well captured by the Extended Unified Viscoelastic Model. The apparent viscosities indicated in the figures were measured during coreflood experiments. Moreover, the bulk viscosities, if available, were obtained from the bulk rheology tests conducted in corresponding studies.

It is worth mentioning that Experiments № 1, 16, and 17 were conducted at low and moderate shear rates where mechanical degradation was not observed. Therefore, for these experiments, the fitting parameters for the degradation regime were assumed based on the rock and fluid properties. Moreover, Experiment № 11 was conducted using xanthan polymer that does not exhibit shear-thickening and mechanical degradation in porous media. UVM and E-UVM models can predict the rheological behavior of the biopolymer by simply setting some of the fitting parameters to zero. As shown in **Figure 3.11**, both models are in a match since there was no dilatancy or mechanical degradation observed.

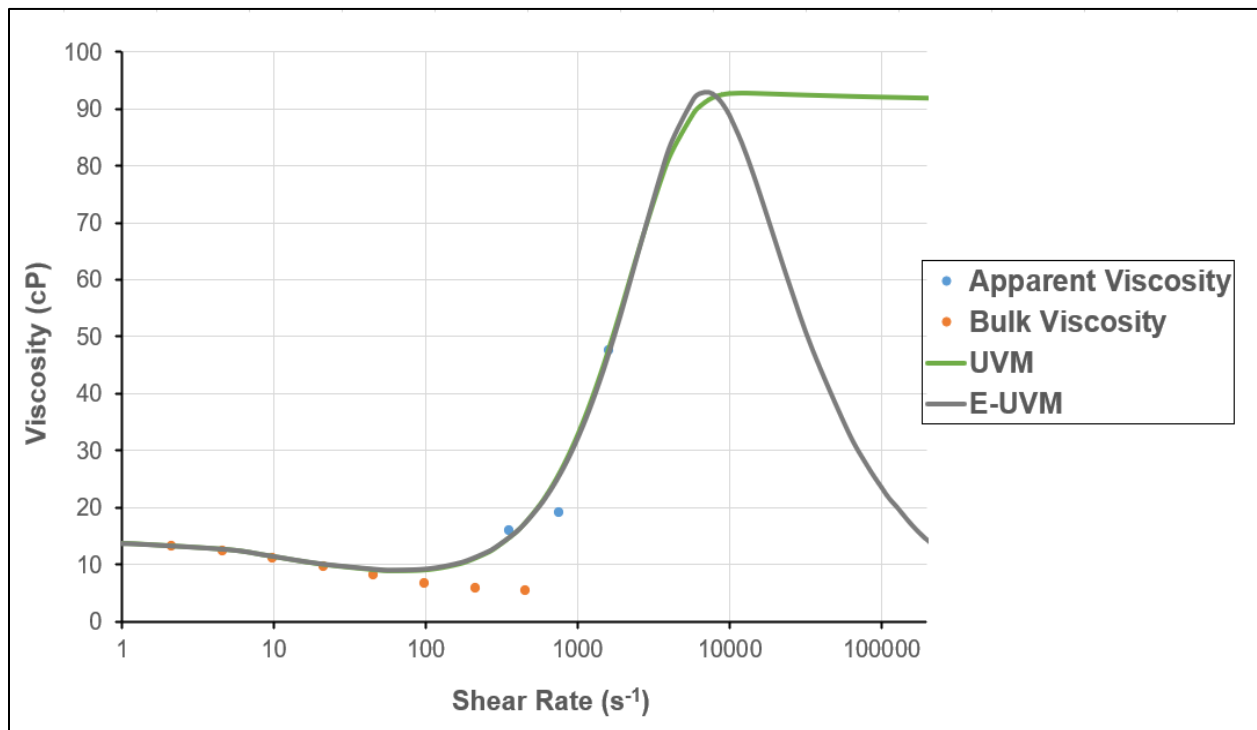


Figure 3.1: Fitting the models to Experiment № 1 data (1.5 g/L-20 MDa-HPAM at 20 g/L TDS, Berea Sandstone Core).

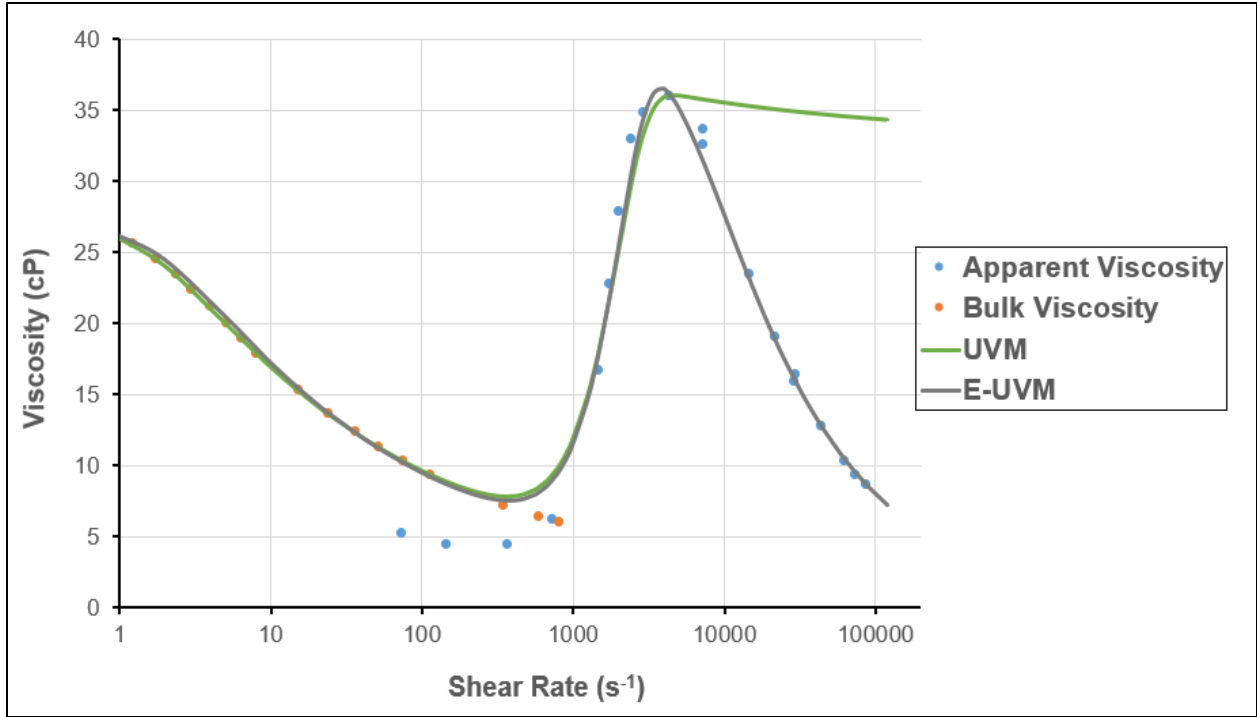


Figure 3.2: Fitting the models to Experiment № 2 data (1.5 g/L-20 MDa-HPAM at 35 g/L TDS, 0.361 D Berea Sandstone Core).

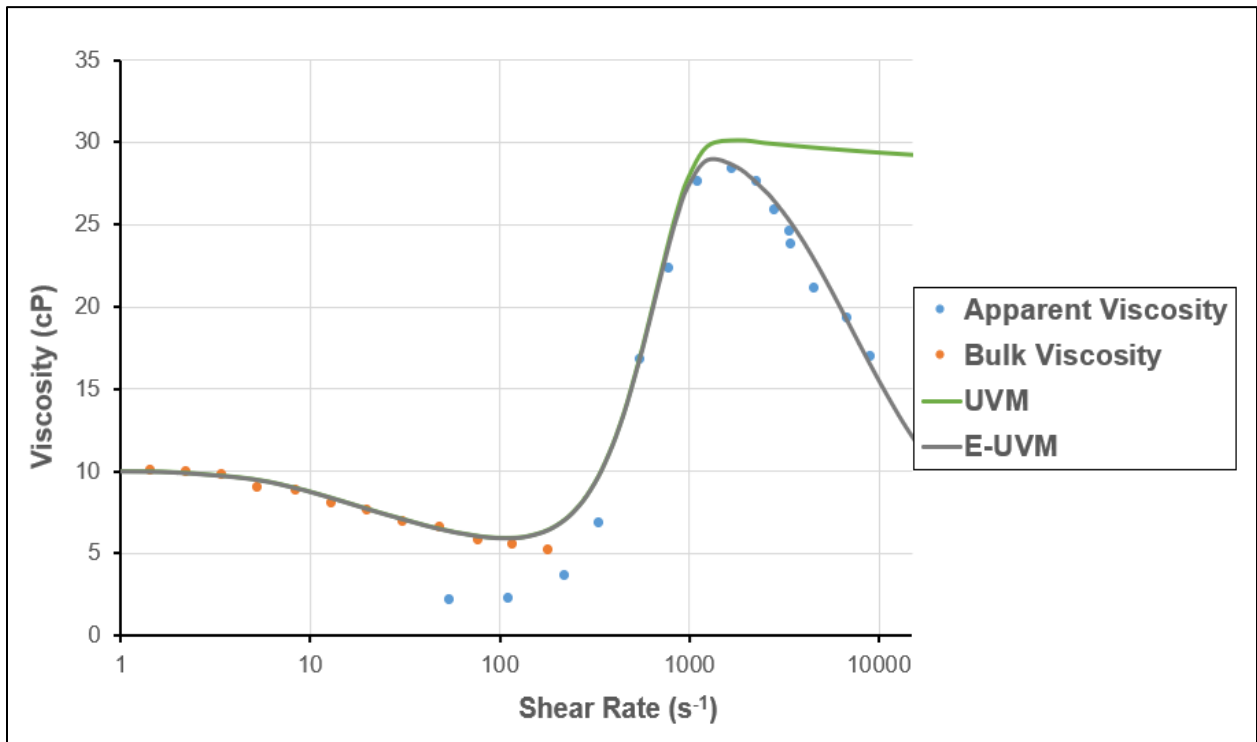


Figure 3.3: Fitting the models to Experiment № 3 data (1 g/L-20 MDa-HPAM at 38.81 g/L TDS, 2.17 D Bentheimer Sandstone Core).

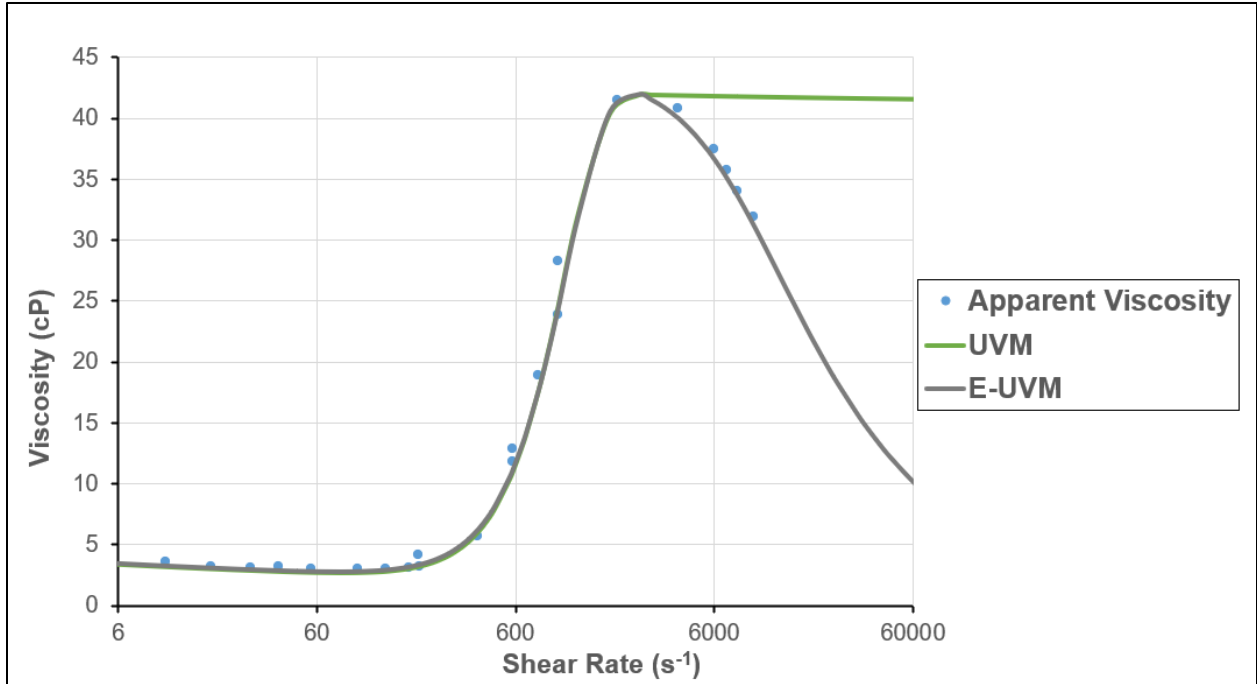


Figure 3.4: Fitting the models to Experiment № 4 data (1 g/L-20 MDa-AMPS at 103.3 g/L TDS, 1.26 D Bentheimer Sandstone Core).

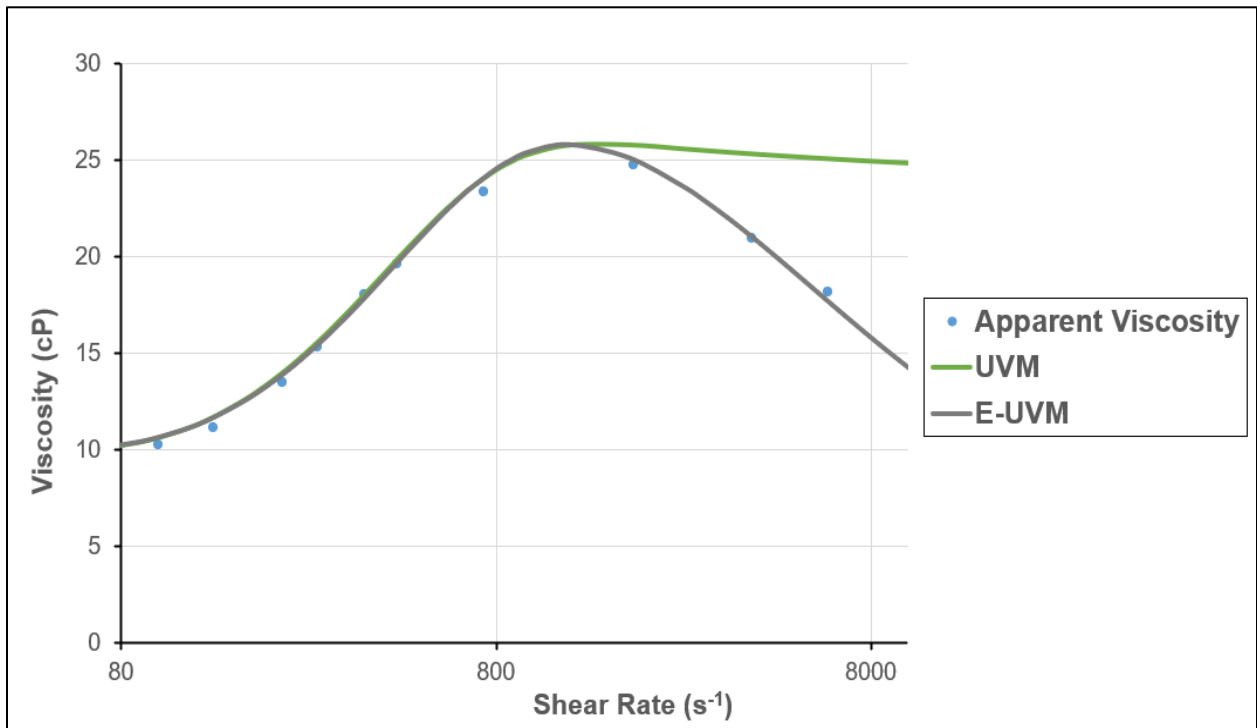


Figure 3.5: Fitting the models to Experiment № 5 data (0.5 g/L-20 MDa-HPAM at 20 g/L TDS, 0.048 D Glass Bead Pack).

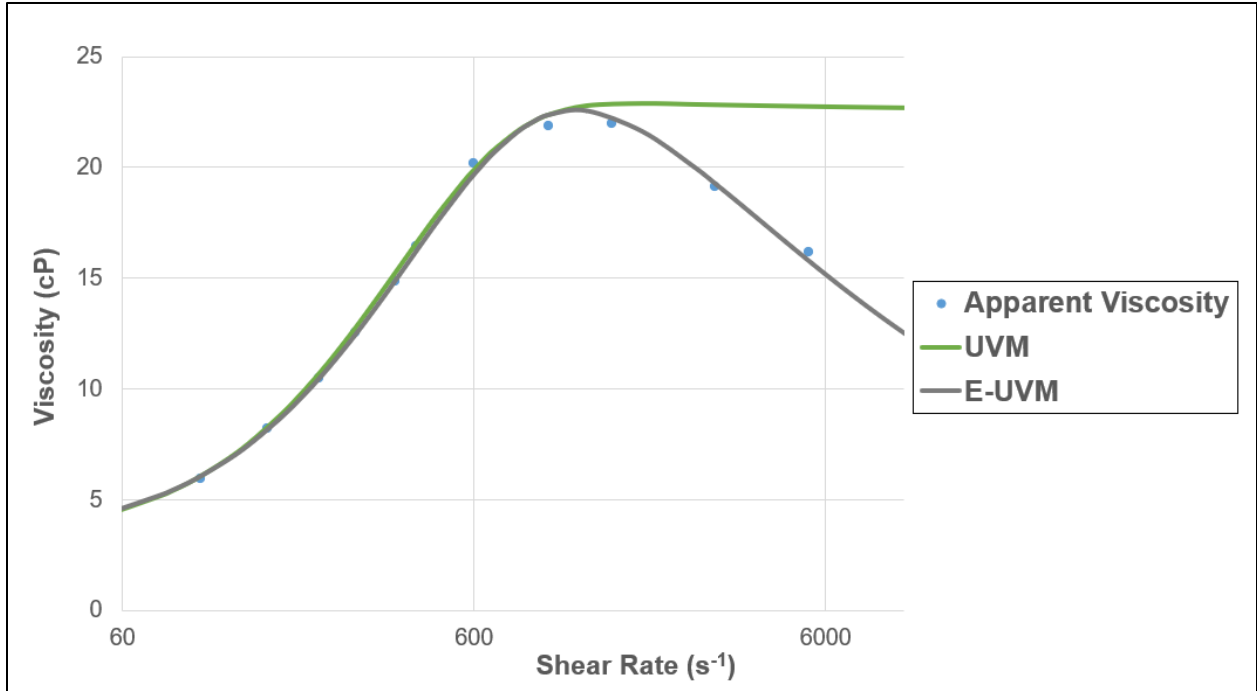


Figure 3.6: Fitting the models to Experiment № 6 data (0.5 g/L-20 MDa-HPAM at 20 g/L TDS, 0.022 D Glass Bead Pack).

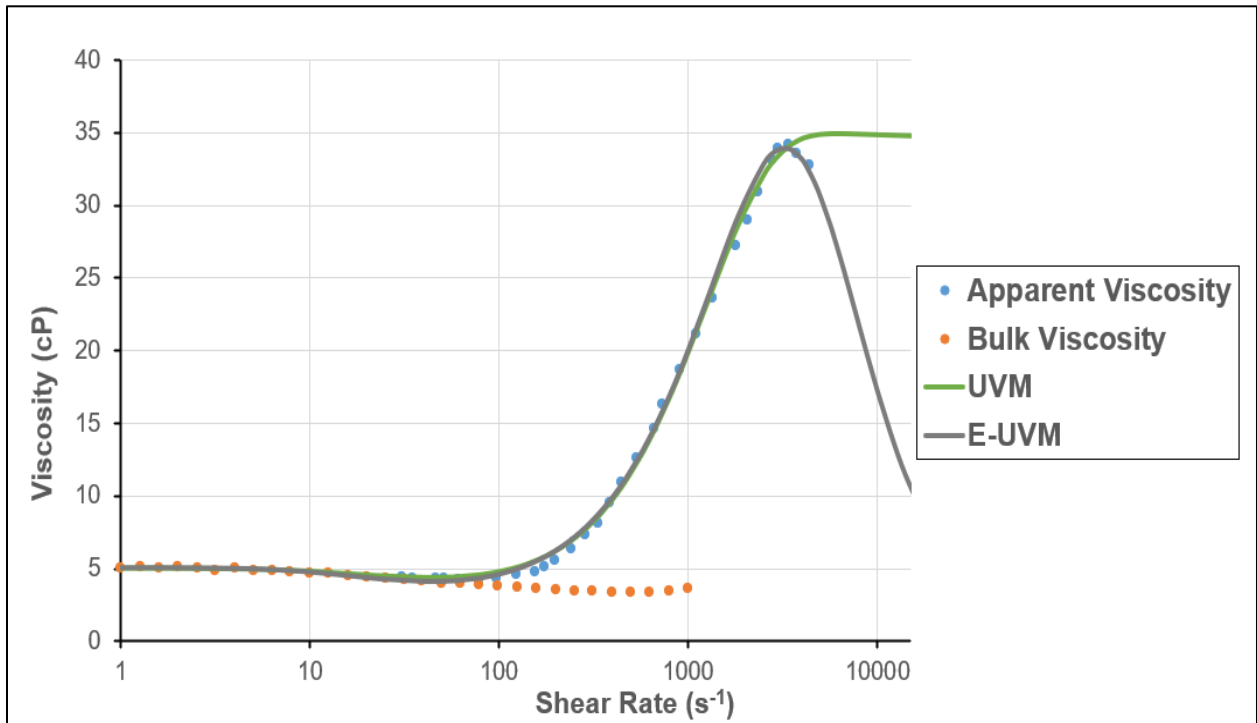


Figure 3.7: Fitting the models to Experiment № 7 data (1 g/L-8 MDa-SAV10 at 180 g/L TDS, 1.616 D Reservoir Carbonate Core).

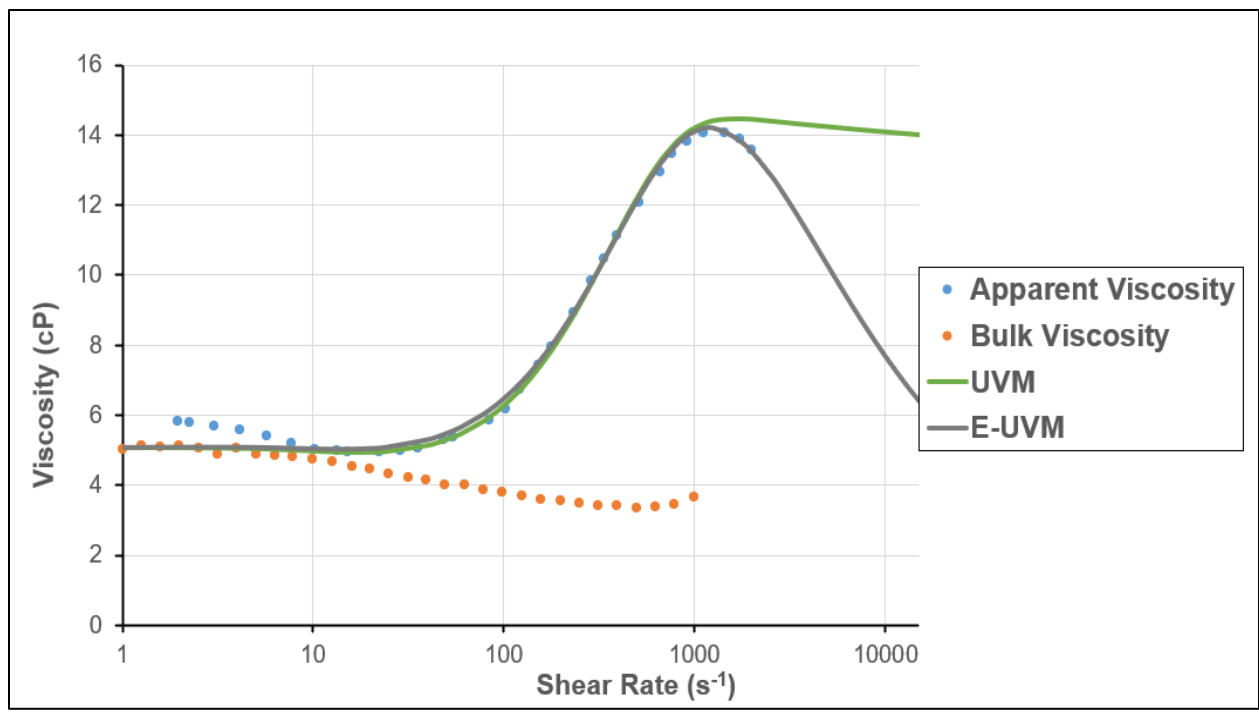


Figure 3.8: Fitting the models to Experiment № 8 data (1 g/L-8 MDa-SAV10 at 180 g/L TDS, 0.121 D Reservoir Carbonate Core).

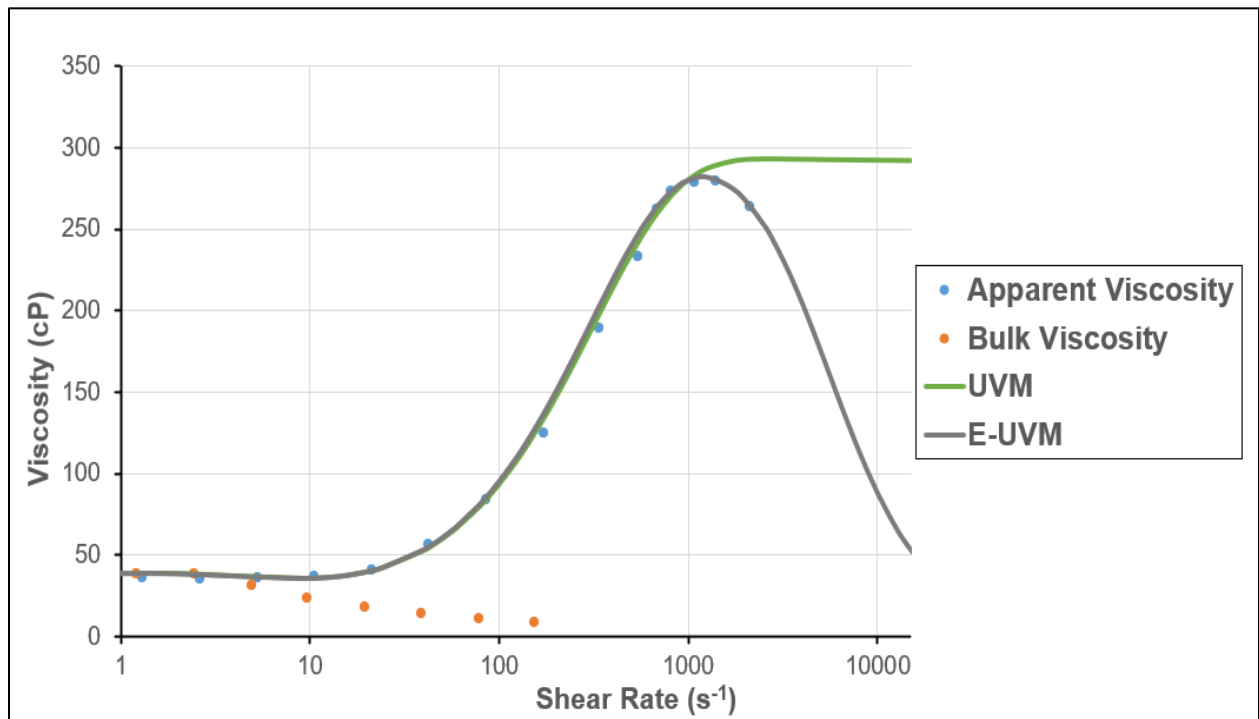


Figure 3.9: Fitting the models to Experiment № 9 data (1 g/L-20 MDa- Flopaam 3830S at 3 g/L TDS, 0.573 D Berea Sandstone Core).

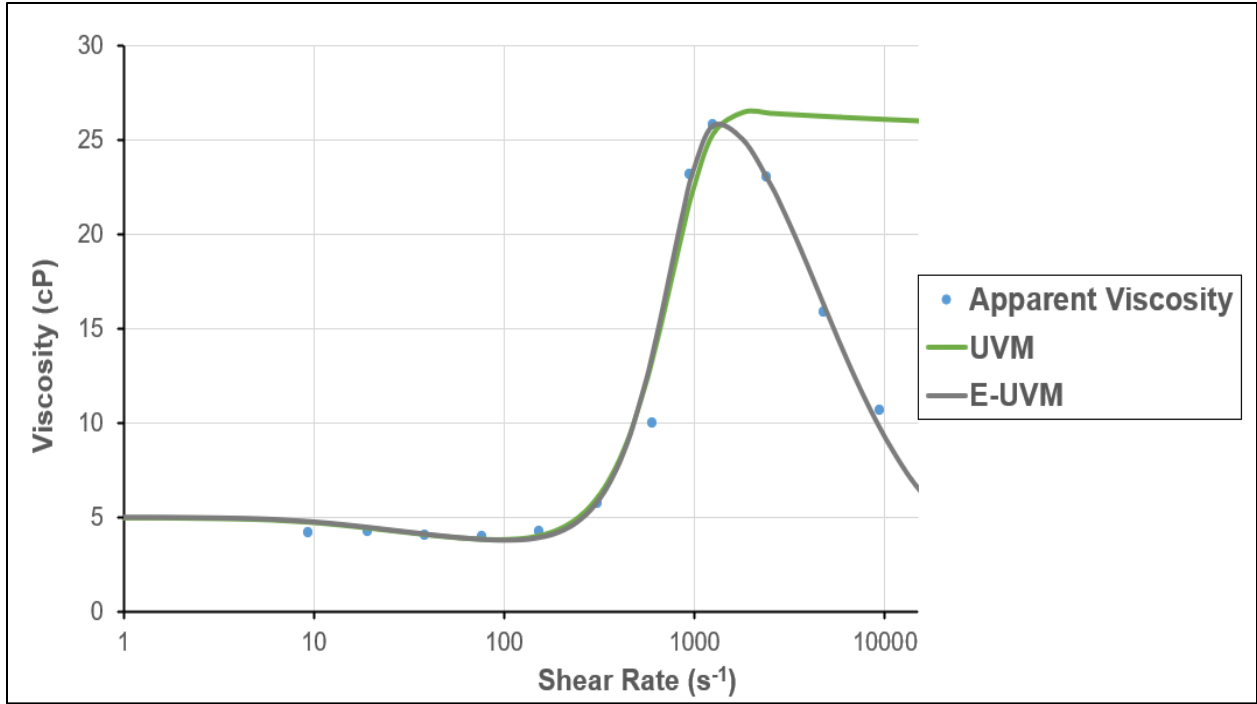


Figure 3.10: Fitting the models to Experiment № 10 data (1 g/L-20 MDa- Flopaam 3830S at 41.95 g/L TDS, 0.573 D Berea Sandstone Core).

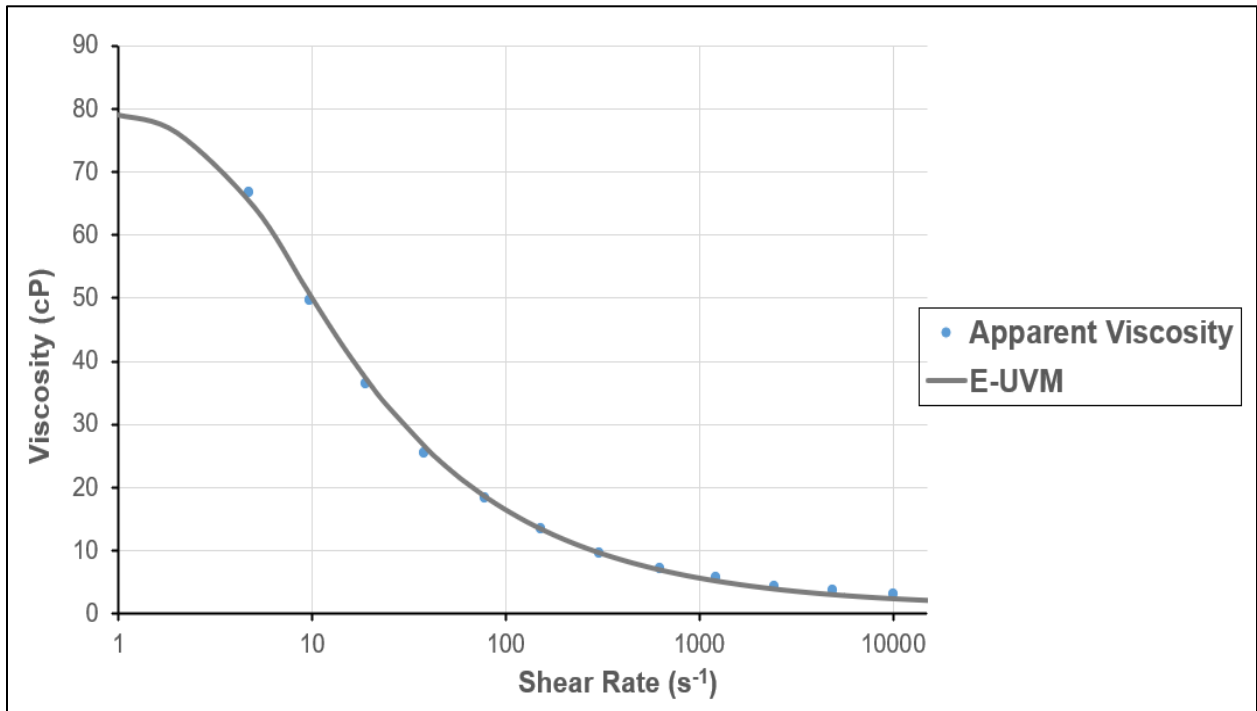


Figure 3.11: Fitting the models to Experiment № 11 data (1 g/L-2 MDa- Xanthan K9D236 at 41.95 g/L TDS, 0.551 D Berea Sandstone Core).

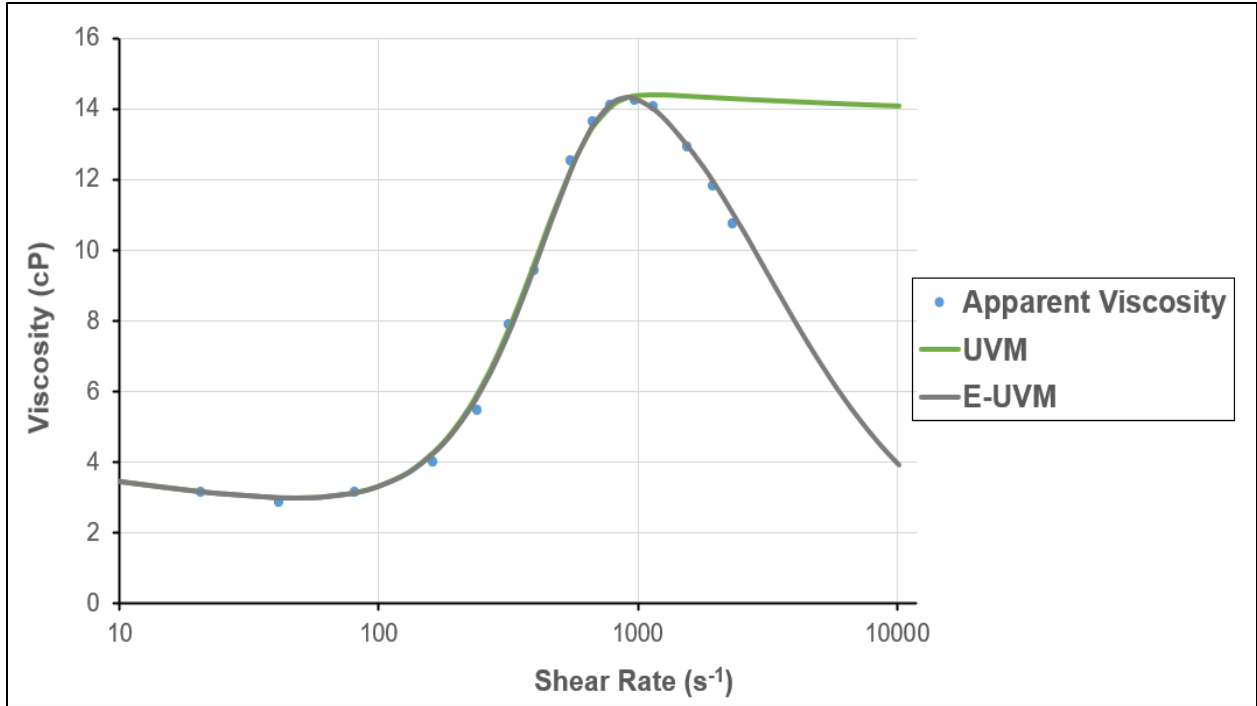


Figure 3.12: Fitting the models to Experiment № 12 data (1.5 g/L-15 MDa- HPAM 3530S at 38.88 g/L TDS, 0.1613 D Berea Sandstone Core).

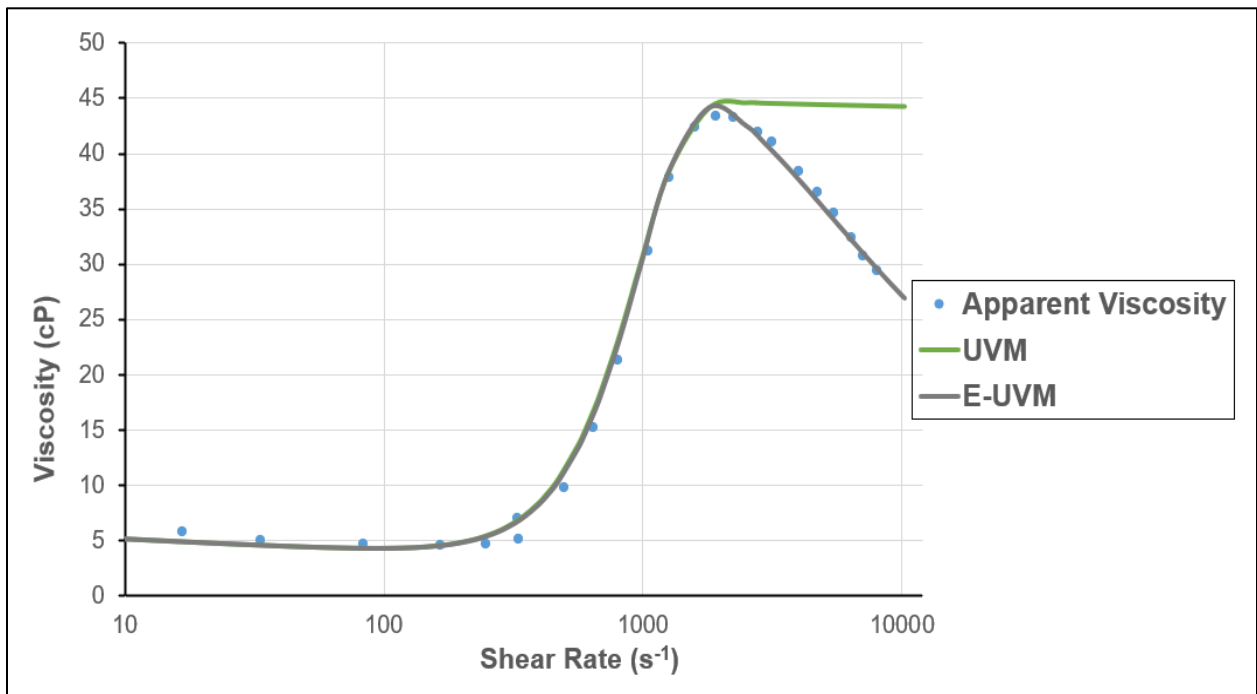


Figure 3.13: Fitting the models to Experiment № 13 data (1.5 g/L-15 MDa- HPAM 3530S at 38.88 g/L TDS, 2.0188 D Berea Sandstone Core).

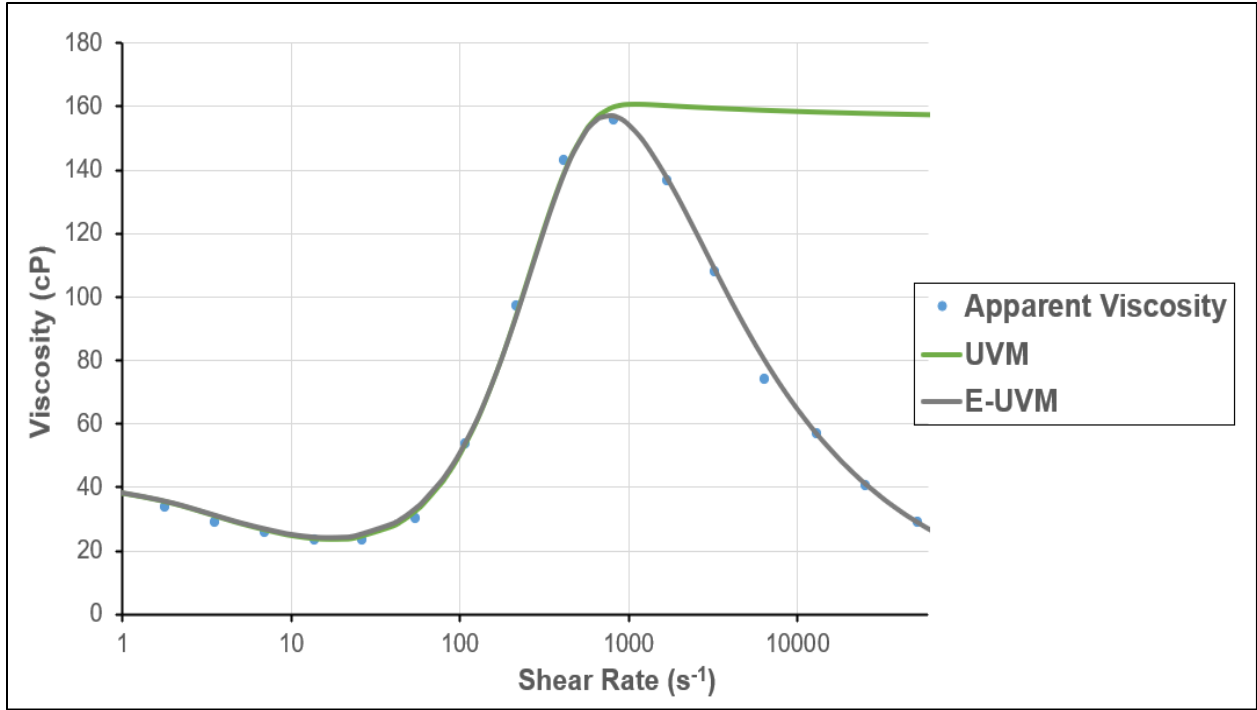


Figure 3.14: Fitting the models to Experiment № 14 data (1 g/L-18 MDa- Flopaam 3630S at 0.5 g/L TDS, 4 D Reservoir Sandstone Core).

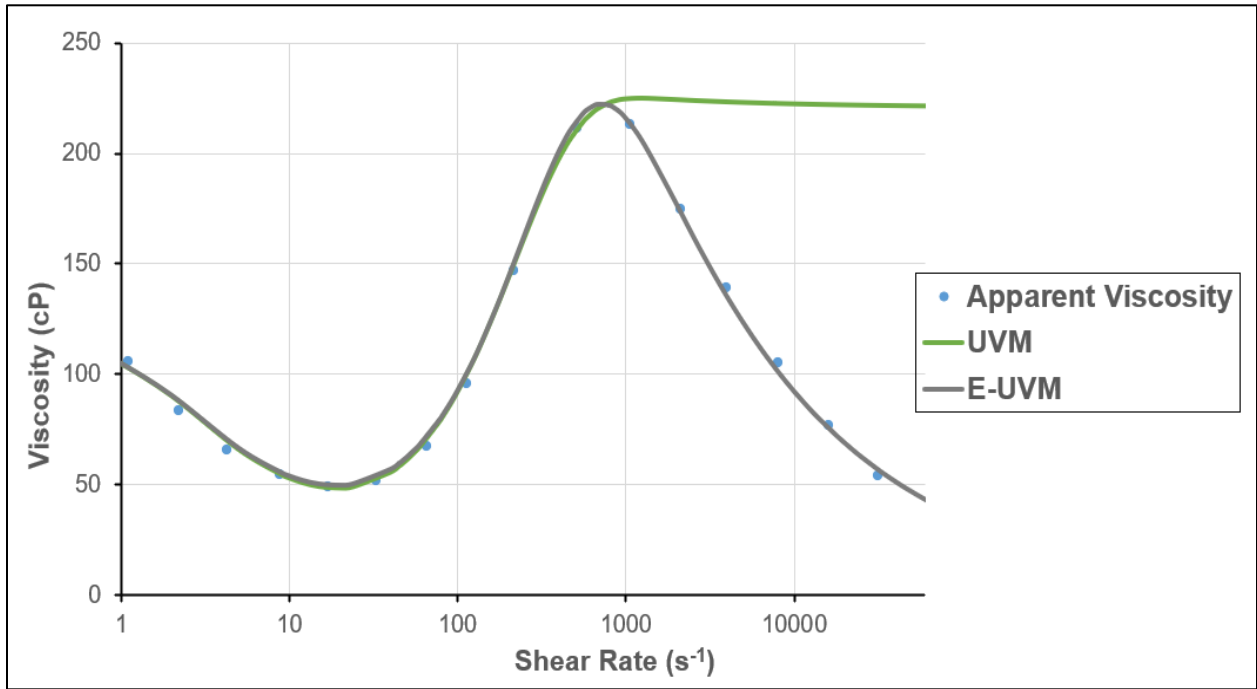


Figure 3.15: Fitting the models to Experiment № 15 data (1.35 g/L-18 MDa- Flopaam 3630S at 0.5 g/L TDS, 4 D Reservoir Sandstone Core).

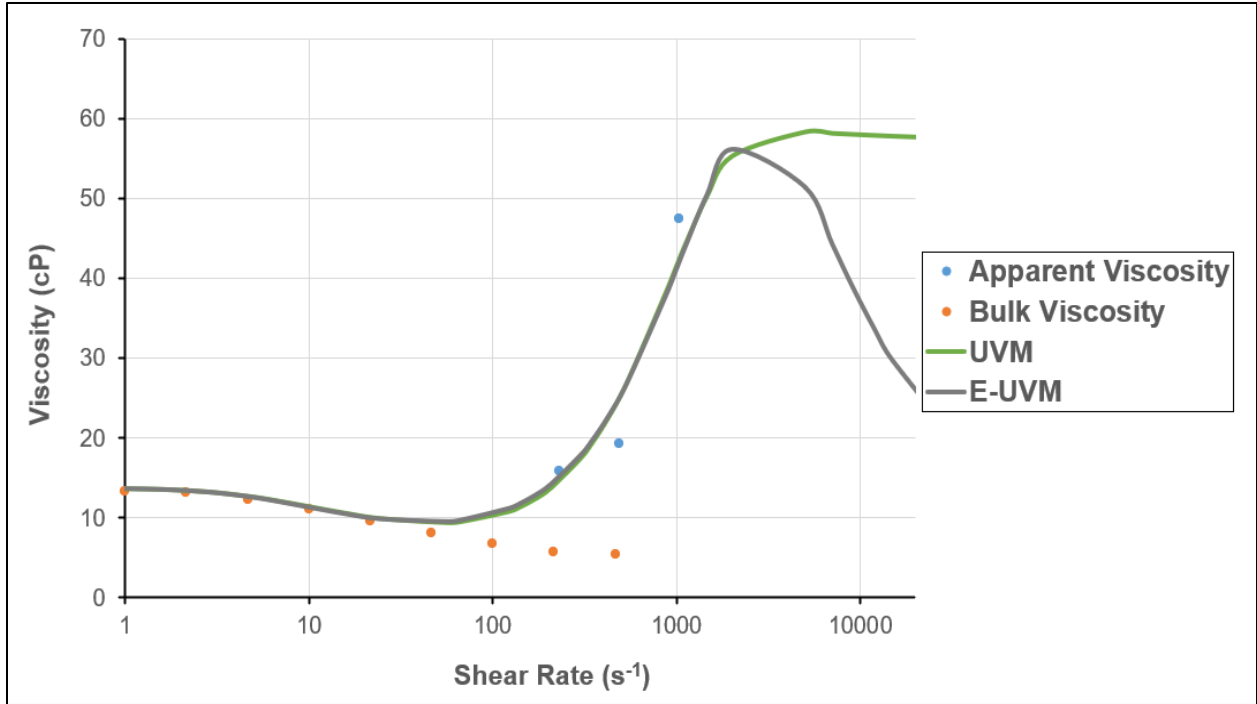


Figure 3.16: Fitting the models to Experiment № 16 data (1.5 g/L-20 MDa- Flopaam 3630S at 20.04 g/L TDS, 0.647 D Berea Sandstone Core).

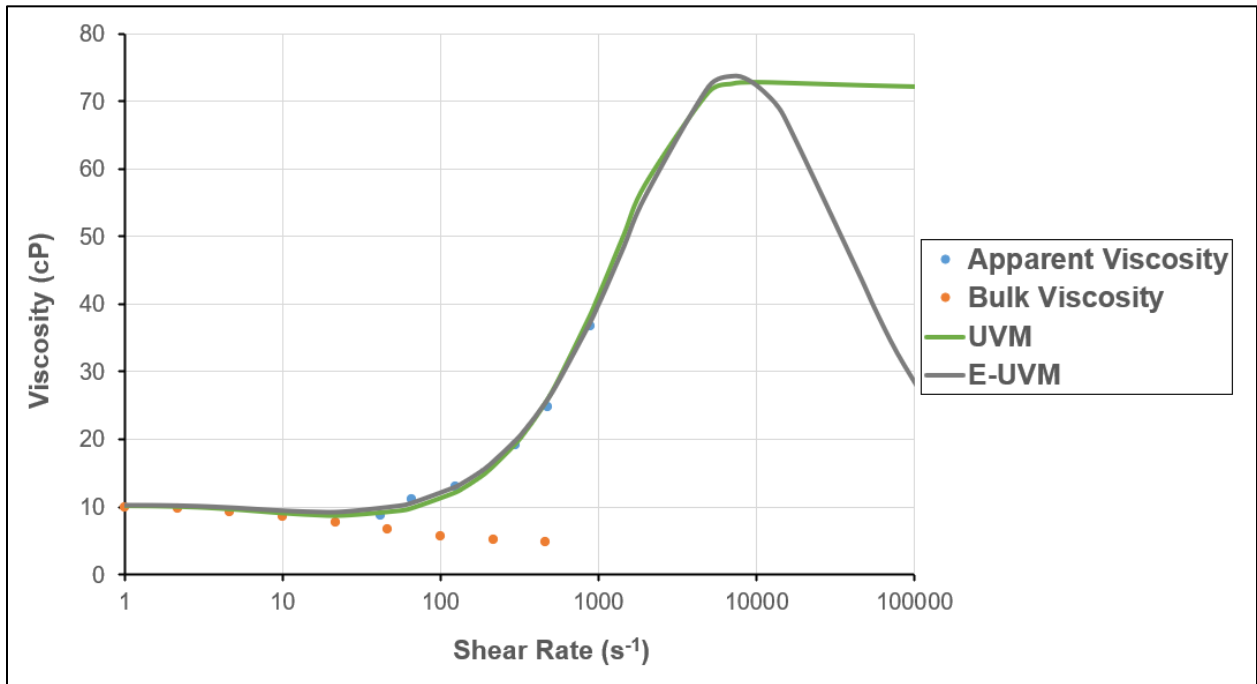


Figure 3.17: Fitting the models to Experiment № 17 data (1.5 g/L-8 MDa- AN-125 at 20.04 g/L TDS, 0.578 D Berea Sandstone Core).

Furthermore, the effect of different factors on polymer dilatant behavior and mechanical degradation was analyzed. It was observed that decreasing rock permeability shifts the onset for shear-thickening and mechanical degradation to lower shear rates. The permeability effect was captured in Experiments 5-6 (Southwick and Manke, 1988), Experiments 7-8 (Masalmeh *et al.*, 2019), and Experiments 12-13 (Lohne *et al.*, 2017). For example, Experiments 7 and 8 (**Figures 3.7** and **3.8**, respectively) were conducted under the same conditions but using cores of different permeabilities. It is seen from the figures that the onsets for shear-thickening and mechanical degradation in Experiment 7 ($k=1616$ mD) are around 100 s^{-1} and 3000 s^{-1} , respectively. These critical shear rates for Experiment 8 conducted using a core with lower permeability ($k=121$ mD) are approximately 20 s^{-1} and 1000 s^{-1} . Similar observations are applicable for the other two sets of experiments mentioned above (5-6 and 12-13). Such impact is related to a rapid increase in the stresses exerted on the polymer solution in low-permeable rock enhancing polymer deformation and accelerating dilatancy and degradation, as discussed in Chapter 2.

The solution salinity is another factor affecting polymer rheological behavior in porous media. Experiments 9-10 (**Figure 3.9** and **3.10**, respectively) illustrate that the polymer solution with 3 g/L TDS exhibits stronger viscoelasticity than the one with the salinity of 41.95 g/L. It resulted in earlier shear-thickening and higher maximum elongational viscosities (μ_{max}) in porous media. Namely, the onset for dilatant behavior in Experiment 9 is around 20 s^{-1} , while for Experiment 10, it is ten times greater, confirming a negative salinity effect on the viscoelastic onset. On the other hand, mechanical degradation also depends on salinity. It was found that the degradation becomes more severe with higher salinity. However, there was a negligible salinity impact on the mechanical degradation onset ($\approx 1200\text{ s}^{-1}$ for both).

Finally, the polymer concentration effect was also investigated. It is observed from **Figures 3.14** and **3.15** that Experiments 14 and 15 performed using the polymer concentration of 1 g/L and 1.35 g/L, respectively, reveals similar mechanical degradation behavior. The critical shear rate for degradation is around 700 s^{-1} for both experiments, and the degree and severity of degradation are also similar for given polymer concentrations. In contrast, the dilatant behavior was affected by C_p . Particularly, for a higher concentration, the onset for shear-thickening was observed earlier, in addition to the increased shear-thickening degree (slope).

In conclusion, it was found that polymer properties, rock permeability, and salinity can

significantly affect polymer rheological behavior. Particularly in carbonates, the heterogeneity with low permeability may result in early shear-thickening behavior and mechanical degradation, as discussed earlier (**Figures 3.7** and **3.8**). Although the polymer elasticity and dilatant behavior are enhanced in low permeable rock, severe mechanical degradation may occur if injection rates and polymer molecular weight are not appropriately designed. In addition, high connate water salinity in carbonates may also deteriorate the viscoelastic behavior of polymers and accelerate mechanical degradation.

Furthermore, reservoir temperature and polymer molecular weight were not discussed here. However, these factors are believed to have a considerable effect on polymer shear-thickening and degradation. Elevated temperatures in carbonates may result in substantial polymer thermal degradation and impair the elastic properties. On the other hand, injected polymer molecular weight is believed to improve the dilatant behavior. Nevertheless, injecting high molecular weight polymers in low permeable rock may plug the pore space and negatively affect injectivity. Therefore, further experimental studies are required to comprehensively investigate the effect of each factor on polymer rheological behavior in carbonate rocks.

3.3 Empirical Correlations for Estimating the Model Parameters

3.3.1 Model Parameters Obtained from Fitting the E-UVM to Coreflooding Data

This chapter discusses the model parameters used for fitting E-UVM to the coreflooding data. Polymer shear-thinning behavior in E-UVM is controlled by the shear-thinning constant (λ_1) and index (n_1), as in the original Carreau model. On the other, the shear-thickening section of the model depends on the Deborah number. It was found that the critical shear rate when the dilatant behavior is first observed is a function of polymer relaxation time. As discussed in Section 2.5.2, the relaxation time of polymers strongly depends on fluid flow conditions in porous media and polymer molecular parameters. Higher relaxation time leads to the earlier shear-thickening onset. Additionally, the slope for dilatant behavior is controlled by another fitting parameter, shear-thickening index (n_2). Higher polymer molecular weight and concentrations as well as lower salinities increase n_2 leading to more pronounced shear-thickening.

Furthermore, the model parameters responsible for mechanical degradation are also

discussed. Namely, mechanical degradation constant (λ_3) controls the degradation onset; higher λ_3 shifts onset to the lower shear rates. This parameter is usually taken from the range 10^{-5} - 10^{-3} , where λ_3 increases mainly with polymer molecular weight and decreases with rock permeability. Neglecting this parameter in the model will convert the E-UVM to the original UVM model. On the other hand, the degree of degradation is controlled by the mechanical degradation index (n_3). Higher n_3 in E-UVM is used to visualize more severe degradation cases.

Finally, since the xanthan gum and other biopolymer do not exhibit shear-thickening and mechanical degradation in porous media, μ_{max} and λ_3 for Experiment 11 were tuned as zero, converting the E-UVM to the Carreau model. All fitting parameters determined by matching the proposed model to the coreflooding data from literature are listed in **Table 3.2**.

Table 3.2: Fitting parameters of E-UVM used to match experimental data from literature

Nº	References	μ_0	μ_∞	λ_1	n_1	μ_{max}	λ_2	τ_r	n_2	λ_3	n_3	
1	Delshad <i>et al.</i> (2008)	13.7	1.02	0.221	0.755	108	0.01	0.035	2.15	0.0009	0.7	
2	Stavland (2010)	27	1.02	0.51	0.715	37.2	0.01	0.047	3.25	0.00014	0.56	
3	Asen <i>et al.</i> (2019)	10	1.02	0.15	0.74	27	0.01	0.15	3.15	0.000235	0.68	
4	Brakstad and Rosenkilde (2016)	4	1.02	0.62	0.842	41.6	0.01	0.09	3.2	0.000132	0.694	
5	Southwick and Manke (1988)	Exp1	20	1.02	0.32	0.662	24	0.01	0.225	2.18	0.00034	0.48
6		Exp2	5	1.02	0.32	0.662	23.4	0.01	0.24	2.21	0.00056	0.39
7	Masalmeh <i>et al.</i> (2019)	C-2	5.05	1.02	0.09	0.59	67	0.01	0.036	2.1	0.000245	1.4
8		C-6	5.05	1.02	0.14	0.87	12.4	0.01	0.25	2.05	0.00043	0.45
9	Seright <i>et al.</i> (2009)	Exp1	38	1.02	0.25	0.56	299	0.01	0.32	1.957	0.00021	1.45
10		Exp2	5	1.02	0.1	0.81	26	0.01	0.13	3.4	0.00032	0.92
11		Exp3	80	1.02	0.23	0.48	0	N.A.	N.A.	N.A.	0	N.A.

12	Lohne <i>et al.</i> (2017)	Exp1	4	1.02	0.25	0.79	13.8	0.01	0.22	2.88	0.00048	0.85
13		Exp2	6	1.02	0.45	0.87	46.2	0.01	0.098	3.35	0.00041	0.41
14	Manichand <i>et al.</i> (2013)	Exp 1	40	1.02	0.62	0.68	165	0.01	0.36	2.27	0.0007	0.49
15		Exp 2	114	1.02	0.68	0.52	260	0.01	0.365	2.04	0.0012	0.42
16	Magbagbeola (2008)	BV1	13.76	1.02	0.221	0.7316	78	0.01	0.072	2.12	0.00021	0.72
17		BV2	10.15	1.02	0.25	0.8152	75	0.01	0.061	1.899	0.00005	0.65

3.3.2 Development of Empirical Correlations to Predict Model Parameters

As discussed before, most of the existing viscoelastic models for predicting apparent polymer viscosity at various shear rates require extensive coreflooding tests to estimate the fitting parameters. However, generally, conducting the coreflooding experiment is a time-consuming and costly process. Besides, the cores obtained from a reservoir are usually not available since their extraction may be pretty challenging and expensive. Therefore, difficulties in conducting extensive coreflood experiments strongly limit the application of traditional viscoelastic models. Consequently, in this study, we attempted to reduce the need for coreflooding data to predict polymer rheological behavior in porous media since it might lead to faster polymer screening for future studies and polymer field applications.

For this purpose, we related the E-UVM fitting parameters to rock and polymer properties using several correlations developed in the EUREQA software. EUREQA is a software that detects latent mathematical relationships in the data using a machine learning method called Symbolic Regression and provides a mathematical expression to represent that relationship (Informer Technologies, 2021). Generally, Symbolic Regression is a regression analysis method searching the space of analytical expressions to estimate the most suitable model for the given dataset in terms of both simplicity and accuracy. In this technique, initial expressions are generated by randomly merging mathematical building blocks including analytic functions, state variables, mathematical operators, and constants. While conventional regression techniques attempt to adjust the parameters for a pre-determined model structure, symbolic regression avoids imposing

assumptions in advance and instead infers the model from the data (Minnebo and Stijven, 2011).

Hence, the data from **Tables 3.1** and **3.2** were imported and analyzed in the software. The correlations with reasonable accuracy and complexity were then selected among the developed expressions and used in our study. These expressions relating E-UVM fitting parameters to polymer and rock properties as well as solution salinities are presented below:

$$\mu_{max} = (0.226)kS + \frac{(1.19)C_p - (110)k}{S + k} - 339 - (259)\phi - (1.15 * 10^3)\phi \ln \phi, \quad (3.5)$$

$$\begin{aligned} \tau_r = & (0.12)M_w + (0.00447)S + (0.01242)kM_w - 0.104 - (0.249)k - (0.0769)S^{0.5} - \\ & - 7.5 * 10^{-8}C_p^2 - 0.00444M_w^2, \end{aligned} \quad (3.6)$$

$$n_2 = 2.07 + (0.00102)S^2 + (7.2 * 10^{-5})M_w S^2 - (0.0377)S - (9.62 * 10^{-7})M_w S^3, \quad (3.7)$$

$$\begin{aligned} \lambda_3 = & (3.17 * 10^{-5})M_w + (1.7 * 10^{-7})kC_p + \frac{(0.00756)k}{M_w} + \frac{(0.03316)}{k\phi C_p} - 0.0008142 \\ & - (0.0003905)k, \end{aligned} \quad (3.8)$$

$$\begin{aligned} n_3 = & (42.9)\phi + (0.00656)M_w + (0.00236)S + (0.000274)\phi S^2 - 1.13 - (120)\phi^2 \\ & - 2.14((0.0293)S)^\phi, \end{aligned} \quad (3.9)$$

where k is the permeability in Darcy, S is the solution salinity in g/L, C_p is the polymer concentration in ppm, ϕ is the porosity in fraction, and M_w is the polymer molecular weight in MDa.

These correlations may be used to predict the fitting parameters of the E-UVM with an acceptable error if the coreflooding data is not present. In the figures below, the E-UVM is plotted using original fitting parameters reported in **Table 3.2** (Case A) and modified ones estimated from the correlations (Case B):

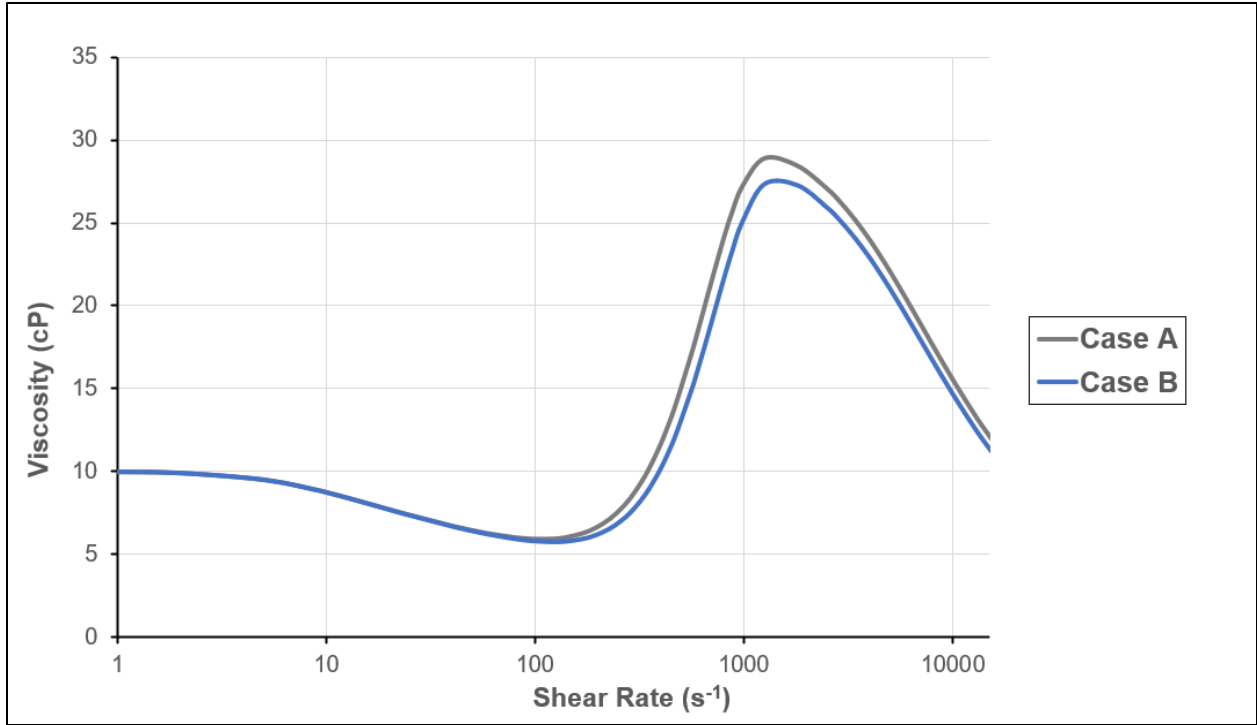


Figure 3.18: E-UVM results for Experiment 3 using original fitting parameters (Case A) and modified fitting parameters (Case B).

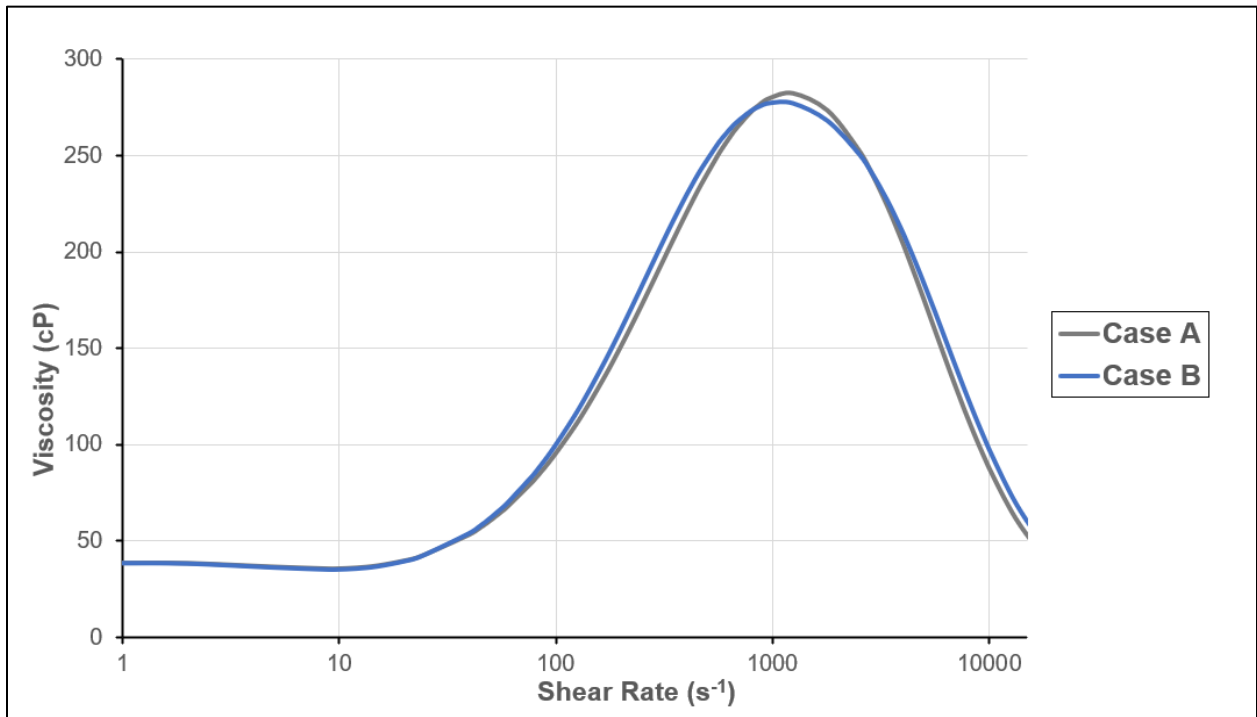


Figure 3.19: E-UVM results for Experiment 9 using original fitting parameters (Case A) and modified fitting parameters (Case B).

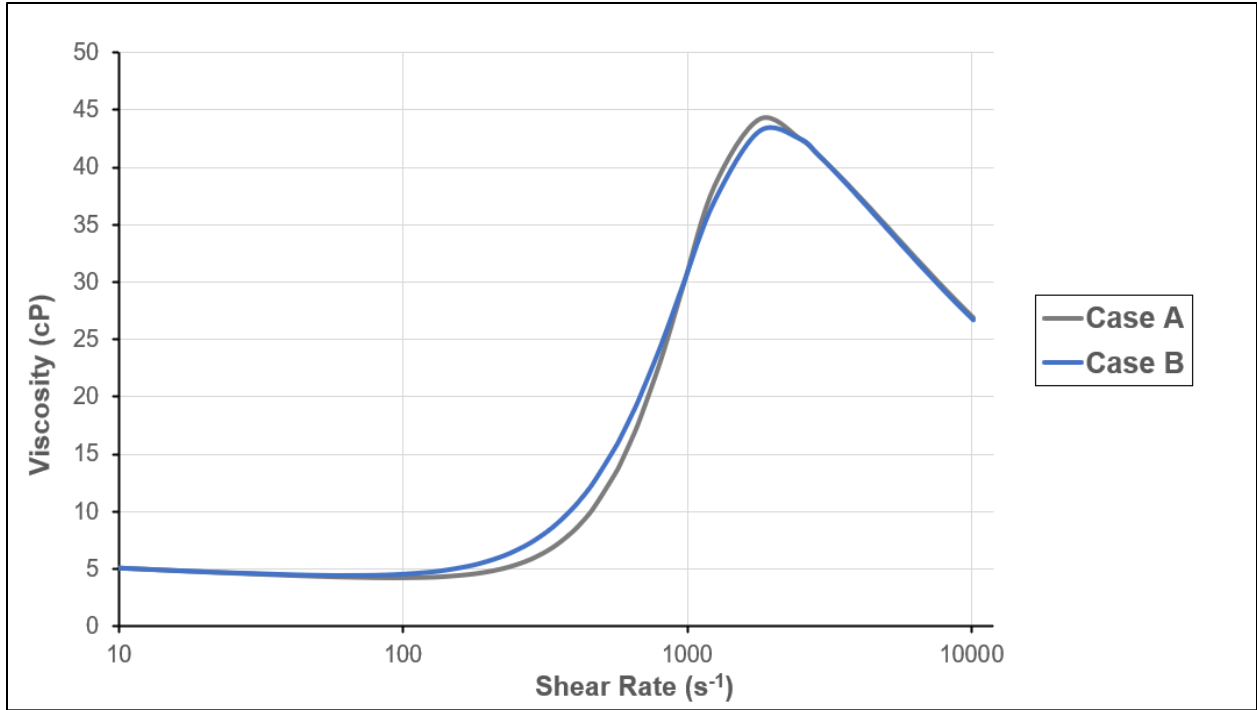


Figure 3.20: E-UVM results for Experiment 13 using original fitting parameters (Case A) and modified fitting parameters (Case B).

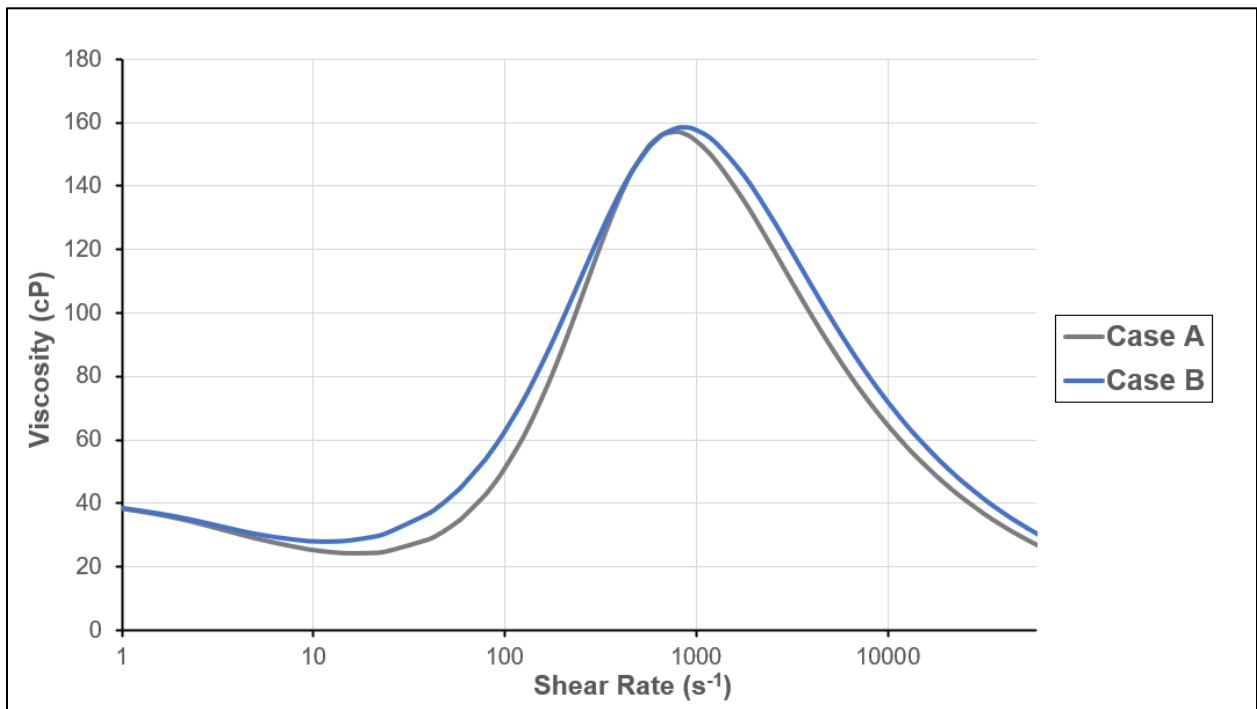


Figure 3.21: E-UVM results for Experiment 14 using original fitting parameters (Case A) and modified fitting parameters (Case B).

Apparently, there is a minor error, and E-UVM may be used to predict polymer rheological behavior for future polymer screening even if extensive coreflooding measurements are not performed. However, future studies may be conducted to obtain more experimental data as an input for software and improve the correlation accuracy for a wider range of flow conditions. It is recommended to derive separate correlations based on low and high permeability ranges and to capture the effect of rock lithology.

CHAPTER 4: POLYMER FLOODING SIMULATION WITH MATLAB RESERVOIR SIMULATION TOOLBOX

One of the primary stages in executing a successful polymer flooding project is understanding the polymer rheological behavior in porous media and accurately simulating it on a field scale. In this study, viscoelastic polymer flooding was modeled at both core- and field-scales using MATLAB Reservoir Simulation Toolbox (MRST). The MRST simulator was introduced in several publications (Lie, 2016; Bao *et al.*, 2017). The core-scale studies were conducted mainly to implement the proposed Extended Unified Apparent Viscosity Model in the reservoir simulator and verify it against the original rheological model existing in MRST. As stated before, E-UVM successfully captures all flow regimes exhibited by polymers at different shear rates; therefore, it was decided to use this model in simulation studies to predict polymer rheological behavior. It is also essential to note that the polymer effect on residual oil saturation is originally neglected in MRST. In this study, the residual-phase saturations were also modeled through the trapping number (N_T), as shown in **Equation 2.29**. The calculation of trapping numbers and residual-phase saturation was then verified at a core scale using the UTCHEM simulator. Furthermore, the field-scale simulations were also conducted to evaluate polymer injection in a quarter 5-spot well pattern. Sensitivity analysis was performed for a field-scale simulation by changing reservoir permeability, reservoir heterogeneity, polymer concentration, and injection rate to determine the effect of each variable on oil recovery. The core-scale and field-scale simulation studies are extensively reported in Chapter 5.

4.1 Introduction to MATLAB Reservoir Simulation Toolbox (MRST)

MATLAB Reservoir Simulation Toolbox (MRST) is an open-source software based on black-oil formulation with fully implicit time stepping and upstream weighting for spatial discretization. The software has been developed into a practical platform for rapid prototyping and testing the new simulation methods and mathematical models. More extensive information about MRST can be found elsewhere (Lie, 2016; Bao *et al.*, 2017).

4.2 Core-Scale Simulation Model

4.2.1 Experimental Data

The core-scale simulation studies of this work were performed under representative conditions of the Middle East carbonate reservoirs. The experimental two-phase flow data for oil and water as well as that of the rock were obtained from Chandrasekhar and Mohanty (2013). They conducted a series of vertical coreflooding measurements to analyze the effect of brine ionic composition on oil recovery for limestone reservoirs. The first coreflooding test was performed by injecting the formation brine with a total dissolved solids (TDS) of 179,730 ppm through heterogeneous carbonate core plugs with rock and fluid properties given in **Tables 4.1 – 4.3**. The formation water injection was performed with the injection velocity of 1 ft/day at temperatures of 120°C. The authors reported about 40% OOIP recovery following the injection of 5 pore volumes of formation water. The core petrophysical characteristics and fluid properties used during this coreflooding test are collected and listed in the tables below. Additional information about the experimental study may be obtained elsewhere (Chandrasekhar and Mohanty, 2013).

Table 4.1: Core petrophysical properties (Chandrasekhar and Mohanty, 2013)

Pore Volume (cm³)	14.6	Length (cm)	7.8
Porosity	0.178	Permeability (mD)	23.2
Cross Sectional Area (cm²)	10.987	Diameter (cm)	3.74
S_{wirr}	0.21	S_{orw}	0.47
Injection Rate (cm³/min)	0.045		

Table 4.2: Oil properties (Chandrasekhar and Mohanty, 2013)

Viscosity at 120 °C (cP)	0.9
Density at 120 °C (g/cm³)	0.82
API (Degrees)	41.06

Table 4.3: Water properties (Chandrasekhar and Mohanty, 2013)

Ion \ Brine	Concentration (ppm)
Na ⁺	49,933
Mg ²⁺	3,248
Ca ²⁺	14,501
Cl ⁻	111,810
SO ₄ ²⁻	234
TDS	179,730

Furthermore, in addition to the experimental two-phase flow data taken from Chandrasekhar and Mohanty (2013) for rock, oil, and formation brine, **Table 4.4** lists the polymer parameters that were assumed and used for viscoelastic polymer flooding simulations.

Table 4.4: Polymer properties used in polymer flooding simulations

Polymer Type	HPAM-based
Molecular Weight (MDa)	8
Degree of Hydrolysis	0.28
Concentration (ppm)	500-1000-1500-2000

As stated earlier, it is preferred to use comparatively lower molecular weight polymers in low-permeable rock to reduce mechanical degradation and improve injectivity. The latter justifies the selection of 8 MDa as a M_w for viscoelastic polymer flooding. Moreover, the polymer injection was simulated at varying polymer concentrations of 500 ppm, 1000 ppm, 1500 ppm, and 2000 ppm. Using rock and polymer solution properties in **Table 4.5** for the different polymer

concentrations considered, E-UVM fitting parameters for the given rock, water, and polymer properties were predicted using **Equations 3.5-3.9** and listed in **Table 4.6**.

Table 4.5: Rock and polymer solution properties used for core-scale simulation studies

N_o	Polymer Type	M_w (MDa)	C_p (g/L)	S (g/L)	Rock Type	k (Darcy)	Porosity
1	HPAM-based	8	0.5	179.73	Carbonate	0.0232	0.178
2	HPAM-based	8	1	179.73	Carbonate	0.0232	0.178
3	HPAM-based	8	1.5	179.73	Carbonate	0.0232	0.178
4	HPAM-based	8	2	179.73	Carbonate	0.0232	0.178

Table 4.6: Predicted E-UVM fitting parameters based on known properties

N_o	μ_0	μ_∞	λ_1	n_1	μ_{max}	λ_2	τ_r	n_2	λ_3	n_3
1	5.05	1.02	0.14	0.87	12.4	0.01	0.31	2.05	0.00065	0.45
2	9.2	1.02	0.14	0.76	17	0.01	0.45	2.15	0.00066	0.47
3	14.35	1.02	0.14	0.68	28	0.01	0.75	2.25	0.00067	0.476
4	17.86	1.02	0.62	0.36	37	0.01	0.82	2.37	0.00068	0.56

To visualize the effect of polymer concentration on the rheological behavior, the E-UVM apparent viscosity vs. shear rate curves were obtained for different polymer concentrations and plotted in **Figure 4.1**. According to the figure, the degree of shear-thickening is increasing with polymer concentration. Moreover, polymer solution injected at a higher concentration starts to exhibit dilatant behavior at lower shear rates. On the other hand, the effect of polymer concentration on shear-thinning and mechanical degradation degree is less pronounced.

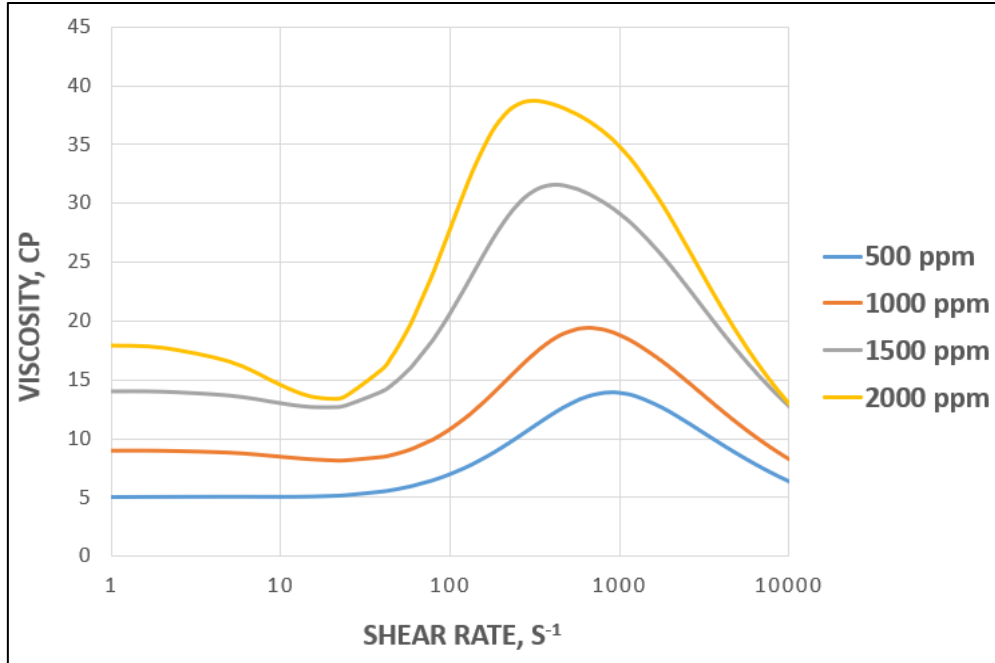


Figure 4.1: E-UVM results for different polymer concentrations.

4.2.2 Core-Scale Simulation Model Data

The core-scale simulation model was designed similar to the work of Adegbite *et al.* (2017). The heterogeneous 2D Cartesian grid system incorporating 10×1×10 gridblocks was used to simulate viscoelastic polymer flooding. The model dimensions are shown in **Table 4.7**.

Table 4.7: Core-scale simulation model data

Parameter	Value	Comments
Number of Gridblocks	100	2D Model (10×1×10)
Gridblock Size (m)	$\Delta x = 0.0033145$ $\Delta y = 0.033145$ $\Delta z = 0.0078$	Constant grid size in each direction
Core Model Dimensions (m)	0.033145×0.033145×0.078	Length × Width × Height

Moreover, the core heterogeneity was modeled using the log-normal permeability

distribution in x and z directions as well as a sequential Gaussian simulation (SGS) method with a spherical variogram. The standard deviation of the log-normal distribution can be related to Dykstra Parson's coefficient of variation as follows (Dykstra and Parsons, 1950):

$$DP = 1 - e^{-\sigma}, \quad (4.1)$$

where σ is the standard deviation and DP is the Dykstra Parson's coefficient of variation, which is taken as 0.8 for the highly heterogeneous simulation model used. The permeability distribution of the model used is depicted in **Figure 4.2**.

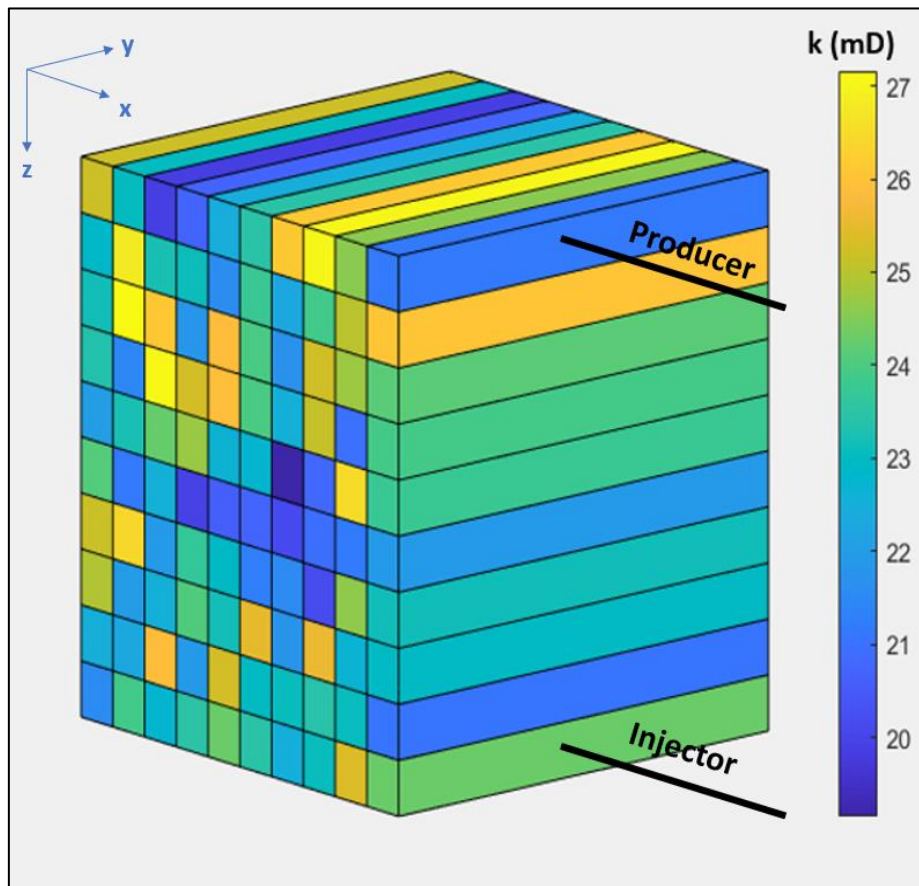


Figure 4.2: Core-scale simulation model with heterogeneous permeability.

The simulation model was designed vertically based on the experimental work of Chandrasekhar and Mohanty (2013), with two horizontal wells; production well at the top and injection well at the bottom of the model. Moreover, the production well was set at a constant bottom-hole pressure of 50 psi, while the injection rates for the injector varied from 0.045 ml/min (≈ 1 ft/d) to 4.5 ml/min (≈ 100 ft/d) to capture the flow rate effect on viscoelastic polymer flow.

4.3 The Polymer Model Used in MRST

The polymer model used in MRST assumes that the polymer component is transported in the aqueous phase, altering only its mobility. In contrast, the oleic and gaseous phases are not affected by the polymers and are represented with the standard three-phase black-oil equations.

Several factors are affecting aqueous phase mobility during polymer flooding. Primarily, polymers are mixed in the aqueous phase, increasing the viscosity. Secondly, polymers are adsorbed on the rock surface or retained in the narrow pore throats, reducing the effective permeability to water. Both factors are considered in MRST using corresponding multipliers that modify the aqueous phase mobility. Moreover, polymer non-Newtonian (shear-thinning or shear-thickening) behavior is also modeled based on the water velocity, obtaining new multipliers representing shear effects.

4.3.1 Polymer Mixing Effect

As stated before, polymers mixed in the aqueous phase tend to increase the solution viscosity. Effective viscosities are computed using the Todd-Longstaff mixing model as follows (Bao *et al.*, 2017):

$$\mu_{eff} = m_{mix} * \mu_w, \quad (4.2)$$

$$m_{mix} = \frac{m_\mu (C_p)^\omega}{1 - \bar{C}_p + \bar{C}_p / m_\mu (C_p^*)^{1-\omega}}, \quad (4.3)$$

$$\bar{C}_p = C_p / C_p^*, \quad (4.4)$$

where μ_{eff} is the aqueous effective viscosity after mixing with polymers, m_{mix} is the multiplier representing polymer mixing effect, μ_w is the water viscosity, C_p is the polymer concentration, C_p^* is the maximum possible polymer concentration, m_μ is the user-prescribed function depending on polymer concentration, and ω is the mixing parameter. The mixing parameter (ω) is equal to 1 when polymers are fully mixed in the water, while polymers are completely segregated at $\omega=0$. In this study, the solution was assumed fully mixed, and ω was taken as 1.

4.3.2 Permeability Reduction Effect

Reduction in effective aqueous permeability is another mechanism improving injectant mobility during polymer flooding. In MRST, this effect is captured as follows (Bao *et al.*, 2017):

$$m_{pr} = 1 + (RRF - 1) \frac{c^a}{c_{max}^a}, \quad (4.5)$$

where m_{pr} is the multiplier representing permeability reduction, RRF is the residual resistance factor, c^a is the adsorbed polymer concentration, and c_{max}^a is the maximum adsorbed polymer concentration. Furthermore, aqueous phase mobilities can be modified using the multipliers for mixing and permeability reduction:

$$M_{eff} = \frac{M_w}{m_{mix} m_{pr}}, \quad (4.6)$$

where M_{eff} is the effective aqueous phase mobility and M_w is the water mobility.

4.3.3 Polymer Non-Newtonian Behavior

In addition to the mechanisms discussed above, aqueous phase mobility can be dramatically altered

with the shear rates. This mobility change during polymer flooding is related to polymer non-Newtonian behavior, where the viscosity changes with water velocity. The shear factor (Z) representing the shear effects in MRST is calculated as follows (Bao *et al.*, 2017):

$$Z = \frac{\mu_{w,sh}(u_{w,sh})}{\mu_{w,eff}} = \frac{1 + (m_{\mu}(C_p) - 1)m_{sh}(u_{w,sh})}{m_{\mu}(C_p)}, \quad (4.7)$$

$$u_{w,sh} = \frac{u_{w,0}}{Z} = u_{w,0} \frac{\mu_{w,eff}}{\mu_{w,sh}(u_{w,sh})}, \quad (4.8)$$

where $u_{w,0}$ and $\mu_{w,eff}$ are the effective water velocity and viscosity without shear effects, respectively; $u_{w,sh}$ and $\mu_{w,sh}$ are the shear-modified water velocity and viscosity, respectively; and m_{sh} is the user-prescribed function. $m_{sh}=1$ if the polymer solution does not exhibit shearing and keeps its constant Newtonian viscosity. $m_{sh}<1$ if the polymer solution exhibits shear-thinning behavior, and $m_{sh}>1$ when shear-thickening of polymers occurs. Moreover, during the complete shear-thinning ($m_{sh}=0$), the polymer solution viscosity becomes equal to water viscosity:

$$\mu_{w,sh} = \frac{\mu_{w,eff}}{m_{\mu}(C_p)}. \quad (4.9)$$

Furthermore, **Equations 4.7** and **4.8** are combined to derive the following implicit equation:

$$u_{w,sh} [1 + (m_{\mu}(C_p) - 1)m_{sh}(u_{w,sh})] - m_{\mu}(C_p)u_{w,0} = 0. \quad (4.10)$$

Equation 4.10 is then used to compute $u_{w,sh}$ by standard Newton iteration process (Bao *et al.*, 2017). Later, estimated $u_{w,sh}$ can be used in **Equation 4.8** to calculate shear factor (Z). Finally, the shear-modified viscosity ($\mu_{w,sh}$) is calculated using **Equation 4.7**.

4.4 Implementation of E-UVM in MRST

4.4.1 Modifying Shear Multipliers by E-UVM Viscosities

As discussed earlier, the MRST model is based on the water velocities defined on the grid faces. Moreover, the shear effects are also controlled by other factors, such as m_μ and m_{sh} . The former function represents the viscosity multiplier where there are no shear effects encountered. The upstream value of m_μ is used to evaluate the multipliers at the faces (Bao *et al.*, 2017).

On the other hand, m_{sh} factors also control polymer non-Newtonian behavior. They are usually tabulated in the input file as a water velocity function. Within this table, the velocity values should monotonically increase starting from zero. The first m_{sh} factor that corresponds to zero velocity is usually equal to one since negligible shear effects are observed at minimal fluxes. Then, the factors may decrease with velocities if the polymer exhibits shear-thinning or may increase in the shear-thickening case (Schlumberger, 2013). When the viscosity dependence on shear rate is activated, the MRST model determines the m_{sh} factor corresponding to the specific shear-modified water velocity ($u_{w,sh}$) and uses it to iteratively solve for new $u_{w,sh}$, as shown in **Equation 4.10**. Eventually, the final shear-modified velocity and respective m_{sh} are used to estimate the shear factors (Z).

Our study aimed to replace the technique described above with the E-UVM model that can independently from input deck files estimate the apparent polymer viscosity and corresponding shear factors (Z). For this purpose, firstly, the water Darcy's velocities (u_w) were calculated on each face F of the discrete grid as follows:

$$u_w[F] = \frac{q_{w,0}[F]}{A[F]}, \quad (4.11)$$

where $q_{w,0}[F]$ is the water flux across the face F , and $A[F]$ is the face F area. Furthermore, the shear rate values ($\dot{\gamma}$) used in E-UVM were also computed on the faces of grids, as shown below:

$$\dot{\gamma}[F] = C \left[\left(\frac{3n_1 + 1}{4n_1} \right)^{n_1/(n_1-1)} \left(\frac{4u_w [F]}{\sqrt{8(S_w \phi k_w)[F]}} \right) \right], \quad (4.12)$$

where C is the shear correction factor, n is the shear-thinning index, u_w is the water Darcy's velocity, S_w is the aqueous phase saturation, ϕ is the porosity, and k_w is the effective aqueous phase permeability for the face F . Moreover, apparent viscosities (μ_{app}) were estimated at interfaces using the Extended Unified Apparent Viscosity Model, as follows:

$$\begin{aligned} \mu_{app}[F] = & \left(\mu_\infty + (\mu_0 - \mu_\infty) \cdot (1 + (\lambda_1 \dot{\gamma}[F])^2)^{\frac{n_1-1}{2}} + \mu_{max} [1 - \exp(-(\lambda_2 \tau_r \dot{\gamma}[F])^{n_2-1})] \right) \\ & * (1 + (\lambda_3 \dot{\gamma}[F])^2)^{\frac{-n_3}{2}}, \end{aligned} \quad (4.13)$$

where μ_0 and μ_∞ are the zero-shear rate and infinite-shear rate viscosities, respectively; n_1 is the shear-thinning index, λ_1 is the time constant, μ_{max} is the maximum elongational viscosity, λ_2 is the universal constant, τ_r is the relaxation time, n_2 is the shear-thickening index, λ_3 is the mechanical degradation constant, and n_3 is the mechanical degradation index. These model parameters can be predicted separately by fitting the E-UVM to the coreflooding data and adding them to the code as constant input values. Alternatively, the fitting parameters can also be estimated using the correlations provided in Section 3.3. If it is the case, the correlations are added to the code, and the fitting parameters depend on rock or polymer input data. Finally, the shear factors (Z) at the faces were calculated by dividing the apparent viscosity to zero-shear rate viscosity, as given below:

$$Z[F] = \frac{\mu_{app}[F]}{\mu_0}, \quad (4.14)$$

It is worth mentioning that with E-UVM, we modified only the shear factors representing

polymer non-Newtonian behavior. In contrast, the multipliers accounting for polymer mixing and permeability reduction were not affected by E-UVM implementation and were calculated similarly using Todd–Longstaff mixing model.

4.4.2 Verification of the E-UVM Technique Against Original Implementation

In order to verify the E-UVM implementation, shear factors (Z) were first calculated using the E-UVM model by following the procedures specified in the previous section. The estimated shear factors were then used to predict the corresponding m_{sh} values, as follows:

$$m_{sh} = \frac{Z * m_{\mu} - 1}{m_{\mu} - 1}, \quad (4.15)$$

where Z are the shear factors calculated using E-UVM model and m_{μ} are the multipliers with no shear effects encountered. m_{μ} factors were not affected by E-UVM and were estimated before implementing E-UVM model in MRST. Furthermore, the m_{sh} values were used to compute the corresponding shear-modified velocities ($u_{w,sh}$), as shown below:

$$u_{w,sh} = \frac{u_{w,0} * m_{\mu}}{1 + (m_{\mu} - 1)m_{sh}}. \quad (4.16)$$

As explained before, m_{sh} is one of the factors controlling shear effects in the MRST model (PLYSHEAR). It is usually tabulated in the input deck file as a function of shear-modified water velocities. The polymer shear response strongly depends on m_{sh} values change with water velocities within the table. Therefore, it is possible to compare two rheological models (PLYSHEAR and E-UVM) by modifying the input file table with new m_{sh} and $u_{w,sh}$ values estimated using **Equations 4.15** and **4.16**.

The verification of E-UVM against the original PLYSHEAR model was conducted using

the core-scale simulation model defined in Section 4.2. In this analysis, a comparison between the two rheological models was performed for around 5 PVs of secondary polymer flooding. Other input parameters for MRST are listed in the **Table 4.8**.

Table 4.8: Input parameters used to verify E-UVM implementation

Number of Gridblocks	100 (10×1×10)	Number of Interfaces between the Grids	180
Average Permeability (mD)	23.2	Dykstra-Parsons Coefficient	0.8
Porosity	0.178	Polymer Concentration (ppm)	1500
Oil Density (kg/m³)	820	Oil Viscosity (cP)	0.9
Injection Rate (ml/min)	0.045 (≈ 1 ft/day)	Producer BHP (psi)	50
S_{orw}	0.47	S_{wirr}	0.21

The core-scale simulation model containing 100 gridblocks had 180 interfaces between those grids. Therefore, the calculation of m_{sh} factors in MRST using **Equation 4.15** revealed a matrix containing 180×1 elements, where each element of the matrix denoted an individual m_{sh} factor per interface. Similarly, the shear-modified water velocities were also given in the 180×1 matrix. Since the water velocities usually monotonically increase in the original PLYSHEAR table, we filtered the elements in the velocity matrix from the smallest to the largest with corresponding m_{sh} factors. The generated table from modified $u_{w,sh}$ and m_{sh} was then exported to the input file and used as a new table for the PLYSHEAR model.

After modifying the table in the input file with updated $u_{w,sh}$ and m_{sh} , polymer flooding simulation was run using the PLYSHEAR model and compared with the results of E-UVM. Particularly, pressure drop and oil recovery curves obtained by these two models were compared as shown in **Figures 4.3** and **4.4**, respectively.

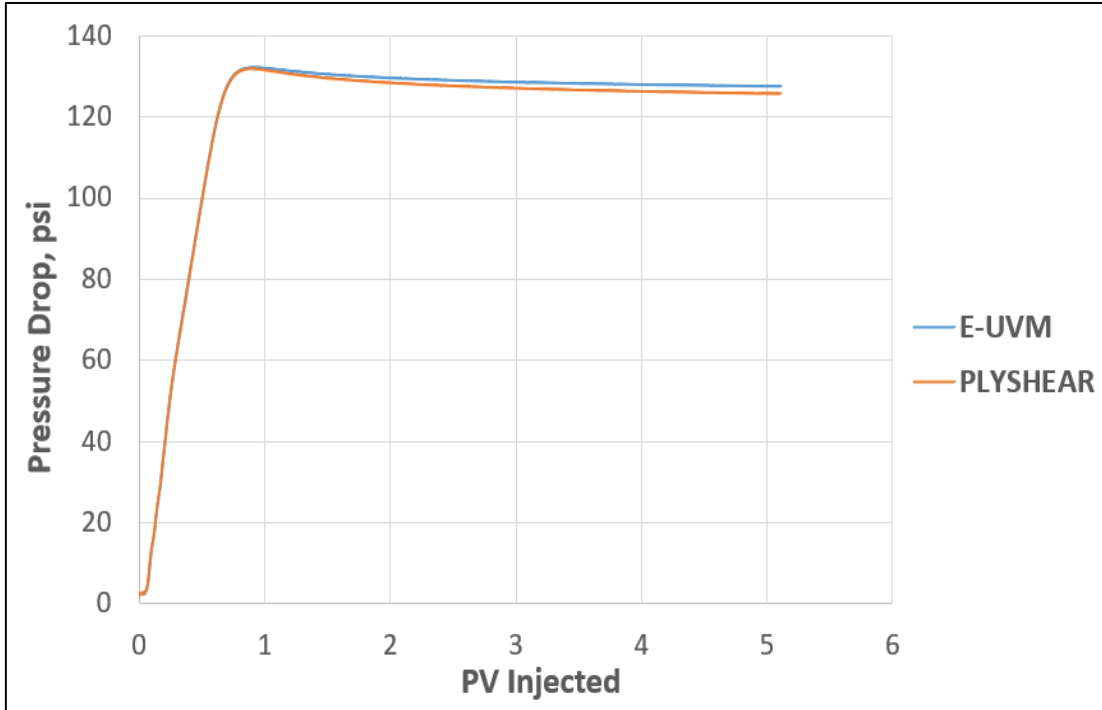


Figure 4.3: Comparison of pressure drops for PLYSHEAR and E-UVM models.

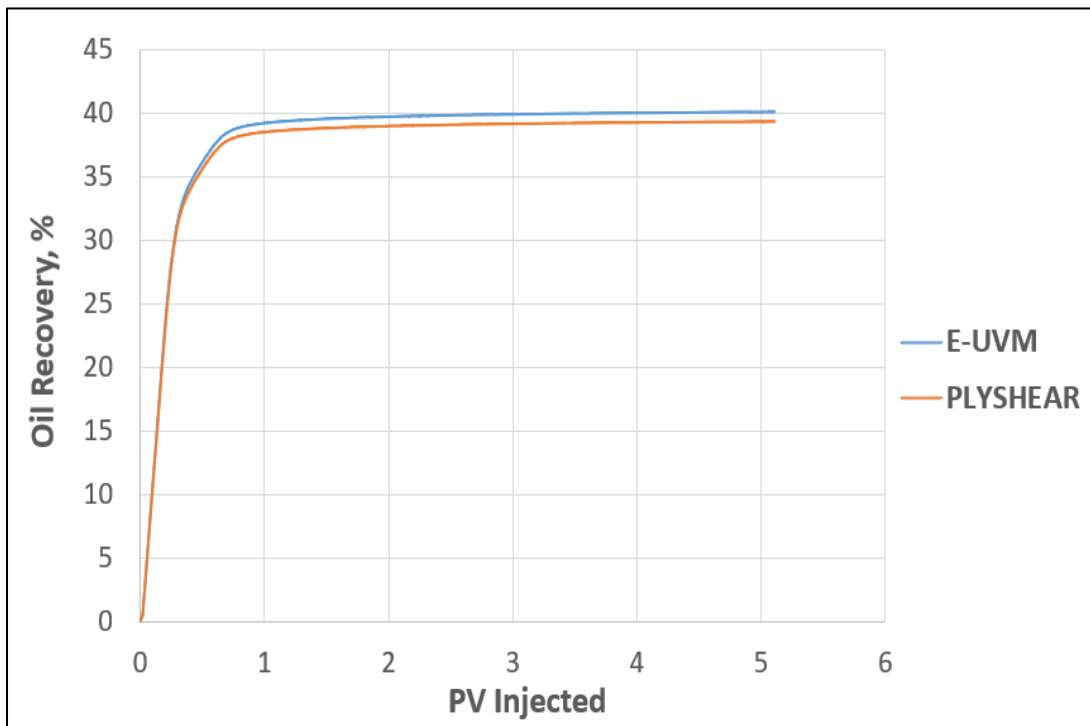


Figure 4.4: Comparison of oil recoveries for PLYSHEAR and E-UVM models.

The latter figures show that the simulation results obtained by PLYSHEAR and E-UVM for pressure drop and oil recovery are in a good agreement. This confirms the implementation of E-UVM to predict the polymer viscosities and shear multipliers directly from the correlation. Moreover, we believe that this method is more accurate and practical than importing the data from external files/tables and iteratively solving for multipliers.

4.5 Modeling the Effect of Polymer Viscoelasticity on Displacement Efficiency

This section extensively describes the modeling of polymer viscoelasticity effect on residual-phase saturation. Traditionally, it was believed that polymers reduce injectant mobility and improve volumetric sweep efficiency only. However, recently, researchers investigated and reported the positive impact of viscoelastic polymer flooding on oil mobilization and displacement efficiency improvement.

As discussed earlier, polymer flooding in MRST is modeled by the multipliers accounting for permeability reduction, polymer mixing, and non-Newtonian behavior. However, the effect of polymers on residual saturation is not captured initially in MRST. Therefore, we decided to quantify additional oil recovery obtained by viscoelastic polymers by modeling the effect of trapping number on residual saturation. The following sections explain implementation of trapping numbers for the core-scale simulation model in MRST and capturing its effect on both residual-oil saturation and relative permeabilities. Additionally, this implementation is verified against the UTCHEM simulator in Section 4.5.3.

4.5.1 Trapping Numbers Implementation

In order to compute the additional oil recovery obtained by viscoelastic polymers, we modified the polymer flooding model used in MRST by defining trapping number as well as updating residual-phase saturations and relative permeabilities (Corey's end-points and exponents) as functions of trapping number in each gridblock. The trapping numbers were calculated based on the method provided in Schlumberger (2013). As a first step, the capillary number for each cell was calculated as follows:

$$N_c = \frac{|k \cdot \vec{\nabla} \Phi_p|}{\sigma_{p'p}}, \quad (4.17)$$

where k is the absolute permeability, $\vec{\nabla} \Phi$ is the flow potential gradient, and $\sigma_{p'p}$ is the interfacial tension between the phases and is considered as constant 30 mN/m in this study. Furthermore, the central difference rule is applied to solve for Root Mean Squared (RMS) form of $|k \cdot \vec{\nabla} \Phi|$ term (Schlumberger, 2013):

$$|k \cdot \vec{\nabla} \Phi| = \sqrt{\left(k_x \frac{d\Phi}{dx}\right)^2 + \left(k_y \frac{d\Phi}{dy}\right)^2 + \left(k_z \frac{d\Phi}{dz}\right)^2}, \quad (4.18)$$

$$k_x \frac{d\Phi}{dx} = 0.5 \left[\left(\frac{k_x}{dx}\right)_{i-\frac{1}{2}} * (\Phi_i - \Phi_{i-1}) + \left(\frac{k_x}{dx}\right)_{i+\frac{1}{2}} * (\Phi_{i+1} - \Phi_i) \right], \quad (4.19)$$

$$k_y \frac{d\Phi}{dy} = 0.5 \left[\left(\frac{k_y}{dy}\right)_{j-\frac{1}{2}} * (\Phi_j - \Phi_{j-1}) + \left(\frac{k_y}{dy}\right)_{j+\frac{1}{2}} * (\Phi_{j+1} - \Phi_j) \right], \quad (4.20)$$

$$k_z \frac{d\Phi}{dz} = 0.5 \left[\left(\frac{k_z}{dz}\right)_{k-\frac{1}{2}} * (\Phi_z - \Phi_{z-1}) + \left(\frac{k_z}{dz}\right)_{k+\frac{1}{2}} * (\Phi_{k+1} - \Phi_k) \right], \quad (4.21)$$

$$\Phi = P - g\rho_w \Delta D, \quad (4.22)$$

where Φ is the flow potential defined in each cell, ρ_w is the water density also estimated in every cell, ΔD is the vertical distance from the datum (top of the simulation model) to the gridblock center, k_d is the permeability defined at the interfaces in each direction (where $d = i, j, k$), and dx , dy , and dz are the gridblock dimensions in x, y, and z directions, respectively. As a result, the term $|k \cdot \vec{\nabla} \Phi|$ was calculated for all 100 gridblocks in the simulation model and used to estimate corresponding capillary numbers. One should note that this implementation for capillary number can handle the variation in the dimensions (1D, 2D, and 3D) as well as gridblock number. Therefore, it can be applied for predictions at both core- and field-scale simulations. Furthermore,

the Bond number was calculated for each gridblock as follows:

$$N_B = \frac{kg(\rho_w - \rho_o)}{\sigma_{p'p}}, \quad (4.23)$$

where g is the gravitational constant and ρ_o is the oil density estimated in every cell. Finally, since the simulation model was designed vertically and the flow was from the bottom to the top of the model (vertical upward flow), the trapping number was calculated as given below:

$$N_T = |N_C + N_B|. \quad (4.24)$$

4.5.2 Modeling N_T Effect on Residual Saturation and Relative Permeabilities

Residual Saturation. Following the calculation of trapping number, the residual saturation was updated accordingly for each gridblock using **Equation 2.29** (Delshad, 1990). In order to analyze the effect of trapping numbers on oil mobilization, the capillary desaturation curve representing a carbonate mineralogy was designed based on **Equation 2.29** and plotted in **Figure 4.5**. Here, the broader range for trapping numbers is selected (10^{-10} - 10^{-1}) to obtain a complete CDC model. The input parameters required to construct the CDC for mixed-wet carbonate are listed in **Table 4.9**.

Table 4.9: Input parameters for Capillary Desaturation Curve

S_{or}^{low}	0.47	S_{or}^{high}	0
T_p	500	τ	0.45

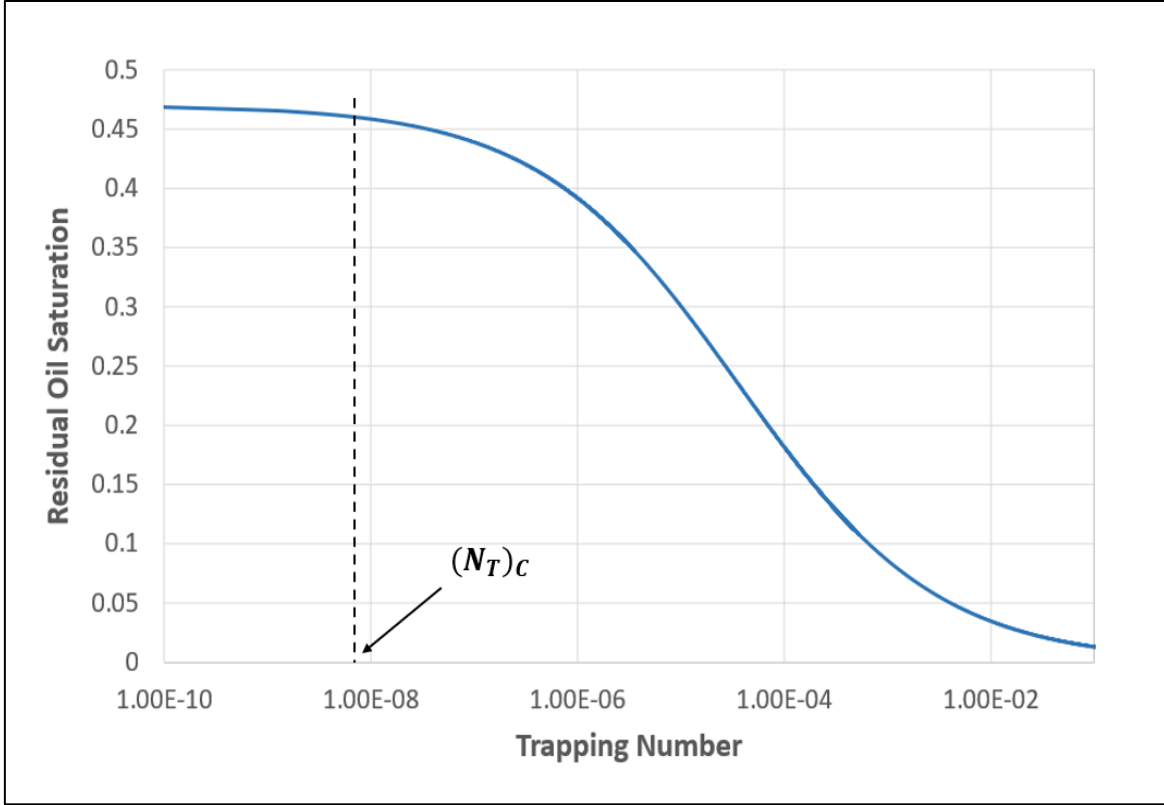


Figure 4.5: Capillary Desaturation Curve for the given input parameters.

According to the figure, the critical trapping numbers to mobilize the oleic phase $(N_T)_{C-oil}$ is approximately 8×10^{-9} . Therefore, the residual saturation was kept unchanged until the trapping number exceeded this threshold value. Moreover, beyond the "knee" in CDC, the residual saturations were estimated using **Equation 2.29** shown previously as follows:

$$S_{or} = \begin{cases} S_{or}^{low} & \text{if } N_T \leq (N_T)_{C-oil} \\ S_{or}^{high} + \frac{S_{or}^{low} - S_{or}^{high}}{1 + T_o N_T^{T_o}} & \text{if } N_T > (N_T)_{C-oil} \end{cases} \quad (4.25)$$

The typical plot illustrating the reduction in residual oil saturation as the trapping number increases is shown in **Figure 4.6**.

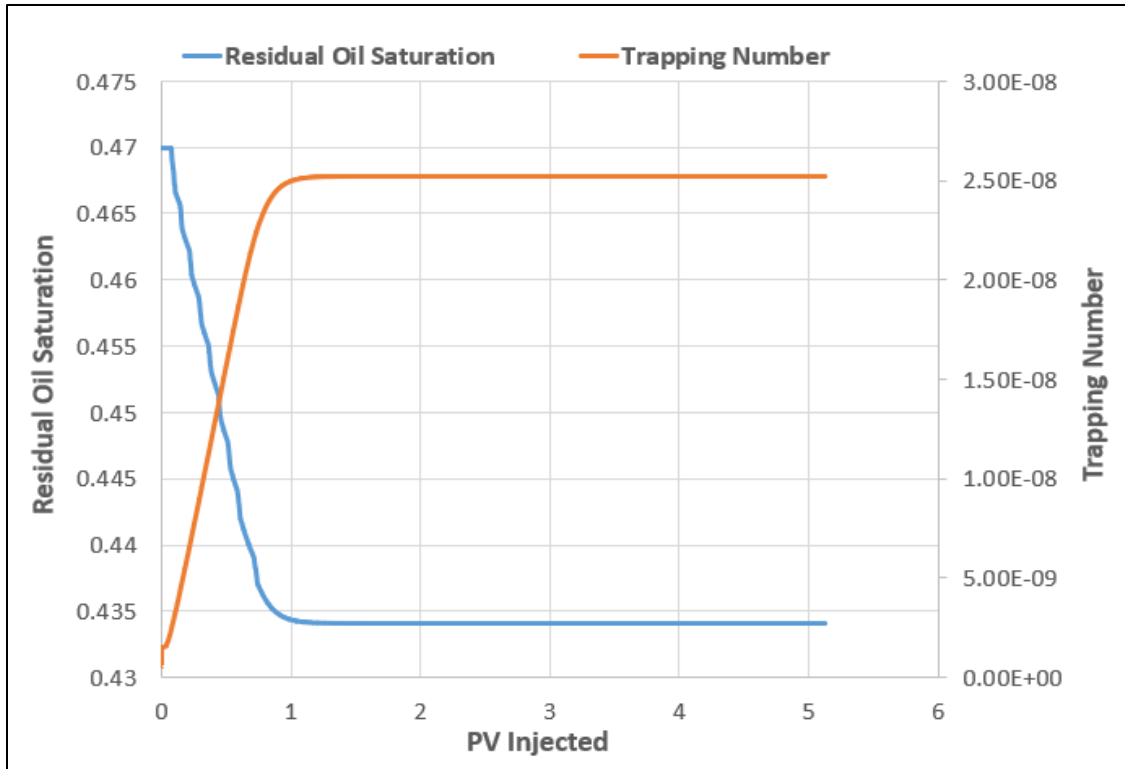


Figure 4.6: The typical plot illustrating residual oil saturation as a function of trapping number.

Relative Permeabilities. Corey's relative permeability endpoints and exponents corresponding to the modified residual saturations were calculated using **Equations 2.38** and **2.39**, respectively (Delshad *et al.*, 1986). It is worth mentioning that the irreducible water saturation was assumed constant and not being affected by trapping number. Hence, oil endpoint relative permeability and Corey's exponent were constant during the secondary polymer flooding simulation. Finally, the oil and water relative permeabilities were estimated using the Brooks and Corey (1964) model shown previously in **Equations 2.36** and **2.37**, respectively.

At low trapping numbers before the CDC's knee was reached, we assumed that residual-phase saturations and Corey's relative permeability model parameters were constant and equal to the initial values obtained from the waterflooding data. Particularly for this study, these initial parameters were obtained from Adegbite *et al.* (2017) for waterflooding in representative carbonate cores and are summarized in **Table 4.10**.

Table 4.10: Corey's relative permeability model parameters for initial conditions
(Adegbite *et al.*, 2017)

S_{or}	0.47	S_{wir}	0.21
k_{ro}^*	0.123	k_{rw}^*	0.02
n_o	3.03	n_w	2.55

As indicated above, the initial parameters were estimated during the waterflooding test. In particular, the oil endpoint relative permeability was calculated from the ratio of effective to absolute permeabilities, while the water endpoint relative permeability was predicted by applying Darcy's law at the stabilized pressure drop. Additionally, oil and water Corey's exponents were obtained by matching the waterflooding pressure drop and oil recovery data. Furthermore, the resultant oil and water relative permeability curves at the initial conditions were established and are shown in **Figure 4.7**.

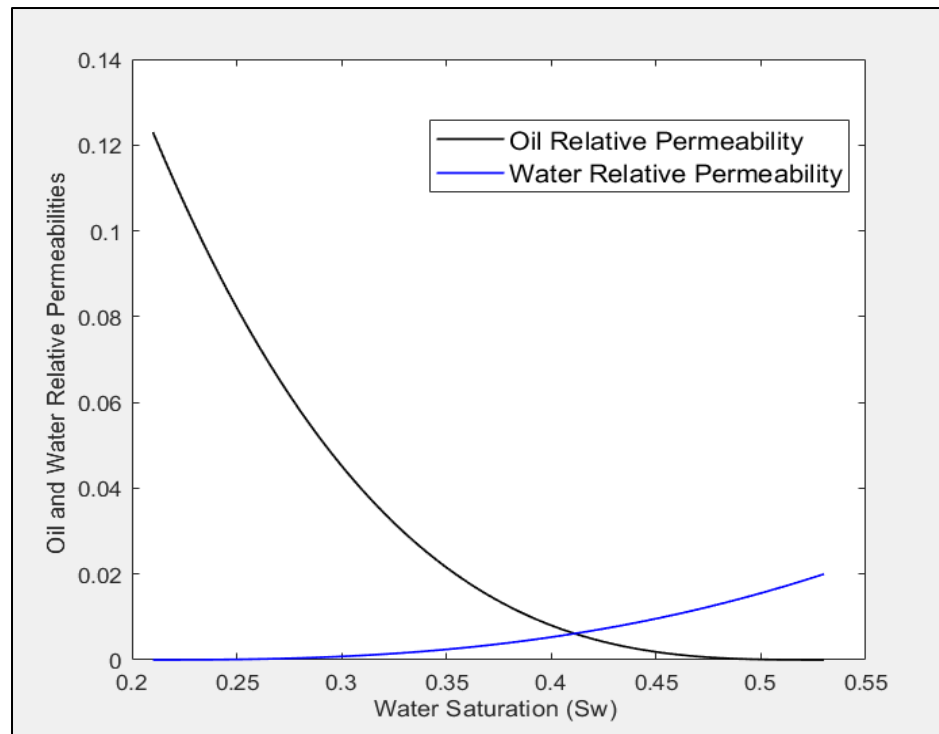


Figure 4.7: Relative permeability curves used in simulations.

The latter figure shows the oil and water relative permeability curves intersect at a water saturation of 0.42, confirming the mixed-wettability nature of the cores used.

Furthermore, the trapping number may increase with the injection rates or polymer concentration and eventually exceed the critical trapping number. Beyond this point, the residual oil saturation and corresponding Corey's parameters for water were modeled as a function of trapping numbers. We observed that viscoelastic polymer flooding at low injection rates would not yield a notable oil recovery, while incrementing the rate might lead to a 10% reduction in residual oil saturation. The effect of injection rate on residual oil saturation and the corresponding shift in relative permeability curves are depicted in **Figure 4.8**. For comparison purposes, the polymer flooding with a concentration of 1500 ppm was modeled at 0.045 ml/min (≈ 1 ft/d) and 4.5 ml/min (≈ 100 ft/d). Other input data were taken from **Table 4.8**.

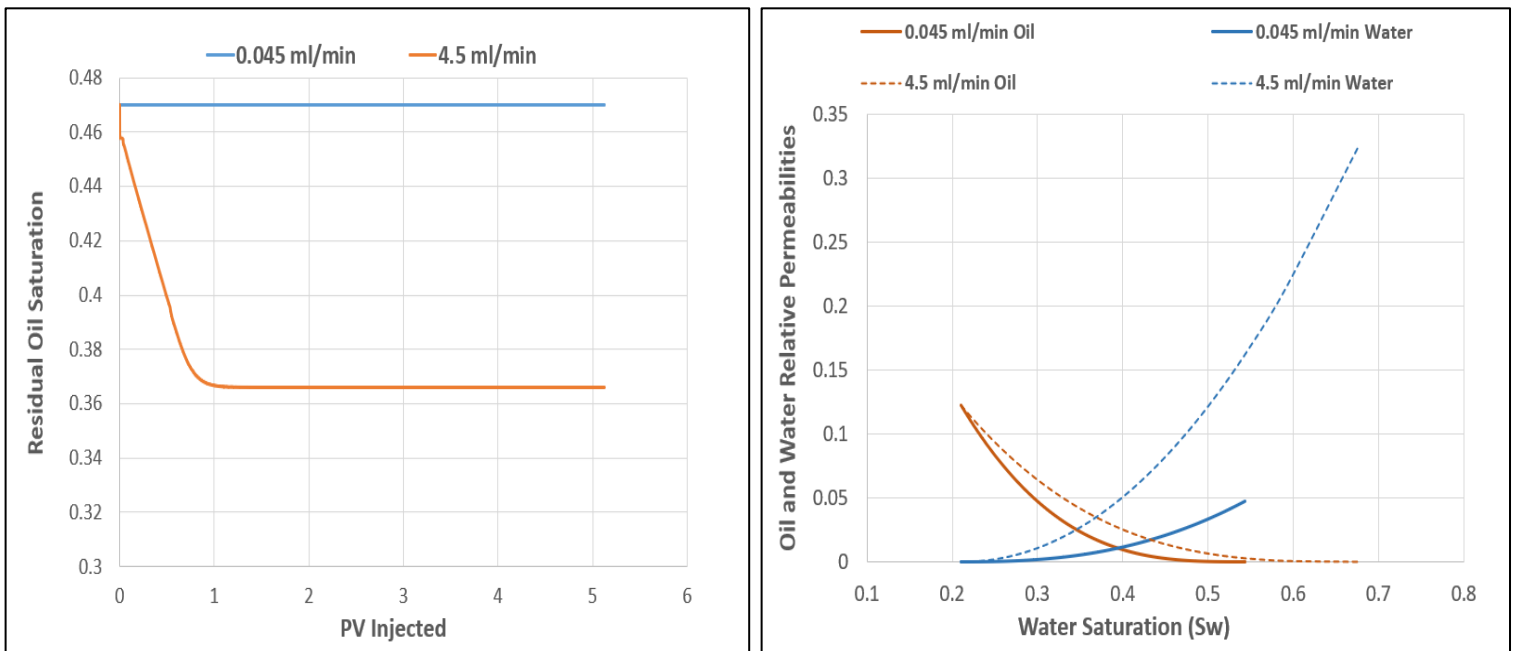


Figure 4.8: The effect of injection rates on residual oil saturation (left) and relative permeabilities (right) at $C_p=1500$ ppm.

According to **Figure 4.8**, viscoelastic polymer flooding simulated at 0.045 ml/min does not result in residual oil mobilization. As explained before, low injection rates led to insignificant trapping numbers at the CDC plateau, explaining no reduction in residual oil saturation at 0.045

ml/min. Moreover, the increment in injection rates up to 4.5 ml/min correspondingly increased the trapping number and resulted in a residual oil saturation reduction of about 10%. The altered residual oil saturation was then used to update the water endpoint relative permeability and Corey's exponent. However, the oil endpoint relative permeability and Corey's exponent were kept constant and similar to that of waterflooding since the irreducible water saturation was assumed constant. The resultant relative permeability curves are also depicted in **Figure 4.8**. Due to no oil mobilization at low injection rates, relative permeability curves for oil and water at 0.045 ml/min were constructed using initial condition parameters reported in **Table 4.10**. Increasing the injection rates increased water endpoint relative permeability to 0.33 and reduced water Corey's exponent to 2.07 (**Table 4.11**). Additionally, the intersection point was slightly shifted to lower water saturations, indicating very little rock wettability change toward oil-wet.

Table 4.11: Relative permeability parameters before and after exceeding critical N_T at 4.5 ml/min

Below $(N_T)_c$		Above $(N_T)_c$	
S_{or}	0.47	S_{or}	0.365
S_{wir}	0.21	S_{wir}	0.21
k_{ro}^*	0.123	k_{ro}^*	0.123
k_{rw}^*	0.02	k_{rw}^*	0.33
n_o	3.03	n_o	3.03
n_w	2.55	n_w	2.07

4.5.3 Verification Against the UTCHEM Simulator

In order to verify the calculation of trapping number and corresponding changes in residual oil saturation and relative permeabilities, the results obtained from Matlab Reservoir Simulation Toolbox were compared against the UTCHEM simulator. UTCHEM, introduced by The University of Texas at Austin, is a three-dimensional, non-isothermal, multicomponent,

multiphase, IMPEC (implicit pressure and explicit concentration), chemical compositional simulator. It can simulate various chemical EOR processes and handle up to 4 phases (aqueous, oleic, microemulsion, and gaseous phases). UTCHEM uses advanced concepts in high-order numerical accuracy and dispersion control. The reservoir simulator can model wettability alteration, capillary pressures, chemical reactions, three-phase relative permeabilities, diffusion, dispersion, adsorption, non-equilibrium mass transfer between phases, and other related phenomena (Al-Shalabi, 2014a).

To simplify the verification process, 1D secondary waterflooding was simulated without polymer flooding. However, the interfacial tension between aqueous and oleic phases was reduced to 0.1 to increase the trapping numbers in the system and emphasize their effect on residual oil mobilization.

The 1D core-scale simulation model used in verifying the trapping number calculation had a Cartesian grid of $100 \times 1 \times 1$ with the dimensions identical to the main core-scale simulation model defined in Section 4.2. The model was homogenous with a permeability of 200 mD. The water injection was simulated for 5 PV at a rate of 0.45 ml/min. The vertical production well was constrained by a constant BHP of 50 psi, while the injection well was controlled by a constant rate of 0.45 ml/min. Other input parameters are listed in **Tables 4.12**.

Table 4.12: Input parameters for the simulation model used to verify trapping numbers

Number of Gridblocks	100 ($100 \times 1 \times 1$)	Model Dimensions (m)	$0.033145 \times 0.033145 \times 0.078$
Permeability (mD)	200	Porosity	0.178
Initial Oil Saturation	0.75	Initial Pressure (psi)	50
Water Viscosity (cP)	0.5	Oil Viscosity (cP)	0.9
Water Density (g/cm^3)	1.118	Oil Density (g/cm^3)	0.9
Wellbore Radius (m)	0.0005	Interfacial Tension (mN/m)	0.1

The residual saturations are modeled in UTCHEM using the modified version of **Equation 2.29** where the model parameter (τ) is assumed to be 1 as follows:

$$S_{pr} = S_{or}^{high} + \frac{S_{pr}^{low} - S_{or}^{high}}{1 + T_p N_T}, \quad (4.26)$$

In order to be consistent with UTCHEM calculations, residual saturations were estimated similarly in MRST. The trapping number parameters (T_p) were adjusted to compensate for the modification in the equation. Furthermore, the endpoint relative permeabilities and Corey's exponents were computed using **Equations 2.38** and **2.39**. The input parameters used for calculation residual saturations and relative permeabilities at initial conditions are listed in **Table 4.13**.

Table 4.13: Input parameters used for calculation of residual saturations and relative permeabilities at initial conditions

T_{p-oil}	200000	$T_{p-water}$	1865
S_{or}^{low}	0.47	S_{wir}^{low}	0.21
S_{or}^{high}	0	S_{wir}^{high}	0
$(k_{ro}^*)^{low}$	0.123	$(k_{wr}^*)^{low}$	0.02
$(k_{ro}^*)^{high}$	1	$(k_{wr}^*)^{high}$	1
$(n_o)^{low}$	3.03	$(n_w)^{low}$	2.55
$(n_o)^{high}$	1	$(n_w)^{high}$	1

The results from both MRST and UTCHEM are reported in **Table 4.14**. Similar average trapping numbers and corresponding residual phase saturations were obtained in both simulators. Moreover, **Figures 4.9** and **4.10** show the resultant oil recoveries and average pressures are in match, which also verify the implementation.

Table 4.14: Average trapping numbers and corresponding residual saturations estimated in MRST and UTCHEM at initial condition and after 5 PVs

Parameter	Initial Conditions- Below $(N_T)c$	After 5 PVs-above $(N_T)c$	
	MRST and UTCHEM	MRST	UTCHEM
N_T	3.67×10^{-9}	1.08×10^{-6}	0.97×10^{-6}
S_{or}	0.47	0.39	0.387
S_{wir}	0.21	0.2096	0.20954

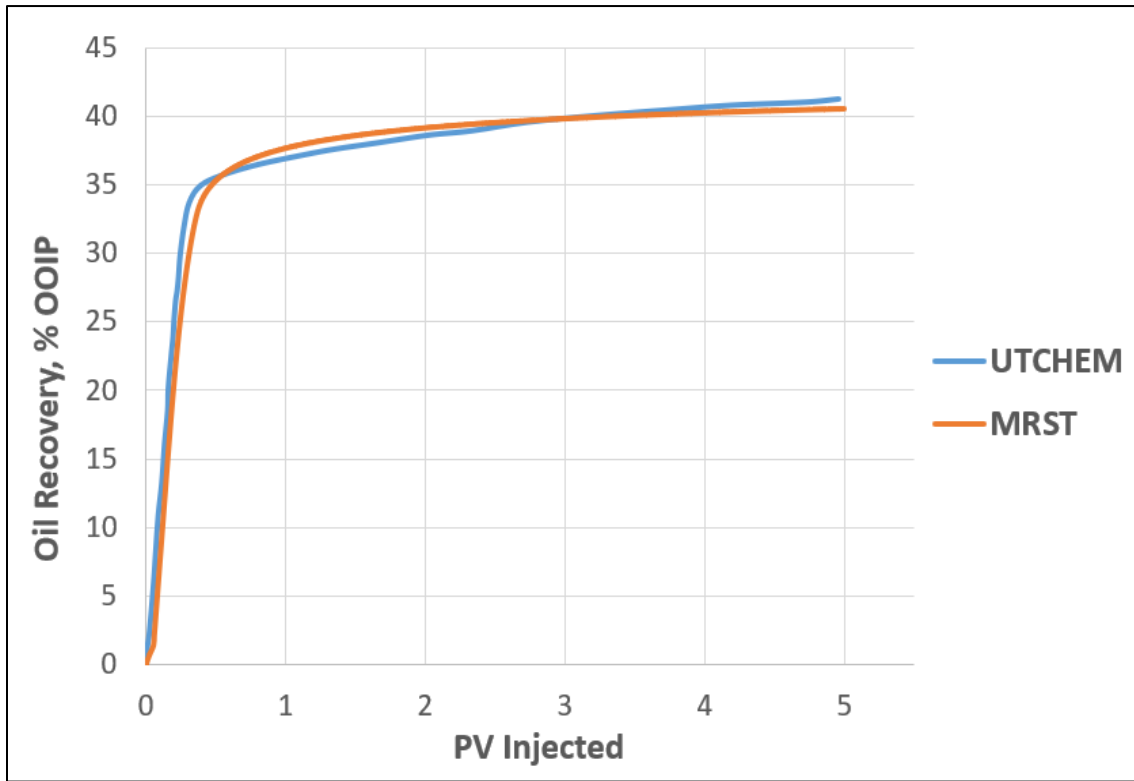


Figure 4.9: Oil recoveries estimated using UTCHEM and MRST simulators.

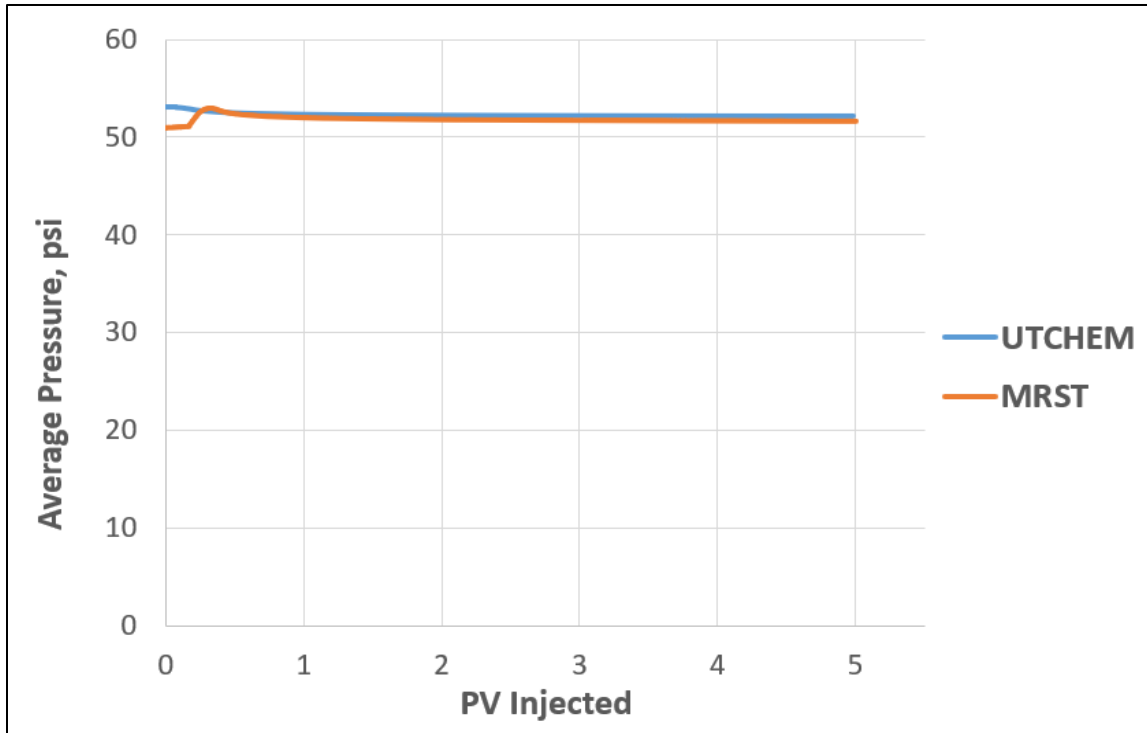


Figure 4.10: Pressure drop estimated using UTCHEM and MRST simulators.

CHAPTER 5: SIMULATION STUDIES AT CORE- AND FIELD-SCALES

This chapter summarizes the core-scale predictions and introduces field-scale simulation studies. The field-scale simulations were performed to evaluate polymer injection in a quarter 5-spot well pattern. Sensitivity analysis was performed at a field-scale simulation by investigating the effect of several factors on oil recovery. These factors were categorized into uncontrollable natural factors (reservoir permeability and reservoir heterogeneity) and controllable factors (polymer concentration and injection pressure).

5.1 Core-Scale Simulation Studies

All core-scale studies were performed in MRST using the simulation model defined in Section 4.2. Initially, secondary waterflooding was simulated and history matched with the experimental data, followed by tertiary polymer flooding. Polymer rheological behavior was evaluated at different injection rates. Besides, the effect of polymer concentration and injection rate on polymer flooding performance were investigated at the core scale.

5.1.1 Simulation and History Matching of Waterflooding Cycle

The waterflooding cycle for this study was simulated based on the experimental data obtained from Chandrasekhar and Mohanty (2013). They performed the waterflooding at a rate of 0.045 ml/min (≈ 1 ft/d) and obtained around 40% OOIP of oil recovery. The remaining oil of 47% after injecting about five pore volumes was assumed very close to the actual residual oil saturation.

The simulation results for pressure drop and oil recovery were successfully history matched with the laboratory data. It is worth mentioning that the capillary pressure effect was not considered in simulating waterflooding. However, Adegbite *et al.* (2017) recommended incorporating both heterogeneity and capillary pressure effects to obtain better matching.

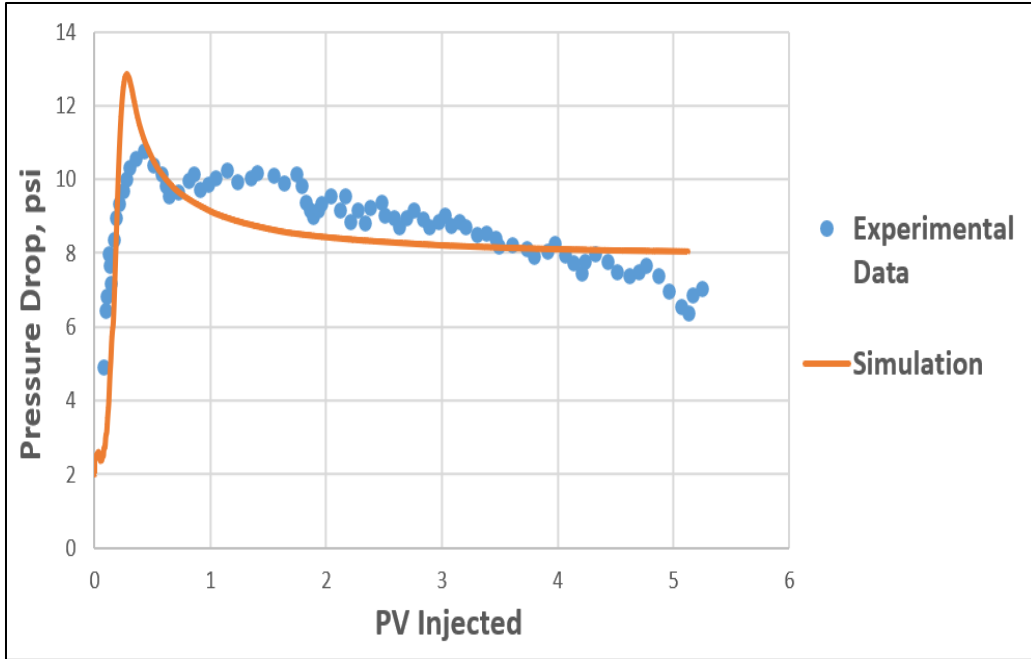


Figure 5.1: Pressure drop match for waterflooding experiment of Chandrasekhar and Mohanty (2013).

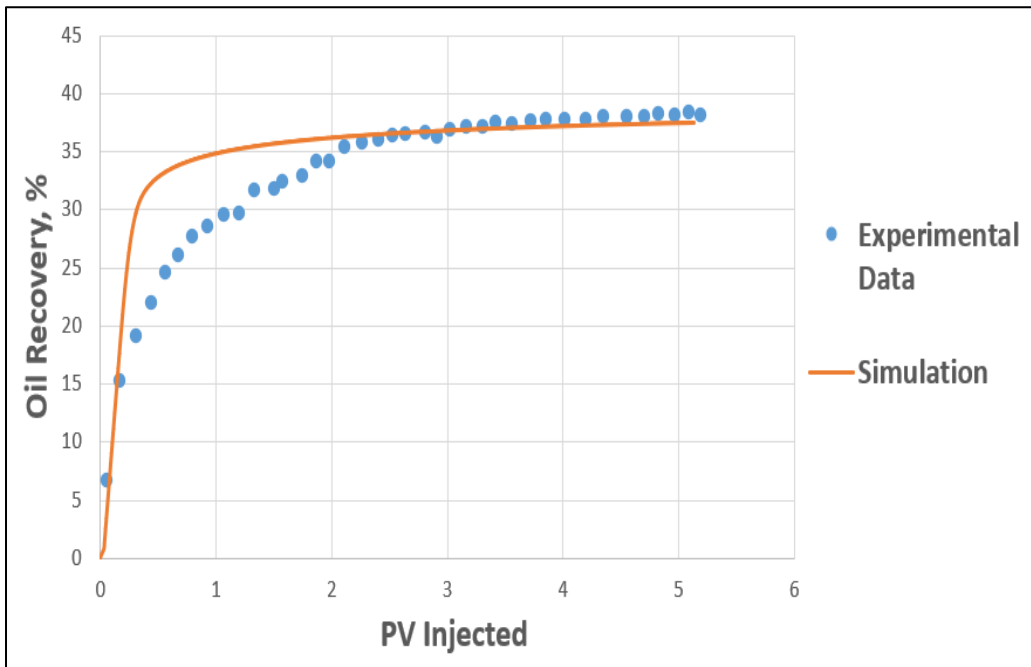


Figure 5.2: Oil recovery match for waterflooding experiment of Chandrasekhar and Mohanty (2013).

5.1.2 Polymer Rheological Studies

As was discussed in Chapter 3, the Extended Unified Apparent Viscosity Model (E-UVM) captures different regimes exhibited by polymers in porous media. In E-UVM, the Newtonian and shear-thinning flow is governed by the Carreau model, shear-thickening behavior is captured by Deborah number, and the degradation multiplier controls mechanical degradation of polymers. The model is based on UVM published earlier (Delshad *et al.*, 2008) that accommodates polymer Newtonian and shear-thinning behavior at low shear rates and shear-thickening at high rates observed primarily near the wellbores. In addition, E-UVM also characterizes the viscosity drop due to degradation at ultimate shear rates. In summary, the Carreau model defines only Newtonian and shear-thinning behavior. On the other hand, the UVM also accounts for the shear-thickening of viscoelastic polymers in porous media. Finally, the E-UVM captures all previously mentioned regimes and mechanical degradation of polymers.

Viscoelastic polymer flooding was simulated in the tertiary mode of injection after the secondary waterflooding stage using the MRST simulator. All three models (Carreau, UVM, and E-UVM) were separately implemented in MRST to distinguish the effect of different rheological regimes on oil recovery. The simulation results for C_p of 2000 ppm at 0.045 ml/min are depicted in **Figures 5.3, 5.4, and 5.5** for average inlet apparent viscosity, average trapping number, and oil recovery, respectively.

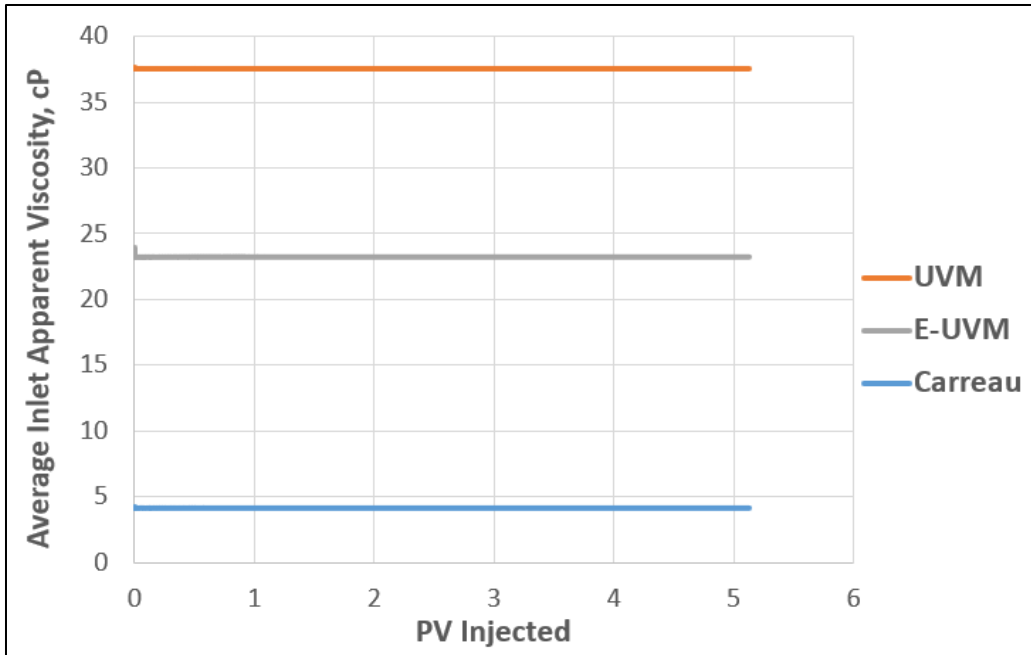


Figure 5.3: Average inlet apparent viscosities for different rheological models at 0.045 ml/min and $C_p=2000$ ppm.

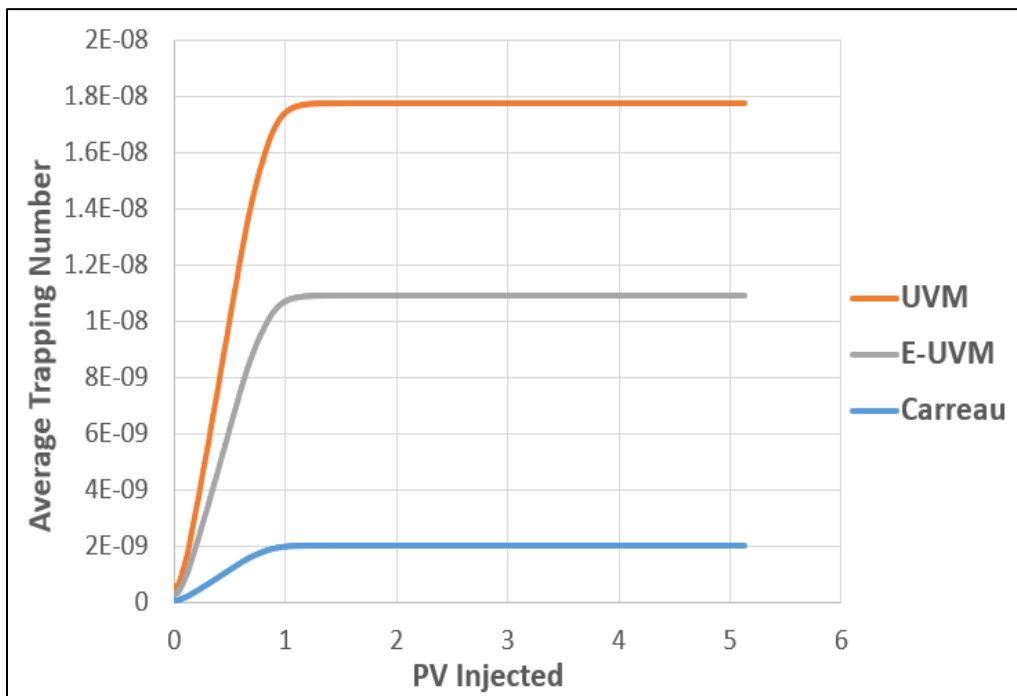


Figure 5.4: Average trapping numbers for different rheological models at 0.045 ml/min and $C_p=2000$ ppm.

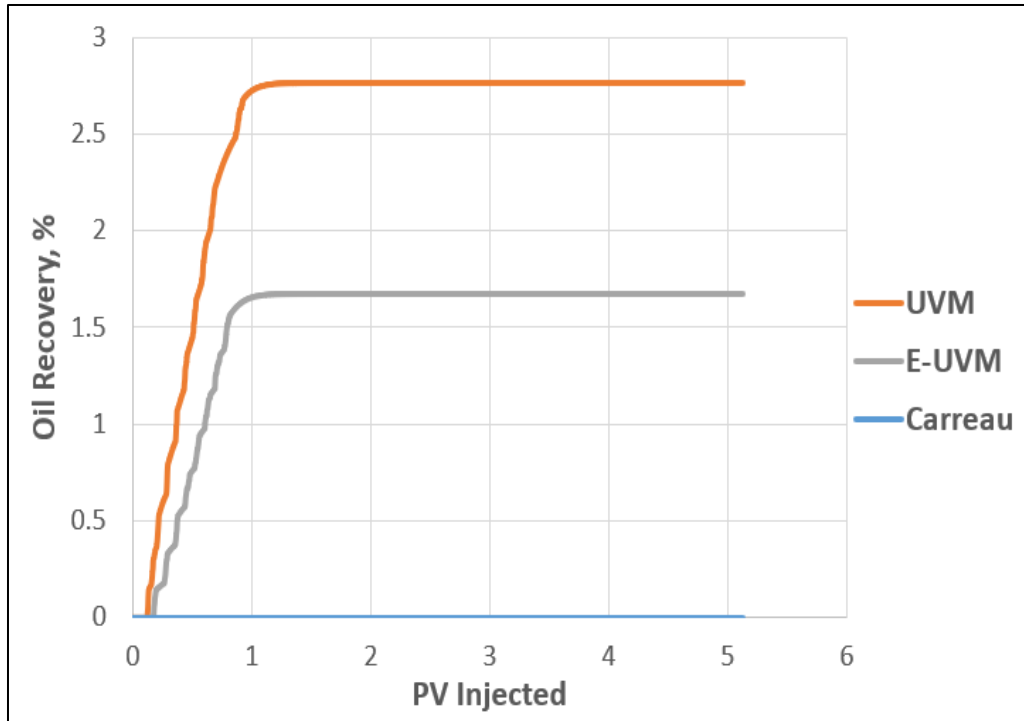


Figure 5.5: Oil recoveries for different rheological models at 0.045 ml/min and $C_p=2000$ ppm.

Since the onset for shear-thickening and mechanical degradation of polymers is observed at high shear rates, the main difference between the models arises near the wellbores. Therefore, we averaged the apparent viscosities at the cell interfaces near the injection well and visualized them in **Figure 5.3**. It is worth mentioning that average shear rates in the wellbore vicinity exceeded the third critical shear rate, and mechanical degradation occurred (**Figure 4.1**). Accordingly, the Carreau model yielded the lowest viscosities at high shear rates due to excessive shear-thinning of polymers. In contrast, viscosities estimated by the UVM were the highest since the model considered the viscosity increment due to shear-thickening. Notably, the E-UVM viscosities were comparatively lower, explained by the mechanical degradation occurring at ultimate shear rates.

The calculated trapping numbers were consistent with the apparent viscosities yielding the highest oil recovery for the UVM model. On the contrary, the Carreau model did not result in oil mobilization at 0.045 ml/min due to the negligible viscosifying power of polymers. Furthermore, the simulations were repeated for a higher injection rate of 4.5 ml/min, and the results are presented in **Figures 5.6, 5.7, and 5.8** for average inlet apparent viscosity, average trapping number, and oil recovery, respectively.

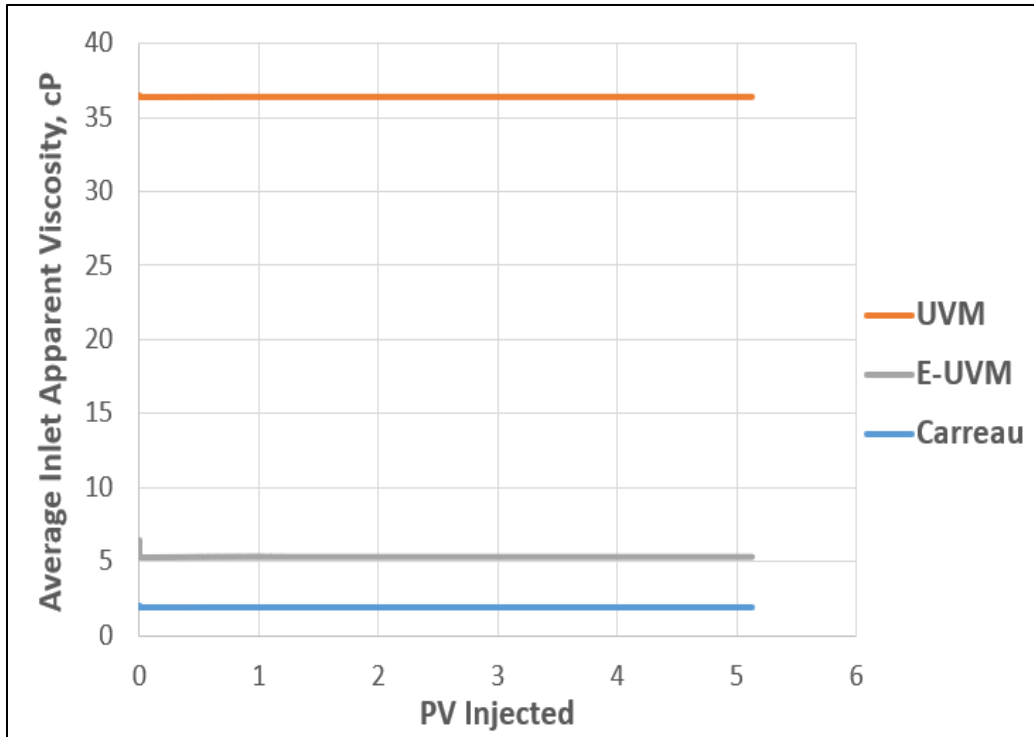


Figure 5.6: Average inlet apparent viscosities for different rheological models at 4.5 ml/min and $C_p=2000$ ppm.

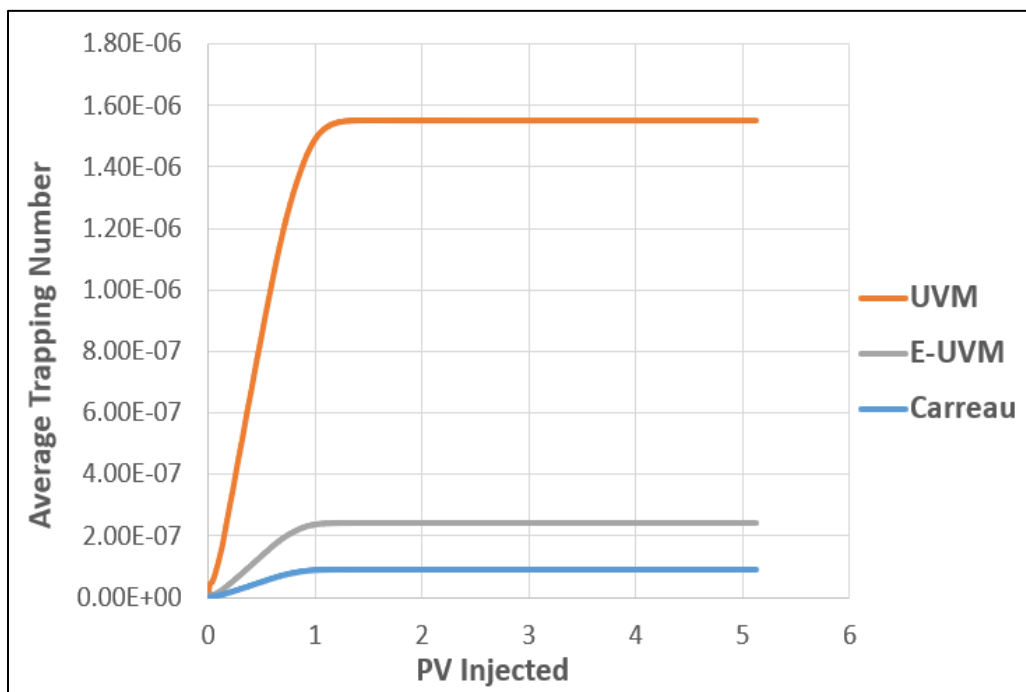


Figure 5.7: Average trapping numbers for different rheological models at 4.5 ml/min and $C_p=2000$ ppm.

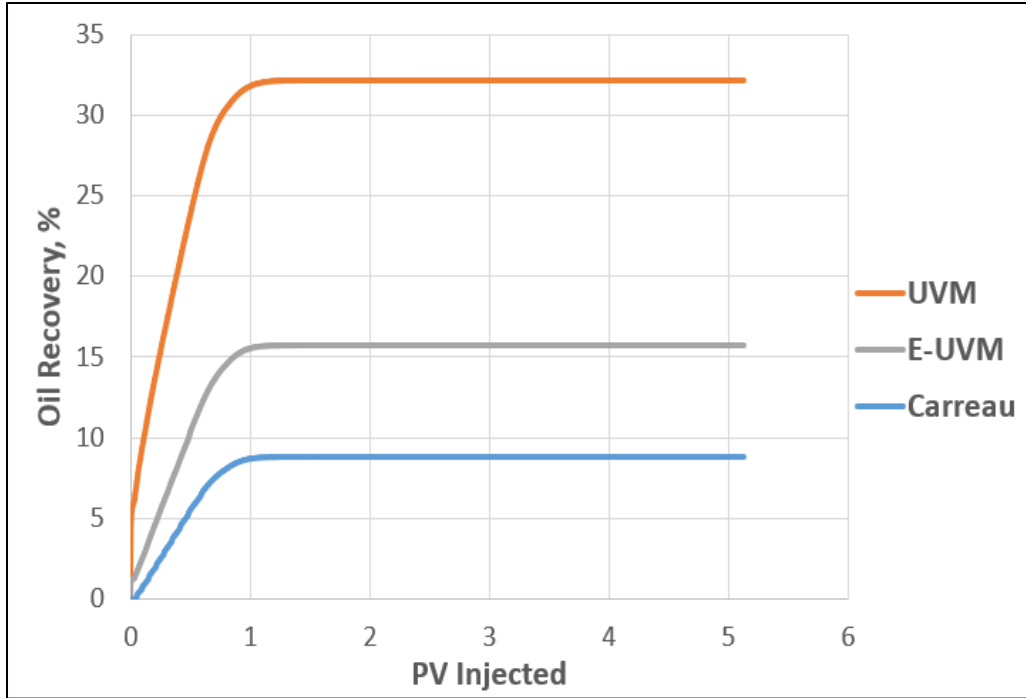


Figure 5.8: Oil recoveries for different rheological models at 4.5 ml/min and $C_p=2000$ ppm.

The increment in injection rate from 0.045 ml/min to 4.5 ml/min significantly increased the shear rates in the simulation model and exacerbated mechanical degradation. The average inlet apparent viscosities estimated at a given shear rate were correspondingly changed; however, the same trend of results still holds. For this case, the E-UVM viscosities decreased about five times due to injection rate increment leading to severe mechanical degradation. On the other hand, the UVM viscosities, reaching their maximum plateau values (μ_{max}) at 0.045 ml/min, were not notably increased with the injection rate.

Nevertheless, an increase in injection rate improved oil mobilization for all models (**Figure 5.8**). Namely, although the significant viscosity decrease for the E-UVM and Carreau models, the oil recoveries increased to 15% and 9%, respectively. The latter shows that at a constant injection rate, the oil recovery is a function of apparent viscosity, and the higher viscosity predicted by the model yields correspondingly high oil recovery. However, the injection rate was also found to have a more predominant effect on oil recovery as opposed to apparent viscosities.

These observations confirmed that using a suitable rheological model is essential in polymer flooding simulation to predict more accurate results. Therefore, for the regions where developed

shear rates exceed the critical shear rate for the mechanical degradation, utilizing UVM may result in overestimated oil recoveries since this model does not capture the viscosity drop. On the other hand, E-UVM accommodates all regimes and provides more accurate and representative results.

5.1.3 Polymer Concentration and Injection Rate Effects on Polymer Flooding

After implementing E-UVM in the reservoir simulator, the effect of different factors was investigated at the core scale. Since the simulation model represents a carbonate rock with low permeability, it was decided to keep the molecular weight of the polymers constant and vary their concentration. This is because using higher molecular weight polymers might be inefficient in such tight rock due to injectivity constraints. Additionally, the injection rate effect was also analyzed.

It was found that for all ranges of polymer concentrations and injection rates, the shear rates for the wellbore cells exceeded the critical shear rate for mechanical degradation, while shear-thinning and shear-thickening regimes were observed in the inner parts of the model. Moreover, increasing injection rates from 0.045 ml/min to 4.5 ml/min significantly increased the shear rates near wellbores and resulted in lower polymer viscosities due to severe degradation.

Polymer Concentration Effect. Polymer concentration effect on polymer flooding was investigated at constant injection rate. Firstly, we present the simulation results for 0.045 ml/min as depicted in **Figures 5.9, 5.10, 5.11** for pressure drop, average trapping number, and oil recovery, respectively.

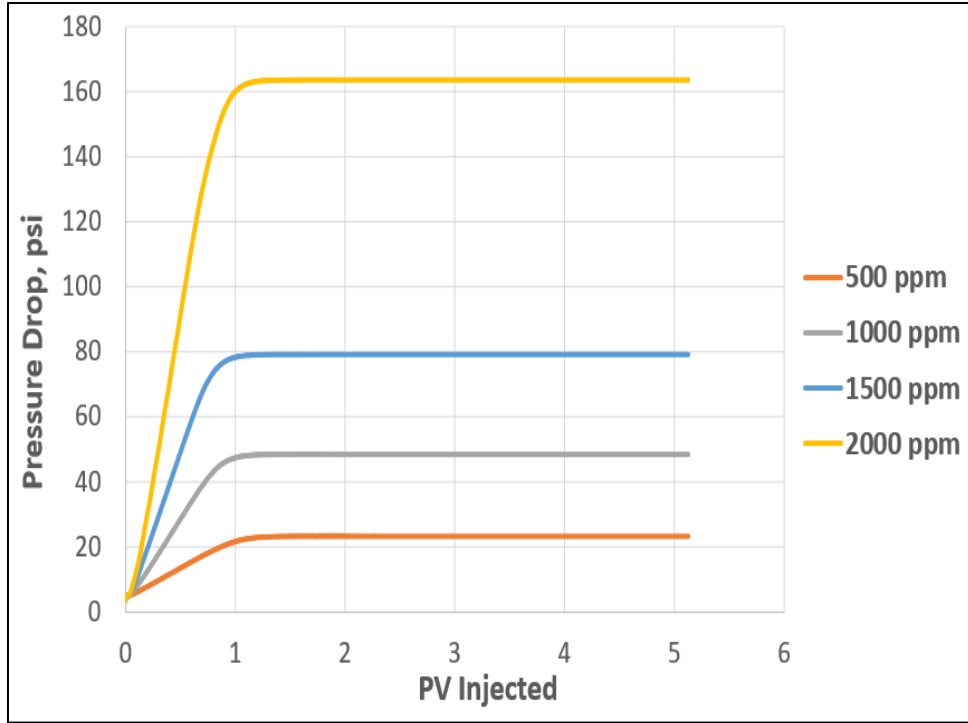


Figure 5.9: Pressure Drops as a function of polymer concentrations at 0.045 ml/min.

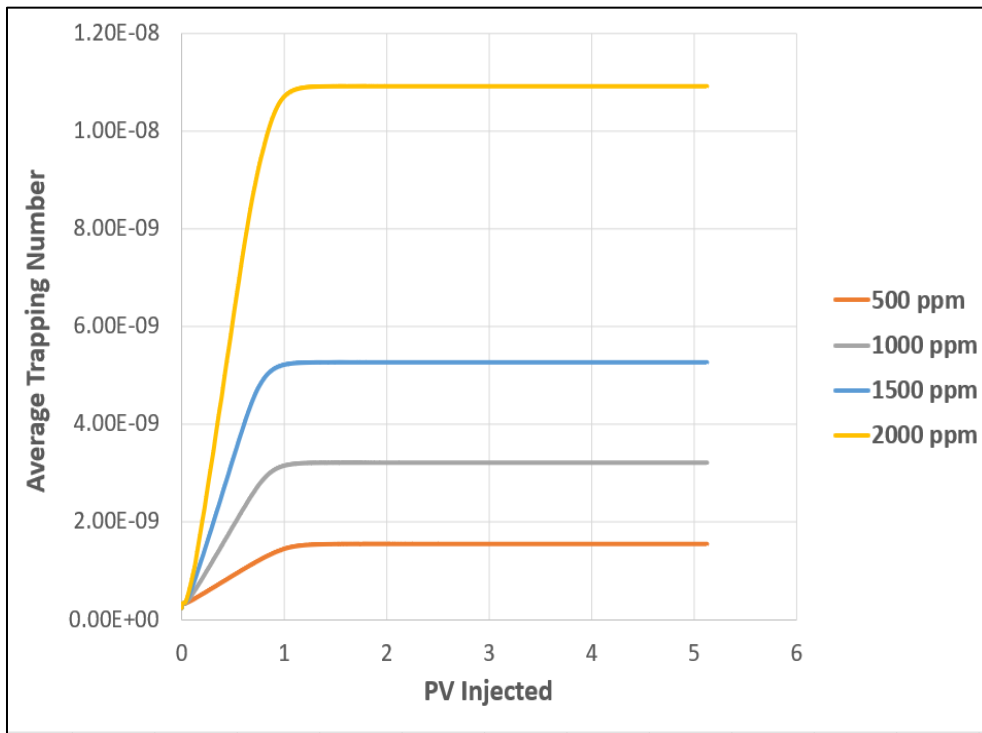


Figure 5.10: Average trapping numbers as a function of polymer concentrations at 0.045 ml/min.

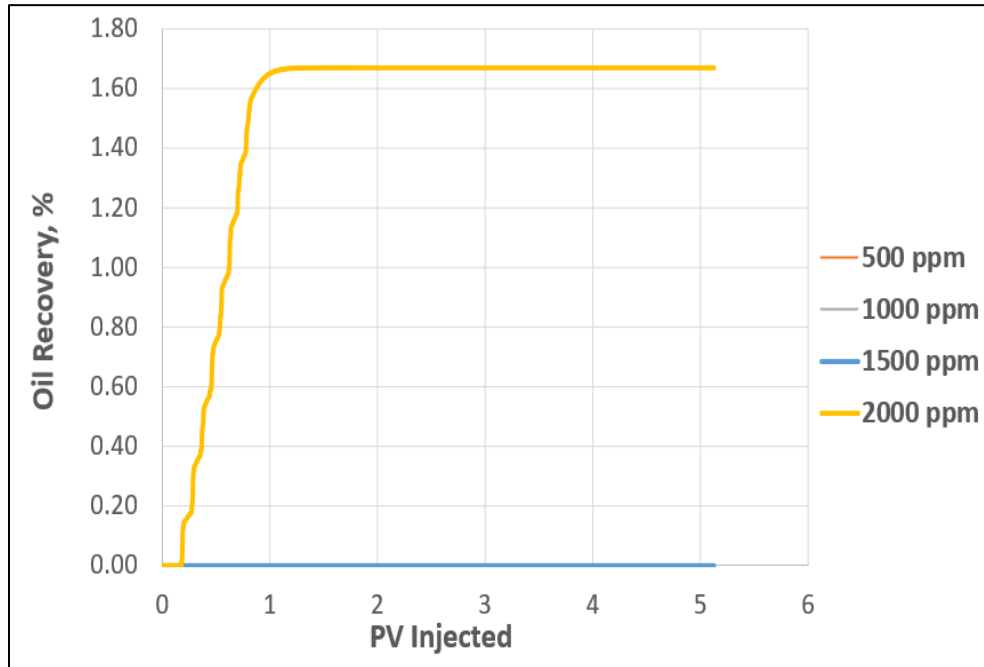


Figure 5.11: Oil recoveries as a function of polymer concentrations at 0.045 ml/min.

As can be observed from **Figure 5.9**, the pressure drops increased with polymer concentration. Moreover, the calculated trapping numbers were mainly driven by the pressure gradients. As was indicated before, the trapping numbers at low injection rates (0.045 ml/min) did not exceed the critical trapping number for a broad range of polymer concentrations. **Figure 5.10** shows that only 2000 ppm viscoelastic polymer flow obtained trapping numbers higher than the critical ($(N_T)_c \approx 8 \times 10^{-9}$). Therefore, we observe a slight incremental oil recovery of 2% only for 2000 ppm polymer injection (**Figure 5.11**).

Next, the simulation was repeated at the higher injection rate of 4.5 ml/min. The results for pressure drop, average trapping number, and oil recovery as functions of polymer concentration are depicted in **Figures 5.12, 5.13, 5.14**, respectively.

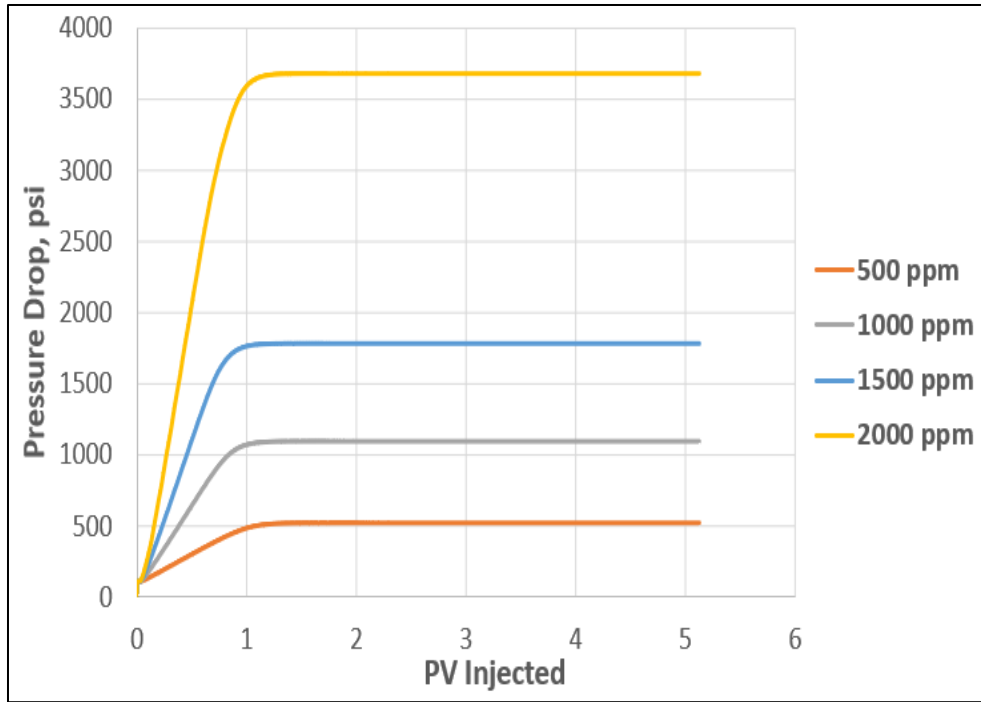


Figure 5.12: Pressure Drops as a function of polymer concentrations at 4.5 ml/min.

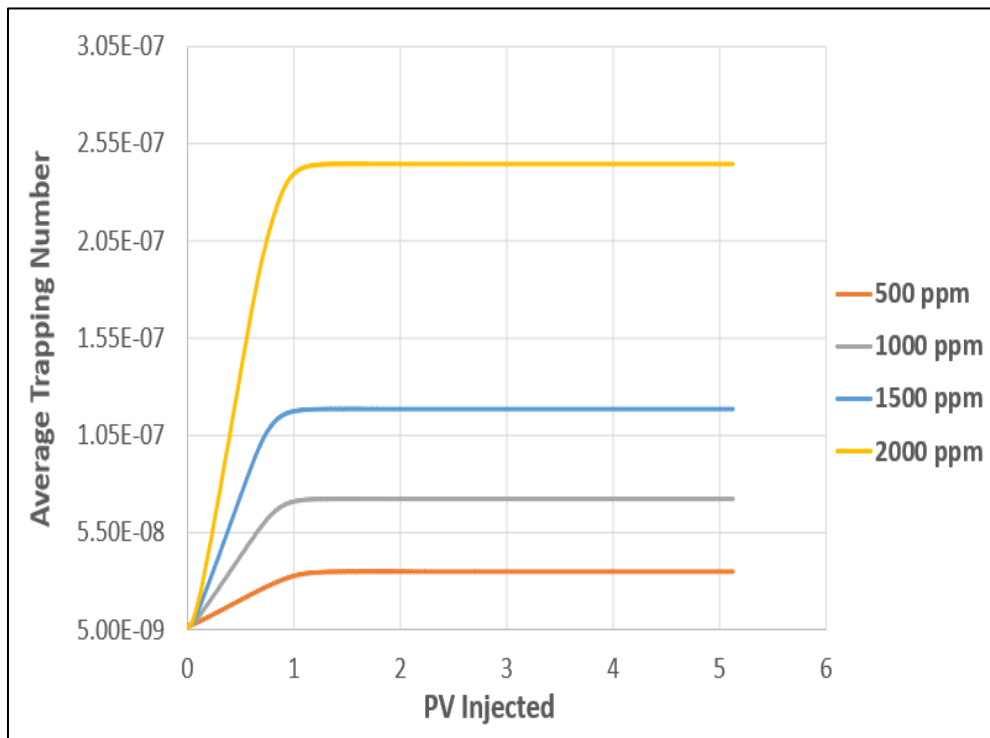


Figure 5.13: Average trapping numbers as a function of polymer concentrations at 4.5 ml/min.

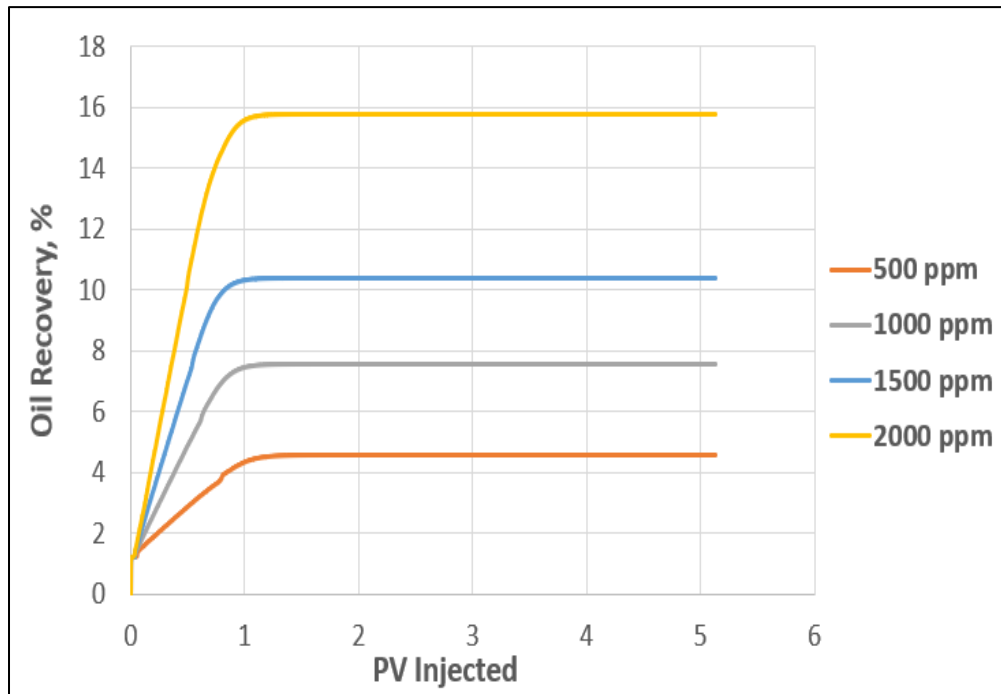


Figure 5.14: Oil recoveries as a function of polymer concentrations at 4.5 ml/min.

Similar to the case with a lower injection rate, the trapping numbers and corresponding oil recoveries increased with the increment in polymer concentration. Moreover, the trapping numbers for all polymer concentrations exceeded the critical trapping number and considerably displaced oil. More pronounced incremental oil recoveries were obtained in this case ranging between 4 – 16% OOIP.

Injection Rate Effect. Effect of injection rate was also investigated for a constant polymer concentration. Incremental oil recovery at low rates was obtained only for 2000 ppm polymer solution. Therefore, this particular concentration was used in the predictive studies. One should note that three injection rates were considered including 0.045, 0.45, and 4.5 ml/min. The results for pressure drop, average trapping number, and residual oil saturation as functions of injection rate are depicted in **Figures 5.15, 5.16, 5.17**, respectively.

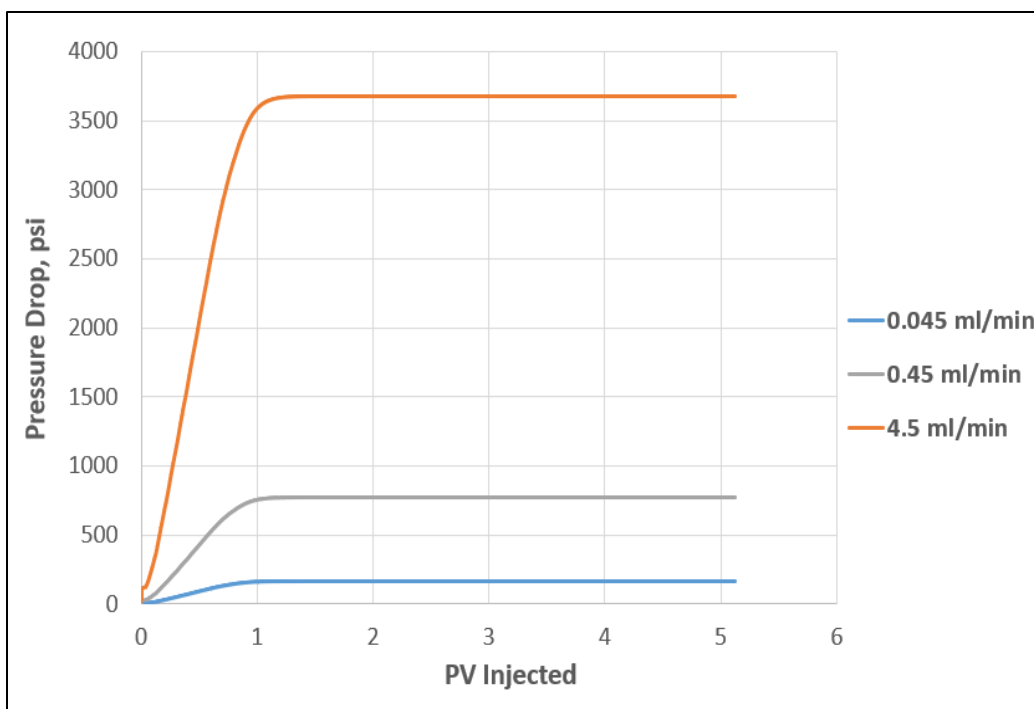


Figure 5.15: Pressure drops as a function of injection rate at $C_p=2000$ ppm.

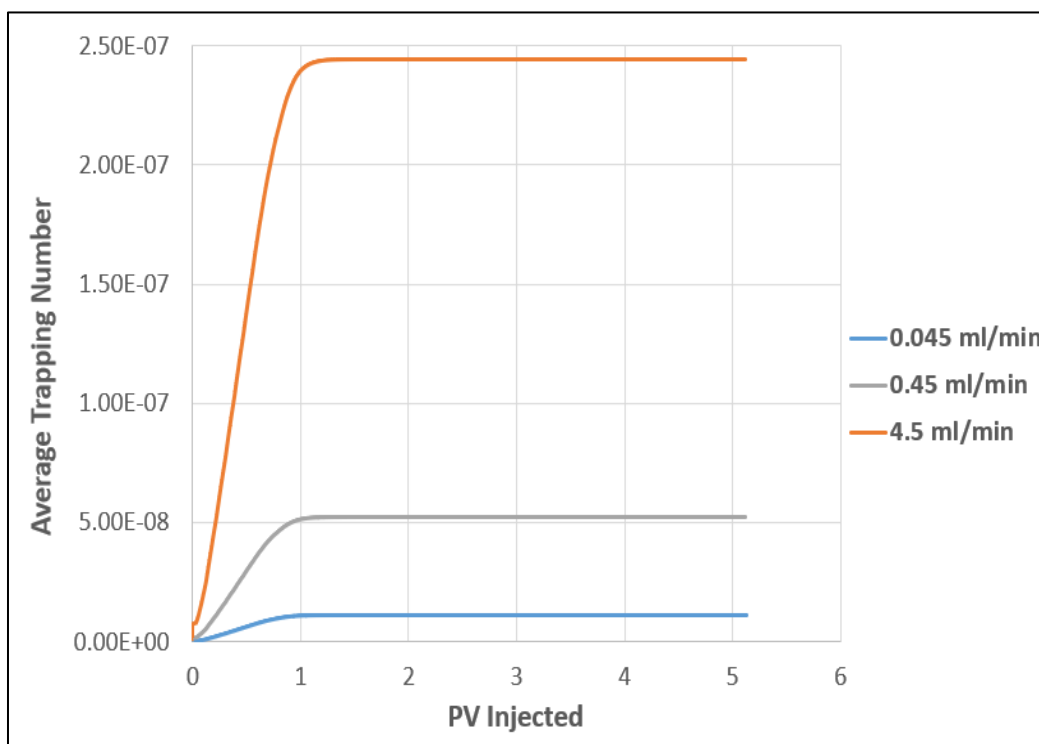


Figure 5.16: Average trapping numbers as a function of injection rate at $C_p=2000$ ppm.

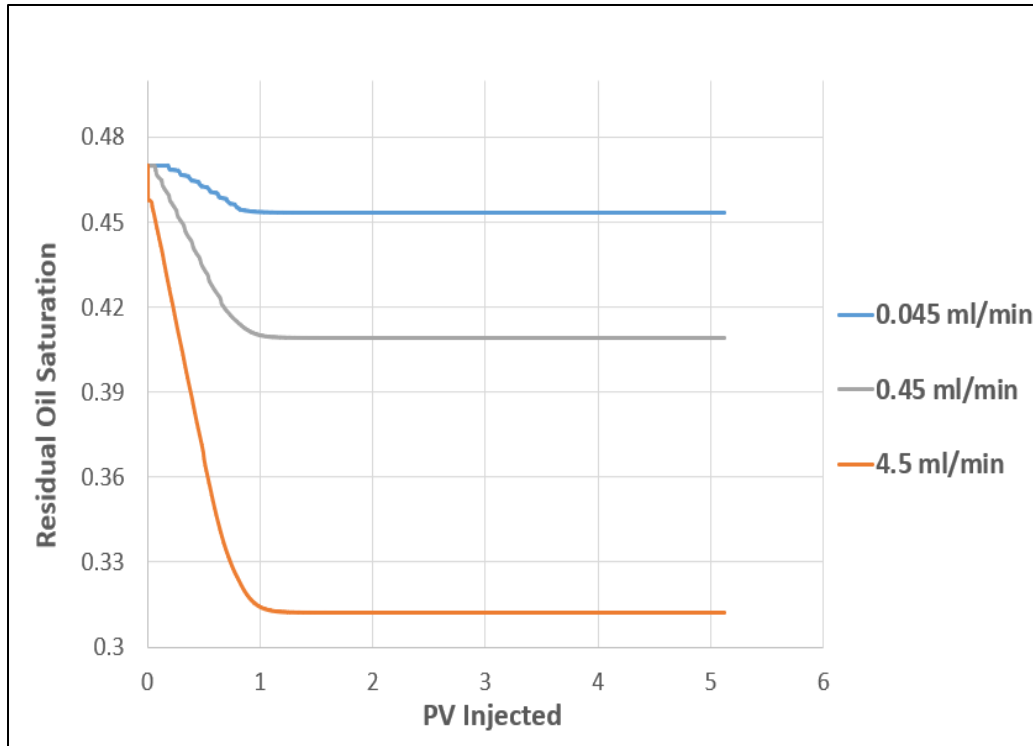


Figure 5.17: Residual oil saturations as a function of injection rate at $C_p=2000$ ppm.

Similar to polymer concentrations, injection rate also had a positive effect on residual oil saturation reduction. Particularly for 2000 ppm polymer injection, slight oil mobilization of 2% occurred even at 0.045 ml/min. Furthermore, with the increase in injection rate, the oil displacement was improved. Namely, residual oil saturation was reduced from 47 to 40% at 0.45 ml/min and further reduced to 31% at 4.5 ml/min. Additionally, the delay in oil displacement at low injection rates was related to the slow accumulation of trapping numbers in the system. Therefore, it took more time to exceed the critical trapping number at low injection rates (**Figure 5.16**).

5.1.4 Polymer Flooding Simulation at Secondary and Tertiary Injection Modes

The core-scale predictions for secondary and tertiary polymer injection of 2000 ppm concentration are discussed in this chapter. Firstly, the waterflooding at 0.045 ml/min was simulated as a secondary injection mode, followed by tertiary polymer flooding at 0.45 ml/min, and then polymer injection rate was increased to 4.5 ml/min. All injection stages were conducted for identical pore

volumes; 5 PVs for each injection cycle (**Figure 5.18**). Next, we simulated the case where a 2000 ppm polymer solution was injected in the secondary mode at 4.5 ml/min. The results of the latter simulation study is presented in **Figure 5.19**.

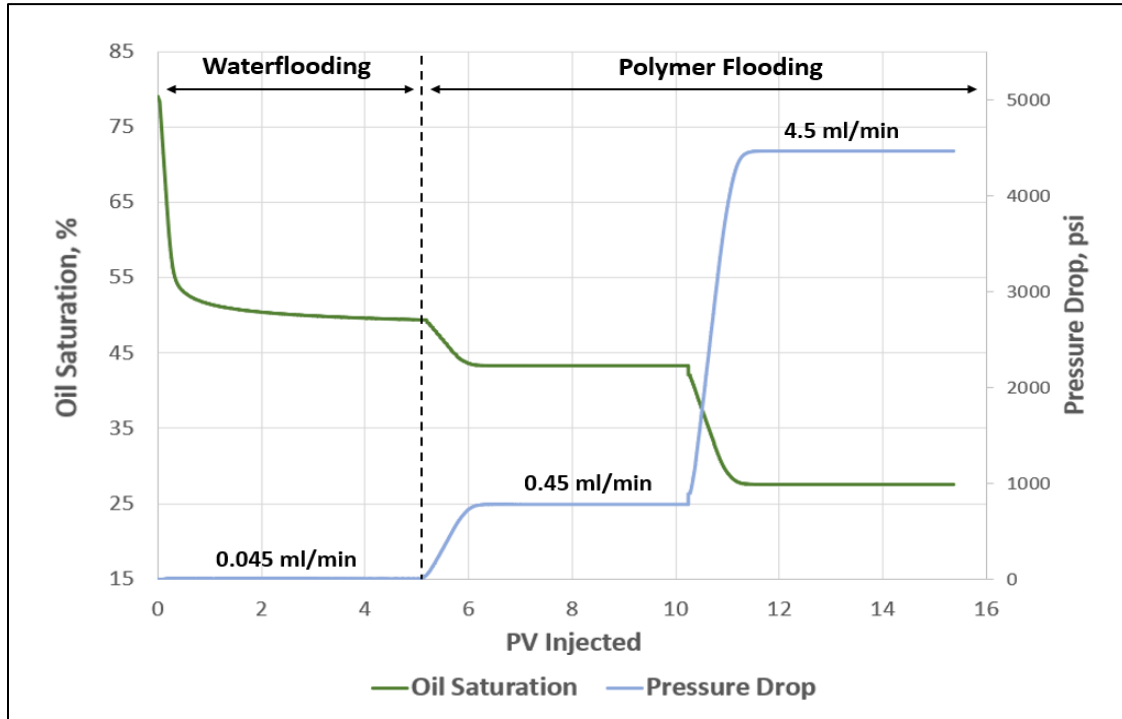


Figure 5.18: Simulation results for tertiary polymer flooding ($C_p=2000$ ppm).

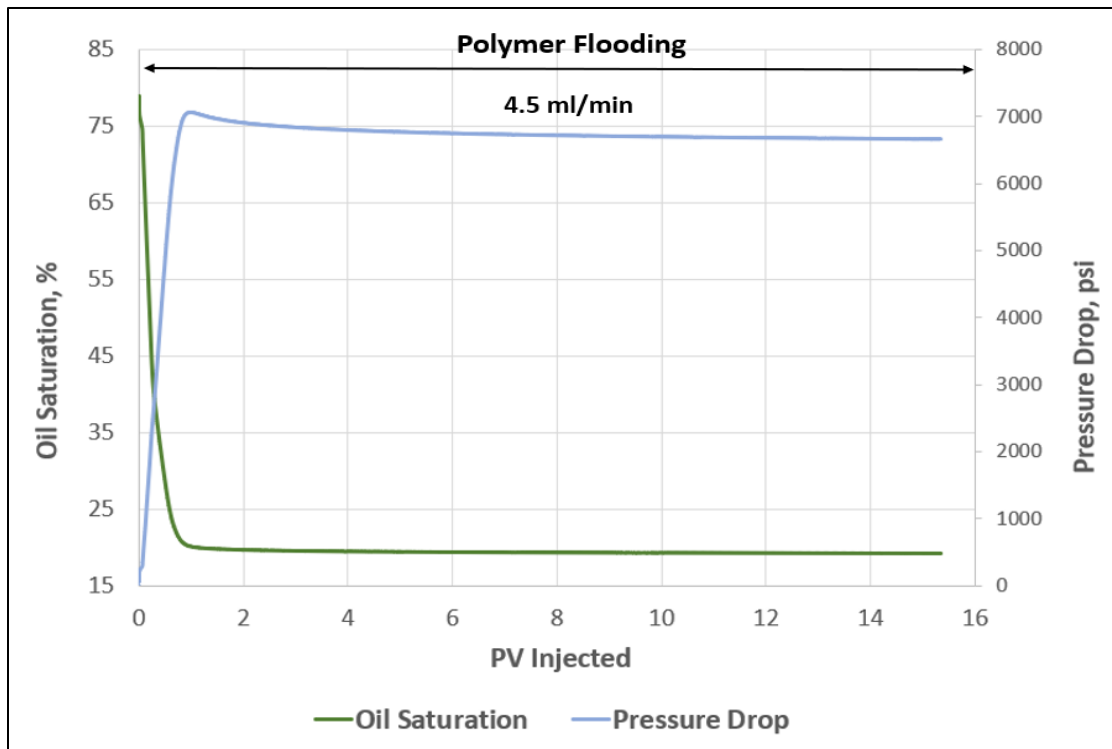


Figure 5.19: Simulation results for secondary polymer flooding ($C_p=2000$ ppm).

For the first case (**Figure 5.18**), the water injection was first initiated, leading to around 40% OOIP of oil recovery after injecting about five pore volumes. The remaining 47% of oil saturation was assumed very close to true residual oil saturation to water. Next, the polymer solution with a concentration of 2000 ppm was selected for simulations. The polymer solution was first injected at 0.45 ml/min for additional five pore volumes and reduced the residual saturation to 40%. Finally, the polymer injection rate was increased to 4.5 ml/min and continued for the subsequent five pore volumes. Eventually, the remaining oil saturation to the three injection stages was predicted as 27%. Moreover, as was expected, the pressure drop was rapidly increased with injection rates.

On the other hand, we also simulated the case where the polymer solution was injected at the secondary mode of injection (**Figure 5.19**). In this case, pronounced pressure drop increase and oil saturation decrease to 20% were observed after injecting only one pore volume. Then, the pressure drop was stabilized, and no additional oil was produced. Consequently, the results showed that secondary polymer flooding might yield more oil recovery at fewer pore volumes (more cost-efficient) as opposed to tertiary polymer flooding. This is because for tertiary polymer flooding, it

takes time for the polymer front to displace the water, contact the remaining oil, and build an oil bank, and hence, more pore volumes are required. Nevertheless, for the actual polymer flooding project implemented in the field, many other factors must be considered before injecting the polymers in the secondary mode, including project economics, injectivity constraints, and other uncertainties.

5.2 Field-Scale Simulation Studies

Section 5.2 introduces field-scale predictions of polymer flooding technique by upscaling the core-scale simulation model. The field-scale simulation studies of this work were conducted in a quarter 5-spot well pattern, using rock and fluid properties representing the Middle East carbonate reservoirs. Moreover, sensitivity analysis was performed by changing reservoir permeability, reservoir heterogeneity, polymer concentration, and injection pressure to investigate their effects on incremental oil recovery.

5.2.1 Field-Scale Simulation Model

A field-scale simulation model was constructed based on rock and fluid properties used for core-scale predictions. A quarter 5-spot model with the dimensions of 360ft \times 360ft \times 60ft had a Cartesian grid of 15 \times 15 \times 5 gridblocks in the x, y, and z directions, respectively. **Table 5.1** summarizes all parameters of the reservoir model.

Table 5.1: Field-scale simulation model dimensions

Parameter	Value	Comments
Number of Gridblocks	1125	3D Model (15 \times 15 \times 5)
Gridblock Size (ft)	$\Delta x = 24$ $\Delta y = 24$ $\Delta z = 12$	Constant grid size in each direction
Reservoir Model Dimensions (ft)	360 \times 360 \times 60	Length \times Width \times Height
Distance between Injector and Producer (ft)	509.12	Quarter 5-spot model

Furthermore, for the base case simulations, the model was set heterogeneous with the average permeability of 50 mD and Dykstra-Parsons coefficient of 0.8. The permeability distribution is depicted in **Figure 5.20**. Moreover, the porosity was taken as 0.2, and the initial reservoir pressure was 3000 psia. The initial oil saturation was equal to 0.75, similar to the core-scale model. The formation water salinity was taken as 180,000 ppm, and the same salinity was assumed for injected polymer solution (ppm). All other input parameters used for the base case simulation study are listed in **Table 5.2**.

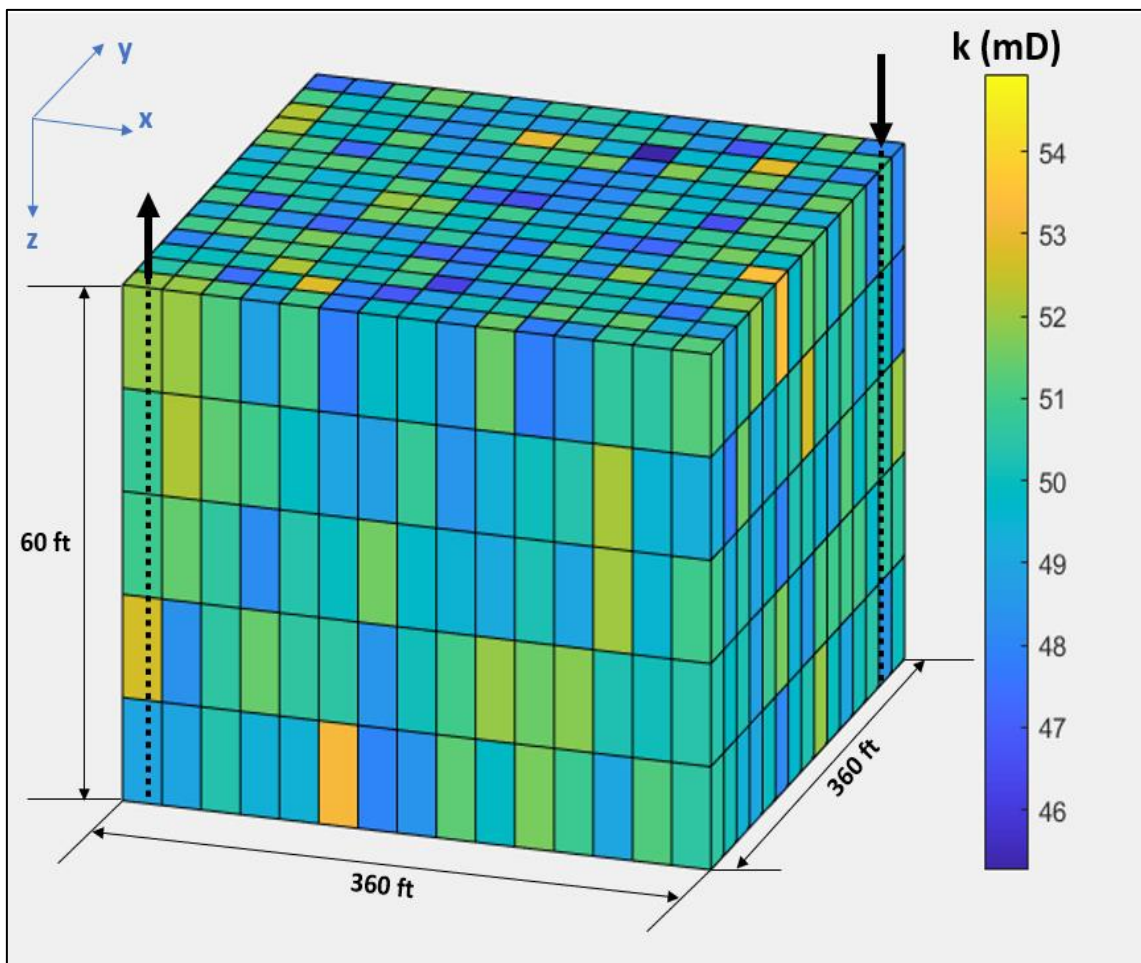


Figure 5.20: Field-scale simulation model with heterogeneous permeability.

Table 5.2: Input parameters for the field-scale simulation model (base case)

Pore Volume (ft³)	11.64×10 ⁵	Reservoir Model Area (acres)	3
Average Permeability (mD)	50	Dykstra-Parsons Coefficient	0.8
Porosity	0.19	Initial Oil Saturation	0.75
Water Viscosity (cP)	0.5	Oil Viscosity (cP)	0.9
Water Density (g/cm³)	1.118	Oil Density (g/cm³)	0.9
Residual Oil Saturation to Waterflooding	0.43	Irreducible Water Saturation	0.25
k_{ro}^*	0.23	k_{rw}^*	0.2
n_o	2.67	n_w	2.55
Injected Polymer Concentration (ppm)	1500	Polymer Molecular Weight (MDa)	8
Wellbore Radius (ft)	0.3	Interfacial Tension (mN/m)	30
Time to inject 1 PV of formation water (years)	0.5	Time to inject 1 PV of polymers (years)	15
OOIP (M STB)	23.67	P_{initial} (psi)	3000

It is worth mentioning that the oil formation volume factor was estimated as 1.248 bbl/STB using the correlations of Ahmed (1989) and used in the calculation of OOIP. Moreover, the bubble-point pressure of 1800 psi was calculated using Standing (1981) correlation (**Appendix A**). Furthermore, the typical fracture gradient for Middle East carbonate reservoirs was taken as 0.797 psi/ft (Aftab *et al.*, 2020), and formation fracturing pressure was estimated assuming the reservoir depth as 6900 ft.

During secondary waterflooding, the production well was set at constant bottom-hole pressure of 2000 psi, while the injection well was controlled by the rate of 1000 bbl/d. We simulated the waterflooding for 2 PV, which took approximately 365 days. Later, water injection was switched to polymer flooding that was simulated for an additional 2 PV. During tertiary

polymer flooding, the injection well was controlled by constant bottom-hole pressure of 4500 psi, which is lower than the formation fracturing pressure (Table 5.3). Moreover, due to injectivity constraints and gradual reservoir sweep by viscous polymers, the injection rates decreased considerably as the polymer flooding was initiated (Figure 5.21).

Table 5.3: Applied pressure gradient and trapping number calculations (base case)

Water Injection Rate (bbl/d)	1000	Producer BHP (psi)	2000
Polymer Injection Pressure (psi)	4500	Depth (ft)	6900
Maximum Applied Pressure Gradient for Water Injection (psi/ft)	2.94	Applied Pressure Gradient for Polymer Injection (psi/ft)	2.45
Bubble-point pressure (psi)	1800	Formation Fracturing Pressure (psi)	5500
Formation Water Average Trapping Number	1.2×10^{-9}	Polymer Solution Average Trapping Number	3.2×10^{-8}

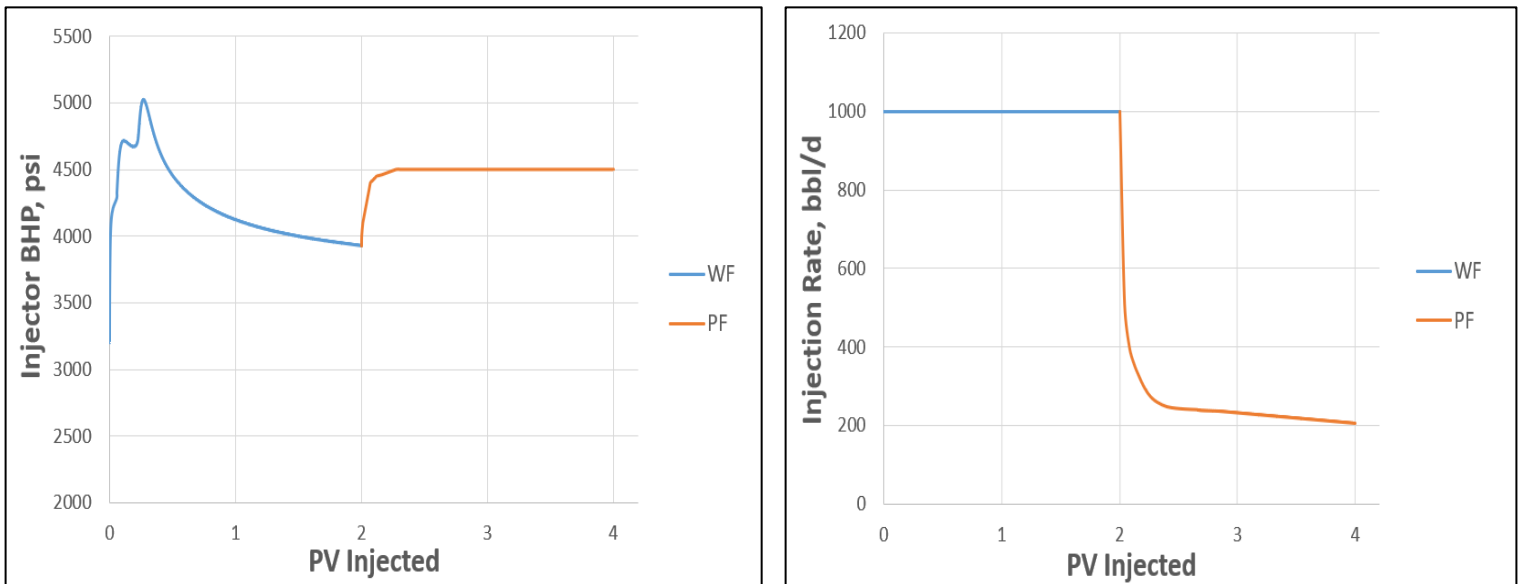


Figure 5.21: BHP (left) and injection rate (right) for injection well during secondary waterflooding and tertiary polymer flooding.

Grid Refinement Study. The proper number of gridblocks for the field-scale model was selected based on grid refinement analysis. The coarse-grid model used in base case simulations was compared with a fine-grid model having dimensions of $22 \times 22 \times 17$ to capture the physics of the problem and investigate the numerical accuracy of the simulation. Eventually, it was decided to use the model incorporating $15 \times 15 \times 5$ gridblocks since increasing resolution did not considerably impact the simulation results. **Table 5.4** and **Figure 5.22** below show the results of grid refinement study for the reservoir model.

Table 5.4: Grid refinement analysis for the quarter 5-spot field model

Reservoir Model	Coarse Reservoir Model	Fine Reservoir Model	Recovery Absolute Error (%)
Dimensions	$15 \times 15 \times 5$	$22 \times 22 \times 17$	
Injection Cycle	Ultimate Oil Recovery (% OOIP)		
Water Injection	34.859	35.105	0.246
Polymer Injection	55.501	55.892	0.391

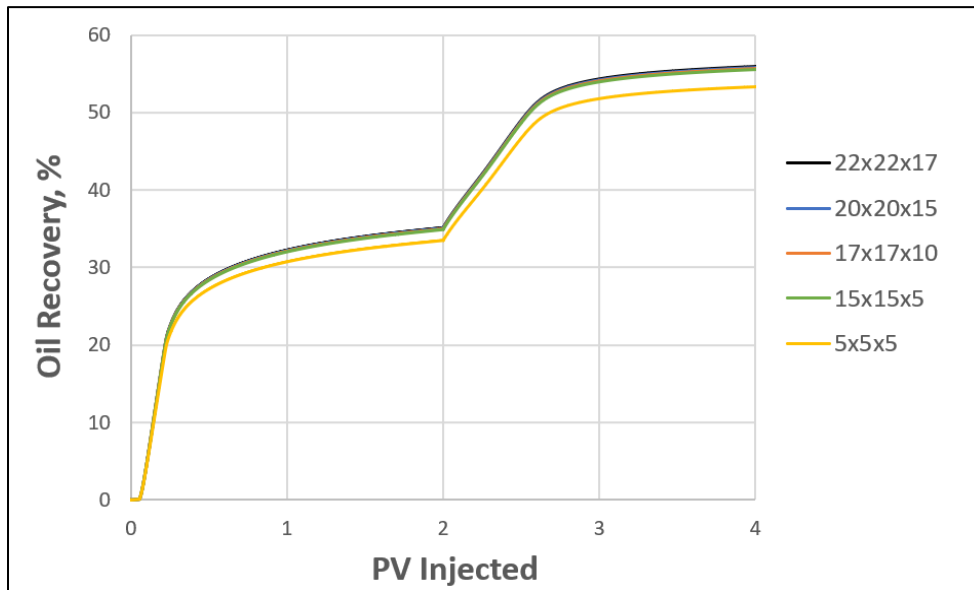


Figure 5.22: Effect of grid resolution on oil recovery during both waterflooding and polymer flooding processes.

5.2.2 Base Case Simulation Results

The base case predictions for remaining oil and water saturations after simulating waterflooding for 2 PVs are illustrated in **Figures 5.23-5.26** as 2D and 3D maps. It is worth mentioning that all 2D maps are illustrated for the first (upper) layer.

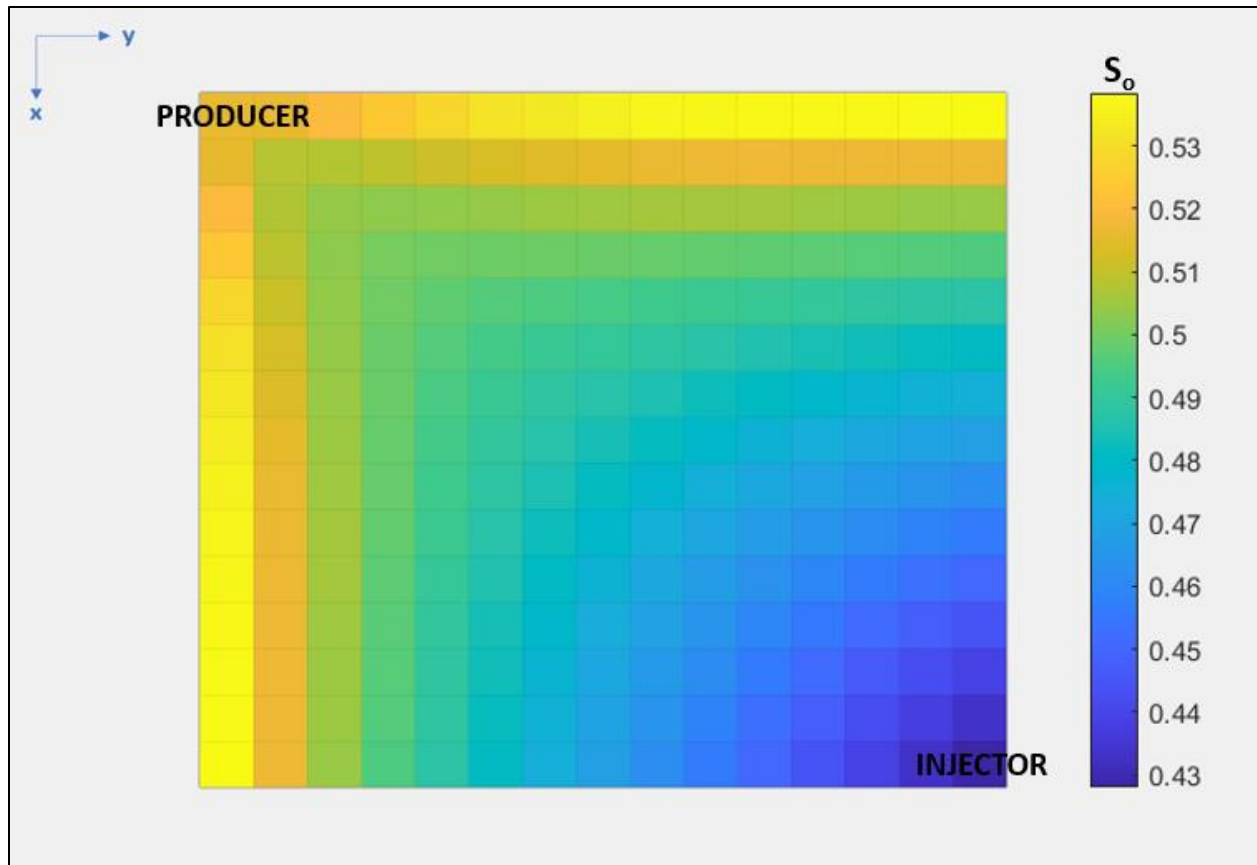


Figure 5.23: 2D map of remaining oil saturation at 2 injected PVs (after secondary waterflooding).

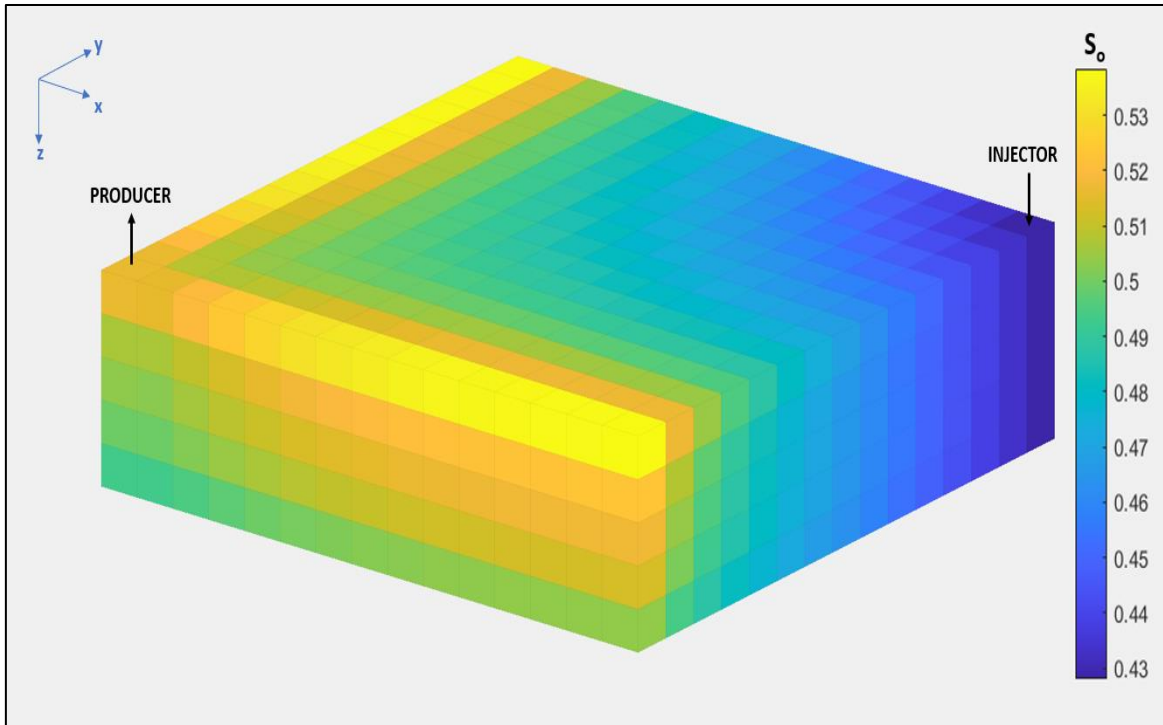


Figure 5.24: 3D map of remaining oil saturation at 2 injected PVs (after secondary waterflooding).

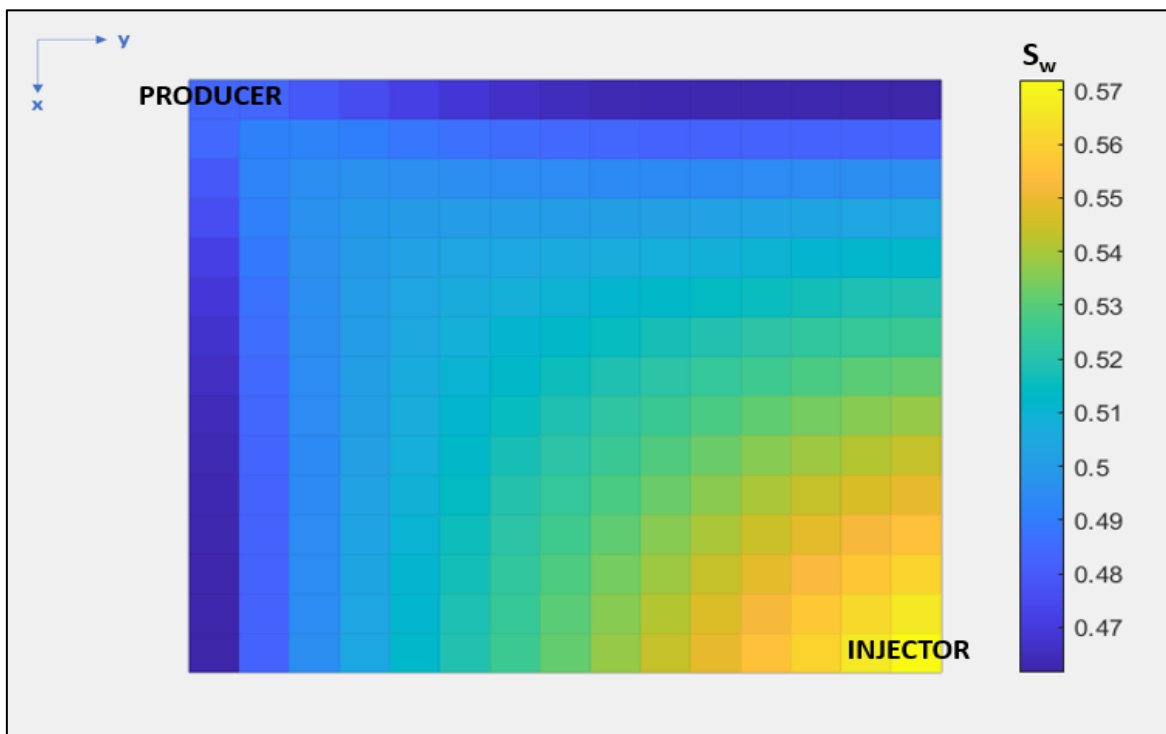


Figure 5.25: 2D map of water saturation at 2 injected PVs (secondary waterflooding).

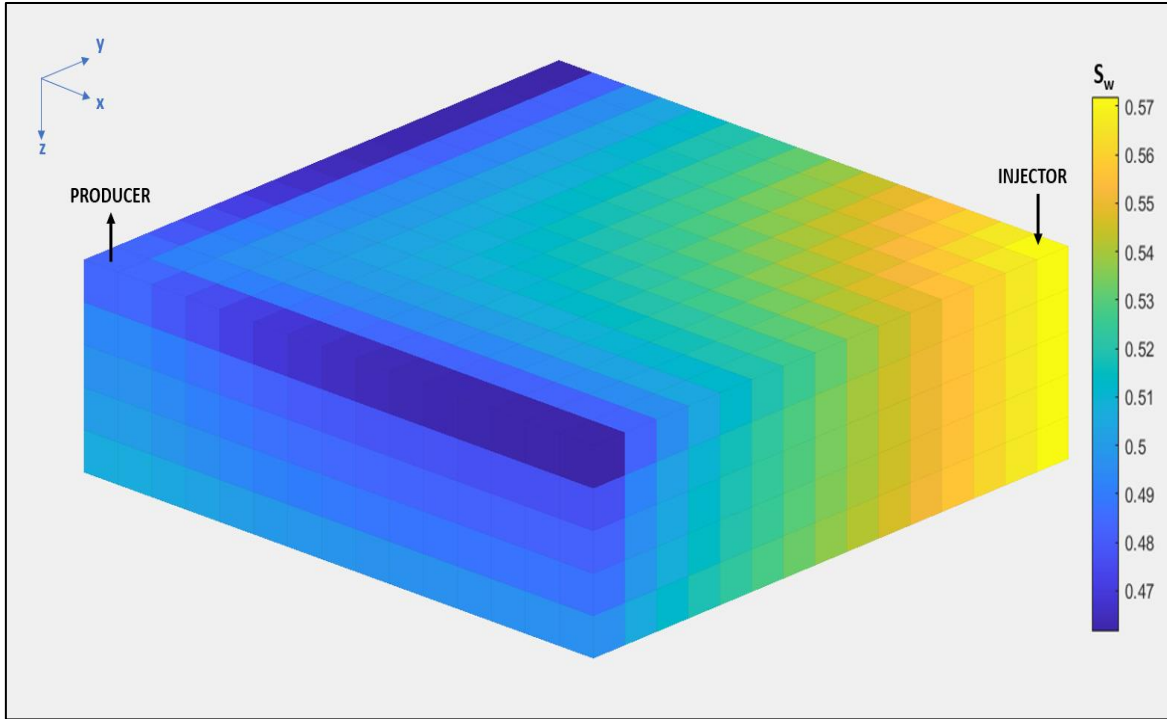


Figure 5.26: 3D map of water saturation at 2 injected PV (after secondary waterflooding).

The figures above show satisfactory areal and vertical sweep efficiencies of water in the reservoir except for some upper layers where gravity override is observed. Furthermore, the simulation studies were also conducted for the tertiary polymer flooding. 2D and 3D maps of remaining oil and water saturations after injecting an additional 2 PV of polymers are shown in **Figures 5.27-5.30**.

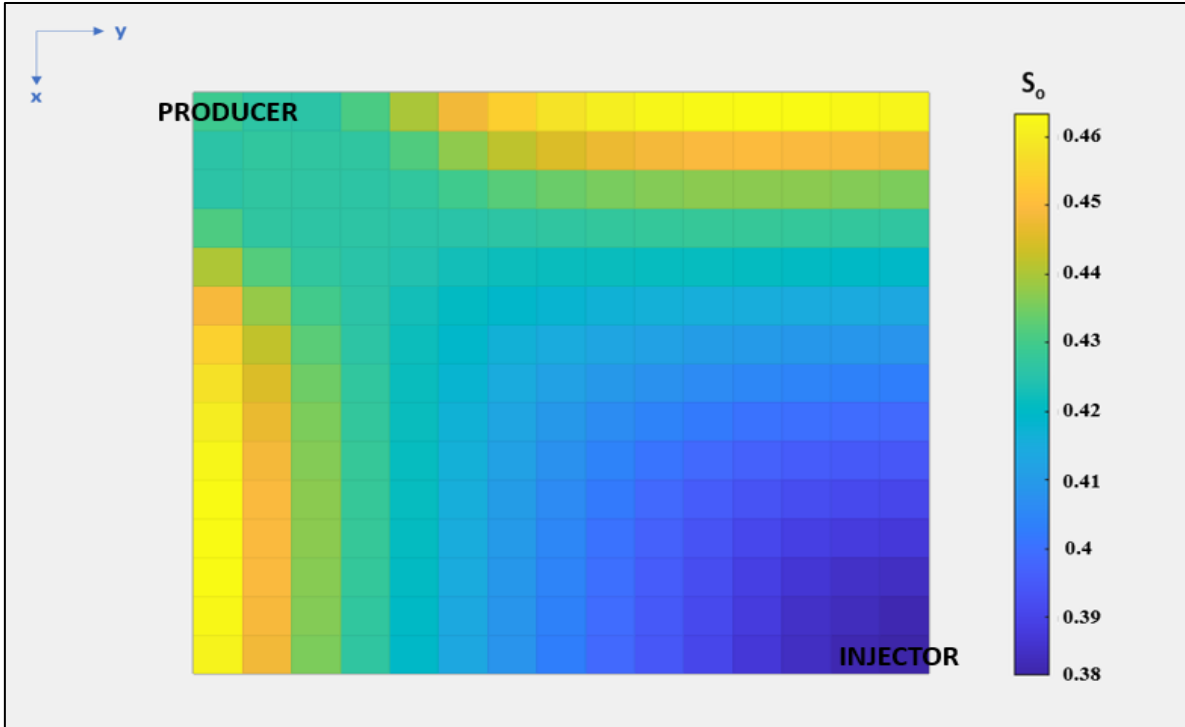


Figure 5.27: 2D map of remaining oil saturation at 4 injected PVs (after tertiary polymer flooding).

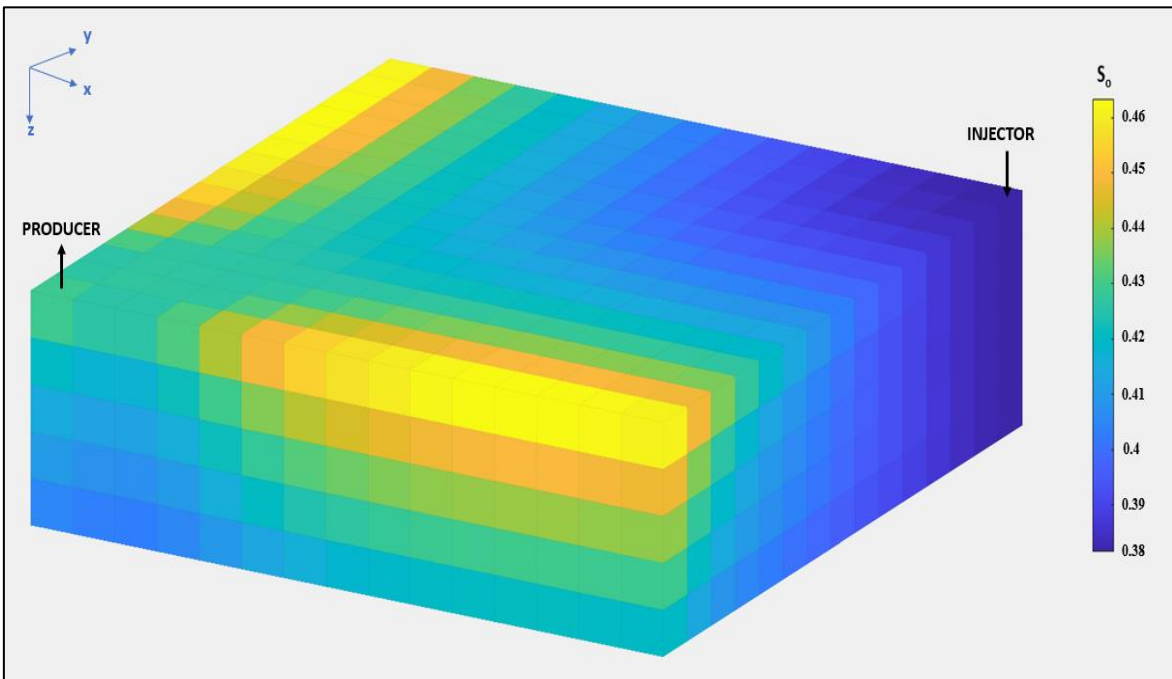


Figure 5.28: 3D map of remaining oil saturation at 4 injected PVs (after tertiary polymer flooding).

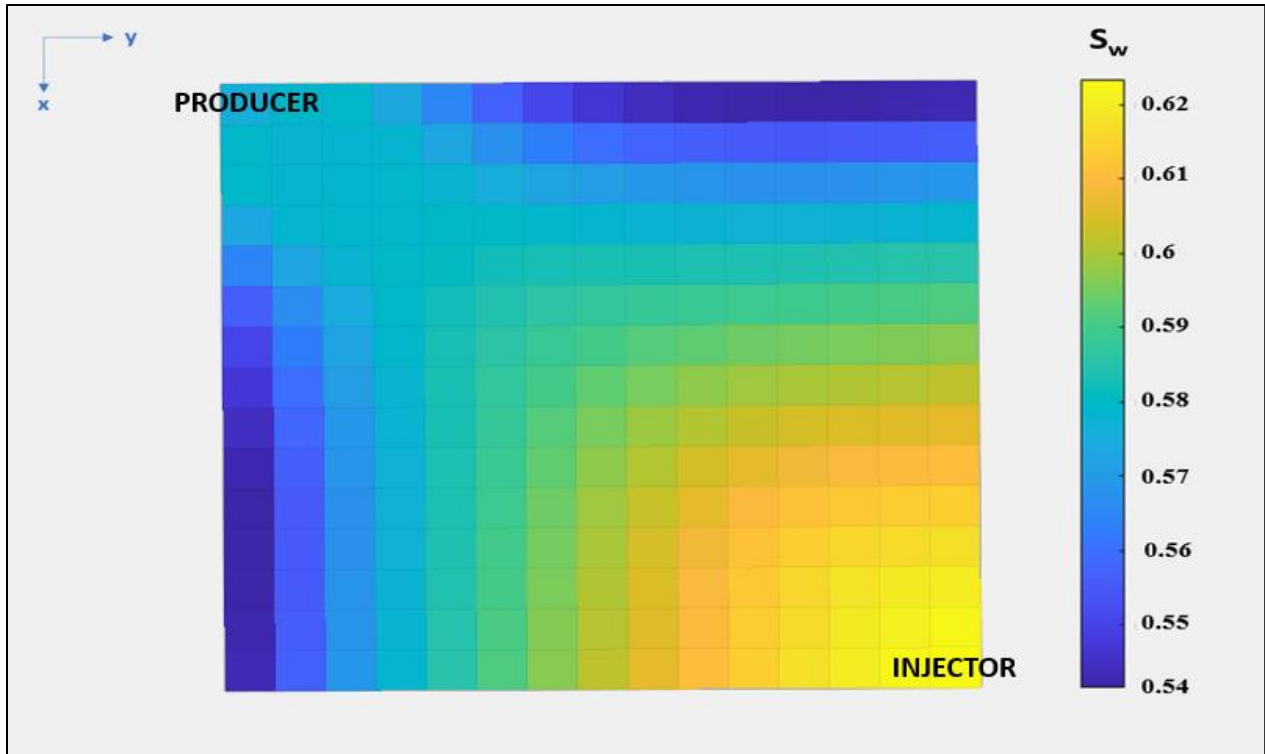


Figure 5.29: 2D map of water saturation at 4 injected PVs (after tertiary polymer flooding).

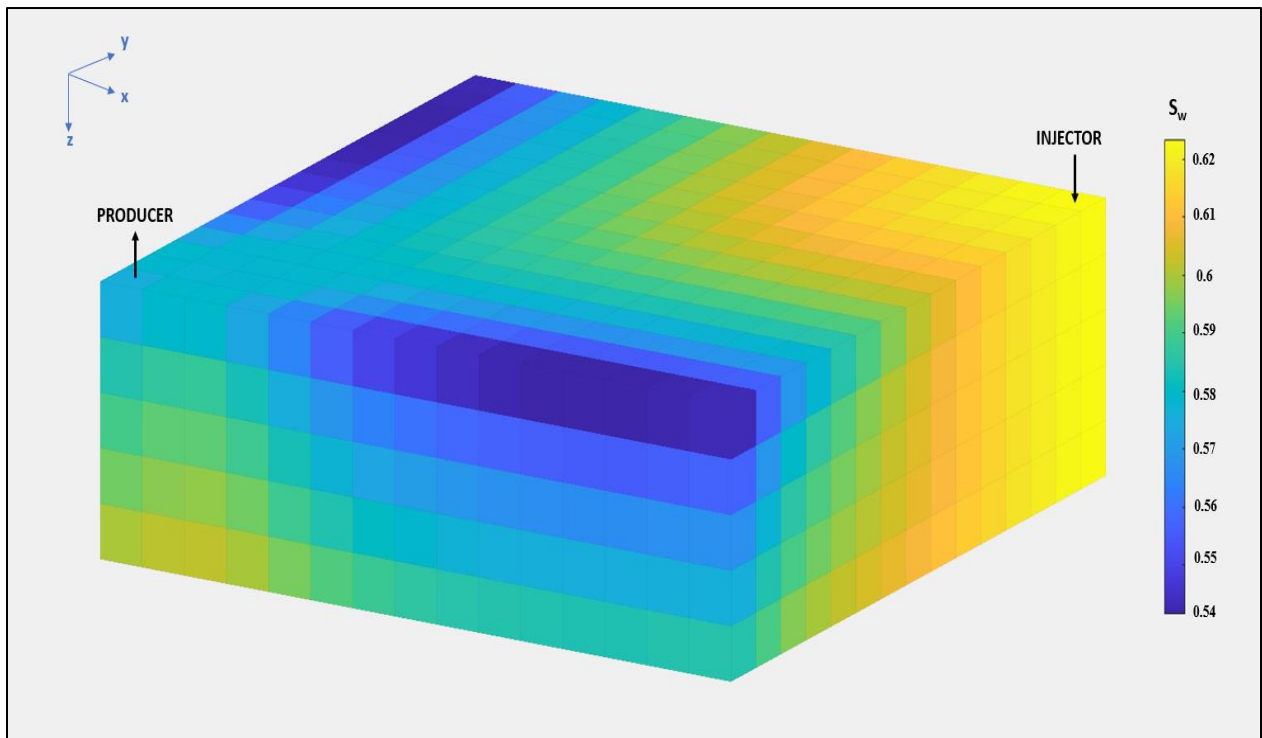


Figure 5.30: 3D map of water saturation at 4 injected PV (after tertiary polymer flooding).

According to the figures above, tertiary polymer injection, following the secondary waterflooding, considerably reduced remaining oil saturation and improved volumetric sweep efficiency. Improvements in sweep efficiency may also be observed in **Figure 5.31**, which illustrates polymer concentration distribution in a reservoir model after injecting 2 PVs of a polymer solution. In this case, the polymer concentration is uniformly distributed almost in the entire reservoir showing good sweep efficiency. Moreover, the normalized effluent concentration of polymers is also reported in **Figure 5.32**. According to the figure, polymers were first produced at 0.5 PV upon polymer flooding was initiated, and normalized concentration reached unity after injecting around 1.4 PV of the polymer solution, explained by the high heterogeneity of carbonate rock ($DP=0.8$). Furthermore, the effect of polymer flooding on displacement efficiency was also analyzed in **Figures 5.33** and **5.34**. It was found that for the base case simulation study, oil mobilization is pronounced only in the vicinity of the wellbores where high pressure (potential) gradients generate large trapping numbers. Namely, the residual oil saturation was reduced to around 37% in the regions adjacent to the wellbores. However, generally, trapping numbers did not exceed the critical trapping number, and residual oil saturation remained 43% similar to that of waterflooding.

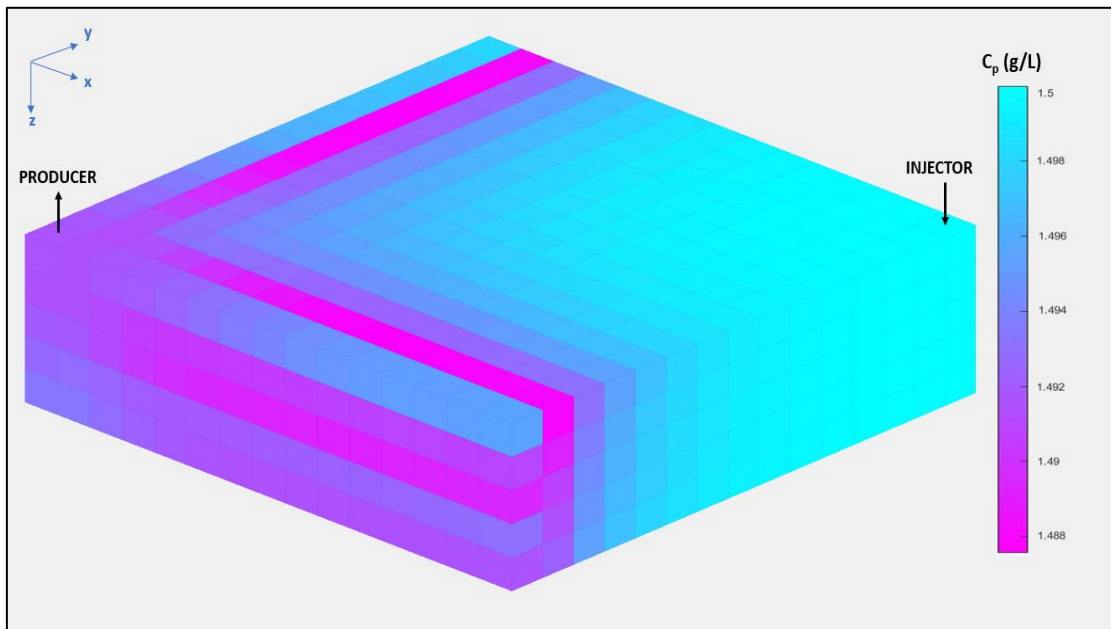


Figure 5.31: Polymer concentration in the reservoir model at 4 PVs.

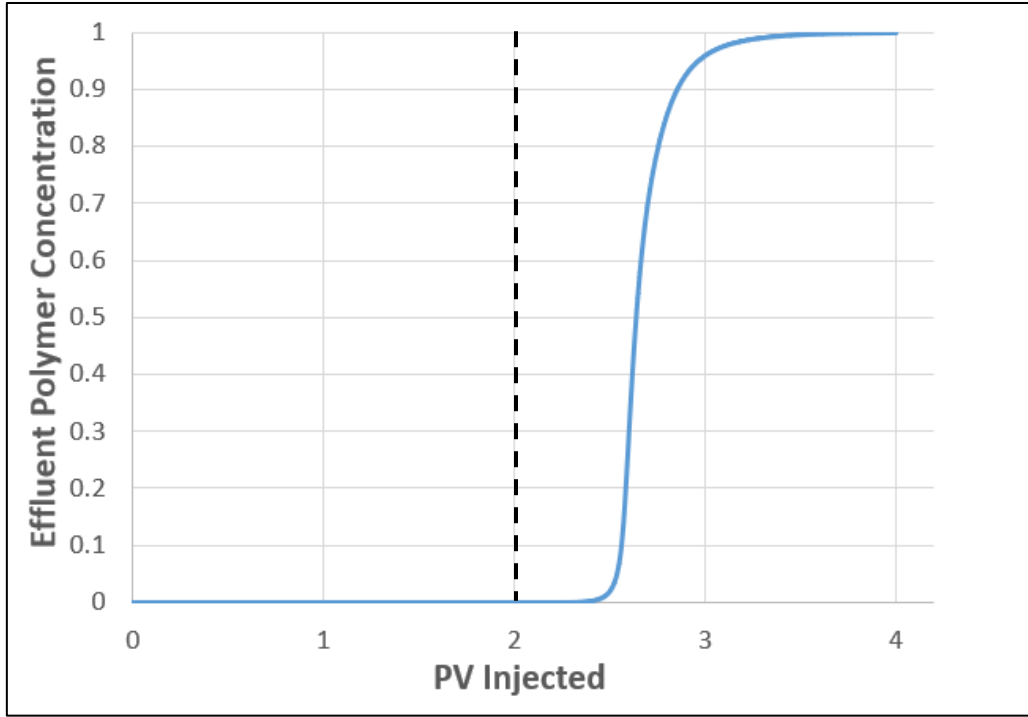


Figure 5.32: Normalized effluent polymer concentration vs. injected pore volumes.

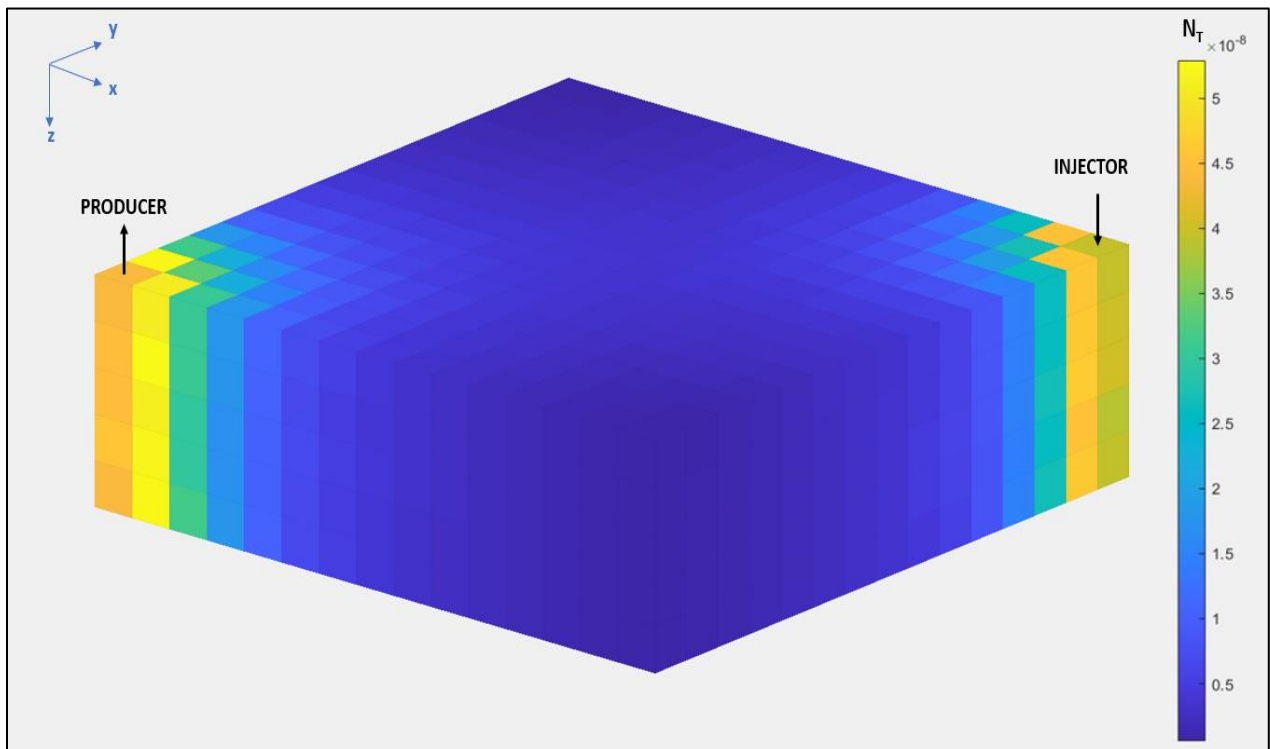


Figure 5.33: Trapping numbers in the reservoir model at 4 PVs.

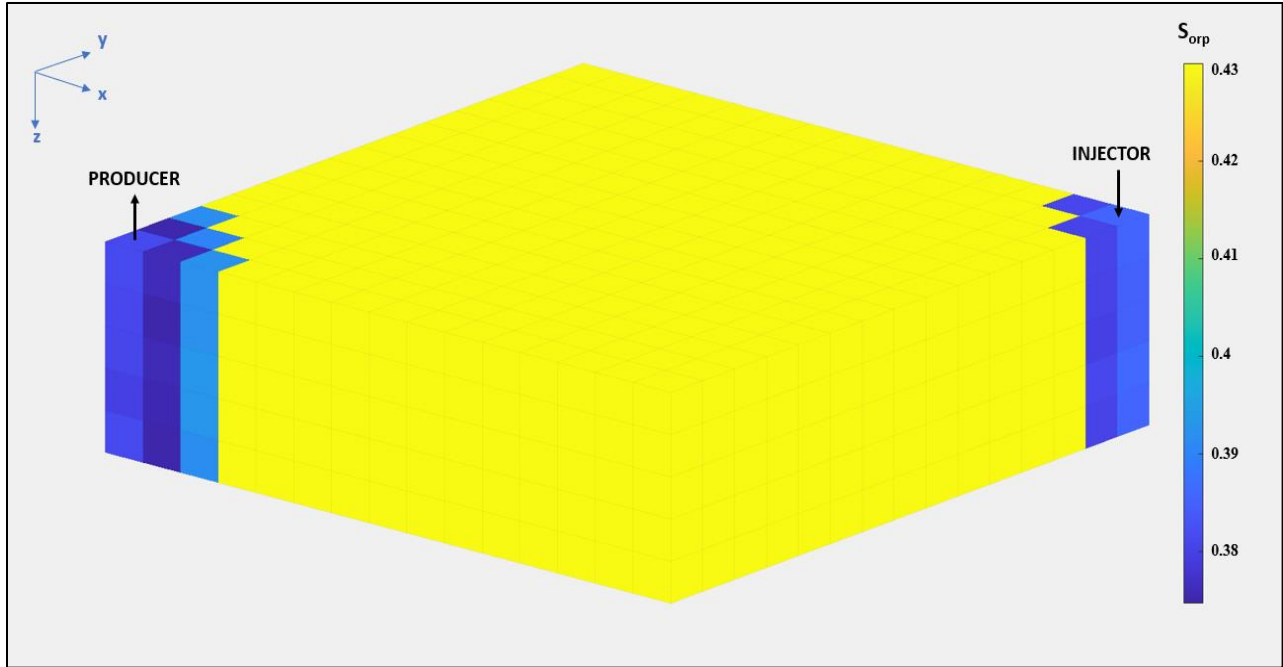


Figure 5.34: Residual oil saturations to polymer flooding at 4 PVs.

Finally, the overall results for cumulative oil recovery as well as water and oil cuts for secondary and tertiary oil recoveries are depicted in **Figures 5.35** and **5.36**, respectively.

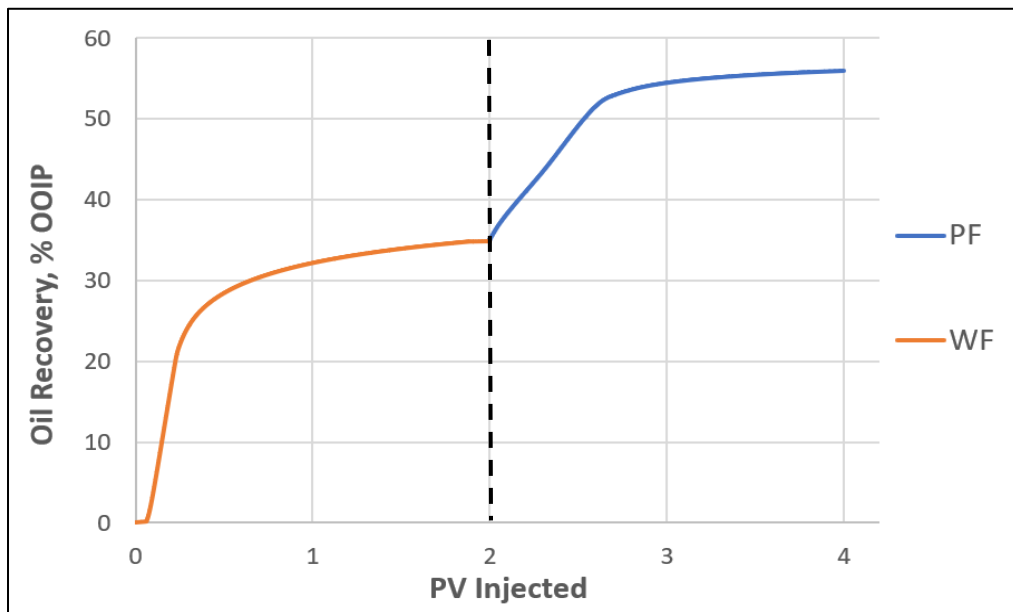


Figure 5.35: Base case predictions of oil recovery for secondary waterflooding and tertiary polymer flooding.

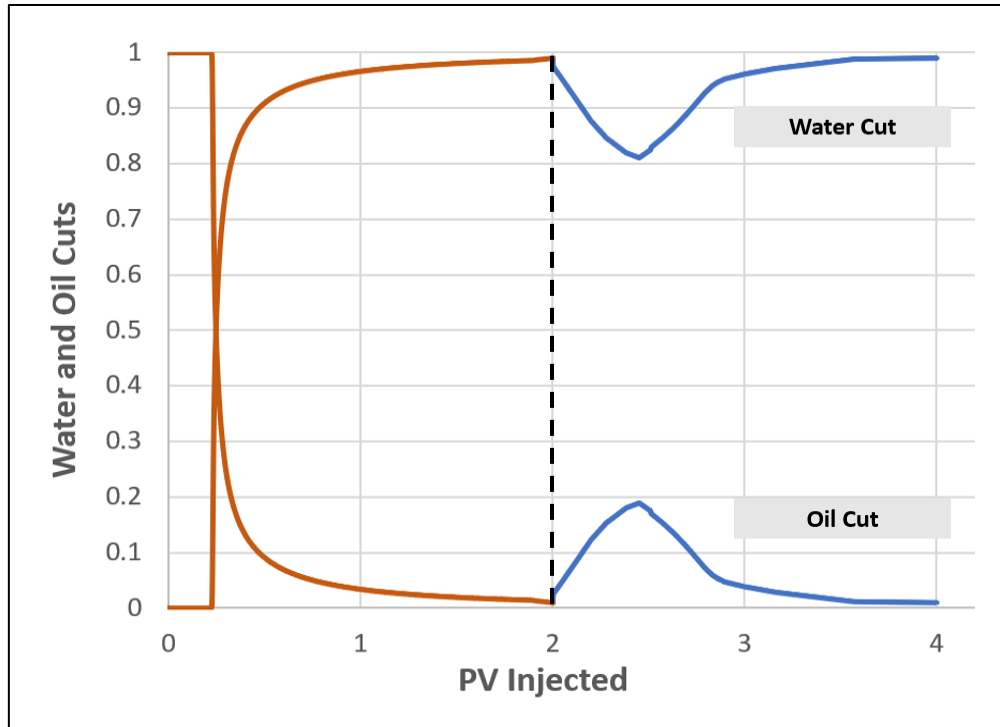


Figure 5.36: Base case predictions of water and oil cuts for secondary waterflooding and tertiary polymer flooding.

It is worth mentioning that both water and polymer injection cycles were simulated till the economic limit when the water cut reached around 99%. Moreover, the initial waterflood conducted for 2 PVs recovered about 35% of OOIP, and it was required to inject noticeably more pore volumes to reach the residual oil saturation of 43%. Performing polymer flooding for an additional 2 PVs yielded around 21% of incremental oil recovery and increased the recovery efficiency to 56%.

5.2.3 Sensitivity Analysis

Furthermore, the sensitivity analysis following base case simulation studies was conducted to investigate the effect of four different factors on incremental oil recovery. These factors were categorized into uncontrollable natural factors (reservoir permeability and reservoir heterogeneity) and controllable factors (polymer concentration and injection pressure). All variables are summarized in **Table 5.5**.

Table 5.5: Parameters used for sensitivity analysis

Parameter	Case 1	Case 2	Case 3
Reservoir Permeability (mD)	20	50 (base case)	200
Reservoir Heterogeneity (DP)	0	0.5	0.8 (base case)
Polymer Concentration (ppm)	1000	1500 (base case)	2000
Injection Pressure (psi)	3500	4500 (base case)	5200

Average Reservoir Permeability Effect. Firstly, the average reservoir permeability effect on oil recovery was investigated. In this case, the permeability was varied including 20, 50, and 200 mD. All other parameters were taken from the base case simulation study. The simulation results are reported in **Table 5.6** and **Figure 5.37**. Apparently, average reservoir permeability positively affected oil recovery, which might be explained by the higher Darcy's velocities in more permeable rock.

Table 5.6: Effect of average reservoir permeability on oil recovery

Parameter	Case 1	Case 2	Case 3
Injection Pressure (psi)	4500		
Polymer Concentration (ppm)	1500		
Reservoir Heterogeneity (DP)	0.8		
Reservoir Permeability (mD)	20	50	200
Injection Cycle	Incremental Oil Recovery (% OOIP)		
Water Injection (0-2 PVs)	31.405	34.904	39.358
Polymer Injection (2-4 PVs)	20.12	21.553	24.58
Ultimate Oil Recovery (% OOIP)	51.525	56.457	63.938

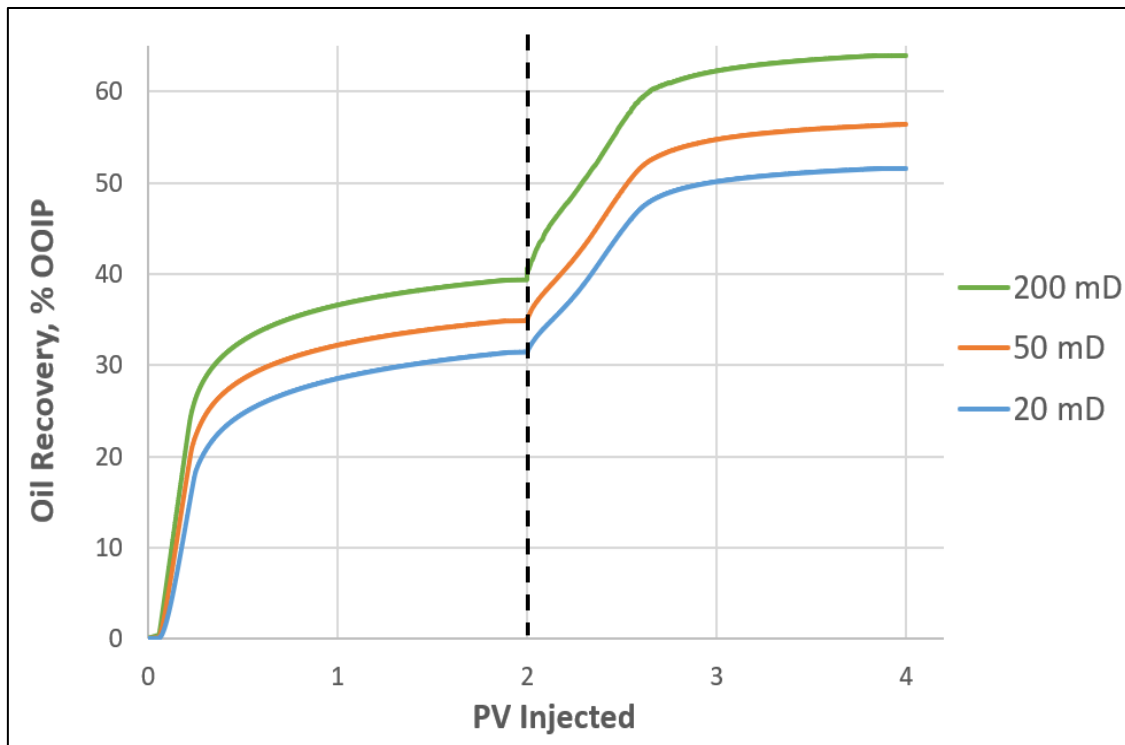


Figure 5.37: Effect of average reservoir permeability on oil recovery.

Reservoir Heterogeneity Effect. Reservoir heterogeneity was the next factor investigated in this study. Three cases were used in sensitivity analyses: the homogenous model with the Dykstra-Parsons coefficient (DP) of 0, and two heterogeneous models with DP of 0.5 and 0.8 (base case). All other factors were identical to the base case values. It was found that the homogenous model yields the highest ultimate oil recovery of around 65%. Moreover, increasing reservoir heterogeneity hindered reservoir sweep and caused a delay in oil recovery. Therefore, the heterogeneous model with the highest DP of 0.8 had the worst recovery efficiency. Additionally, it is worth mentioning that the delay in oil recovery due to heterogeneity was more pronounced during secondary waterflooding. Switching to the tertiary polymer flooding improved volumetric sweep efficiency in the reservoir and mitigated the adverse effect of reservoir heterogeneity to some extent. The simulation results are reported in **Table 5.7** and **Figure 5.38**.

Table 5.7: Effect of reservoir heterogeneity on oil recovery

Parameter	Case 1	Case 2	Case 3
Injection Pressure (psi)	4500		
Polymer Concentration (ppm)	1500		
Reservoir Permeability (mD)	50		
Reservoir Heterogeneity (DP)	0	0.5	0.8
Injection Cycle	Incremental Oil Recovery (% OOIP)		
Water Injection (0-2 PVs)	39.903	37.497	34.904
Polymer Injection (2-4 PVs)	22.304	21.855	21.553
Ultimate Oil Recovery (% OOIP)	62.207	59.352	56.457

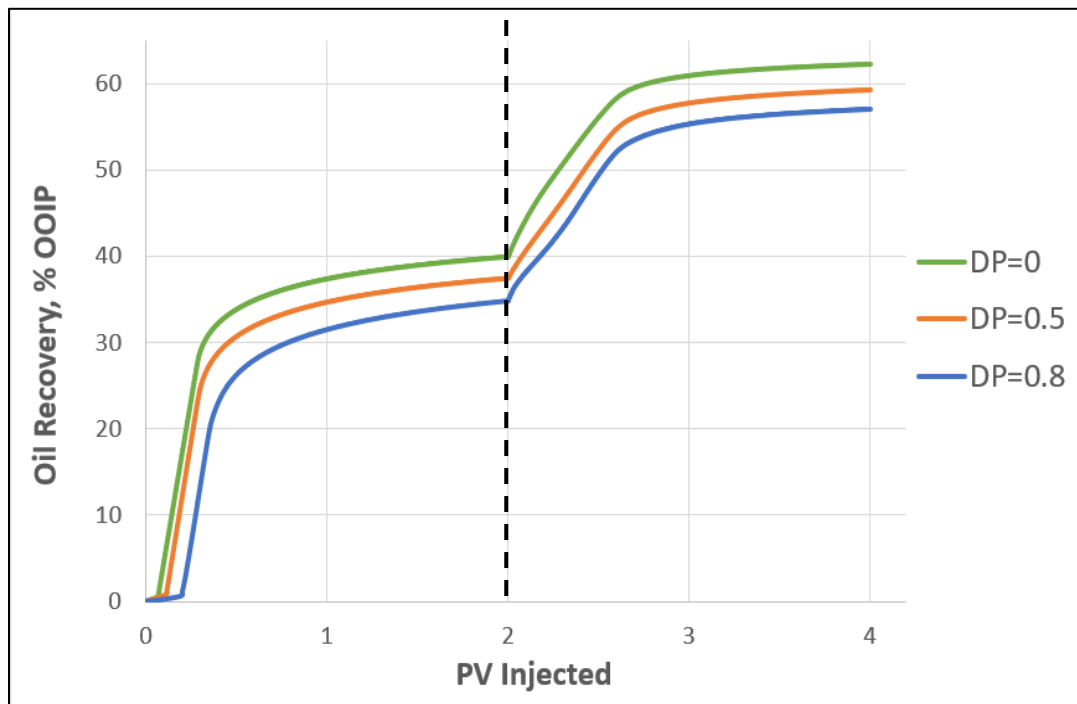


Figure 5.38: Effect of reservoir heterogeneity on oil recovery.

Polymer Concentration Effect. Similarly, the effect of polymer concentration was also analyzed. The concentration was varied including 1000, 1500, and 2000 ppm. The simulation results show that polymer concentration slightly increases oil recovery due to improved mobility ratio and sweep efficiency. However, since the mobility ratio of unity was obtained even at lower polymer concentrations for a given oil viscosity of 0.9 cP, the further increase in polymer concentration did not yield a considerable incremental oil recovery. The results are reported in **Table 5.8** and **Figure 5.39**.

Table 5.8: Effect of polymer concentration on oil recovery

Parameter	Case 1	Case 2	Case 3
Injection Pressure (psi)	4500		
Reservoir Permeability (mD)	50		
Reservoir Heterogeneity (DP)	0.8		
Polymer Concentration (ppm)	1000	1500	2000
Injection Cycle	Incremental Oil Recovery (% OOIP)		
Water Injection (0-2 PVs)	34.904	34.904	34.904
Polymer Injection (2-4 PVs)	20.535	21.553	22.756
Ultimate Oil Recovery (% OOIP)	55.439	56.457	57.66

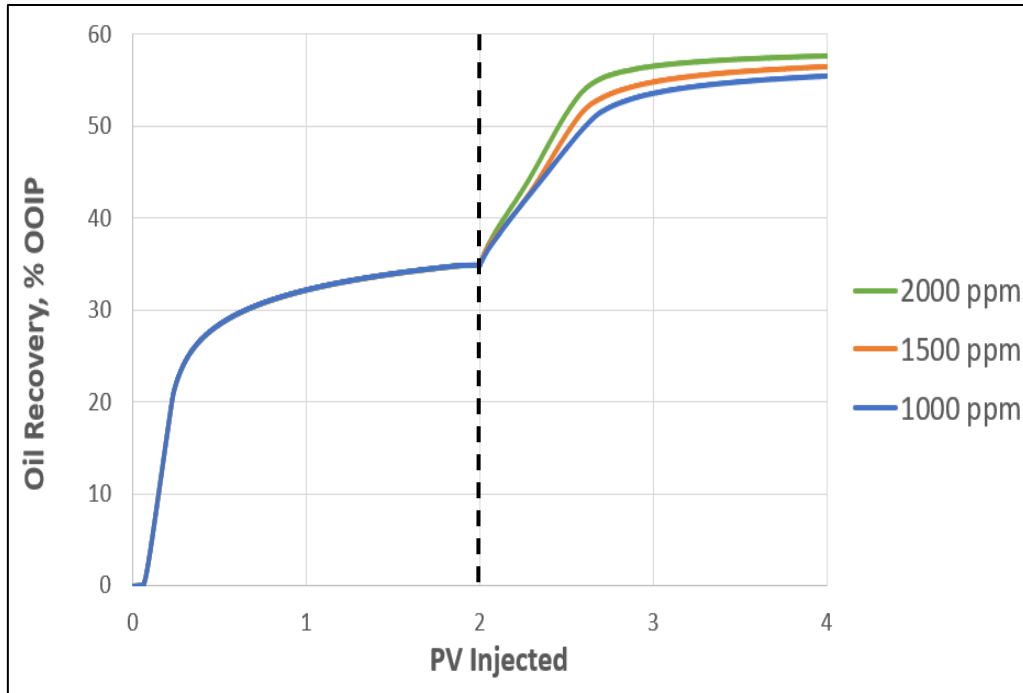


Figure 5.39: Effect of polymer concentration on oil recovery.

Injection Pressure Effect. Finally, the effect of injector BHP on recovery efficiency was also investigated. As was expected, increasing injection pressures improved oil recovery, which is justified by the higher pressure drops and fluxes in the reservoir. It is worth mentioning that injecting 1500 ppm polymer solution at the highest BHP of 5200 psi resulted in insignificant mechanical degradation near wellbores as low molecular weight (8 MDa) polymers were used in polymer flooding predictions. Therefore, the detrimental effect of mechanical degradation was less pronounced than the positive impact of injection pressures on oil recovery, as was discussed in Section 5.1.2. Moreover, it was also found that higher pressure drops increased the trapping number around the wellbores and reduced the residual oil saturation to around 35% in those regions.

Nevertheless, it is crucial to consider reservoir fracturing pressures during polymer flooding since the injection pressures higher than the fracturing pressure might generate extensive fractures around the injector and significantly reduce sweep efficiency. The simulation results are presented in **Table 5.9** and **Figure 5.40**.

Table 5.9: Effect of polymer injection pressure on oil recovery

Parameter	Case 1	Case 2	Case 3
Polymer Concentration (ppm)	1500		
Reservoir Permeability (mD)	50		
Reservoir Heterogeneity (DP)	0.8		
Injection Pressure (psi)	3500	4500	5200
Injection Cycle	Incremental Oil Recovery (% OOIP)		
Water Injection (0-2 PVs)	34.904	34.904	34.904
Polymer Injection (2-4 PVs)	20.013	21.553	23.773
Ultimate Oil Recovery (% OOIP)	54.917	56.457	58.677

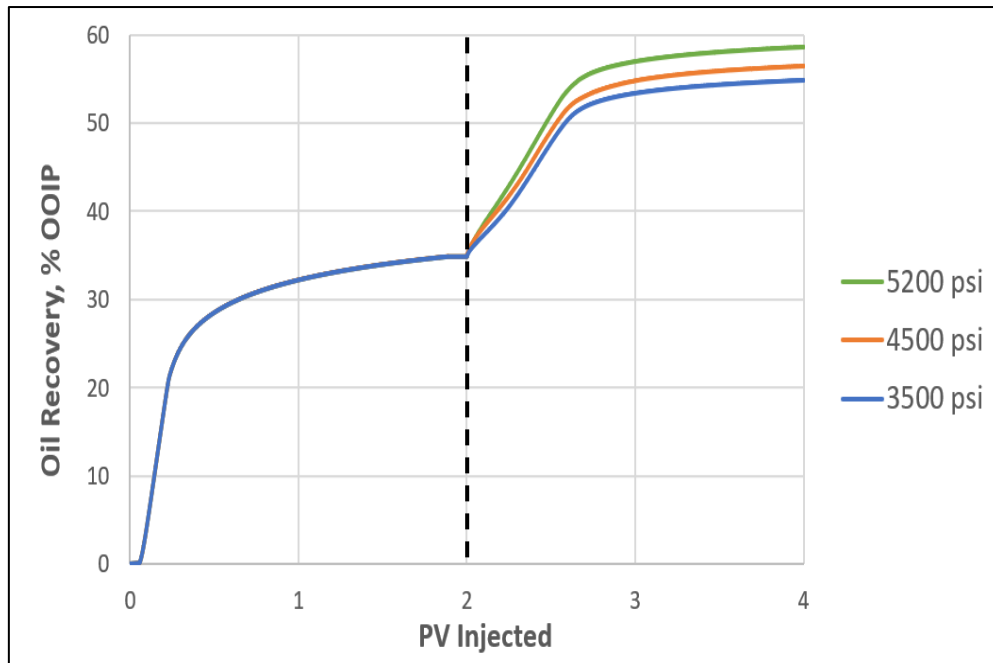


Figure 5.40: Effect of polymer injection pressure effect on oil recovery.

Generally, sensitivity analyses showed that reservoir permeability and heterogeneity have the most pronounced effect on the delay in oil recovery. Moreover, among the controllable factors, the impact of injection pressure on oil recovery was more emphasized than that of polymer concentration. However, it was believed that in the reservoirs with more viscous hydrocarbons (that is usually not the case in the Middle East carbonates), polymer concentration might be one of the predominant factors significantly improving sweep efficiency and oil recovery. Additionally, it is recommended to carefully design the injection pressure since its rapid increase might cause the severe mechanical degradation of polymers and the generation of extensive fractures.

CHAPTER 6: CONCLUSIONS AND RECOMMENDATIONS

6.1 Summary and Conclusions

The summary of the work and the main conclusions derived are listed below:

- The Extended Unified Apparent Viscosity Model (E-UVM) proposed in this study captures all four regimes observed during viscoelastic polymer flooding, including Newtonian, shear-thinning, shear-thickening, and mechanical degradation regimes. In E-UVM, the Newtonian and shear-thinning regimes are captured using the Carreau model, while the shear-thickening behavior is modeled by relating elastic viscosity to the Deborah number. Moreover, we provided a degradation multiplier for the mechanical degradation part reducing the apparent viscosity beyond critical shear rates.
- Furthermore, the model parameters were analyzed. Particularly, mechanical degradation constant (λ_3) controls the degradation onset; higher λ_3 shifts onset to the lower shear rates. λ_3 primarily increases with polymer molecular weight and decreases with rock permeability. On the other hand, the degree of degradation is controlled by the mechanical degradation index (n_3). Higher n_3 in E-UVM is used to visualize more severe degradation cases.
- The fitting parameters of the viscoelastic model were related to rock and polymer properties using the Symbolic Regression technique embedded in EUREQA. The correlations with reasonable accuracy and complexity were selected among the developed expressions and used in our study. Using these correlations may reduce the need for performing extensive coreflooding measurements.
- The proposed viscoelastic model was implemented in the reservoir simulator at core and field scales. The E-UVM viscosities were estimated as a function of the apparent shear rates. Then, the implementation of E-UVM was verified with the original shear model in MRST. It is believed that using E-UVM for shear factors may be more accurate and practical than the original implementation, which imports the data from external files/tables and iteratively solves for shear multipliers.
- The effect of viscoelastic polymer flooding on oil mobilization was also modeled in this

study through the trapping numbers. The respective residual-phase saturation and relative permeabilities were updated accordingly. The trapping numbers were computed for each gridblock of the simulation model, and the calculations were verified using the UTCHEM simulator.

- The effects of polymer concentration and injection rate on oil recovery were analyzed at a core scale. The tertiary polymer flooding predictions revealed the positive effect of these parameters on oil displacement. It was found that viscoelastic polymers could displace no residual oil at low injection rates (0.045 ml/min) using a broad range of polymer concentrations. However, with the increment in injection rates, oil recoveries were significantly increased.
- Moreover, the comparison between Carreau, UVM, and E-UVM models in the simulator revealed that using the UVM model might overestimate the oil recoveries due to excessive shear-thickening without mechanical degradation evaluation.
- The field-scale simulation studies of this work were performed in a quarter 5-spot well pattern, using representative rock and fluid properties from the Middle East carbonate reservoirs. The base case simulations showed that tertiary polymer flooding might improve volumetric sweep efficiency by mitigating the challenge of gravity override and sweeping upper layers in the reservoir model. On the other hand, an increase in displacement efficiency was pronounced only in the vicinity of the wellbores, where higher pressure gradients generated large trapping numbers.
- Sensitivity analyses showed that reservoir permeability and heterogeneity have the most noticeable effect on the delay in oil recovery. Additionally, the impact of injection pressure on oil recovery was more emphasized than that of polymer concentration. However, it was believed that in the reservoirs with more viscous oil, polymer concentration might be one of the dominant factors considerably increasing sweep efficiency and oil recovery.
- Finally, it is recommended to carefully design the injection pressure since its rapid increment might result in severe mechanical degradation and generate extensive fractures.

6.2 Recommendations

The following is recommended for future research:

- Performing the coreflooding tests at high shear rates might help to comprehensively investigate the effect of various factors on polymer shear-thickening and mechanical degradation. These factors include solution salinity and hardness, rock permeability, polymer concentration, molecular weight, and degree of pre-shearing.
- It is recommended to consider the effect of polymer molecular structure by conducting molecular dynamic studies to improve predictions in polymer rheological behavior.
- The fitting parameters of the viscoelastic model were correlated to rock and polymer properties for a given set of experimental data collected from the literature. However, to improve the accuracy of proposed correlations, it is possible to conduct more coreflooding tests under various flow conditions and obtain broader experimental input data for the machine learning software.
- In addition, it is recommended to have a more detailed simulation study in the future by modeling the effect of temperature, hardness, and geochemical interactions between the polymer/rock/fluid system in MRST since these effects have not been well established in the simulator.
- The injectivity of viscoelastic polymers is another aspect that might be more thoughtfully investigated during future simulation studies.
- It is also recommended to validate the E-UVM model implemented in MRST against different coreflooding tests through history matching polymer flooding oil recovery and pressure drop curves.
- Detailed sensitivity analysis and optimization studies on polymer viscoelastic behavior and its effect on oil recovery can be further investigated.
- It is recommended to experimentally investigate the effect of several factors representing harsh carbonate reservoir conditions on polymer viscoelastic behavior including high temperature (120 °C), high salinity (200,000 ppm), and mixed-to-oil wettability conditions.

REFERENCES

- Abas, N., Kalair, A., and Khan, N., 2015. Review of fossil fuel sand future energy technologies. *Futures*, 69: 31–49.
- Adegbite, J. O., Al-Shalabi, E. W., and Ghosh, B., 2017. Modeling the Effect of Engineered Water Injection on Oil Recovery from Carbonate Cores. Paper SPE-184505-MS, *SPE International Conference on Oilfield Chemistry*, Montgomery, Texas, USA.
- Afsharpoor, A., Balhoff, M. T., Bonnecaze, R., and Huh, C., 2012. CFD modeling of the effect of polymer elasticity on residual oil saturation at the pore-scale. *Journal of Petroleum Science and Engineering*, 94-95: 79-88.
- Aftab, M., Talib, N., Subaihi, M., Lazreq, N., Nechakh, A., Leguizamon, J., and Dunlop, T., 2020. First Multistage Fracturing of Horizontal Well Drilled in Conventional Tight Carbonate Reservoir in An Onshore Field in the UAE – Challenges and Lessons Learned. Paper SPE-203226-MS, *Abu Dhabi International Petroleum Exhibition & Conference*, Abu Dhabi, UAE.
- Ahmed, T., 1989. *Hydrocarbon Phase Behavior*. Gulf Publication Company, Houston, Texas, USA.
- Ahmed, T., 2000. *Reservoir Engineering Handbook*. Gulf Publishing Company, Houston, Texas, USA.
- Akstinat, M. H., 1980. Polymers for Enhanced Oil Recovery in Reservoirs of Extremely High Salinities and High Temperatures. Paper SPE 8979, *SPE Fifth International Symposium on Oilfield and Geothermal Chemistry*, Stanford, California, USA.
- Aladasani, A. and Bai, B., 2010. Recent Developments and Updated Screening Criteria of Enhanced Oil Recovery Techniques. Paper SPE 130726, *CPS/SPE International Oil & Gas Conference and Exhibition*, Beijing, China.
- Alameri, W., Teklu, T. W., Graves, R. M., Kazemi, H., and AlSumaiti, A. M., 2015. Experimental and Numerical Modeling of Low-Salinity Waterflood in a Low Permeability Carbonate Reservoir. Paper SPE 174001, *SPE Western Regional Meeting*, Garden Grove, California, USA.
- Alfazazi, U., AlAmeri, W., and Hashmet, M. R., 2018. Screening of New HPAM Base Polymers for Applications in High Temperature and High Salinity Carbonate Reservoirs. Paper SPE

- 192805, *Abu Dhabi International Petroleum Exhibition & Conference*, Abu Dhabi, UAE.
- Alfazazi, U., Thomas, N. C., AlAmeri, W., Al-Shalabi, E. W., and Shaik, A. R., 2019. An Experimental Investigation of Polymer Performance in Harsh Carbonate Reservoir Conditions. Paper SPE-198607-MS, *SPE Gas & Oil Technology Showcase and Conference*, Dubai, UAE.
- Al-Murayri, M. T., Kamal, D. S., Al-Sabah, H. M., AbdulSalam, T., Al-Shamali, A., Quttainah, R., Glushko, D., Britton, C., Delshad, M., Liyanage, J., and Matthew, R., 2019. Low-Salinity Polymer Flooding in a High-Temperature Low-Permeability Carbonate Reservoir in West Kuwait. Paper SPE-198000-MS, *SPE Kuwait Oil & Gas Conference and Show*, Mishref, Kuwait.
- Al-Shakry, B., Shiran, B. S., Skauge, T., and Skauge, A., 2018. Enhanced Oil Recovery by Polymer Flooding: Optimizing Polymer Injectivity. Paper SPE-192437-MS, *SPE Kingdom of Saudi Arabia Annual Technical Symposium and Exhibition*, Dammam, Saudi Arabia.
- Al-Shalabi, E.W., 2014a. *Modeling the Effect of Injecting Low Salinity Water on Oil Recovery from Carbonate Reservoirs*. Ph.D. dissertation, The University of Texas at Austin, Texas, USA.
- Al-Shalabi, E. W., Sepehrnoori, K., and Delshad, M., 2014b. Optimization of the Low Salinity Water Injection Process in Carbonate Reservoirs. Paper IPTC-17821-MS, *International Petroleum Technology Conference*, Kuala Lumpur, Malaysia.
- Al-Shalabi, E. W. and Sepehrnoori, K., 2016. A comprehensive review of low salinity/engineered water injections and their applications in sandstone and carbonate rocks. *Journal of Petroleum Science and Engineering*, 139: 137-161.
- Al-Shalabi, E. W., 2020. A New Insight into Modeling of Polymer Flooding in Carbonate Reservoirs. Paper SPE-198958-MS, *SPE Latin American and Caribbean Petroleum Engineering Conference*, virtual event.
- Alvarado, V. and Manrique, E., 2010. Enhanced Oil Recovery: An Update Review. *Energies*, 3: 1529-1575.
- Asen, S. M., Stavland, A., Strand, D., and Hiorth, A., 2019. An Experimental Investigation of Polymer Mechanical Degradation at the Centimeter and Meter Scale. *SPE Journal*, 24(4): 1700–1713.
- Azad, M. S. and Sultan, A. S., 2014. Extending the Applicability of Chemical EOR in High

- Salinity, High Temperature and Fractured Carbonate Reservoir Through Viscoelastic Surfactants. Paper SPE-172188-MS, *SPE Saudi Arabia Section Annual Technical Symposium and Exhibition*, Al -Khobar, Saudi Arabia.
- Azad, M. S., Dalsania, Y. G., and Trivedi, J. J., 2018. Capillary breakup extensional rheometry of associative and hydrolyzed polyacrylamide polymers for oil recovery applications. *Journal of Applied Polymer Science*, 135(22): 46253–46264.
- Azad, M. S. and Trivedi, J. J., 2018. Novel viscoelastic model for predicting the synthetic polymer's viscoelastic behavior in porous media using direct extensional rheological measurements. *Fuel*, 235: 218-226.
- Azad, M. S. and Trivedi, J. J., 2019. Quantification of the Viscoelastic Effects During Polymer Flooding: A Critical Review. Paper SPE 195687, *SPE Journal*, 24(6): 2731-2757.
- Azad, M. S., and Trivedi, J. J., 2020. Quantification of S_{or} Reduction during Polymer Flooding Using Extensional Capillary Number. Paper SPE 204212, *SPE Journal*, 1-30.
- Bao, K., Lie, K.A., Møyner, O., and Liu, M., 2017. Fully Implicit Simulation of Polymer Flooding with MRST. *Computational Geosciences*, 21(5): 1219-1244.
- Barnes, H. A., Hutton, J. F., and Walters, K., 1989. *An Introduction to Rheology*. First edition, Elsevier Science Publishers B. V., Amsterdam.
- Bird, R. B., Stewart, W. E., and Lightfoot, E. N., 1960. *Transport Phenomena*. Wiley, New York.
- BP, 2014. *Statistical Review of World Energy*. Annual Report 63.
- Brakstad, K. and Rosenkilde, C., 2016. Modelling Viscosity and Mechanical Degradation of Polyacrylamide Solutions in Porous Media. Paper SPE-179593-MS, *SPE Improved Oil Recovery Conference*, Tulsa, Oklahoma, USA.
- Brooks, A. N. and Corey, A. T., 1964. Hydraulic Properties of Porous Media. *Hydrology Papers*, Fort Collins, Colorado State University.
- Canella, W. J., Huh, C., and Seright, R. S., 1988. Prediction of Xanthan Rheology in Porous Media. Paper SPE 18089, *Annual Technical Conference and Exhibition*, Houston, USA.
- Carreau, P. J., 1972. Rheological Equations from Molecular Network Theories. *Transactions of the Society of Rheology*, 16(1): 99-127.
- Castelletto, V., Hamley, I. W., Xue, W., Sommer, C., Pedersen, J. S., and Olmsted, P. D., 2004. Rheological and Structural Characterization of Hydrophobically Modified Polyacrylamide Solutions in the Semidilute Regime. *Macromolecules*, 37(4): 1492-1501.

- Chandrasekhar, S. and Mohanty, K. K., 2013. Wettability Alteration with Brine Composition in High-Temperature Carbonate Reservoirs. Paper SPE 166280, *SPE Annual Technical Conference and Exhibition*, New Orleans, Louisiana, USA.
- Chauveteau, G., 1981. Molecular Interpretation of Several Different Properties of Flow of Coiled Polymer Solutions Through Porous Media in Oil Recovery Conditions. Paper SPE 10060, *SPE Annual Technical Conference and Exhibition*, San Antonio, Texas, USA.
- Chen, J. C., Wang, D. M., and Wu, J. Z., 2001. Optimum on Molecular Weight of Polymer for Oil Displacement. *Acta Petrolei Sinica*, 21(1): 103–106.
- Clarke, A., Howe1, A. M., Mitchell, J., Staniland, J., and Hawkes, L. A., 2016. How Viscoelastic-Polymer Flooding Enhances Displacement Efficiency. Paper SPE 174654, *SPE Journal*, 21(3): 675-687.
- Davison, P. and Mentzer, E., 1982. Polymer Flooding in North Sea Reservoirs. Paper SPE-9300-PA, *SPE Journal*, 22(3): 353–362.
- Delamaide, E., Moe-Soe-Let, K., Bhoendie, K., Jong-A-Pin, S., and Paidin, W. R., 2016. Results of a Polymer Flooding Pilot in the Tambaredjo Heavy Oil Field, Suriname. Paper SPE-180739-MS, *SPE Canada Heavy Oil Technical Conference*, Calgary, Alberta, Canada.
- Delshad, M., Bhuyan, D., Pope, G. A., and Lake, L. W., 1986. Effect of Capillary Number on the Residual Saturation of a Three-Phase Micellar Solution. Paper SPE/DOE 14911, *SPE/DOE Fifth Symposium on Enhanced Oil Recovery*, Tulsa, Oklahoma, USA.
- Delshad, M., 1990. *Trapping of Micellar Fluids in Berea Sandstone*. PhD Dissertation, The University of Texas at Austin, Texas, USA.
- Delshad, M., Kim, D. H., Magbagbeola, O. A., Huh, C., Pope, G., and Tarahhom, F., 2008. Mechanistic Interpretation and Utilization of Viscoelastic Behavior of Polymer Solutions for Improved Polymer-Flood Efficiency. Paper SPE 113620, *SPE/DOE Improved Oil Recovery Symposium*, Tulsa, Oklahoma, USA.
- Diab, W. N. and Al-Shalabi, E. W., 2019. Recent Developments in Polymer Flooding for Carbonate Reservoirs under Harsh Conditions. Paper OTC-29739-MS, *Offshore Technology Conference*, Rio de Janeiro, Brazil.
- Druetta, P., Raffa, P., and Picchioni, F., 2019. Chemical enhanced oil recovery and the role of chemical product design. *Applied Energy*, 252(113480): 1-43.
- Dupuis, G., Antignard, S., Giovannetti, B., Gaillard, N., Jouenne, S., Bourdarot, G., Morel, D.,

- and Zaitoun, A., 2017. A New Thermally Stable Synthetic Polymer for Harsh Conditions of Middle East Reservoirs. Part I. Thermal Stability and Injection in Carbonate Cores. Paper SPE-188479-MS, *Abu Dhabi International Petroleum Exhibition & Conference*, Abu Dhabi, UAE.
- Dykstra, H. and Parsons, R. L., 1950. *The Prediction of Oil Recovery by Water Flooding, Secondary Recovery of Oil in the United States*. Second Edition, American Petroleum Institute, pp. 160–174.
- Edwards, B. J., Keffer, D. J., and Reneau, C. W., 2002. An Examination of the Shear-Thickening Behavior of High Molecular Weight Polymers Dissolved in Low-Viscosity Newtonian Solvents. *Journal of Applied Polymer Science*, 85(8): 1714–1735.
- Ehrenfried, D. H., 2013. *Impact of Viscoelastic Polymer flooding on Residual Oil Saturation in Sandstones*. MS thesis, The University of Texas at Austin, Texas, USA.
- Erincik, M., Qi, P., Balhoff, M. T., and Pope, G. A., 2017. New Method to Reduce Residual Oil Saturation by Polymer Flooding. Paper SPE-187230, *SPE Annual Technical Conference and Exhibition*, San Antonio, Texas, USA.
- Fixman, M., 1962. Radius of Gyration of Polymer Chains. *The Journal of Chemical Physics*, 36(2): 306–310.
- Gaillard, N., Giovannetti, B., and Favero, C., 2010. Improved Oil Recovery using Thermally and Chemically Protected Compositions Based on co- and ter-polymers Containing Acrylamide. Paper SPE 129756, *SPE Improved Oil Recovery Symposium*, Tulsa, Oklahoma, USA.
- Gaillard, N., Giovannetti, B., Favero, C., Caritey, J. P., Dupuis, G., and Zaitoun, A., 2014. New Water Soluble Anionic NVP Acrylamide Terpolymers for Use in Harsh EOR Conditions. Paper SPE-169108-MS, *SPE Improved Oil Recovery Symposium*, Tulsa, Oklahoma, USA.
- Garrepally, S., Jouenne, S., Olmsted, P. D., and Lequeux, F., 2020. Scission of flexible polymers in contraction flow: predicting the effects of multiple passages. *Journal of Rheology*, 64(3): 601–614.
- Garrouch, A. A., 1999. A Viscoelastic Model for Polymer Flow in Reservoir Rocks. Paper SPE 54379, *SPE Asia Pacific Oil and Gas Conference and Exhibition*, Jakarta, Indonesia.
- Gbadamosi, A. O., Junin, R., Manan, M. A., Agi, A., and Yusuff, A. S., 2019. An overview of chemical enhanced oil recovery: recent advances and prospects. *International Nano Letters*, 9(3): 171-202.

- Green, D. W. and Willhite, G. P., 1998. *Enhanced Oil Recovery*. Richardson Texas: Society of Petroleum Engineers, SPE Textbook Series (6).
- Guo, H., Song, K., Liu, S., Zhao, F., Wang, Z., Xu, Y., Liu, J., Tang, E., and Yang, Z., 2020. Recent Advances in Polymer Flooding in China: Lessons Learned and Continuing Development. *SPE Journal*, 1-15.
- Haas, R. and Durst, F., 1982. Viscoelastic Flow of Dilute Polymer-Solutions in Regularly Packed-Beds. *Rheologica Acta*, 21(4-5): 566–571.
- Han, M., Zhou, X., Alhasan, F. B., Zahrani, B., and AlSofi, A. M., 2012. Laboratory Investigation of the Injectivity of Sulfonated Polymer Solutions into Carbonate Reservoir Rocks. Paper SPE 155390, *SPE EOR Conference at Oil and Gas West Asia*, Muscat, Oman.
- Hashmet, M. R., Qaiser, Y., Mathew, E. S., AlAmeri, W., and AlSumaiti, A. M., 2017. Injection of Polymer for Improved Sweep Efficiency in High Temperature High Salinity Carbonate Reservoirs: Linear X-Ray Aided Flood Front Monitoring. Paper SPE-188125-MS, *SPE Kingdom of Saudi Arabia Annual Technical Symposium and Exhibition*, Dammam, Saudi Arabia.
- Heemskerk, J., Rosmalen, R. J., Holtslag, R. J., and Teeuw, D., 1984. Quantification of Viscoelastic Effects of Polyacrylamide Solutions. Paper SPE/DOE 12652, *SPE/DOE Fourth Symposium on Enhanced Oil Recovery*, Tulsa, Oklahoma, USA.
- Hester, R. D., Flesher, L. M., and McCormick, C. L., 1994. Polymer Solution Extension Viscosity Effects During Reservoir Flooding. Paper SPE/DOE 27823, *SPE/DOE Symposium on Improved Oil Recovery*, Tulsa, Oklahoma, USA.
- Hincapie, R. E., Rock, A., Wegner, J., and Ganzer, L., 2017. Oil Mobilization by Viscoelastic Flow Instabilities Effects during Polymer EOR: A Pore-Scale Visualization Approach. Paper SPE-185489-MS, *SPE Latin America and Caribbean Petroleum Engineering Conference*, Buenos Aires, Argentina.
- Hirasaki, G. J. and Pope, G. A., 1974. Analysis of Factors Influencing Mobility and Adsorption in the Flow of Polymer Solution Through Porous Media. Paper SPE 4026, *SPE Journal*, 14(4): 337–346.
- Informer Technologies, 2021. <https://eureqa.software.informer.com/0.9/>.
- Internal Energy Agency (IEA), 2020. *Oil Market Report*.
- Jensen, T., Kadhum, M., Kozlowicz, B., Sumner, E. S., Malsam, J., Muhammed, F., and

- Ravikiran, R., 2018. Chemical EOR Under Harsh Conditions: Scleroglucan As A Viable Commercial Solution. Paper SPE-190216-MS, *SPE Improved Oil Recovery Conference*, Tulsa, Oklahoma, USA.
- Jiang, B., Keffer, D. J., Edwards, B. J., and Allred, J. N., 2003. Modeling shear thickening in dilute polymer solutions: Temperature, concentration, and molecular weight dependencies. *Journal of Applied Polymer Science*, 90(11): 2997–3011.
- Jin, M., 1995. *A Study of Nonaqueous Phase Liquid Characterization and Surfactant Remediation*. PhD Dissertation, The University of Texas at Austin, Texas, USA.
- Jouenne, S., Chakibi, H., and Levitt, D., 2018. Polymer Stability after Successive Mechanical-Degradation Events. *SPE Journal*, 23(1): 18–33.
- Kamal, M. S., Sultan, A. S., Al-Mubaiyedh, U. A., and Hussein, I. A., 2015. Review on Polymer Flooding; Rheology, Adsorption, Stability and Field Applications of Various Polymer Systems. *Polymer Reviews*, 55(3): 491–530.
- Khamees, T. K. and Flori, R. E., 2019. Can the Viscoelasticity of HPAM Polymer Solution Make the Polymer Flooding Compete with Gel Treatment to Improve Sweep Efficiency? A Comparison with Different Polymer Gel Systems. Paper SPE-193592-MS, *SPE International Conference on Oilfield Chemistry*, Galveston, Texas, USA.
- Kim, D. H., Lee, S., Ahn, C. H., Huh, C., and Pope, G. A., 2010. Development of a Viscoelastic Property Database for EOR Polymers. Paper SPE 129971, *SPE Improved Oil Recovery Symposium*, Tulsa, Oklahoma, USA.
- Kumar, M. S., Amitabh Pandey, A., and Jha, M. K., 2012. Polymer Injectivity Test in Mangala Field - A Significant Step towards Field Wide Implementation. Paper SPE 155162, *SPE Oil and Gas India Conference and Exhibition*, Mumbai, India.
- Lake, L. W., 1989. *Enhanced Oil Recovery*. Upper Saddle River, Prentice Hall, New Jersey.
- Lake, L. W., Johns, R. T., Rossen, W. R., and Pope, G. A., 2014. *Fundamentals of Enhanced Oil Recovery*. Society of Petroleum Engineers.
- Levitt, D. B. and Pope, G. A., 2008. Selection and Screening of Polymers for Enhanced-Oil Recovery. Paper SPE 113845, *SPE/DOE Improved Oil Recovery Symposium*, Tulsa, Oklahoma, USA.
- Lewandowska, K., 2007. Comparative Studies of Rheological Properties of Polyacrylamide and Partially Hydrolyzed Polyacrylamide Solutions. *Journal of Applied Polymer Science*,

103(4): 2235–2241.

- Lie, K. A. 2016. *An introduction to reservoir simulation using MATLAB: user guide for the Matlab Reservoir Simulation Toolbox (MRST)*. SINTEF ICT.
- Lohne, A., Nødland, O., Stavland, A., and Hiorth, A., 2017. A model for non-Newtonian flow in porous media at different flow regimes. *Computational Geosciences*, 21: 1289–1312.
- Lotfollahi, M., Farajzadeh, R., Delshad, M., Al-Abri, A., Wassing, B. M., Al-Mjeni, R., Awan, K., and Bedrikovetsky, P., 2016a. Mechanistic Simulation of Polymer Injectivity in Field Tests. Paper SPE 174665, *SPE Journal*, 21(4): 1178-1191.
- Lotfollahi, M., Koh, H., Li, Z., Delshad, M., and Pope, G. A., 2016b. Mechanistic Simulation of Residual Oil Saturation in Viscoelastic Polymer Floods. Paper SPE-179844-MS, *SPE EOR Conference at Oil and Gas West Asia*, Muscat, Oman.
- Ma, Q., Shuler, P. J., Aften, C. W., and Tang, Y., 2015. Theoretical studies of hydrolysis and stability of polyacrylamide polymers. *Polymer Degradation and Stability*, 121: 69-77.
- Macosko, K. W., 1994. *Rheology: Principles, Measurements and Applications*. Wiley VCH, New York.
- Maerker, J. M., 1975. Shear Degradation of Partially Hydrolyzed Polyacrylamide Solutions. *SPE Journal*, 15(4): 311-321.
- Magbagbeola, O. A., 2008. *Quantification of the Viscoelastic Behavior of High Molecular Weight Polymers used for Chemical Enhanced Oil Recovery*. MS thesis, The University of Texas at Austin, Texas, USA.
- Manichand, R. N., Moe Soe Let, K. P., Gil, L., Quillien, B., and Seright, R. S., 2013. Effective Propagation of HPAM Solutions Through the Tambaredjo Reservoir During a Polymer Flood. *SPE Production and Operations*, 28(4): 358–368.
- Manrique, E., Thomas, C., Ravikiran, R., Izadi, M., Lantz, M., Romero, J., and Alvarado, V., 2010. EOR: Current Status and Opportunities. Paper SPE 130113, *SPE Improved Oil Recovery Symposium*, Tulsa, Oklahoma, USA.
- Manrique, E., Ahmadi, M., and Samani, S., 2017. Historical and recent observations in polymer floods: an update review. *CT&F-Ciencia, Tecnología & Futuro*, 6(5): 17–48.
- Marshall, R. J. and Metzner, A. B., 1967. Flow of Viscoelastic Fluids Through Porous Media. *Industrial and Engineering Chemistry Fundamentals*, 6(3): 393–400.
- Martin, D. D., 1986. Mechanical Degradation of Polyacrylamide Solutions in Core Plugs from

- Several Carbonate Reservoirs. *SPE Formation Evaluation*, 1(2): 139–150.
- Masalmeh, S. K., AlSumaiti, A., Gaillard, N., Daguerre, F., Skauge, T., and Skauge, A., 2019. Extending Polymer Flooding Towards High-Temperature and High-Salinity Carbonate Reservoirs. Paper SPE-197647-MS, *Abu Dhabi International Petroleum Exhibition & Conference*, Abu Dhabi, UAE.
- Masuda, Y., Tang, K., Miyazawa, M., and Tanaka, S., 1992. 1 D Simulation of Polymer Flooding Including the Viscoelastic Effect of Polymer Solution. Paper SPE 19499, *SPE Reservoir Engineering Journal*, 7(2): 247–252.
- Mehta, N., Kapadia, G., and Selvam, V. P., 2016. Challenges in Full Field Polymer Injection Mangala in Field. Paper SPE-179807-MS, *SPE EOR Conference at Oil and Gas West Asia*, Muscat, Oman.
- Minnebo, W. and Stijven, S., 2011. *Empowering Knowledge Computing with Variable Selection*. MSc Thesis, University of Antwerp.
- Mogollon, J. L. and Lokhandwala, T., 2013. Rejuvenating Viscous Oil Reservoirs by Polymer Injection: Lessons Learned in the Field. Paper 165275, *SPE Enhanced Oil Recovery Conference*, Kuala Lumpur, Malaysia
- Moore, T. P. and Slobod, R. L., 1956. Effect of Viscosity and Capillarity on Displacement of Oil by Water. *Prod Monthly*, 20: 20-30.
- Moradi-Araghi, A. and Doe, P. H., 1987. Hydrolysis and Precipitation of Polyacrylamides in Hard Brines at Elevated Temperatures. Paper SPE-13033-PA, *SPE Reservoir Engineering*, 2(2): 189-198.
- Morel, D. C., Zaugg, E., Jouenne, S., Danquigny, J. A., and Cordelier P. R., 2015. Dalia/Camelia Polymer Injection in Deep Offshore Field Angola Learnings and In Situ Polymer Sampling Results. Paper SPE-174699-MS, *SPE Enhanced Oil Recovery Conference*, Kuala Lumpur, Malaysia.
- Odell, J. A. and Keller, A. 1986. Flow-Induced Chain Fracture of Isolated Linear Macromolecules in Solution. *Journal of Polymer Science: Part B: Polymer Physics*, 24(9): 1889–1916.
- Oil and Gas Journal, 1990. *Biennial Survey of EOR*. Pennwell Press.
- Pennell, K. D., Pope, G. A., and Abriola, L. M., 1996. Influence of Viscous and Buoyancy Forces on the Mobilization of Residual Tetrachloroethylene during Surfactant Flushing.

- Environmental Science and Technology*, 30(4): 1328-1335.
- Qi, P., Ehrenfried, D. H., Koh, H., and Balhoff, M. T., 2017. Reduction of Residual Oil Saturation in Sandstone Cores by Use of Viscoelastic Polymers. Paper SPE 179689, *SPE Journal*, 22(2): 447–458.
- Qi, P., 2018. *The Effect of Polymer Viscoelasticity on Residual Oil Saturation*. PhD Dissertation, The University of Texas at Austin, Texas, USA.
- Qi, P., Lashgari, H., Luo, H., Delshad, M., Pope, G., and Balhoff, M., 2018. Simulation of Viscoelastic Polymer Flooding - From the Lab to the Field. Paper SPE-191498-MS, *SPE Annual Technical Conference and Exhibition*, Dallas, Texas.
- Rachapudi, R. V., Alshehhi, S. S., BinAmro, A. A., Masalmeh, S. K., Dey, A., Al Nuimi, S. M., Kenawy, M. M., Fabbri, C., Romero, C., Xu, S., Mabrook, M., Garnier, O. F., Wang, K., Jouenne, S., Cordelier, P., and Dupuis, G., 2020. World First Polymer Injectivity Test in High Salinity and High Temperature Carbonate Reservoir, Case Study from a Giant Reservoir in UAE. Paper SPE-203405-MS, *Abu Dhabi International Petroleum Exhibition & Conference*, Abu Dhabi, UAE.
- Ranjbar, M., Rupp, J., Pusch, G., and Meyn, R., 1992. Quantification and Optimization of Viscoelastic Effects of Polymer Solutions for Enhanced Oil Recovery. Paper SPE/DOE 24154, *SPE/DOE Symposium on Enhanced Oil Recovery*, Tulsa, Oklahoma, USA.
- Rouse, P. E., 1953. A Theory of the Linear Viscoelastic Properties of Dilute Solutions of Coiling Polymers. *Journal of Chemical Physics*, 21(7): 1272-1280.
- Schlumberger, 2013. *Eclipse technical description*. Version 2013, 2.
- Seright, R. S., 1983. The Effects of Mechanical Degradation and Viscoelastic Behavior on Injectivity of Polyacrylamide Solutions. *SPE Journal*, 23(3): 475–485.
- Seright, R. S., Seheult, M., and Talashek Todd, 2009. Injectivity Characteristics of EOR Polymers. *SPE Reservoir Evaluation and Engineering*, 12(5): 783–792.
- Sheng, J. J., 2011. *Modern Chemical Enhanced Oil Recovery: Theory and Practice*. Gulf Professional Publishing.
- Sheng, J. J., 2013. *Enhanced Oil Recovery Field Case Studies*. Gulf Professional Publishing, Boston, Massachusetts, USA.
- Sheng, J. J., Leonhardt, B., and Azri, N., 2015. Status of Polymer-Flooding Technology. SPE-174541-PA, *SPE Journal of Canadian Petroleum Technology*, 54(2): 116–126.

- Shuler, P.J., Kuehne, D. L., Uhl, J. T., and Walkup, G. W., 1987. Improving Polymer Injectivity at West Coyote Field, California. *SPE Reservoir Engineering*, 2(3): 271–280.
- Skauge, A., Zamani, N., Jacobsen, J. G., Shiran, B. S., Al-Shakry, B., and Skauge, T., 2018. Polymer Flow in Porous Media. *Colloids Interfaces*, 2(3): 1-27.
- Sochi, T., 2010. Non-Newtonian flow in porous media. *Polymer*, 51(22): 5007-5023.
- Sorbie, K. S., 1991. *Polymer Improved Oil Recovery*. Blackie and Son Ltd, Glasgow and London.
- Southwick, J. G and Manke, C. W., 1988. Molecular Degradation, Injectivity, and Elastic Properties of Polymer Solutions. *SPE Reservoir Engineering*, 3(4): 1193–1201.
- Standing, M. B., 1981. *Volumetric and Phase Behavior of Oil Field Hydrocarbon Systems*. 9th edition, Richardson, Texas: Society of Petroleum Engineers of AIME.
- Standnes, D. C. and Skjevrak, I., 2014. Literature Review of Implemented Polymer Field Projects. *Journal of Petroleum Science and Engineering*, 122: 761-775.
- Stavland, A., Jonsbraten, H. C., Lohne, A., Moen, A., and Giske, N. H., 2010. Polymer Flooding-Flow Properties in Porous Media Versus Rheological Parameters. Paper SPE 131103, *SPE EUROPEC/EAGE Annual Conference and Exhibition*, Barcelona, Spain.
- Taber, J. J., Martin, F. D., and Seright, R. S., 1997. EOR Screening Criteria Revisited – Part 1: Introduction to Screening Criteria and Enhanced Oil Recovery Projects. *SPE Reservoir Engineering*, 12(3): 189-198.
- Tahir, M., Hincapie, R. E., Be, M., and Ganzer, L., 2017. Experimental Evaluation of Polymer Viscoelasticity During Flow in Porous Media: Elongational and Shear Analysis. Paper SPE-185823-MS, *SPE Europec featured at 79th EAGE Conference and Exhibition*, Paris, France.
- Taylor, K. C. and Nasr-El-Din, H. A., 1995. Water-Soluble Hydrophobically Associating Polymers for Improved Oil Recovery: A Literature Review. Paper SPE 29008, *SPE International Symposium on Oilfield Chemistry*, San Antonio, Texas, USA.
- Urbissinova, T. S., Trivedi, J. J., and Kuru, E., 2010. Effect of Elasticity During Viscoelastic Polymer Flooding: A Possible Mechanism of Increasing the Sweep Efficiency. *Journal of Canadian Petroleum Technology*, 49(12): 49-56.
- Vermolen, E. C. M., Haasterecht, M. J. T., Masalmeh, S. K., Faber, M. J., Boersma, D. M., and Gruenenfelder, M., 2011. Pushing the Envelope for Polymer Flooding Towards High-temperature and High-salinity Reservoirs with Polyacrylamide Based Ter-polymers. Paper SPE 141497, *SPE Middle East Oil and Gas Show and Conference*, Manama, Bahrain.

- Walter, A. V., Jimenez, L. N., Dinic, J., Sharma, V., and Erk, K. A., 2019. Effect of salt valency and concentration on shear and extensional rheology of aqueous polyelectrolyte solutions for enhanced oil recovery. *Rheologica Acta*, 58(3-4): 145–157.
- Wang, D., Liu, H., Niu, J., and Chen, F., 1998. Application results and understanding of several problems of industrial scale polymer flooding in Daqing Oil Field. Paper SPE 50928, *SPE International Oil and Gas Conference and Exhibition*, Beijing, China.
- Wang, D., Jiecheng, C., Qingyan, Y., Wenchao, G., and Qun, L., 2000a. Viscous-Elastic Polymer Can Increase Microscale Displacement Efficiency in Cores. Paper SPE 63227, *SPE Annual Technical Conference and Exhibition*, Dallas, Texas, USA.
- Wang, D., Qun, L., Xiaohong, G., and Yan, W., 2000b. The Engineering and Technical Aspects of Polymer Flooding in Daqing Oil Field. Paper SPE 64722, *SPE International Oil and Gas Conference and Exhibition*, Beijing, China.
- Wang, D., Han, P., Shao, Z., Hou, W., and Seright, R. S., 2008. Sweep-Improvement Options for the Daqing Oil Field. *SPE Reservoir Evaluation and Engineering*, 11(1): 18-26.
- Weiss, W. W. and Baldwin, R. W., 1985. Planning and Implementing a Large-Scale Polymer Flood. *Journal of Petroleum Technology*, 37(4): 720–730.
- Weiss, W. W., 1992. Performance Review of a Large-Scale Polymer Flood. Paper SPE/DOE 241 45, *SPE/DOE Eighth Symposium on Enhanced Oil Recovery*, Tulsa, Oklahoma, USA.
- Wilton, R. R. and Torabi, F., 2013. Rheological Assessment of the Elasticity of Polymers for Enhanced Heavy Oil Recovery. Paper SPE 165488, *SPE Heavy Oil Conference*, Calgary, Alberta, Canada.
- Wreath, D., Pope, G. A., and Sepehrnoori, K., 1990. Dependence of Polymer Apparent Viscosity on the Permeable Media and Flow Conditions. *In Situ*, 14(3): 263-283.
- Zamani, N., Bondino, I., Kaufmann, R., and Skauge, A., 2015. Effect of porous media properties on the onset of polymer extensional viscosity. *Journal of Petroleum Science and Engineering*, 133: 483–495.
- Zitha, P., Felder, R., Zornes, D., Brown, K., and Mohanty, K., 2011. Increasing Hydrocarbon Recovery Factors. *SPE technological updates*.

APPENDICES

Appendix A: Correlations Used to Estimate the Properties of Fluid

- The bubble-point pressure can be calculated by the following correlation (Standing, 1981):

$$P_b = 18.2 \left[\left(\frac{R_s}{\gamma_g} \right)^{0.83} \left(\frac{10^{0.00091(T-460)}}{10^{0.0125 API}} \right) - 1.4 \right], \quad (A1)$$

where P_b is the bubble-point pressure in psi, R_s is the gas solubility in SCF/STB, γ_g is the solution gas specific gravity, T is the reservoir temperature in °R, and API° is the stock-tank oil API gravity.

- The oil formation volume factor can be calculated by the following correlation (Ahmed, 1989):

$$B_o = B_{ob} \exp[D(\exp(aP) - \exp(aP_b))], \quad (A2)$$

$$D = [4.588893 + 0.0025999 R_s]^{-1}, \quad (A3)$$

$$a = -0.00018473, \quad (A4)$$

where B_{ob} is the formation volume factor at saturation pressure in bbl/STB and P is the reservoir pressure in psi.

Appendix B: E-UVM Implementation in MRST (note: both codes in Appendices B and C must be added to the “*equationsThreePhaseBlackOilPolymer*” MRST file)

%%%

% Simulation Model Parameters

```
dx=350*ft;
dy=350*ft;
dz=50*ft;
nx=15;
ny=15;
nz=5;
G = cartGrid([nx, ny, nz], [dx, dy, dz]);
G = computeGeometry(G);
G.dimensionsx=dx/nx;
G.dimensionsy=dy/ny;
G.dimensionsz=dz/nz;
```

% Calculation of the number of interfaces between the gridblocks

```
x=G.cartDims(1,1); %number of cells in x-directions
y=G.cartDims(1,2); %number of cells in y-directions
z=G.cartDims(1,3); %number of cells in z-directions
```

```
if x==1
    Nfaces=y*(x-1)+y*(z-1)+z*(y-1)+z*(x-1);
elseif y==1
    Nfaces=x*(z-1)+x*(y-1)+z*(y-1)+z*(x-1);
elseif z==1
    Nfaces=x*(z-1)+x*(y-1)+y*(x-1)+y*(z-1);
else
    Nfaces=y*(x*(z-1)+z*(x-1))+x*z*(y-1);
end
```

```

if model.usingExtendedUVM

    if ~opt.resOnly
        krwF = s.faceUpstr(upcw, krW.val);
        swF = s.faceUpstr(upcw, sW.val);
    end

    if opt.resOnly
        krwF = s.faceUpstr(upcw, krW);
        swF = s.faceUpstr(upcw, sW);
    end

    end

ShearRate=zeros(numel(Vw),1);
index = find(abs(Vw) > 0);

% Effective Shear Rate Equation (Lake et al., 2014)
C = Csh*(((3*n1+1)/(4*n1))^(n1/(n1-1)));
ShearRate(index)= C*((4*abs(Vw(index)))/sqrt(8*krwF(index).*kabsF(index).*poroFace(index).*swF(index)));

% Extended Viscoelastic Model (E-UVM)
EUVMVisc=(myuinf+(myu0-myuinf)*((1+(lamda1*abs(ShearRate)).^2).^(n1-1)/2))+myumax*(1-exp(-
((lamda2*relaxtime*abs(ShearRate)).^(n2-1))))).*((1+(lamda3*abs(ShearRate)).^2).^(-n3/2));

% Shear factors (Z) calculation
shearMultf=EUVMVisc/myu0;

%% Calculations for wellbores
ShearRateW=zeros(numel(VwW),1);
indexW = find(abs(VwW) > 0);

% Defining the permeabilities and saturations for wellbore cells
swW=value(sW(wc));
kabsW=kabs(wc);
krwW=value(krW(wc));

```

```

% Replacing zeros in rel perm term to avoid "Inf" in ShearRateW
ind=find(krwW==0);
krwW(ind)=10^(-8);

% Effective Shear Rate Equation for wellbore cells
ShearRateW(indexW)=C*((4*abs(VwW(indexW)))/sqrt(8*krwW(indexW).*kabsW(indexW).*poroW(index
W).*swW(indexW))));

% E-UVM for wellbore cells
EUVMViscW=(myuinf+(myu0-myuinf)*((1+(lamda1*abs(ShearRateW)).^2).^((n1-1)/2))+myumax*(1-exp(-
((lamda2*relaxtime*abs(ShearRateW)).^(n2-1))))).*((1+(lamda3*abs(ShearRateW)).^2).^(-n3/2)));

% Shear factors (Z) for wellbore cells
shearMultW=EUVMViscW/myu0;

%Modifying fluxes and mobilities
vW = vW ./ shearMultf;
vP = vP ./ shearMultf;

mob{1}(wc) = mob{1}(wc)./shearMultW;

end
%%%%%%%%%%%%%%%%%%%%%%%%%%%%%%%%%%%%%%%%%%%%%%%%%%%%%%%%%%%%%%%%%%%%%%%%

```



```

kabsFz=zeros(z_interface,1);
deltaPhix=zeros(x_interface,1);
deltaPhiy=zeros(y_interface,1);
deltaPhiz=zeros(z_interface,1);

for i=1:x_interface
kabsFx(i)=kabsF(i);
deltaPhix(i)=deltaPhi(i);
end

for i=(x_interface+1):(x_interface+y_interface)
kabsFy(i-x_interface)=kabsF(i);
deltaPhiy(i-x_interface)=deltaPhi(i);
end

for i=(f.Nfaces-z_interface+1):f.Nfaces
kabsFz(i-(f.Nfaces-z_interface))=kabsF(i);
deltaPhiz(i-(f.Nfaces-z_interface))=deltaPhi(i);
end

```

% Factors used in calculation of KPhi

```

w=0;
r=1;
xx=0;
yy=0;
e=1;
d=0;
dd=0;
q=model.G.cartDims(1,1)*(model.G.cartDims(1,2)-1);

```

% The dimension of the cell in a corresponding direction

```

Dx=G.dimensionsx;
Dy=G.dimensionsy;
Dz=G.dimensionsz;

```

% Preallocating parameters

```

KxPhix=zeros(model.G.cells.num,1);
KyPhiy=zeros(model.G.cells.num,1);

```

```

KzPhiz=zeros(model.G.cells.num,1);
KPhi=zeros(model.G.cells.num,1);
Nc=zeros(model.G.cells.num,1);
Nb=zeros(model.G.cells.num,1);
Nt=zeros(model.G.cells.num,1);

%%% Generating KPhi for x direction
for i=1:model.G.cells.num

% The case with only one cell in x direction
if model.G.cartDims(1,1)==1
    KxPhix=0;

% For the cell where x=1
elseif i==1
    KxPhix(i) = 0.5*((kabsFx(i-w)/Dx)*deltaPhix(i-w));
    w=w+1;

elseif rem(i,(model.G.cartDims(1,1)))==1
    KxPhix(i) = 0.5*((kabsFx(i-w)/Dx)*deltaPhix(i-w));
    w=w+1;

% For the cells where x=last cell
elseif rem(i,(model.G.cartDims(1,1)))==0
    KxPhix(i) = 0.5*((kabsFx(i-r)/Dx)*deltaPhix(i-r));
    r=r+1;

% For the x-middle cells
else
    KxPhix(i) = 0.5*((kabsFx(i-xx-1)/Dx)*deltaPhix(i-xx-1)+(kabsFx(i-xx)/Dx)*deltaPhix(i-xx));
    qq=i+1;
    if rem(qq,(model.G.cartDims(1,1)))==0
        xx=xx+1;
    end
end
end

%%% Generating KPhi for y direction
for i=1:model.G.cells.num

% The case with only one cell in y direction
if model.G.cartDims(1,2)==1
    KyPhiy=0;

% The case with two cells in y direction
elseif model.G.cartDims(1,2)==2

```

```

    if rem(i,(model.G.cartDims(1,1)*model.G.cartDims(1,2)))>0 &&
rem(i,(model.G.cartDims(1,1)*model.G.cartDims(1,2)))<(model.G.cartDims(1,1)+1)

        if rem(i,(model.G.cartDims(1,1)*model.G.cartDims(1,2)))==1 &&
i>(model.G.cartDims(1,1)*model.G.cartDims(1,2))
            yy=yy+1;
        end
        KyPhiy(i) = 0.5*((kabsFy(i-(model.G.cartDims(1,1)*yy))/Dy)*deltaPhiy(i-
(model.G.cartDims(1,1)*yy)));

    else
        KyPhiy(i) = 0.5*((kabsFy(i-(model.G.cartDims(1,1)*e))/Dy)*deltaPhiy(i-
(model.G.cartDims(1,1)*e)));

        if rem(i,(model.G.cartDims(1,1)*model.G.cartDims(1,2)))==0
            e=e+1;
        end
    end

% For the first y-layer (the case with more than two cells in y direction)
elseif rem(i,(model.G.cartDims(1,1)*model.G.cartDims(1,2)))>0 &&
rem(i,(model.G.cartDims(1,1)*model.G.cartDims(1,2)))<(model.G.cartDims(1,1)+1)

    if rem(i,(model.G.cartDims(1,1)*model.G.cartDims(1,2)))==1 &&
i>(model.G.cartDims(1,1)*model.G.cartDims(1,2))
        yy=yy+1;
    end
    KyPhiy(i) = 0.5*((kabsFy(i-(model.G.cartDims(1,1)*yy))/Dy)*deltaPhiy(i-
(model.G.cartDims(1,1)*yy)));

% For the last y-layer (the case with more than two cells in y direction)
elseif rem(i,q)>0 && rem(i,q)<(model.G.cartDims(1,1)+1) &&
i<=(e*model.G.cartDims(1,1)*model.G.cartDims(1,2))

    KyPhiy(i) = 0.5*((kabsFy(i-(model.G.cartDims(1,1)*e))/Dy)*deltaPhiy(i-
(model.G.cartDims(1,1)*e)));

    if rem(i,q)==model.G.cartDims(1,1)
        q=q+model.G.cartDims(1,1)*(model.G.cartDims(1,2)-1)+model.G.cartDims(1,1);
        e=e+1;
    end

% For the y-middle layers
else
    KyPhiy(i) = 0.5*((kabsFy(i-model.G.cartDims(1,1)*d-
model.G.cartDims(1,1))/Dy)*deltaPhiy(i-model.G.cartDims(1,1)*d-model.G.cartDims(1,1))+
(kabsFy(i-
model.G.cartDims(1,1)*d)/Dy)*deltaPhiy(i-model.G.cartDims(1,1)*d));
    dd=dd+1;

    if rem(dd,(model.G.cartDims(1,1)*(model.G.cartDims(1,2)-2)))==0
        d=d+1;
    end
end
end
end

```

```

%%% Generating KPhi for z direction
for i=1:model.G.cells.num

    % The case with only one cell in z direction
    if model.G.cartDims(1,3)==1
        KzPhiz=0;

    % For the cell where z=1
    elseif i<((model.G.cartDims(1,1)*model.G.cartDims(1,2))+1)
        KzPhiz(i) = 0.5*((kabsFz(i)/Dz)*deltaPhiz(i));

    % For the cells where z=last cell
    elseif i>(model.G.cells.num-(model.G.cartDims(1,1)*model.G.cartDims(1,2)))
        KzPhiz(i) = 0.5*((kabsFz(i-(model.G.cartDims(1,1)*model.G.cartDims(1,2)))/Dz)*deltaPhiz(i-
(model.G.cartDims(1,1)*model.G.cartDims(1,2))));

    % For the z-middle cells
    else
        KzPhiz(i) = 0.5*((kabsFz(i-(model.G.cartDims(1,1)*model.G.cartDims(1,2)))/Dz)*deltaPhiz(i-
(model.G.cartDims(1,1)*model.G.cartDims(1,2)))+(kabsFz(i)/Dz)*deltaPhiz(i));
    end
end

%%% Root Mean Square (RMS) value of KPhi is used to compute capillary number
IFT=30;
for i=1:model.G.cells.num

    % 1-Dimensional
    if model.G.cartDims(1,1)>1 && model.G.cartDims(1,2)==1 && model.G.cartDims(1,3)==1
        KPhi(i) = sqrt(KxPhix(i).^2);
    elseif model.G.cartDims(1,2)>1 && model.G.cartDims(1,1)==1 && model.G.cartDims(1,3)==1
        KPhi(i) = sqrt(KyPhiy(i).^2);
    elseif model.G.cartDims(1,3)>1 && model.G.cartDims(1,1)==1 && model.G.cartDims(1,2)==1
        KPhi(i) = sqrt(KzPhiz(i).^2);

    % 2-Dimensional
    elseif model.G.cartDims(1,1)==1
        KPhi(i) = sqrt(KyPhiy(i).^2+KzPhiz(i).^2);
    elseif model.G.cartDims(1,2)==1
        KPhi(i) = sqrt(KxPhix(i).^2+KzPhiz(i).^2);
    elseif model.G.cartDims(1,3)==1
        KPhi(i) = sqrt(KxPhix(i).^2+KyPhiy(i).^2);

    % 3-Dimensional
    else
        KPhi(i) = sqrt(KxPhix(i).^2+KyPhiy(i).^2+KzPhiz(i).^2);
    end
end

```

```

%Capillary Number calculation
    Nc(i) = KPhi(i)/IFT;
end

%%% Estimating the Bond number and Trapping number
    for i=1:model.G.cells.num
        Nb(i) = (kabs(i)*9.80665*value(rhoW(i)-rhoO(i)))/IFT;

        Nt(i) =sqrt((Nb(i))^2+(Nc(i))^2); % for horizontal flow
    end

%% Calculation of Residual Oil Saturations and Corey's model modified parameters %%%

if model.Delshadetal_1986

    %%% Defining Corey's model initial waterflooding parameters
    Swiri=0.21*ones(model.G.cells.num,1);
    Sori=0.47*ones(model.G.cells.num,1);
    nwi=2.55*ones(model.G.cells.num,1);
    noi=3.03*ones(model.G.cells.num,1);
    kerWi=0.02*ones(model.G.cells.num,1);
    kerOi=0.123*ones(model.G.cells.num,1);

    %%% Defining Corey's model modified parameters
    sOr_high=0*ones(model.G.cells.num,1);           %residual oil saturation at high Nc/Nt
    sWir_high=0*ones(model.G.cells.num,1);          %residual water saturation at high Nc/Nt
    T_1_oil=500*ones(model.G.cells.num,1);          %phase trapping parameter
    T_1_water=100000*ones(model.G.cells.num,1);     %phase trapping parameter
    tau_oil=0.45*ones(model.G.cells.num,1);         %pore-size distribution factor
    tau_water=1*ones(model.G.cells.num,1);          %pore-size distribution factor
    kerw_high=ones(model.G.cells.num,1);            % water endpoint rel perm at high Nc/Nt
    kero_high=ones(model.G.cells.num,1);            % water endpoint rel perm at high Nc/Nt
    nw_high=ones(model.G.cells.num,1);              % water exponent at high Nc/Nt
    no_high=ones(model.G.cells.num,1);              %oil exponent at high Nc/Nt

    % Estimating residual saturations from Delshad et al. (1990) model
    Sor = sOr_high+((Sori-sOr_high)/(1+T_1_oil.*(Nt.^tau)));
    Swir = sWir_high+((Swiri-sWir_high)/(1+T_1_water.*(Nt.^tau)));

    % Estimating endpoint relative permeabilities from Delshad et al. (1986) model
    kerO = kerOi+((Swiri-Swir)/(Swiri-sWir_high)).*(kero_high-kerOi);
    kerW = kerWi+((Sori-Sor)/(Sori-sOr_high)).*(kerw_high-kerWi);

    %Estimating exponents from Delshad et al. (1986) model
    no = noi+((Swiri-Swir)/(Swiri-sWir_high)).*(no_high-noi);
    nw = nwi+((Sori-Sor)/(Sori-sOr_high)).*(nw_high-nwi);

end

```

```
%% Calculation of Relative Permeabilities %%%%
```

```
krG=zeros(model.G.cells.num,1);
```

```
%%% Estimating relative permeabilities
```

```
krW=kerW.*((sW-Swir)/(1-Swir-Sor)).^nw;
```

```
krO=kerO.*((1-sW-Sor)/(1-Swir-Sor)).^no;
```

```
%%% Getting rid of complex numbers in the matrix
```

```
krW(imag(value(krW)) ~= 0) = 0;
```

```
krO(imag(value(krO)) ~= 0) = 0;
```